INCORPORATING NITROGEN STABLE ISOTOPES INTO ATMOSPHERIC CHEMISTRY MODELS

by

Huan Fang

A Dissertation

Submitted to the Faculty of Purdue University

In Partial Fulfillment of the Requirements for the degree of

Doctor of Philosophy

Department of Earth, Atmospheric and Planetary Sciences

West Lafayette, Indiana

May 2021

THE PURDUE UNIVERSITY GRADUATE SCHOOL
STATEMENT OF COMMITTEE APPROVAL

Dr. Greg Michalski, Chair

Department of Earth, Atmospheric and Planetary Sciences

Dr. Harshvardhan

Department of Earth, Atmospheric and Planetary Sciences

Dr. Michael Baldwin

Department of Earth, Atmospheric and Planetary Sciences

Dr. Robert Jacko

Lyles School of Civil Engineerin

Dr. Gouri Prabhakar

Department of Earth, Atmospheric and Planetary Sciences

Approved by:

Dr. Michael Baldwin

To my friends and family:

Thank you for the support

ACKNOWLEDGMENTS

I would like to express my deep appreciation and gratitude to my advisor Dr. Greg Michalski. It is a great fortune to start my research career under the guidance and mentorship of Greg. From my undergraduate studies to Ph.D. researches, his immense knowledge enlightens my research ideas; his patient and encouragement resolve every moment that I was struggling; his enthusiasm promotes the progress of my research. After a seven-year research experience (undergraduate and Ph.D.) with Greg, I gradually become a qualified researcher with strong enthusiasm, concentration, and persistence in my research. I hope I would have more chances to do research with Greg after I finish my Ph.D. research.

I would also like to thank my committee members, Drs. Michael Baldwin, Robert Jacko, Gouri Prabhakar, and Harshvardhan for the friendly guidance and thought provoking-suggestions that each of them offered to me. I would like to recognize Scott Spak for providing emission dataset generated from SMOKE, Wendell Walters for providing $\delta^{15}N$ values for different emission sources based on his lab work, Ben Murphy for helping on reconstructing aerosol module for nitrogen isotopes, as well as Tomas Ratkus, Frank Bakhit, and Steven Plite for setting up CMAQ on Purdue research computing.

Special thanks are also due to the Purdue Research Foundation (PRF), Purdue Climate Change Research Center (PCCRC), and Purdue Center for the Environment (C4E), and Department of Earth, Atmospheric, and Planetary Sciences at Purdue for their financial supports that have allowed me to conduct independent research, and/or attend numerous academic conferences leading to my intellectual growth during the past five years.

TABLE OF CONTENTS

LIST OF TABLES

LIST OF FIGURES

PREFACE

This dissertation is original, independent work by the author, Huan Fang.

ABSTRACT

The nitrogen stable isotope composition ($\delta^{15}N$) of nitrogen oxides (NO_x) may be an effective tool to evaluate the accuracy of the NO_x emission inventories, which are based on different assumptions. In order to approach this goal, the understanding of (1) the $\delta^{15}N(NO_x)$ values of the major emission sources, (2) how atmospheric processes, such as mixing, transport, and deposition, alters the composition of atmospheric NO_x, (3) gas-phase isotope effects that occur during the oxidation of NO_x into NO_y (NO_x + NO_3, N_2O_5 HNO_3, + HNO_4 + HONO + Peroxyacetyl nitrate (PAN) + organic nitrates + any oxidized N compound), and (4) the corresponding $\delta^{15}N$ measurement of atmospheric NO_x under different scenarios are necessary. Therefore, I developed ^{15}N incorporated CMAQ (The Community Multiscale Air Quality Modeling System), to explore the changes in $\delta^{15}N$ driven by atmospheric processes and tropospheric photochemistry after different sources of NO_x being emitted to the atmosphere. The ^{15}N was first incorporated into the emission dataset, based on the amount of NO_x emission from each source retrieved from the emission inventories, and the corresponding $\delta^{15}N(NO_x)$ values characterized from the prior studies. Then the ^{15}N incorporated emission dataset was used as input to run CMAQ, to trace how atmospheric processes alter the composition of NO_x, by using WRF (Weather Research and Forecasting) model to prepare meteorology conditions. Finally, ^{15}N was incorporated into the chemical mechanisms of CMAQ to explore the gas phase isotope effects associated with NO_x oxidation, by adding the ^{15}N of N compounds and replicate the chemical reactions involving N compounds, with the corresponding fractionation factors (α) based on prior experimental and theoretical studies. The simulated $\delta^{15}N(NO_x)$ was compared with corresponding measurements at NADP sides within Indiana, Illinois, Ohio, and Kentucky.

Overall, this research explores changes in $\delta^{15}N$ values along the "journey" of atmospheric NO_x, for better understanding the spatial distributions of the NO_x emission budgets, as well as the impacts from the associated atmospheric processes and NO_x oxidation chemistry.

CHAPTER 1. INTRODUCTION

1.1 Nitrogen Oxides

Emissions and oxidation of nitrogen oxides (NO_x = NO and NO_2) is the key driver of atmospheric chemistry, air quality, and climate (IPCC, 2014). The atmospheric NO_x oxidizes into NO_y (NO_x + NO_3, N_2O_5 HNO_3, + HNO_4 + HONO + Peroxyacetyl nitrate (PAN) + organic nitrates (ONIT) + any oxidized N compounds) through various pathways, which is known as NO_y cycling (Fig. 1.1). With the presence of ozone, NO and NO_2 interconvert rapidly in the troposphere and stratosphere. During the daytime, the concentration of O_3 is controlled by the photochemical cycling of NO_x, known as Leighton Cycle (Eq. (1.1-1.3)) (Leighton, 1961; Finlayson-Pitts and Pitts, 1999):

$$NO + O_3 \rightarrow NO_2 + O_2 \quad \text{Eq. (1.1)}$$

$$NO_2 + h\nu \rightarrow NO + O(^3P) \quad \text{Eq. (1.2)}$$

$$O(^3P) + O_2 + M \rightarrow NO + O_3 + M \quad \text{Eq. (1.3)}$$

Another pathway of NO oxidation is driven by peroxy radicals Eq. (1.4-1.5) (Ingold, 1969):

$$NO + HO_2 \rightarrow OH + NO_2 \quad \text{Eq. (1.4)}$$

$$NO + RO_2 \rightarrow RO + NO_2 \quad \text{Eq. (1.5)}$$

The atmospheric NO_2 could oxidize further to HNO_3 through two pathways: Reacting with OH radicals during the daytime (Eq. (1.6)) and with O_3 and NO_3 during the nighttime (Eq. (1.7-9)).

$$NO_2 + OH + M \rightarrow HNO_3 + M \quad \text{Eq. (1.6)}$$

$$NO_2 + O_3 \rightarrow NO_3 + O_2 \quad \text{Eq. (1.7)}$$

$$NO_2 + NO_3 \rightarrow N_2O_5 \quad \text{Eq. (1.8)}$$

$$N_2O_5 + H_2O \rightarrow 2HNO_3 \quad \text{Eq. (1.9)}$$

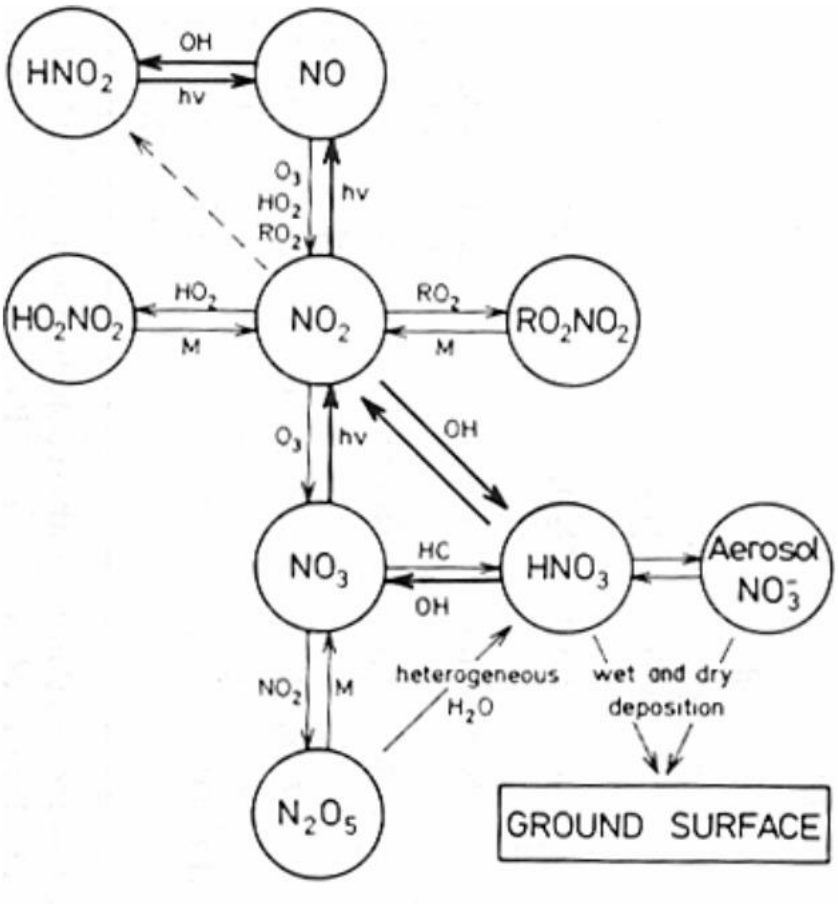

Figure 1.1.1: Atmospheric Nitrogen Cycle

The termination reactions in NO_y cycling produces HNO_3, which could either dissolve into droplets causing acid rain, or turn into aerosols ($NO_3^-{}_{atm} = HNO_{3(g)}$+particulate NO_3^-), resulting in acid rain, groundwater nitrate, and the degradation of terrestrial and aquatic ecosystems (Galloway et al., 2004). NO_x oxidation in the presence of VOCs elevates ground-level O_3 and generates secondary particulates, both of which affect the human respiratory system, causing health problems and mortality in susceptible populations (Lighty et al., 2000, Seinfeld and Pandis, 2006). Aerosols have a pronounced impact on climate, and nitrate particles and secondary aerosols (sulfate, organics) generated by NO_x driven oxidation affect cloud physics by enhancing the reflection of solar radiation, which leads to the largest source of uncertainty in current climate models that predict future warming due to greenhouse gases (Schwartz, S. E., 1996). Due to the importance of NO_x in air quality, climate, and human and environmental health, it is important to

understand the sources of NO_x. However, despite years of research, there are still a number of significant uncertainties in the NO_x budget.

The atmospheric NO_x sources from both anthropogenic emissions, such as automobiles, power plants, agriculture, livestock waste, as well as natural processes, including by-product of nitrification and denitrification occurring in soil, and lightning (Galloway et al., 2004; Reis et al., 2009). The estimation of emissions from each source is called emission inventory, among which the most well-known and commonly used is the National Emission Inventory (NEI), updated by USEPA (the United States Environmental Protection Agency) every three years. The emissions from different sources are categorized into four categories: a) biogenic, the by-products of microbial nitrification and denitrification occurring in the soil; b) mobile, the emission based on on-road vehicle activity; c) point, the anthropogenic emissions that are located at a fixed, stationary position, significantly contribute from power plants; and d) area, the anthropogenic emissions that spread over a spatial extent and individually too small in magnitude to report as point sources, primarily from livestock and off-road vehicles. The geographical distribution of annual NO_x emission from each category in percentage (%) over each grid throughout the Midwest, estimation by 2002 NEI is shown in Figure 1.2. The prevalence of each of these sources varies geographically, showing the dominance of biogenic emission in the western part of the domain; mobile emission dominates in megacities and the counties with major highways; higher area emission in the rural areas; and the strong influence of power plants at the counties, which they are located in.

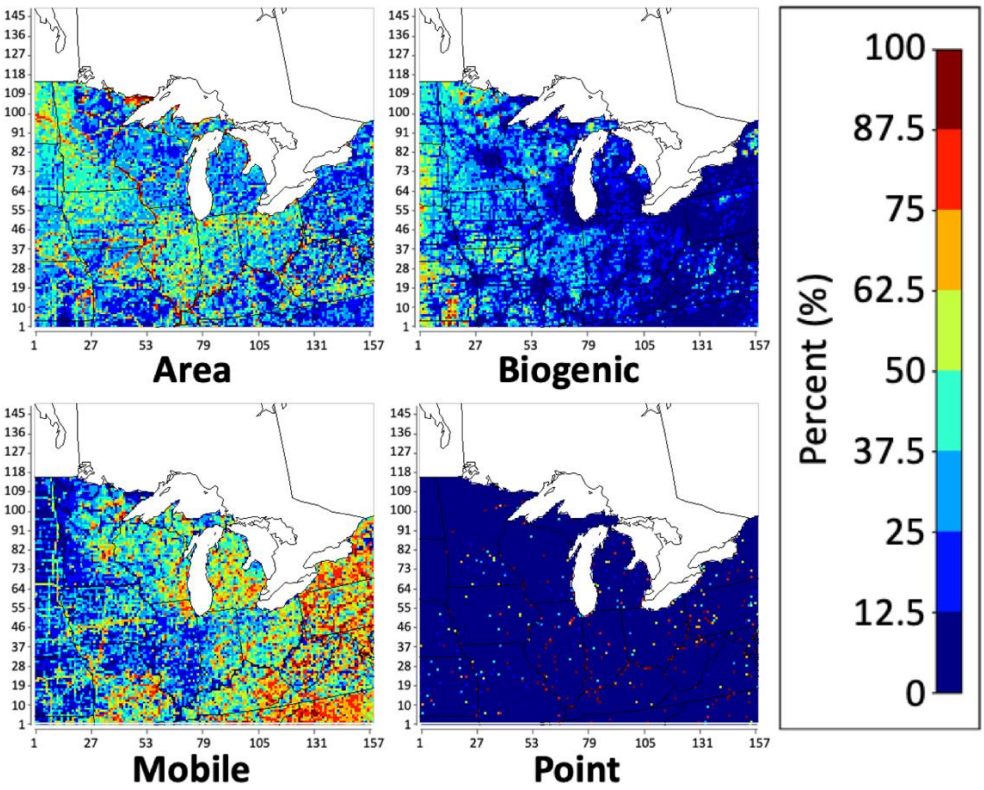

Figure 1.1.2: 2002 NEI for annual NO_x emission from each category in percentage (%)

The NO_x emissions from each source also vary with time. During the growing season of plants, from April to October, the percentage of NO_x emission from biogenic sources over the western regions of the Midwest increases from less than 25% to more than 50%. During the winter, due to the lower ambient air temperature, NO_x emission from mobile sources increases. Besides these, the increase in NO_x emission from point source occurs during the transition from warm to cold and vice versa.

The NO_x emissions budget estimated by different versions of emission inventories varies. The annual NO_x emission amounts from each category, estimated by 2002, 2005, 2008, 2011, and 2014 NEI is shown in Figure 1.3. With the updating methods of the NO_x emission estimation, such as different versions of Biogenic Emissions Inventory System (BEIS) and mobile source emissions models (MOBILE and MOVES), as well as the estimation of the efficiency of different NO_x emission control technologies (SCR, SCNR, LNB, OFA), the estimations of annual NO_x emission from different versions of NEI vary. Some other alternative NO_x emission inventories are using different methods to estimate NO_x emission budget, by considering the uptakes and emissions from

vegetation (Almaraz et al., 2018), or separating NO_x emission from gasoline vehicle and diesel vehicle by fuel consumption (Parrish, 2006) (details in Chapter 2).

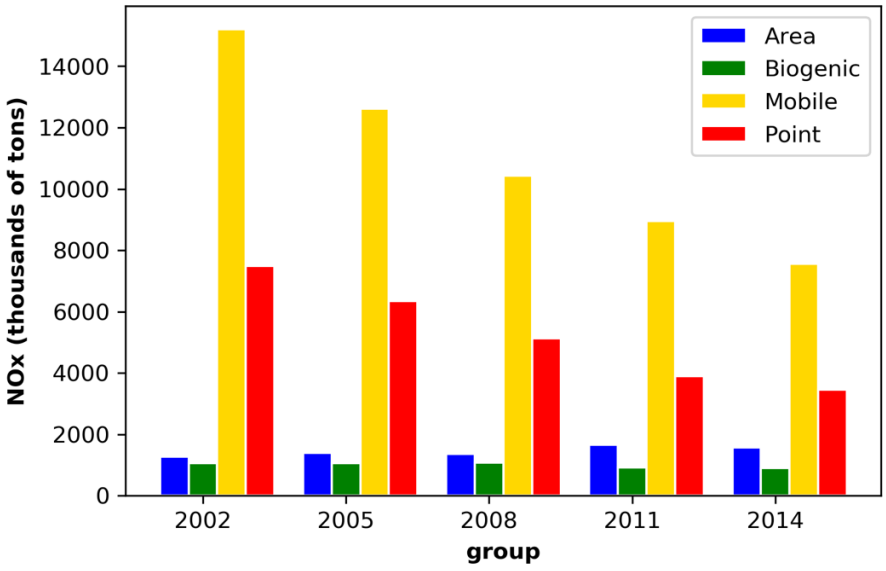

Figure 1.1.3: Annual NO_x emission from each category based on different versions of NEI

1.2 Nitrogen stable isotope composition ($\delta^{15}N$)

The chemical characteristics of an element are determined by the number of protons in its nucleus. For example, any nucleus containing 7 protons is defined as a nitrogen atom. The elements with the same number of protons but a different number of neutrons are called isotopes. For example, a nucleus containing 7 protons and 7 neutrons, and a nucleus containing 7 protons and 8 neutrons are isotopes of nitrogen. The isotopes, which remain stable with multiple nuclear configurations, are called stable isotopes. The stable isotopes of nitrogen are ^{14}N and ^{15}N.

Nitrogen stable isotope composition ($\delta^{15}N$) is the measurement of relative abundance of ^{15}N, comparing with the air (Eq. (1.10))

$$\delta^{15}N_{NOx}\,(‰) = [(^{15}NO_x/^{14}NO_x)_{\,sample} / (^{15}N_2/^{14}N_2)_{\,air} - 1] * 1000 \qquad \text{Eq. (1.10)}$$

where the ratio between $^{15}N_2$ and $^{14}N_2$ in the air is 0.0036. Since the variations in $\delta^{15}N$ values are typically small, $\delta^{15}N$ values are reported in the unit of parts per thousand or per mil (‰). With distinctive differences in $\delta^{15}N$ values for NO_x from different emission sources, based on previous

research, the measurements of $\delta^{15}N$ of atmospheric NO_x could be used for partitioning NO_x emission and evaluating NO_x emission inventories.

1.3 "Journey" of atmospheric NO_x

After NO_x from different sources being emitted into the atmosphere, its composition will change due to atmospheric processes and tropospheric photochemistry. Thus, the measured $\delta^{15}N$ of atmospheric NO_x would be different from the $\delta^{15}N$ of NO_x emission. In order to trace the changes in $\delta^{15}N$ values along the "journey" of atmospheric NO_x, ^{15}N was incorporated into CMAQ (The Community Multiscale Air Quality Modeling System). ^{15}N was first incorporated into the emission dataset to run CMAQ. $^{15}NO_x$ emitted by each emission source category (area, biogenic, mobile, and point) was calculated by

$$^{15}NO_x(i) = {}^{14}NO_x(i) \times {}^{15}R_{NO_x(i)} \quad \text{Eq. (1.11)}$$

where $^{14}NO_x$(i) is the NO_x emissions for each category (i) obtained from NEI and $^{15}R_{NOxi}$ is a ^{15}N emission factor ($^{15}NO_{Xi}/^{14}NO_{xi}$) calculated by:

$$^{15}R_{NO_x(i)} = \left(\frac{\delta^{15}N_{NO_x(i)}}{1000} + 1\right) \times 0.0036 \quad \text{Eq. (1.12)}$$

$\delta^{15}N_{NOx(i)}$ is the $\delta^{15}N$ value of each NO_x source (i = area, biogenic, mobile, and point) and 0.0036 is the $^{15}N/^{14}N$ of N_2 in the air, the reference point for $\delta^{15}N$. Thus, using Eq. (1.11-12), the emission rates of $^{15}NO_x$ were added to the emission inputs to run CMAQ. The meteorology dataset of CMAQ was generated by the Weather Research and Forecasting Model (WRF) using assimilation data of NAM (North American Mesoscale Forecast System) Analyses as the inputs.

The $\delta^{15}N$ of NO_x emission and the simulation of $\delta^{15}N(NO_x)$ that only considers the impacts from atmospheric processes were shown in Figure 1.4a-b, which presents the dispersing and mixture of NO_x emission sources. The plumes from the power plant are transported to the surrounding area, making the NO_x around the power plant heavier. On the other hand, in the urban areas, where on-road vehicles are the dominant source, the atmospheric NO_x became lighter, due to the mixture with soil emission, originate from rural areas.

^{15}N was then incorporated into the chemical mechanisms of CMAQ: RACM (Regional Atmospheric Chemistry Mechanism) and CB (Carbon Bond), after testing in the ^{15}N incorporated box model to find out the reactions, which is sensitive to the changes in $\delta^{15}N$ values (details in Chapter 4). The simulation of $\delta^{15}N(NO_x)$ that considers the impacts from both atmospheric

processes and tropospheric photochemistry were shown in Figure 1.4c, which indicates the isotopically lighter trends of atmospheric NO_x, caused by the gas phase isotope effects associated with NO_x oxidation.

The simulated $\delta^{15}N(NO_x)$ was compared with corresponding measurements (Fig. 1.4d). With the adequate design of the model, the accuracy of emission inventories could be evaluated by comparing the measurement of $\delta^{15}N$ with the simulation of $\delta^{15}N$ using the emission inputs prepared from the target emission inventories. The smaller difference in $\delta^{15}N$ values, the more accurate the emission inventory is.

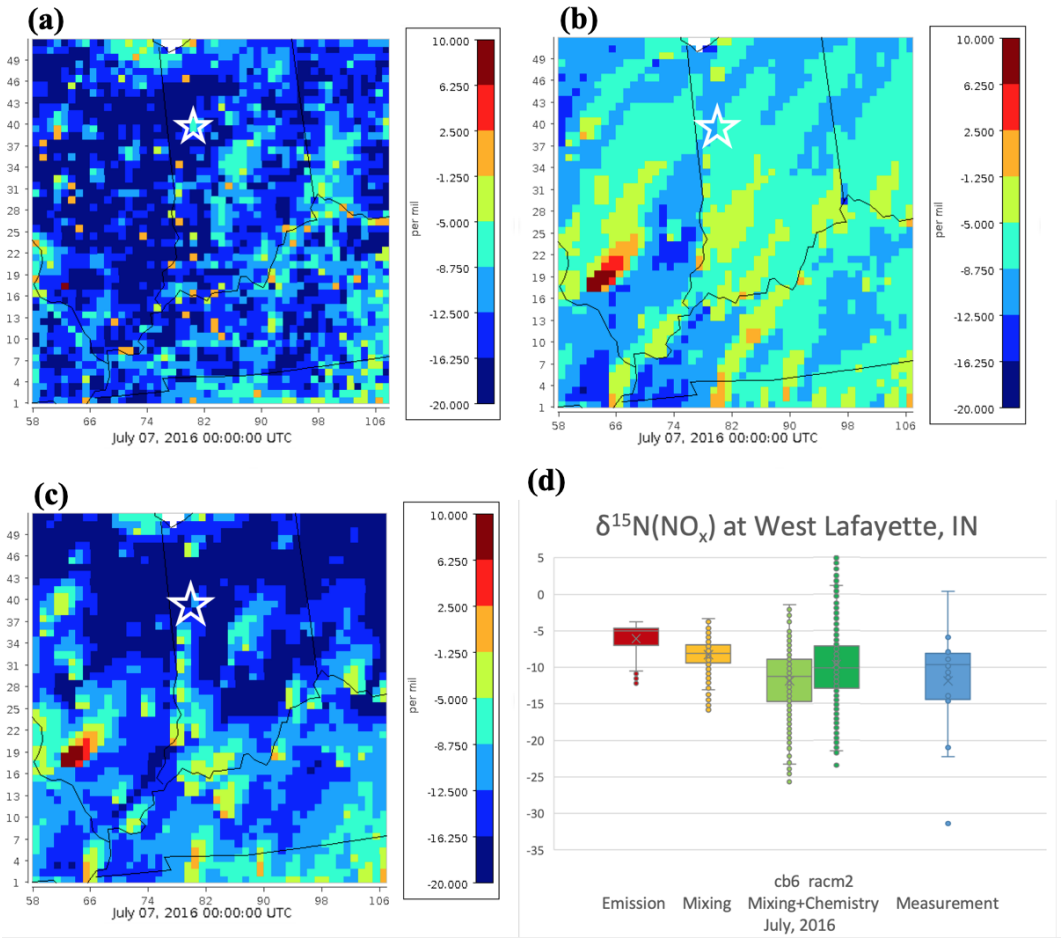

Figure 1.3.1: Evolution of $\delta^{15}N$ values along the "journey" of atmospheric NO_x

1.4 Research Objectives

In order to use nitrogen stable isotopes to explores changes in $\delta^{15}N$ values along the "journey" of atmospheric NO_x, evaluate different NO_x emission inventories, and dissolve the uncertainties in the composition of atmospheric NO_x and NO_y, this dissertation has the following research objectives:

1. The determination of the $\delta^{15}N$ values of different sources of NO_x emission, based on previous research and various lab works.

2. The exploration of the impacts of atmospheric processes on the $\delta^{15}N$ values of atmospheric NO_x, according to the simulation results from CMAQ, of which the ^{15}N is incorporated into the emission inputs.

3. The exploration of the impacts of atmospheric processes and gas-phase tropospheric photochemistry on the $\delta^{15}N$ values of atmospheric NO_x, according to the simulation results from CMAQ, of which the ^{15}N is incorporated into the emission inputs, as well as chemical mechanisms.

1.5 Outline

This dissertation is composed of 6 chapters, including this introduction, and is organized as the following:

- Chapter 2: Incorporating ^{15}N into the outputs of SMOKE version 4.6 as the emission input dataset for CMAQ version 5.2.1 for assessing the role emission sources plays in controlling the isotopic composition of NO_x, NO_y, and atmospheric nitrate. (Published by Fang, H. and Michalski, G. in *Geoscientific Model Development* (in pres))
- Chapter 3: Simulating $\delta^{15}N$ of atmospheric NO_x in CMAQ version 5.2.1, based on ^{15}N incorporated SMOKE version 4.6 and WRF version 4.0 for assessing the role atmospheric processes plays in controlling the isotopic composition of NO_x, NO_y, and atmospheric nitrate. (Published by Fang, H. and Michalski, G. in *Geoscientific Model Development* (in pres))
- Chapter 4: i_NRACM: Incorporating ^{15}N into the Regional Atmospheric Chemistry Mechanism (RACM) for assessing the role photochemistry plays in controlling the isotopic composition of NO_x, NO_y, and atmospheric nitrate. (Published by Michalski, G.; Fang, H.; Walters, W. W.; and Mase, D. in *Geoscientific Model Development* (in pres))
- Chapter 5: Simulating $\delta^{15}N$ of atmospheric NO_x in CMAQ version 5.2.1, based on ^{15}N

incorporated SMOKE version 4.6, WRF version 4.0, ^{15}N incorporated CB, as well as ^{15}N incorporated RACM version 2 and CB version 6, for assessing the role gas-phase tropospheric photochemistry plays in controlling the isotopic composition of NO_x, NO_y, and atmospheric nitrate. . (Published by Fang, H. and Michalski, G. in *Geoscientific Model Development* (in pres))

- Chapter 6: Conclusions.

CHAPTER 2. INCORPORATING 15N INTO THE OUTPUTS OF SMOKE VERSION 4.6 AS THE EMISSION INPUT DATASET FOR CMAQ VERSION 5.2.1 FOR ASSESSING THE ROLE EMISSION SOURCES PLAYS IN CONTROLLING THE ISOTOPIC COMPOSITION OF NOX, NOY, AND ATMOSPHERIC NITRATE

The following chapter is a reprint from an article currently in press (Fang, H. and Michalski, G. Incorporating ^{15}N into the outputs of SMOKE version 4.6 as the emission input dataset for CMAQ version 5.2.1 for assessing the role emission sources plays in controlling the isotopic composition of NO_x, NO_y, and atmospheric nitrate. *Geoscientific Model Development*)

2.1 Introduction

NO_x are important trace gases that affect atmospheric chemistry, air quality, and climate (NO_x = nitric oxide (NO) + nitrogen dioxide (NO_2)). The main sources of tropospheric NO_x are emissions from vehicles, power plants, agriculture, livestock waste, as well as the natural by-product of nitrification and denitrification occurring in soil, and lightning. The NO_x photochemical cycle generates OH and HO_2 radicals, organic peroxy radicals (RO_2), and ozone (O_3), which ultimately oxidize NO_x into NO_y ($NO_y = NO_x + HONO + HNO_3 + HNO_4 + N_2O_5$ + other N oxides). During the photochemical processes that convert NO_x to NO_y, ground-level concentrations of O_3 become elevated and secondary particles are generated. Secondary aerosols in turn affect cloud physics, enhancing the reflection of solar radiation (Schwartz, 1996) and are hazardous to human health (Lighty et al., 2000). Thus, the importance of NO_x in air quality, climate, and human and environmental health makes understanding the spatial and temporal variation in the sources of NO_x a vital scientific question. However, despite years of research, there are still a number of significant uncertainties in the NO_x budget.

There are significant uncertainties in the amount of NO_x emitted by soil at local and global scales. About 15% of global NO_x emissions, ranging from 6.6 to 21 Tg N yr^{-1}, is derived from global soil NO_x emissions yet evaluating and verifying emission rates using both laboratory and field measurements is still a challenge (Galbally & Roy, 1978; Muller, 1992; Potter et al., 1996; Yienger and Levy, 1995; Davidson and Kingerlee, 1997; Ganzeveld et al., 2002; Jaeglé et al., 2005; Yan et al., 2005; Stehfest and Bouwman, 2006; Hudman et al., 2012). Soil NO_x emissions vary by different biome types, meteorological conditions, and soil physicochemical properties. Soil NO_x

emissions also depend on soil moisture that is a function of climate, such as in Mediterranean climates and tropical savannas, where wet and dry seasons cause extreme fluctuations in soil moisture (Davidson, 1992; Yienger and Levy, 1995; Scholes et al., 1997; Zörner et al., 2016). The application of N fertilizer also has a strong effect on soil NO_x emissions, which can dramatically increase during the first 1-2 days after N fertilizer application and can take several weeks for the emission rate to drop to pre-fertilizer levels (Ludwig et al., 2001). N fertilizers nitrogen may have increased soil NO_x emissions by up to 11% (Shepherd, 1991; Pilegaard, 2013), and probably currently contributes 1.8 Tg N yr^{-1} (Hudman, 2012). Furthermore, soil NO_x emissions are likely to increase as the worldwide use of fertilizers grows (Galloway et al., 2004; Houlton et al., 2013). There is also a controversy about the fate of NO_x emitted by the soil in terms of the amount that escapes the canopy and mixes into the boundary layer. Previous research has highlighted the role of vegetation in NO_x removal when the ambient NO_x concentrations are below the "compensation point" (i.e. between 1 and 3 ppbv), vegetation acts as a net source of atmospheric NO_x, but above 4 ppbv acts as a net sink (Johansson, 1987; Thoene, Rennenberg & Weber, 1996; Slovik et al., 1996; Webber & Rennenberg, 1996). However, other research claims the up to 75% of soil NO_x is lost through vegetation canopy reduction even when the ambient NO_x concentration was as low as 0.2 to 0.4 ppbv (Jacob & Wofsy, 1990; Hanson & Lindberg, 1991; Yienger & Levy II, 1995). For example, soil NO_x emission in California may be underestimated by up to 50% net due to the sink by vegetation, significantly changing current the NO_x emission inventory (Almaraz et al., 2018).

On-road vehicles are one of the major sources of NO_x, yet there are also questions about whether emission inventories are accurate. According to Parrish (2006), the estimation of on-road vehicle NO_x emission has at least 10 to 15% uncertainty. The algorithm used in the National Emission Inventory (NEI), is mileage-based, which estimates NO_x emission from on-road vehicles by travel time, speed of travel on different roadways, and emissions from vehicles per distance traveled. The emission factor of each vehicle classification and emission types are based on the represented measurement of NO_x from on-road vehicles in the US, under different ambient temperatures, travel speeds, operating modes, fuel volatility, and mileage accrual rates (Dreher & Harley, 1998; USEPA, 2003). However, the emission factors of vehicle classifications and emission types are derived from the measurements at a relatively small number of sites. As a result, the estimations of NO_x emission from on-road vehicles by mileage-based approach appears to be

inconsistent with some on-road and ambient air measurements (Ingalls, 1989; Pierson et al., 1990; Fujita et al., 1992; Pierson et al., 1996; Singer and Harley, 1996). For example, NO_x emissions from diesel engines are likely underestimated by a factor of 2 (Pierson et al., 1996; Cicero-Fernandez et al., 1997; Sawyer et al., 2000) and estimates by the mileage-based approach does not follow the same spatial and temporal patterns as the NO_x measurements (Dreher & Harley, 1998). An alternative is a fuel-based approach, which directly uses to estimates fuel consumption based on gas tax data and derives the NO_x emission by the emission factors in gram per gallon based on the represented on-road measurements (Singer & Harley, 1996; Dreher & Harley, 1998). By doing so, the only uncertainties are fuel sales data and emission factors, which are easier to determine and get controlled. As a result, the emission inventories derived from the fuel-based approach are closer to the measurements (Singer & Harley, 1996; Dreher & Harley, 1998; Sawyer et al., 2000; Parrish, 2006). At the same time, however, the fuel-based approach fails to provide accurate spatial or temporal NO_x emissions (Sawyer et al., 2000).

The uncertainty in power plant NO_x emissions is mainly the result of the recent implementation of NO_x emission control technologies. The Clean Air Act of 1995 required NO_x emission control technologies to be implemented on new power plants. The major emission control technologies are a). LNB: low NO_x burner, which decreases NO_x emission by lowering the oxygen to nitrogen in the fuel; b). SCR: selective catalytic reduction, which chemically reduces NO_x to N_2 by using NH_3 or urea as a reductant over the metal catalyst; c). SNCR: selective non-catalytic reduction, converts NO_x to N_2 by reacting NO_x with NH_3 or urea; and d). OFA: over-fire air, which increases the fuel combustion efficiency by introducing air during the combustion (Felix et al., 2012; Srivastava et al., 2005; Xing et al., 2013). Between 1990 and 2010, In the United States, NO_x control technology used in coal-fired power plants increased from less than 20% to about 86%, and from less than 2% to 70% for natural gas power plants, which decreased overall US power plant NO_x emissions by about 70% (Xing et al., 2013). The reduction of NO_x emission from power plants varies by the facility, due to the choice of emission control technologies, which cause the uncertainties. The removal efficiencies of NO_x emission are also different for each control technology. LNB can remove up to 50% of NO_x emissions from power plants but using LNB and OFA at the same time could remove 60% to 75%. SNCR can remove 30% to 66% while SCR can remove 80% to more than 90% of power plant NO_x while reburning can remove 39% to 67%

(Srivastava et al., 2005). All of these removal percentages, however, do not apply to initial fire-up times prior to catalyst efficiency reaching its maximum.

The nitrogen stable isotope composition of NO_x might be a useful tool to help resolve the uncertainties of how NO_x emission sources vary in space and time. Previous studies have shown that natural and anthropogenic NO_x sources have distinctive $^{15}N/^{14}N$ ratios (Ammann et al., 1999; Felix et al., 2012; Felix and Elliott, 2013; Fibiger et al., 2014; Heaton, 1987; Hoering, 1957; Miller et al., 2017; Walters et al., 2015a, 2015b, 2018). This variability in NO_x $^{15}N/^{14}N$ ratios quantified by

$$\delta^{15}N(NO_x)\ (‰) = [(^{15}NO_x/^{14}NO_x) / (^{15}N_2/^{14}N_2)_{air} - 1] \times 1000) \quad \text{Eq. (2.1)}$$

where $^{15}NO_x/^{14}NO_x$ is the measurement of relative abundance of ^{15}N to ^{14}N in atmospheric NO_x, compared with the ratio of nitrogen in the air, which has a $^{15}N_2/^{14}N_2 = 0.0036$.

Previous research has shown that there are distinctive differences in $\delta^{15}N$ values for NO_x from different emission sources and significant variations within each source (Fig. 2.1). Soil NO_x has the lowest $\delta^{15}N$ values ranging from -59.8 ‰ to -19.8 ‰ (Li & Wang, 2008; Felix & Elliott, 2014; Yu & Elliott, 2017; Miller et al., 2018). The NO_x emission from waste has the second-lowest $\delta^{15}N$ values, ranging from -29 ‰ to -8.5 ‰ (Felix & Elliott, 2014). The NO_x emissions from vehicles are isotopically heavier relative to soil and waste, showing $\delta^{15}N$ values ranging from -19.2 ‰ to 17 ‰ (Moore, 1977; Heaton, 1990; Ammann et al., 1999; Pearson et al., 2000; Savard et al., 2009; Redling et al., 2013; Fibiger, 2014; Felix & Elliott, 2014; Walters et al., 2015a; Walters et al., 2015b). The NO_x emissions from natural gas power plants are also isotopically heavier than soil and waste, showing $\delta^{15}N$ values ranging from -19.7 ‰ to -13.9 ‰ (Walters et al., 2015b). The $\delta^{15}N$ values of NO_x emissions from coal-fired power plants have the highest values, ranging from 2.1 ‰ to 25.6 ‰ (Heaton, 1987; Heaton, 1990; Snape, 2003; Felix et al., 2012; Felix et al., 2015; Savard et al., 2017). The implement of emission control technology tends to increase NO_x $\delta^{15}N$ values. The $\delta^{15}N$ value of NO_x emitted from coal-fired power plant equipped with SCR ranges from 15.5 ‰ to 25.6 ‰ (Felix et al., 2012), the $\delta^{15}N$ of the NO_x emissions from coal-fired power plant equipped with SNCR ranges from 13.6 ‰ to 15.1 ‰ (Felix et al., 2012), the $\delta^{15}N$ of the NO_x emissions from coal-fired power plants equipped with OFA/LNB ranges from 9.0 ‰ to 12.6 ‰

(Felix et al., 2012). Similar isotope enrichment of NO_x has been noted in vehicles as their catalytic converters warm and become efficient (Walters et al, 2015a).

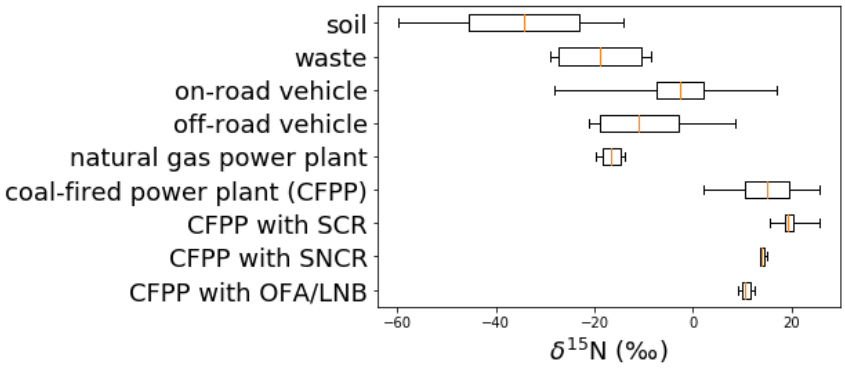

Figure 2.1.1: Box (lower quartile, median, upper quartile) and whisker (lower extreme, upper extreme) plot of the distribution of $\delta^{15}N$ values for various NO_x emission sources.

These distinctive differences in $\delta^{15}N$ values among different NO_x emission sources suggest $\delta^{15}N$ could be an effective tracer of atmospheric NO_x sources. For example, Redling et al. (2003) found higher $\delta^{15}N$ of NO_2 in samples collected closer to the highway compared to those adjacent to a forest, showing the emissions from vehicles were dominant near the highway. In addition, a strong positive correlation between the amount of NO_x emission from coal-fired power plants within 400 km radial area of study sites and $\delta^{15}N(NO_3^-)$ of wet and dry deposition has been demonstrated (Elliott et al., 2007; 2009). What is lacking is a systematic way of connecting $\delta^{15}N$ values of NO_x sources, regional emissions, and data from numerous studies to measurements of $\delta^{15}N$ in NO_y.

Here we have simulated the emission of $^{15}NO_x$ and compared the predicted $\delta^{15}N(NO_x)$ values with the recent measurements. The $\delta^{15}N$ values of atmospheric NO_x are impacted by three main factors. The first is the inherent variability of the $\delta^{15}N$ values of NO_x emissions in time and space. Secondly, atmospheric processes that mix the NO_x emissions, blurring multiple emission sources within a mixing lifetime relative to the NO_x chemical lifetime (~1 day). And thirdly, isotope effects occurring during tropospheric photochemistry may alter the $\delta^{15}N$ of NO_x emissions as they are transformed from NO_x into NO_y. In this chapter, we first consider the effects from the first consideration, the variation in NO_x emission sources over time and space. In Chapters 3~5, we will discuss the impacts from atmospheric mixing and tropospheric photochemistry by using the

emission simulation presented here as the input dataset for the Community Multiscale Air Quality Modeling System (CMAQ) to simulate $\delta^{15}N$ of atmospheric NO_x. Thus, this research examines the variability in NO_x emissions over time and space in the Midwestern US and calculates ^{15}N emissions in order to predict the spatial and temporal changes of $\delta^{15}N$ values of emitted NO_x. The ultimate goal will be to evaluate the accuracy of the NO_x emission inventory using ^{15}N.

2.2 Methodology

The EPA trace gas emission model SMOKE (Sparse Matrix Operator Kernel Emissions) was used to simulate $^{14}NO_x$ and $^{15}NO_x$ emissions. $^{14}NO_x$ emissions we estimated using the SMOKE model based on NO_x emissions from 2002 NEI (National Emission Inventory, USEPA, 2014) emission sectors and ^{15}N emission were determined using these emissions and the corresponding $\delta^{15}N$ values of NO_x sources from previous research (Table 2.1). Using the definition of $\delta^{15}N$ (‰), $^{15}NO_x$ emitted by each SMOKE processing category (area, biogenic, mobile, and point) was calculated by

$$^{15}NO_x(i) = {}^{14}NO_x(i) \times {}^{15}R_{NO_x}(i) \qquad \text{Eq. (2.2)}$$

where $^{14}NO_x$ (i) are the NO_x emissions for each category (i) obtained from NEI and SMOKE and $^{15}R_{NOxi}$ is a ^{15}N emission factor ($^{15}NO_{Xi}/^{14}NO_{xi}$) calculated by:

$$^{15}R_{NO_x}(i) = \left(\frac{\delta^{15}N_{NO_x(i)}}{1000} + 1\right) \times 0.0036 \qquad \text{Eq. (2.3)}$$

$\delta^{15}N_{NOx(i)}$ is the $\delta^{15}N$ value of some NO_x source (i = area, biogenic, mobile, and point) and 0.0036 is the $^{15}N/^{14}N$ of air N_2, the reference point for $\delta^{15}N$ values. Thus, to use Eq. (2.2) we extended a NO_x emission dataset for the Midwestern US ($^{15}NO_x$ (i)) and used recent measurements to determine $\delta^{15}N_{NOx}$ values for major NO_x emission sources ($^{15}R_{NOxi}$) by using Eq. (2.3).

Annual emissions estimates by 2002 NEI for the Midwestern United States was obtained from NEI at the county-level and was converted into hourly emissions on a 12 km x 12 km grid over the Midwestern United States and previously published (Spak, Holloway, & Stone, 2007). The modeling domain includes latitudes between 37 º N and 45 º N, and longitudes between 98º W and

78º W, which fully covers the states of Minnesota, Iowa, Missouri, Wisconsin, Illinois, Michigan, Indiana, Kentucky, Ohio, and West Virginia, and partially covers North Dakota, South Dakota, Nebraska, Kansas, Tennessee, North Carolina, Virginia, Maryland, Pennsylvania, and New York. On-road gasoline, on-road diesel, off-road gasoline, off-road diesel, coal-fired power plant, natural gas power plant, soil, and livestock wastes are the main sources of NO_x emissions in the NEI (USEPA, 2014). These were imported into models that used parameters such as land use, plant species, temperature, growing season, plume rise, roadway type, vehicle classification, and travel time for vehicle emissions to convert them into hourly NO_x emissions. SMOKE categorizes NO_x emissions into four "processing categories": Biogenic, Mobile, Point, and Area (Table 2.1).

The choice of the 2002 version of NEI is, in part, arbitrary for several reasons. First, in order to compare the model estimated $\delta^{15}N$ values with observations, it requires the emission inventory to be relevant to the same timeframe as the $\delta^{15}N$ measurements of the NO_y. The data sets we compare to the model (discussed below) span the late 1990's to 2009, thus the 2002 inventory is more relevant than later inventories (2008 onward). Secondly, the current model is predicting the initial $\delta^{15}N$ value, but this value will be altered by two effects. First, the role of atmospheric transport and deposition, which will blur the regional $\delta^{15}N$ value of emissions based on emission strength, mixing vigor, and deposition schemes. Secondly, photochemical and equilibrium isotope effects that occur during the transformation of NO_x into NO_3^-, which is the most of the available NO_y $\delta^{15}N$ data, measured from either rain or aerosols. Thus, it was not expected that this current "emission only" model would accurately predict the $\delta^{15}N$ values of NO_3^-. Instead, the current work is a proof of concept paper that addresses some basic questions, for instance, do we expect regional and seasonal differences in $\delta^{15}N$ values of NO_x, and are they at least comparable to observations in NO_y? We emphasize that the effects of atmospheric mixing and tropospheric photochemistry will be addressed in Chapter 3.

Table 2.2.1: The $\delta^{15}N$ values (in ‰) for NO_x emission sources based on SMOKE processing category and NEI sector

SMOKE Processing Category	NEI Sector	$\delta^{15}N$-NO_x (‰) from previous research	$\delta^{15}N$-NO_x (‰) choose for this study
Biogenic	Soil	-59.8 ~ -14.0	-34.3 (Felix & Elliott, 2014)
Area	Livestock Waste	-29 ~ -8.5	-18.8 (Felix & Elliott, 2014)
	Off-road Gasoline	-21.1 ~ 8.5	-11.5 (Walters et al., 2015b)
	Off-road Diesel		-10.5 (Walters et al., 2015b)
Mobile	On-road Gasoline	-28.1 ~ 17	-2.7 (Walters et al., 2015b)
	On-road Diesel		-2.5 (Walters et al., 2015b)
Point	Coal-fired Fossil Fuel Combustion	-19.7 ~ 25.6	15 (Felix et al., 2012)
	Natural Gas Fossil Fuel Combustion		-16.5 (Walters et al., 2015)

2.2.1 Biogenic source of NOx emission

Biogenic sources of NO_x are predominately by-products of microbial nitrification and denitrification occurring in soil. The Biogenic Emissions Inventory System (BEIS) was implemented within SMOKE to estimate hourly emissions from biogenic sources. The normalized emission was first generated based on 230 land-use types from the Biogenic Emission Landcover Database (USEPA, 2018), a normalized emission factor of NO_x, and land cover, to indicate the emission under standard environmental conditions (at 30 °C and 1000 μmol m^{-2} s^{-1} photosynthetic active radiation). Then, meteorological data generated by MM5 (Fifth-Generation Penn State/NCAR Mesoscale Model) (Grell, Dudhia, & Stauffer, 1994) was incorporated into BEIS and was used to finalize the speciated and temporally allocated emissions from biogenic sources by the algorithm for NO_x. This algorithm uses three steps. First, the land surface was designated by the land use as agriculture and non-agriculture based on Biogenic Emission Landcover Database. Second, NO_x emissions were normalized based on temperature, precipitation, fertilizer application, and crop canopy coverage during the crop growing season (April 1 to October 31). Finally, for NO_x emissions over agriculture areas during the non-growing season and NO_x emissions over non-agriculture areas throughout the year, the emission NO_x factor was limited to that for grassland, and the only temperature was used to normalize NO_x emission (Pierce, 2001; Vukovich & Pierce, 2002; Schwede et al., 2005; Pouliot & Pierce, 2009; USEPA, 2018).

The NO_x emission from the soil is regarded as a biogenic source in SMOKE, and there are only a few measurements of the $\delta^{15}N$ values of biogenic NO_x. Li & Wang (2008) measured the NO_x fluxes using dynamic flow chambers for 2 to 13 days after cropland soil was fertilized by either urea (n=9) or ammonium bicarbonate (n=9), and the $\delta^{15}N$ values of NO_x ranged from -48.9 ‰ to -19.8 ‰. Felix & Elliott (2014) placed passive NO_2 samplers in a static flux chamber installed in a cornfield. NO_2 was continuously collected from Jun 19-22, 2010 after 135 kg N/ha of fertilizer was applied, and from Jun 2-19, 2011 after 40 kg N/ha of fertilizer application. The $\delta^{15}N$ values of NO_x emissions from these measurements range from -30.8 ‰ to -26.5 ‰. Miller et al. (2018) used a static flux chamber to collect soil NO_x emission 2~3 samples daily from May 17 to 26, 2016, and 2~4 samples daily from May 22 to Jun 3, 2017. The $\delta^{15}N$ values of NO_x emissions from these 37 samples ranged from -44.2 ‰ to -14.0 ‰. Yu & Elliott (2017) collected 15 samples from soil plots for the $\delta^{15}N$ value of NO flux over a fallow field 2 weeks after the precipitation. The $\delta^{15}N$ values of NO_x emissions from these measurements range from -59.8 ‰ to -23.4 ‰, with a standard

deviation of ±11.25 ‰. The $\delta^{15}N$ values of NO_x emissions from soil wetted with NO_3^- aqueous solution treatments averaged -40.3 ± 0.75 ‰, while the $\delta^{15}N$ values of NO_x emissions from soil wetted with NO_2^- aqueous solution treatments averaged -29.1 ± 4.17 ‰ suggesting there are unique isotope effects for each step during $NO_3^- \rightarrow NO_2^- \rightarrow NO$ steps. The $\delta^{15}N$ values of NO_x emissions from soil wetted with NH_4^+ aqueous solution treatments averaged -57.8 ± 1.91 ‰, indicating $\delta^{15}N$ of NO_x derived from nitrification is different than that from denitrification. Based on these studies we adopted a $\delta^{15}N$ value for NO_x emissions from the soil of -34.3 ‰, which is the average value of these previous studies, to determine the emission rate of $^{15}NO_x$ from biogenic sources using Eq. (2.2) and (3).

2.2.2 Mobile source of NO_x emission

The emission of NO_x based on on-road vehicle activity was estimated using MOBILE6, a model developed by the EPA's Office of Transportation and Air Quality. Three main factors are considered to estimate on-road vehicle NO_x emissions. The first is the emission rate per mile traveled for 28 different classifications of vehicles. The second is the emission factor based on 10 different types of operating conditions (running, start, hot soak, diurnal, resting, run loss, crankcase, refueling, brake wear, and tire wear), travel speed over 33 different road types with distinct average speed, types of fuel being consumed, and ambient temperature. Finally, the number of vehicles in each classification, emission type, and fuel type along with each type of roadway during certain periods (USEPA, 2003; Houyoux, 2005). MOBILE6 and SMOKE were used to determine NO_x emissions along the roadways and were converted into hourly emissions within each 12 km × 12 km grid cell.

The NO_x emission from on-road vehicle employ an estimated $\delta^{15}N$ value from -28.1 ‰ to +17 ‰ (Moore, 1977; Heaton, 1990; Ammann et al., 1999; Pearson et al., 2000; Savard et al., 2009; Redling et al., 2013; Felix & Elliott, 2014; Fibiger, 2014; Walters et al., 2015a, 2015b). We have excluded studies that infer NO_x $\delta^{15}N$ by measuring plant proxies or passive sampling in the environment (Ammann et al., 1999; Pearson et al.,2000; Savard et al. 2009; Redling et al., 2013; Felix & Elliott, 2014). This is because of equilibrium and kinetic isotope effects that can occur as NO_x reacts in the atmosphere to form NO_y, prior to NO_x deposition. In addition, the role vegetation plays in NO_x removal and atmospheric processes that mix the $\delta^{15}N$ of emission with the

surroundings can also alter the $\delta^{15}N$ from the mobile source. Instead, we estimated the $\delta^{15}N$ value of NO_x emissions from vehicles only using studies that directly measured tailpipe NO_x emissions.

There is a handful of NO_x $\delta^{15}N$ values measured from tailpipes, that span several decades. Moore (1977) collected 3 samples of tailpipe NO_x from one vehicle at different loads and engine speeds, which had $\delta^{15}N$ values of 3.7 ± 0.3 ‰. Heaton (1990) collected 8 samples from the tailpipes of 6 vehicles, on a testbed and on-road with different load and engine speeds. The resulting $\delta^{15}N$ values spanned -13 ‰ to 2 ‰, with an average of -7.5 ± 4.7 ‰. Neither Heaton nor Moore noted whether these 6 vehicles were equipped with any catalytic NO_x reduction technology, but it is unlikely since late 1970 and 80's s vehicles were seldomly equipped with catalytic NO_x reduction technology. Fibiger (2014) measured 5 samples of NO_x from diesel engines without SCR emitted into a smog chamber, the $\delta^{15}N$ values range from -19.2 ‰ to -16.7 ‰ (±0.97 ‰). The most comprehensive studies on vehicle NO_x $\delta^{15}N$ values are by Walters et al. (2015a, 2015 b). These studies were chosen to assign the $\delta^{15}N$ of NO_x emissions from vehicles in this study because these measurements were taken directly from vehicle tailpipes, rather than inferring them (i.e from roadside plant material, tree rings, or roadside NO_2) and had more samples (n = 73) compared to other studies. In addition, it measured gas and diesel vehicles separately, including those with and without three-way catalytic converter (TCC) and SCR technology. They also measured on-road and off-road vehicles separately. This research showed that the $\delta^{15}N$ of NO_x for vehicles without SCR or when SCR was not functioning was negative, at around -15‰. As SCRs warmed and became efficient at reducing NO_x the $\delta^{15}N$ value became less negative and even went positive. The measurements showed that the $\delta^{15}N$ values of NO_x emitted by on-road gasoline vehicle averages at -2.5 ± 1.5 ‰, and on-road diesel vehicles ranged from -5 ‰ to 0 ‰.

The emission rate of $^{15}NO_x$ from the mobile source was determined by Eq. 4 grid by grid, according to the contributions from on-road gasoline vehicles and on-road diesel vehicles, as well as their corresponding $\delta^{15}N$ values of these two types of vehicles grid by grid. NO_x emissions from off-road vehicles are regarded as area sources in SMOKE, which were processed over each county. In contrast, NO_x emissions from on-road vehicles are regarded as the mobile source in SMOKE, which will be processed along each highway. Each grid emission rate of $^{15}NO_x$ was assigned based on the contributions from gasoline and diesel vehicles, as well as the relative $\delta^{15}N$ values. The $\delta^{15}N$ of on-road gasoline vehicles (-2.7 ± 0.8 ‰) was based on the average vehicle travel time within each region with the same zip code (Walters et al., 2015b).

$$^{15}NO_x\ (mobile) = \left(\frac{\delta^{15}N_{NO_x\ (on-road\ gas)}}{1000} + 1\right) \times 0.0036 \times {}^{14}NO_x\ (on-road\ gas) + \left(\frac{\delta^{15}N_{NO_x\ (on-road\ diesel)}}{1000} + 1\right) \times 0.0036 \times {}^{14}NO_x\ (on-road\ diesel) \quad \text{Eq. (2.4)}$$

Where $\delta^{15}N_{NO_x\ (on-road\ gas)} = -12.35 + 3.02 \times \ln(t + 0.455)$

2.2.3 Point source of NO_x emission

The main NEI sectors for a large number of anthropogenic NO_x emissions that are located at a fixed, stationary position are categorized as NO_x point sources. These include NO_x emitted by fugitive dust and power plants. Fugitive dust does not significantly contribute to point NO_x emissions, so our inventory focused on power plants (Houyoux, 2005). Power plants were separated into two different types: EGU (electric generating units) and Non-EGU (e.g. commercial and industrial combustions). The emissions from EGUs account for 50-55% of the point source NO_x emissions, while non-EGUs account for 45-50%.

The $\delta^{15}N$ value of NO_x emitted from power plants have been estimated to vary from -19.7 ‰ to 25.6 ‰ (Heaton, 1987; Heaton, 1990; Snape, 2003; Felix et al., 2012; Felix et al., 2015; Walters et al., 2015b; Savard et al., 2017). We have ignored studies that measured $\delta^{15}N$ of NO_3^- or HNO_3 from EGUs (Felix et al., 2015, Savard et al., 2017) and instead, only consider those studies that directly measured $\delta^{15}N$ of NO_x. Heaton (1990) collected 5 samples from the different coal-fired power stations with wall-fired and tangentially-fired boilers, at different power of 48, 500, and 600 MW. The $\delta^{15}N$ values of NO_x emissions from these measurements range from 6 ‰ to 13 ‰, with a standard deviation of 2.9 ‰. Snape (2003) measured 36 samples from power plants using three different types of coals in combustion chars in a drop tube reactor. The $\delta^{15}N$ values of NO_x ranged from 2.1 ‰ to 7.2 ‰, with a standard deviation of 1.37 ‰. The most comprehensive study on coal-fired power plant's NO_x values was by Felix et al. (2012). They measured the $\delta^{15}N$ values of NO_x emission from the coal-fired power stations with and without different emission control technologies. 16 coal-fired power plants with SCR, 3 coal-fired power plants with SNCR, 15 coal-fired power plants with OFA/LNB, and 8 coal-fired power plants without emission control technology were measured. The $\delta^{15}N$ values of NO_x emissions from these 42 measurements range from 9 ‰ to 25.6 ‰, with a standard deviation of 4.51 ‰. The NO_x $\delta^{15}N$ values when different emission control technologies were used varied: the $\delta^{15}N$ values of NO_x emissions from coal-fired

power plants with SCR range from 15.5 ‰ to 25.6 ‰, those with SNCR ranged from 13.6 ‰ to 15.1 ‰, and those with OFA/LNB ranged from 9.0 ‰ to 12.6 ‰. The $\delta^{15}N$ values of NO_x emissions from coal-fired power plants without emission control technology range from 9.6 ‰ to 11.7 ‰, with a standard deviation of 0.79 ‰. According to Xing et al. (2013), about half of the coal-fired power plants in the United States are equipped with SCR. Thus, we assume 15 ‰ for the NO_x emissions from coal-fired power plants, which is the average between SCR and other emission control technologies.

The most comprehensive study on natural gas-fired NO_x values (Walters et al. 2015) collected 12 flue samples on the rooftop of a house from the ventilation pipe of a natural gas low-NO_x burner residential furnace without NO_x emission control technology. They also collected 11 flue samples from a sampling-port directly above a natural gas low-NO_x burner power plant. The measurement showed that the $\delta^{15}N$ values of NO_x emitted by natural gas power plants average -16.5 ± 1.7 ‰, which we used for the NO_x emission from natural gas power plants. The reason for using these values because they were measurements taken directly from the exhaust pipes, rather than inferring from downwind area or rain samples, emitted by natural gas power plants, and included power plants with and without SCR technology. The latitude, longitude, and point sources characteristics (EGU and non-EGU, coal-fired or natural gas-fired, implementation of emission control technology) of each power plant was obtained from the US Energy Information Administration (2017). The power plants were assigned grids by their latitudes and longitudes, and the $\delta^{15}N$ values were assigned to these grids based on their emission characteristics, before determining the emission rate of $^{15}NO_x$ from point source using Eq. (2.2) and (2.3).

2.2.4 Area source of NO_x emission

Area sources are the stationary anthropogenic NO_x emissions that spread over a spatial extent and individually too small in magnitude to report as point sources. These include NO_x emitted by off-road vehicles, residential combustion (anthracite coal, bituminous coal, distillate oil, residual oil, natural gas, liquified petroleum gas, and wood), industrial processes (chemical manufacturing, food, and kindred products, metal production, mineral processes, petroleum refining, wood products, construction, machinery, mining, and quarrying, etc), agriculture production (crops, fertilizer application, livestock, animal waste, etc), solvent utilization, storage and transport, waste disposal, treatment, and recovery, forest wildfires, as well as road dust and fugitive dust. Among

these, livestock and off-road vehicles are dominant, accounting for nearly 90% of area NO_x emissions across the contiguous United States (Houyoux, 2005). The annual area emissions from the NEI sectors were estimated at the county level and evenly divided into hourly emissions over the 12 km × 12 km grid for use in chemical transport modeling.

The area NO_x $\delta^{15}N$ values were based on the assumption that livestock waste and off-road vehicles (utility vehicles for agricultural and residential purposes) accounted for total area sources. Livestock waste NO_x $\delta^{15}N$ values were taken from Felix & Elliott (2014) since it is currently the only study about the $\delta^{15}N$ value of NO_x livestock waste emissions. They placed passive sampler with ventilation fans in an open-air and closed room in barns of cows and turkeys, respectively. The $\delta^{15}N$ values of NO_x emissions from these measurements range from -29 ‰ to -8.5 ‰. Among these samples, the $\delta^{15}N$ of NO_x emissions from turkey waste averages at -8.5 ‰, the $\delta^{15}N$ of NO_x emissions from cow waste averages at -24.7 ‰. We used -18.8 ‰ as the values of $\delta^{15}N$ values for NO_x emissions from livestock waste, which is the weighted average of the $\delta^{15}N$ of NO_x from turkey waste and cow waste emissions, roughly based on the population of turkey and cows on farms across the United States. We used the $\delta^{15}N$ values from Walters et al. (2015b) to estimate the $\delta^{15}N$ value of NO_x emissions from the off-road vehicles since it is the latest in detail study that measured the $\delta^{15}N$ value of NO_x specifically from off-road vehicles. They collected 45 samples from the tailpipe of 9 different off-road vehicles (gasoline and diesel) with and without SCR, and before and after the sufficient engine warm-up times. The measurement showed that the $\delta^{15}N$ values of NO_x emitted by gasoline-powered off-road vehicle averaged -11.5 ± 2.7 ‰, diesel off-road vehicles without SCR averaged -19 ‰ ± 2 ‰, and diesel off-road vehicle with SCR averaged -2 ‰ ± 8 ‰. The emission rate of $^{15}NO_x$ from area source was determined by Eq. 5 grid by grid, according to the contributions from waste, off-road gasoline vehicle, and off-road diesel vehicle, as well as their corresponding $\delta^{15}N$ values based on previous researches.

$$
\begin{aligned}
{}^{15}NO_x\ (area) = {} & \left(\frac{\delta^{15}N_{NO_x\ (waste)}}{1000} + 1\right) \times 0.0036 \times {}^{14}NO_x\ (waste) \\
& + \left(\frac{\delta^{15}N_{NO_x\ (off-road\ gas)}}{1000} + 1\right) \times 0.0036 \times {}^{14}NO_x\ (off-road\ gas) \\
& + \left(\frac{\delta^{15}N_{NO_x\ (off-road\ diesel)}}{1000} + 1\right) \times 0.0036 \times {}^{14}NO_x\ (off-road\ diesel) \qquad \text{Eq. (2.5)}
\end{aligned}
$$

The county-level annual $^{14}NO_x$ emission for the Midwestern US from NEI was converted to the dataset with hourly $^{14}NO_x$ emission over 12 × 12 km grids throughout the year. During this process, different NEI emission sectors were treated differently. Livestock waste and off-road vehicles were regarded as area sources by SMOKE, of which the $^{14}NO_x$ emission over each county was evenly divided into the grids. Power plants were regarded as point sources by SMOKE, of which the $^{14}NO_x$ emission from these facilities was located into the corresponding grids according to their latitudes and longitudes. On-road vehicles were regarded as the mobile source by SMOKE, of which the $^{14}NO_x$ emission along the roadways was estimated by MOBILE model, based on vehicle classifications, emission types, road type, fuel type, ambient temperature, and the number of vehicles along each roadway during each hour, before evenly dividing NO_x emission along each roadway into groups of 12 × 12 km grids. The soil was regarded as the biogenic source by SMOKE, of which the $^{14}NO_x$ emission produced by microbial nitrification and denitrification was estimated by BEIS model, based on land use type, normalized emission factor of NO_x, land cover, temperature, precipitation, fertilizer application, crop growing season, and crop canopy coverage during the growing season, over each 12 × 12 km grid. Then, the $^{15}NO_x$ emission of each SMOKE processing category was incorporated into the dataset based on the $\delta^{15}N$ values from previous research (Table 2.1) and Eq. (2.2-5).

$$\delta^{15}N_{NO_x\,(total)} = \left(\frac{\frac{^{15}NO_x\,(area)+{}^{15}NO_x\,(biog)+{}^{15}NO_x\,(mobile)+{}^{15}NO_x\,(point)}{^{14}NO_x\,(area)+{}^{14}NO_x\,(biog)+{}^{14}NO_x\,(mobile)+{}^{14}NO_x\,(point)}}{0.0036} - 1\right) \times 1000 \qquad \text{Eq. (2.6)}$$

2.3 Results and Discussion

2.3.1 Simulated spatial variability of NO_x emission rates

We first examine the spatial heterogeneity of the NO_x emission rate for a single time period to illustrate the overall pattern of NO_x emission over the domain (Fig. 2.2). This is because the $\delta^{15}N$ value of total NO_x emission is determined by the fraction of each NO_x source (Eq. 6), which in turn is a function of their emission rates. Since our NO_x emissions are gridded by SMOKE using the NEI, they are by definition correct with respect to the NEI. However, a brief discussion of the salient geographic distribution of NO_x emissions and comparisons with other studies is warranted for completeness and as a backdrop for the discussion of NO_x fractions and resulting $\delta^{15}N$ values.

We have arbitrarily chosen to sum the NO_x emissions during the April to June time period for this discussion.

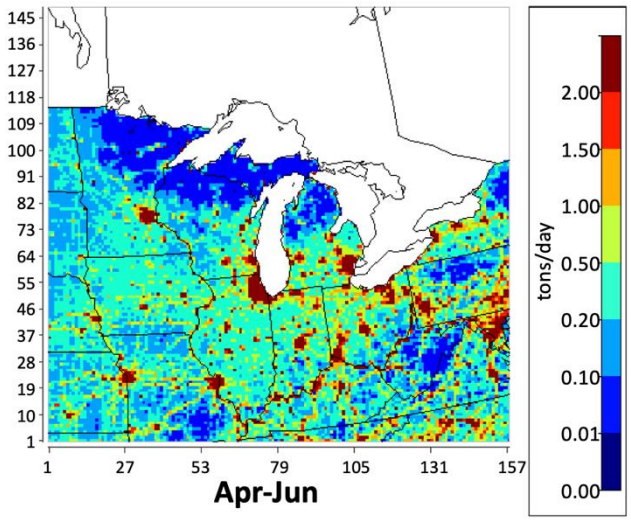

Figure 2.3.1: Total NO_x emission in the Midwest between April and June in tons/day. High NO_x emissions are associated with major urban areas such as Chicago, Detroit, Minneapolis-St Paul, Kansas City, St. Louis, Indianapolis, and Louisville.

The seasonal average NO_x emissions within the geographic domain during April to June range from less than 0.01 tons N/day to more than 15 tons N/day, with the seasonal grid average of 0.904 tons/day. The average NO_x emission over the 12 × 12 km grids simulated by SMOKE agrees well with estimates in previous studies, which was between 0.81 and 1.02 tons/day over the grids with the same size as this research but for the United States nationwide (Dignon & Hameed, 1989; Farrell et al., 1999; Selden et al., 1999; Xing et al, 2012). Within 75% of the grids within the geographic domain, the NO_x emissions are relatively low, ranging from between 0 and 0.5 tons/day (Fig. A.1). Geographically, these grids are located in the rural areas some distance away from metropolitan areas and highways (Fig. 2.2). The NO_x emission within about 20% of the grids are relatively moderate, ranging between 0.5 and 2.0 tons/day (Fig. A.1). Geographically, these grids are mainly located along major highways and areas with medium population densities (Fig. 2.2). Urban centers comprise about 5% of the grids within the geographic domain and these have high NO_x emissions rates, ranging between 2.0 and 15.0 tons/day (Fig. A.1). The metropolitan areas average of 5.03 tons/day, which is nearly 14 times of the average emission rate over the rest of the grids within the geographic domain (0.37 tons/day) due to high vehicle density associated with

high population densities. The highest emissions rates are located within large cities (Fig. 2.2), such as Chicago, Detroit, Minneapolis-St Paul, Kansas City, St. Louis, Indianapolis, and Louisville, as well as the edge of the east coast metropolitan area (dark red). Summing the NO_x emissions among the grids that encompass these major midwestern cities, yields city-level NO_x emission rates that vary from 61.2 tons/day (Louisville, KY) to 634.1 tons/day (Chicago, IL). These city-level NO_x emission rate simulated by SMOKE (Table 2.2) agrees well with estimates derived from the Ozone Monitoring Instrument (OMI) in a previous study (Lu et al., 2015). Grids containing power plants are the significant NO_x hotspots within the geographic domain. These account for less than 1% of the grids within the geographic domain, but the NO_x emissions from a single grid that contains a power plant could be as high as 93.4 tons/day. Geographically, the power plants are mainly located along the Ohio River valley, near other water bodies, and often close to metropolitan areas (Fig. 2.2). The NO_x emission rates of the major power plants within the Midwest simulated by SMOKE (Table 2.3) match well with the measurement from Continuous Emission Monitoring System (CEMS) (de Foy et al., 2015; Duncan et al., 2013; Kim et al., 2009).

The geographic distribution of grid-level annual NO_x emission density in our simulation agrees with the county-level annual NO_x emission density discussed in the 2002 NEI booklet (Fig. A.2; USEPA, 2018). For both grid-level emission density simulated by SMOKE and county-level emission density estimated by NEI, the relatively low values (less than 2.5 tons/mile^2) occur in the rural areas, especially located in the states of Minnesota, Iowa, Missouri, as well as the Plains states on the western edge of the domain. Similarly, the relatively moderate values (between 2.5 tons/mile^2 and 7.5 tons/mile^2) occur in the grids or counties that contain major highways; and the relatively high values (greater than 12.5 tons/mile^2) occurs in the grids or counties within metropolitan areas or in the grids or counties that contain power plants. Comparing the maps in different schemes, in addition, to show the geographic distribution of NO_x emission density at different levels, the map of grid-level NO_x emission density clearly shows locations of the objects with relatively high resolution, such as highways and power plant, as well as the more precise geographical range of metropolitan areas. The map of grid-level total NO_x emission provides a clear view of spatial variation, and show the geographic location of major cities, highways, and power plants, while it has obvious limitations. First, some power plants share the same grids with metropolitan areas or highways, which also has relatively high NO_x emission. As a result, it is hard to determine the dominant source for these grids. Similarly, among the grid with relatively low

NO_x emission, the map of total NO_x emission cannot reveal the dominant source over these areas. In order to explore the composition of NO_x emission, the $\delta^{15}N$ value of total NO_x emission is necessary.

Table 2.3.1: The seasonal average NO_x emission rate for major cities in the Midwest

Urban Area	SMOKE-simulated emission rate		OMI-derived emission rate
	tons/day	tons/hr	tons/hr
Chicago, IL	634.074	24.42	23.3±9.7
Detroit, MI	288.617	12.026	18.7±7.8
Indianapolis, IN	72.487	3.021	3.1±1.3
Kansas City, MO	150.733	6.281	5.1±2.1
Louisville, KY	61.178	2.549	2.5±1.0
Minneapolis, MN	220.957	9.207	9.3±3.9
St. Louis, MO	99.953	4.165	4.9±2.0

Table 2.3.2: The seasonal average NO_x emission rate for major power plants in the Midwest

Power Plant Site	SMOKE-simulated emission rate	CEMS-measured emission rate	
	tons/day	kt/yr	tons/day
Paradise, KY	93.414	38.33	105.014
New Madrid, MO	65.777	23.09	63.260
T. Hill Energy Center, MO	38.686	11.95	32.740
Kincaid, IL	38.934	11.92	32.644
Powerton, IL	62.394	21.56	59.068
Jeffrey Energy Center, KS	59.339	21.39	58.603

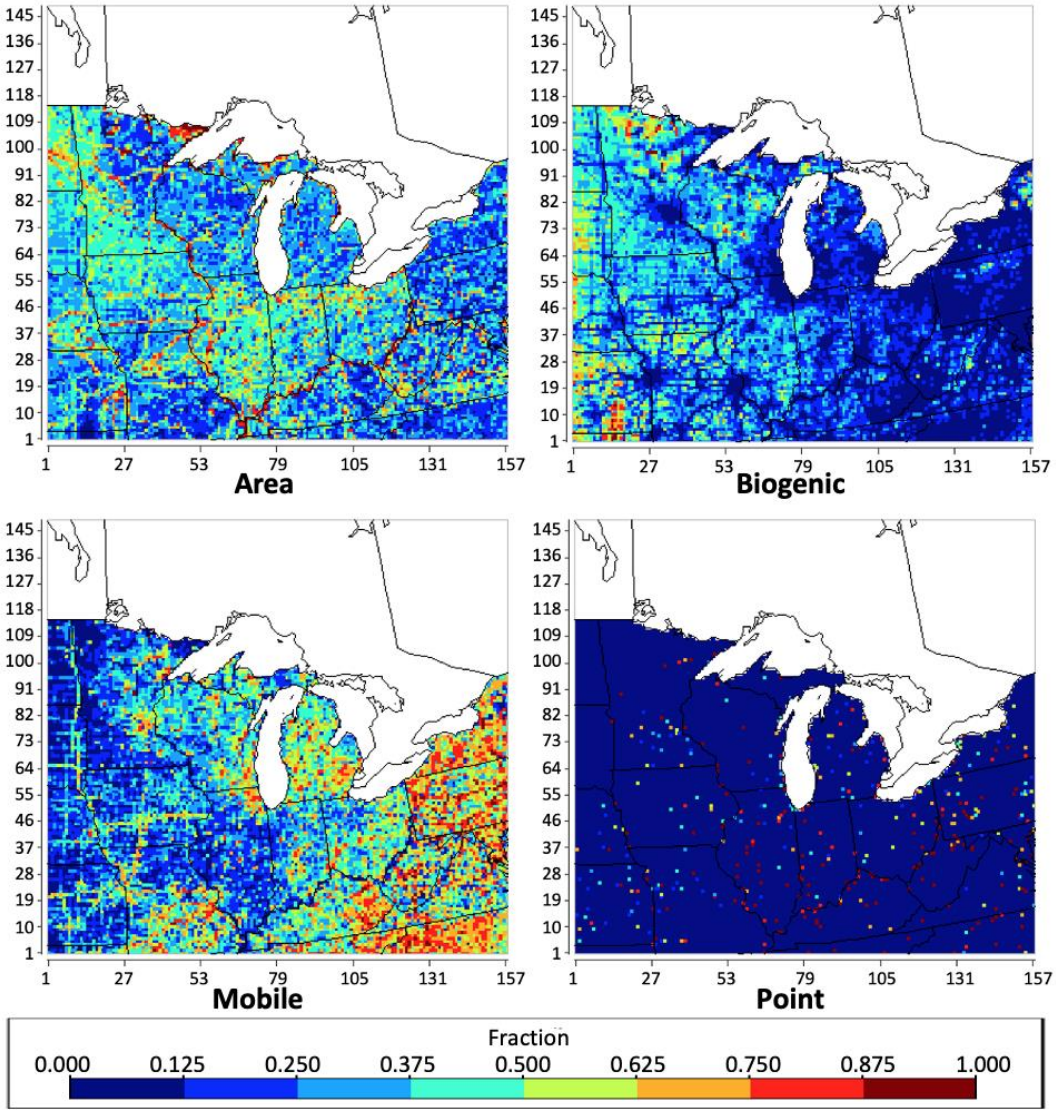

Figure 2.3.2: The geographical distribution of the fraction of NO_x emission from each SMOKE processing category (area, biogenic, mobile, point) over each grid throughout the Midwest between April and June based on NEI-2002.

We next examine the spatial heterogeneity of the NO_x fraction from each source category (Fig. 2.3) for the same time period (April to June). Since the $\delta^{15}N$ value of total NO_x is determined by the fractions of each NO_x emission source over each grid (Eq. 6), it is important to understand where in the domain these fractions differ and why. The area sources, which mainly consist of off-road vehicles, agriculture production, residential combustion, as well as the industrial processes, which are individually too low in magnitude to report as point sources, are fairly uniform in their distribution across the domain. The SMOKE simulation shows that NO_x emissions from area

sources contribute an average NO_x emission fraction (f_{area}) of 0.271 for total NO_x emission and 0.290 for anthropogenic NO_x emission within the Midwest from April to June. This is slightly higher than the fraction of 0.279 for annual anthropogenic NO_x emissions over the Continental United States, estimated by 2002 NEI (USEPA, 2018). The fractions of NO_x emission from area sources over each grid cell within the geographic domain show a clear spatial variation. The area sources account for NO_x emission fraction ranging from 0.125 to 0.5 over about 75% of the grids within the geographic domain (Fig. A.3). Geographically, the grids with relatively higher f_{area} are located in the rural area away from highways, especially in the states of Indiana, Illinois, Iowa, Minnesota, and Ohio, where agricultural is the most common land use classification. In the states of Wisconsin and Missouri, the f_{area} is slightly lower due to the higher fraction of NO_x emission from biogenic sources (f_{biog}). In the states of Pennsylvania and Michigan, the f_{area} is slightly lower due to the higher fraction of NO_x emission from mobile sources (f_{mobile}). In addition, the grids with f_{area} greater than 0.75 are mainly located along the Mississippi River and Ohio River, where the demand for water consumption and wastewater discharging from agriculture production could be satisfied.

The fraction of biogenic NO_x (f_{biog}) that are predominately by-products of microbial nitrification and denitrification occurring in soil, shows the clear spatial variation and is highest (from April to June) in the western portion of the domain (Fig. 2.3). The SMOKE simulation estimates that the fraction of biogenic NO_x emission averages 0.065 within the Midwest from April to June. The biogenic NO_x fraction is less than 0.5 in more than 90% of the grids within the geographic domain (Fig. A.3). Geographically, the grids with relatively high f_{biog} are located in the western regions of the Midwest, away from cities and highways, in the states of Minnesota, Iowa, Missouri, Wisconsin, and Illinois, where the density of agricultural acreage and natural vegetation is higher than other states. Furthermore, within regions with higher f_{biog}, the obvious low f_{biog} values occur in the megacities and along the highways, which agrees well with the land-use related to the biogenic emission.

The SMOKE simulation shows that the NO_x emissions from mobile sources contribute to the fraction (f_{mobile}) of 0.325 for total NO_x emission and 0.347 for anthropologic NO_x emission within the Midwest from April to June, which is slightly lower than the fraction of 0.380 for annual anthropologic NO_x emission over the Continental United States, estimated by 2002 NEI (USEPA, 2018). The fractions of NO_x emission from the mobile source over each grid cell within the

geographic domain show a clear spatial variation. The value of f_{mobile} within the geographic domain distributes evenly on the histogram (Fig. A.3). Geographically, the grids with relatively higher f_{mobile} are located in major metropolitan regions and along the highways, where vehicles have the highest density, especially in the states of Pennsylvania, New York, Virginia, West Virginia, and North Carolina. In addition, within the states with lower f_{mobile}, the obvious high f_{mobile} values occur in the megacities and along the highways, which agrees well with the vehicle activities (US Census Bureau, n.d.).

The point sources consist mainly of EGUs, as well as commercial and industrial processes involving combustion. Based on the SMOKE simulation, the NO_x emission from point sources contributes to the fraction (f_{point}) of 0.339 for total NO_x emission and 0.363 for anthropologic NO_x emission within the Midwest from April to June, which is slightly higher than the fraction of 0.343 for annual anthropologic NO_x emission over the Continental United States, estimated by 2002 NEI (USEPA, 2018). The fractions of NO_x emission from the point source over each grid cell within the geographic domain show a clear spatial variation. Geographically, the NO_x emission from point sources is dominant at the grids, where the power plants are located, mainly along the Ohio River valley and near other water bodies close to metropolitan areas. The point sources have no contribution to the NO_x emission among about 96% of the grids within the geographic domain. The rest of the 4% of the grids within the geographic domain are the locations of power plants. About 1/4 of the power plants are not at the same grids as highways, thus these grids have a fraction of at least 0.9 NO_x emission from point sources. Whereas the other 3/4 of the power plants share the same grids with highways, thus the point sources become relatively less dominant, due to the dilution by the NO_x emission from mobile sources.

Using these NO_x emission source fractions in each grid, the $\delta^{15}N$ values of NO_x were simulated. We then examine the spatial heterogeneity of $\delta^{15}N$ values of NO_x for a single time period and interpret them in terms of changes if NO_x emission fractions over the domain. The predicted $\delta^{15}N$ values of NO_x range from -35 ‰ to +15 ‰, with the seasonal average over the Midwest of -13.18 ‰ during the April to June period. The $\delta^{15}N$ value of total NO_x emissions in the Midwest during the April to June period has a significant spatial variation (Fig. 2.4). This can be qualitatively explained based on which emission source is dominant in a particular grid cell or grouping of cells in a certain region. The NO_x $\delta^{15}N$ model clearly shows the locations of big cities such as Chicago, Detroit, Minneapolis-St Paul, Kansas City, St. Louis, Indianapolis, and Louisville

(gold and green). Likewise, major highways that connect these cities are obvious features (also gold and green), particularly on the western side of the domain. This is a consequence of the fact that in both cities and on major roads, on-road vehicles are the dominant NO_x source with assigned $\delta^{15}N$ values of -2.5 ‰. In these grids, the NO_x $\delta^{15}N$ typically ranges from -5 to -10 ‰. Likewise, in the western part of the domain in the Midwest-Plains state region, where urban centers and population density is sparse and power plants are less numerous, soil emissions, with a $\delta^{15}N$ value of -34.3‰, control the NO_x budget. The predicted NO_x $\delta^{15}N$ values in these areas are very negative (dark blue), ranging from -20 to -34‰. In other grids, there are mixtures of sources such as mobile and biogenic leading to $\delta^{15}N$ values in the negative teens (aqua color), which is a mixture between the agricultural and urban NO_x sources. Similarly, the very positive $\delta^{15}N$ grids (~ +15 ‰) are located in grids that contain major power plants that dominate the NO_x emission budget (red and dark red), such as the Ohio River valley and West Virginia. These results show that there should be strong regional dependence on NO_x $\delta^{15}N$ values in the Midwestern United States.

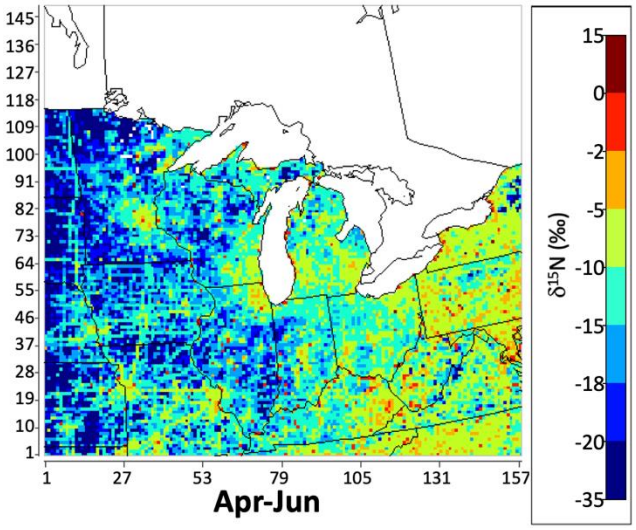

Figure 2.3.3: The $\delta^{15}N$ values of NO_x emission during April-June are presented by color in each grid. The warmer the color, the higher $\delta^{15}N$ values of NO_x emission.

2.3.2 Seasonal variation in $\delta^{15}N$ of NO_x

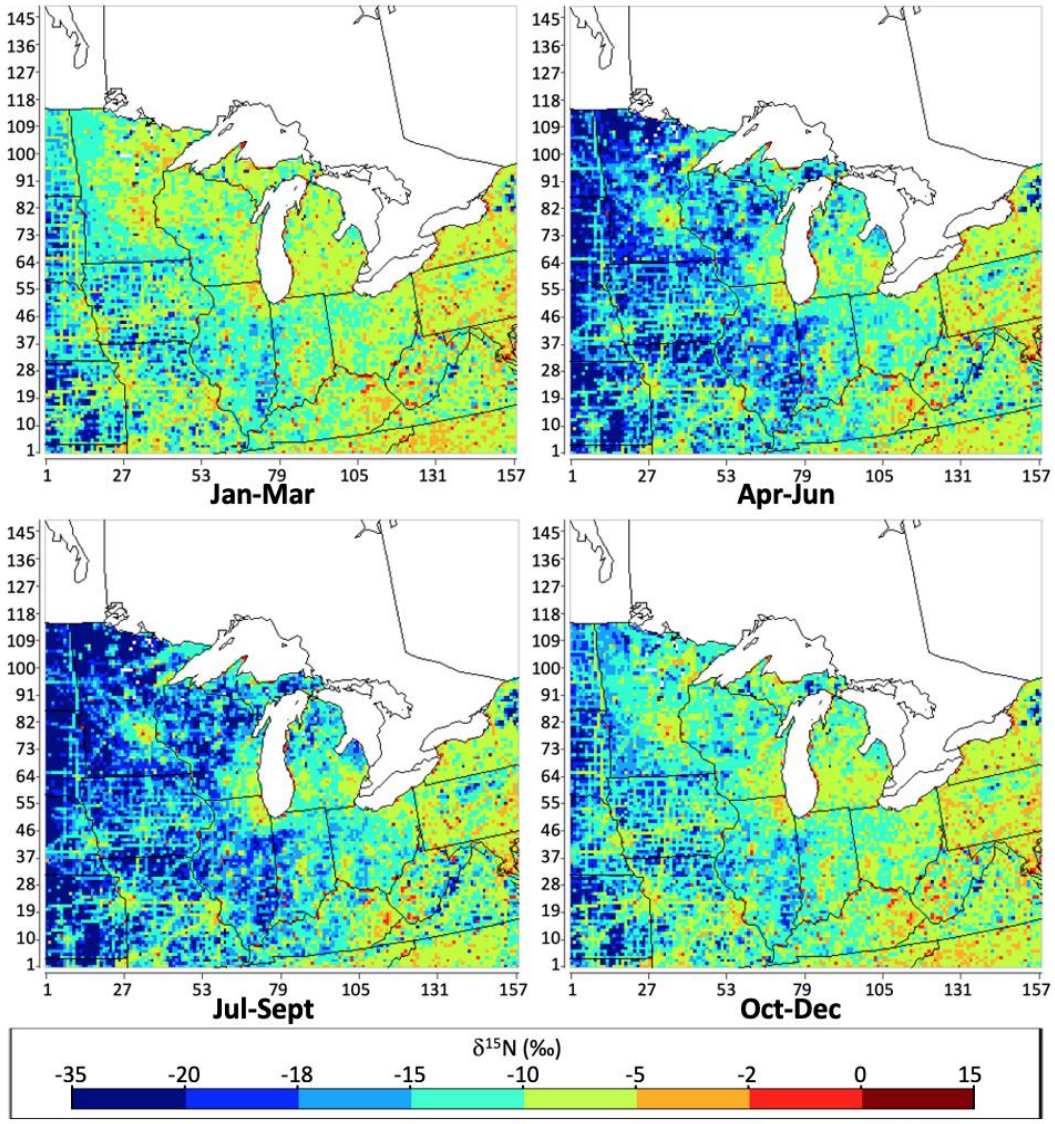

Figure 2.3.4: The geographical distribution of the $\delta^{15}N$ value of total NO_x emissions in each season (Winter: Jan-Mar; Spring: Apr-Jun; Summer: Jul-Sep; Fall: Oct-Dec) in per mil (‰) throughout the Midwest simulated by SMOKE, based on NEI-2002.

We next examine the temporal heterogeneity of NO_x $\delta^{15}N$ values over the domain and interpret them in terms of changes if NO_x emission fractions as a function of time. The predicted $\delta^{15}N$ value of total NO_x emissions in the Midwest during each season shows a significant temporal variation (Fig. 2.5). The $\delta^{15}N$ values of NO_x range from -35 ‰ to 15 ‰, with the annual average

over the Midwest at -6.15 ‰. The maps for different seasons show the obvious changes in $\delta^{15}N$ values over western regions of the Midwest, from green ($\delta^{15}N$ = -15 ~ -5 ‰) to dark blue (-35 ~ -15 ‰) during the month from April to October.

In order to qualitatively analyze the changes in $\delta^{15}N(NO_x)$ among each season, the distributions of $\delta^{15}N(NO_x)$ among the same cut-offs as the maps in Fig. 2.5 were shown in the histograms (Fig. A.4). The grids with $\delta^{15}N(NO_x)$ between -35‰ and -18‰ increase dramatically from less than 10% during fall (Oct-Dec) and winter (Jan-Mar) to more than 20% during spring (Apr-Jun) and summer (Jul-Sep). The grids with $\delta^{15}N(NO_x)$ between -18‰ and -2‰ decrease from around 90% during fall and winter to around 75% during spring and summer. In addition, the distribution of $\delta^{15}N(NO_x)$ shifts to lower values during spring and summer.

The significant temporal variation in the $\delta^{15}N$ value of total NO_x during different seasons can be quantitatively explained by changing fractions of NO_x emission from the biogenic source in any grid (Fig. 2.6) using Eq. (2.6). Unlike other NO_x emission source (figure not shown), the fraction of NO_x emission from biogenic sources changes significantly among each season within the geographic domain, especially over the rural areas of the states of Minnesota, Iowa, Missouri, Wisconsin, Illinois, Indiana, Kentucky, Michigan, and Ohio (Fig. 2.6). The fraction of NO_x emission from biogenic sources over these areas increases from less than 0.25 to more than 0.50 during the month from April to October, which is the growing season of the plant. During this period, the surface temperature and precipitation are relatively higher. As a result, the canopy coverage of the plants becomes higher, which leads to the increase of the NO_x emission from biogenic sources (Pierce, 2001; Vukovich & Pierce, 2002; Schwede et al., 2005; Pouliot & Pierce, 2009; USEPA, 2018). Besides this, the fertilizer application during this period is also responsible for the increase in soil NO_x emission (Li & Wang, 2008; Felix & Elliott, 2014).

In order to qualitatively analyze the changes in the fraction of NO_x emission from biogenic source among each season, the distributions of the fractions among the same cut-offs as the maps on Fig. 2.6 were shown in the histograms (Fig. A.5). Comparing the distributions of the fractions of NO_x emission from biogenic source among the histograms for each season, the effects from the increasing of biogenic NO_x emission during the growing season of plants are clearly shown. In general, the distribution of the fraction shifts to higher values during spring (Apr-Jun) and summer (Jul-Sep), indicating the increase of biogenic emission. As a result, the distribution of $\delta^{15}N(NO_x)$ shifts to lower values during the same period (Fig. 2.5). The percentage of the grids with the

fraction of biogenic emission less than 0.125 decreases dramatically from more than 50% during fall (Oct-Dec) and winter (Jan-Mar) to less than 35% during spring (Apr-Jun) and summer (Jul-Sep). As the NO_x emission from biogenic source becomes dominant, the percentage of the grids with $\delta^{15}N(NO_x)$ between -35‰ and -18‰ increases, while the percentage of the grids with $\delta^{15}N(NO_x)$ between -18‰ and -2‰ decreases, which sufficiently explains the trends shown on Fig. 2.5.

2.3.3 Different versions of emission inventories

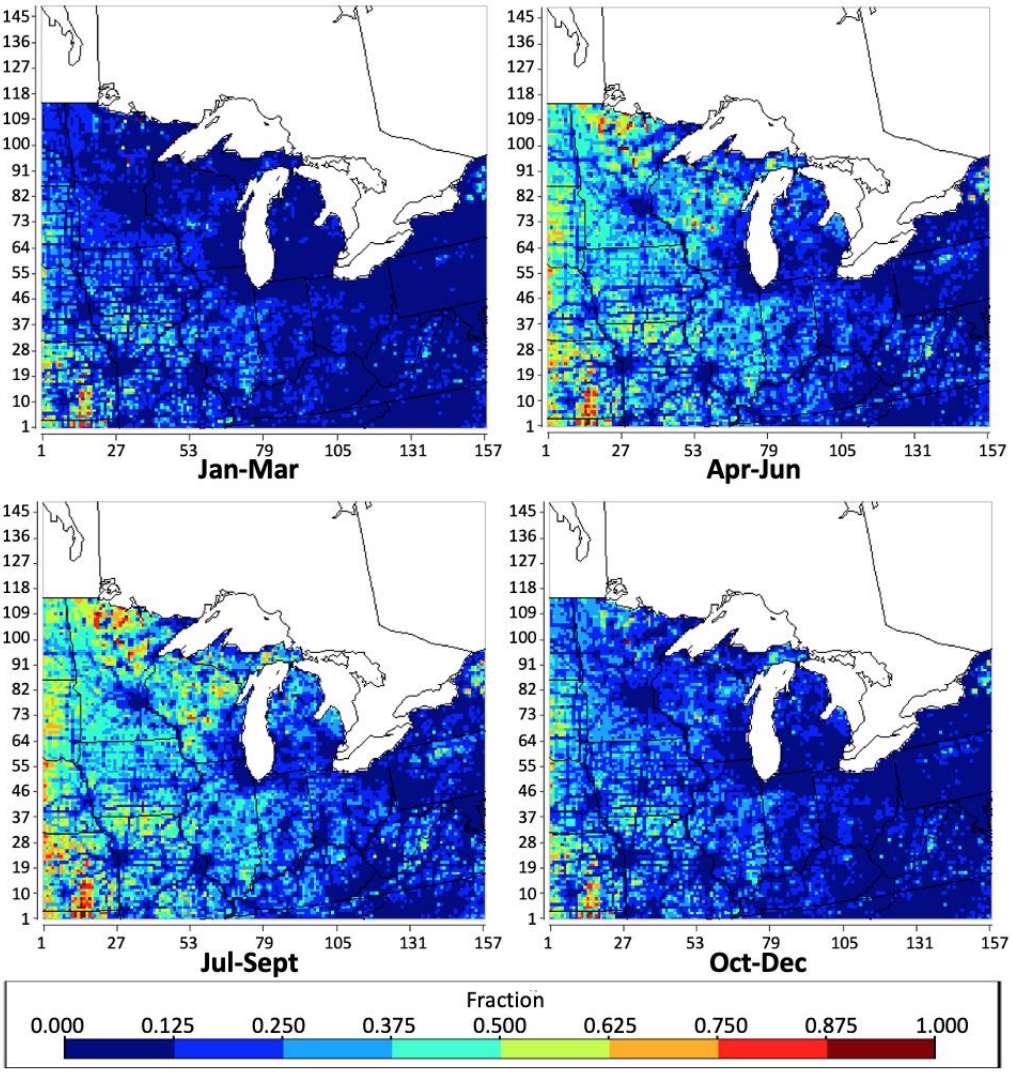

Figure 2.3.5: The geographical distribution of the fraction of NO_x emission from biogenic sources over each grid in each season (Winter: Jan-Mar; Spring: Apr-Jun; Summer: Jul-Sep; Fall: Oct Dec) throughout the Midwest simulated by SMOKE, based on NEI-2002.

The NO_x budget estimated by different versions (years) of the emission inventory varies. In order to compare the spatial heterogeneity of the fraction of NO_x from each source category for different emission inventory versions, the same analysis was done on the 2016 version of NEI (Fig. 2.7). Overall, the anthropologic NO_x emission in the 2016 NEI is lower than in 2002, whereas the NO_x emission from biogenic emission is higher, especially in the western part of the domain. The difference in temperature, precipitation, fertilizer application, and crop canopy coverage during the crop growing season, as well as the adjustments of the algorithms for different versions of BEIS potentially, cause the variation in the fraction of NO_x emission from biogenic sources. The fraction of NO_x emission from area source in the 2016 NEI was lower than 2002 NEI for most of the grids within the domain, except the hotspots in West Virginia, northern Michigan, and eastern Kansas. The 2016 fraction of NO_x emission from the mobile source was lower than the 2002 NEI for most of the grids, especially in the eastern part of the domain. The fraction of NO_x emission from point source based on 2016 NEI shows fewer hotspots comparing 2002 NEI, which indicates less amount of power plant operated within the domain. The implementation of NO_x emission control technologies (SCR, SCNR, LNB, OFA), as well as the adjustments of the algorithms for different versions of MOBILE and MOVES potentially cause the variation in the fraction of NO_x emission from anthropologic sources. Due to the significantly higher fraction of NO_x emission from biogenic source (Fig. A.6) comparing to the estimation from 2002 NEI, the $\delta^{15}N$ value of total NO_x based on 2016 NEI was lower (Fig. A.7).

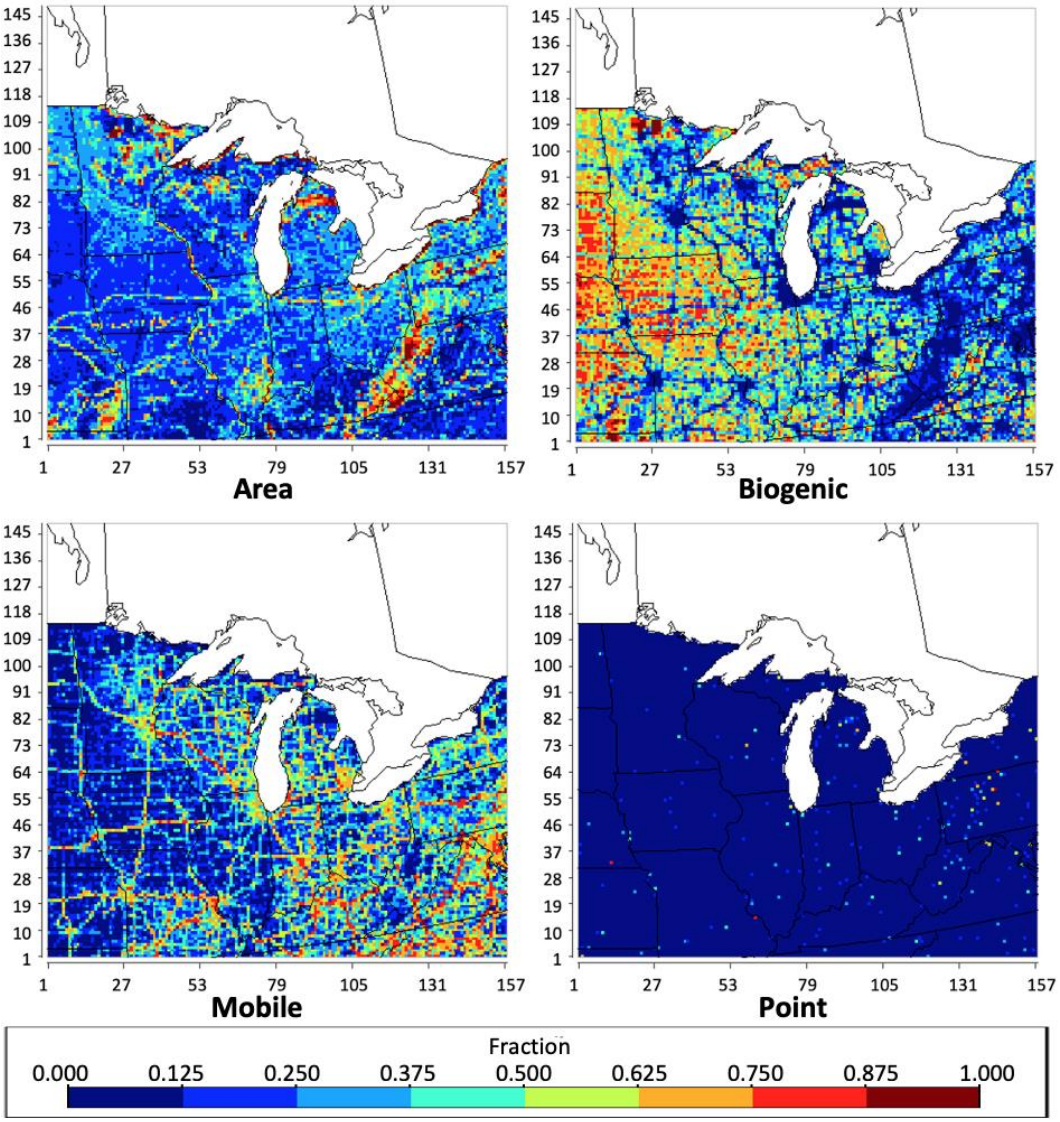

Figure 2.3.6: The geographical distribution of the fraction of NO_x emission from each SMOKE processing category (area, biogenic, mobile, point) over each grid throughout the Midwest between April and June, based on NEI-2016.

2.3.4 Model-observation comparison

In order to evaluate the SMOKE simulation of Midwestern $\delta^{15}N(NO_x)$ values, they were compared to several existing observational datasets. The first comparison is to the only direct measurements of $\delta^{15}N(NO_x)$ within the domain, which occurred in West Lafayette, IN (Walters, Fang, & Michalski, 2018). The West Lafayette, IN site is in the northwest part of Indiana and is an NADP (National Atmospheric Deposition Program) site and home to Purdue University. 30 NO_x samples were collected using denuder tubes between July 8 and August 5, 2016 (Fig. 2.8)

from 8 am to 4 pm during the daytime, and from 9:30 pm to 5:30 am during the nighttime. The measured $\delta^{15}N$ values of NO_x in West Lafayette ranged from -23.3 to 0.2 ‰ during the daytime and ranged from -33.8 to -6.9 ‰ during the nighttime.

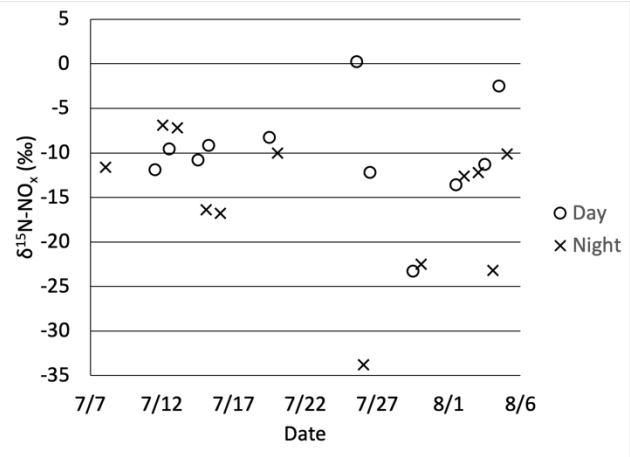

Figure 2.3.7: The $\delta^{15}N(NO_x)$ values measured at West Lafayette, IN between July 9 and August 5, 2016, from 8 am to 4 pm during the daytime (○), and from 9:30 pm to 5:30 am during the nighttime (×)

The simulated $\delta^{15}N$ values of NO_x in West Lafayette show trivial monthly variations, and a small 1‰ seasonal trend (Fig. 2.9, right axis). The simulation shows that the $\delta^{15}N$ values stay around -4 ‰ from January to March, start to decrease in April until reaching -5 ‰ in June, and then start to increase in September until returning to -4 ‰ in November. These $\delta^{15}N(NO_x)$ reflect that in West Lafayette mobile (on-road vehicle) is the dominant NO_x source (Fig. 2.9, left axis). The NO_x fraction from the mobile sector was between 0.8 and 0.9 throughout the year. Mobile NO_x during summer is 10 % lower than average, which could be explained by the decrease in vehicle traffic during the summer holiday, when most students return to their home and when biogenic and area sources slightly increase due to peak agriculture activity. This seasonal change in fractions results in the -1‰ over the summer period.

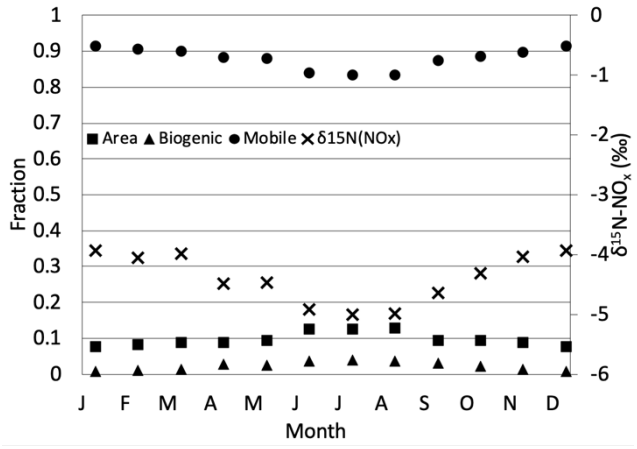

Figure 2.3.8: Fraction of monthly total NO_x emission by each SMOKE processing category (area [■], biogenic [▲], mobile [●]) over the 12-km grid, and the monthly $\delta^{15}N$ values of total NO_x emission over the 12-km grid (right axis) that covers West Lafayette, IN simulated by SMOKE, based on NEI-2002.

The SMOKE simulation of $\delta^{15}N$ values in West Lafayette, IN was compared with the measurement (Walters, Fang, & Michalski, 2018) from July 8 to August 5, 2016 (Fig. 2.10). The range of SMOKE simulated $\delta^{15}N(NO_x)$ from NEI-2002 ranges from -12.2‰ to -3.8‰, which is within the range of the corresponding measurement (-33.8 ~ 0.2 ‰). Whereas, the median (-5.0 ± 2.2 ‰) of SMOKE simulated $\delta^{15}N(NO_x)$ is higher than the median (-11.2 ± 8.0 ‰) of the measured values. As mentioned in section 3.3, the estimation of NO_x emission from biogenic sources by NEI-2016 is higher than the estimation by NEI-2002. As a result, using the data in NEI-2016 as the input, SMOKE simulated $\delta^{15}N(NO_x)$ values are lower, with the median (-7.0 ± 2.4 ‰) and range (-18.4 ~ -4.4 ‰) closer to the corresponding measurement. By comparing the SMOKE simulated $\delta^{15}N(NO_x)$ with the corresponding measurements, the NO_x emission budget in West Lafayette, IN, estimated by NEI-2016 is more accurate. While, the SMOKE simulated $\delta^{15}N(NO_x)$ values in West Lafayette, IN, based on both versions of NEI are higher than the corresponding measurements. Therefore, the emission from the soil, livestock waste, off-road vehicles, and natural gas power plants might be underestimated, and/or the emission from on-road vehicles and coal-fired power plants might be overestimated for both versions of NEI.

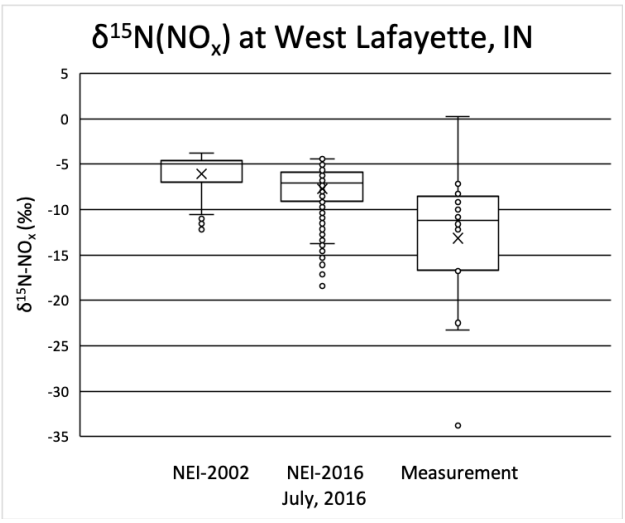

Figure 2.3.9: The distributions of $\delta^{15}N(NO_x)$ values over the 12-km grid that covers West Lafayette, IN from July 8 to August 5, simulated by SMOKE, using NEI-2002 (left) and NEI 2016 (middle) as the input, compare with the corresponding measurement (right) taken on July to August in 2016 (box: lower quartile, median, upper quartile; whisker: lower extreme, upper extreme; dots outside the whisker: outliers)

In addition to the effects from NO_x emission sources, the lower values and greater variations in measured $\delta^{15}N(NO_x)$ might also be caused by the atmospheric mixing with the emission from surrounding grids, driven by the atmospheric processes. The map shows that the NO_x emission around West Lafayette is isotopically lighter than the neighborhood emission (Fig. 2.11). Thus, the mass-weighted average of the emission within 24 grids around West Lafayette, IN was used to calculate the $\delta^{15}N(NO_x)$ values, which considered the equal mixing of the emissions from the neighborhood, driven by 4 m/s of wind speed (National Centers for Environmental Information, 2019) during the 0.84 days of atmospheric NO_x lifetime (Stavrakou et al., 2013) (Eq. (2.7)). Using this method, the simulated $\delta^{15}N$ values (median: -13.3 ± 2.5 ‰, range: -19.4 to -10.0 ‰) during the study period was closer to the measured values (median: -9.7 ± 7.6 ‰, range: -31.4 ~ 0.4 ‰) (Walters, Fang, & Michalski, 2018). Therefore, the $\delta^{15}N$ values are sensitive to effects from neighborhood emissions (Fig. 2.11). The more appropriate method will be tested on CMAQ (The Community Multiscale Air Quality Modeling System) in later researches, which takes the detailed atmospheric conditions into account for the atmospheric mixing of the pollutants.

$$(\delta^{15}N_{NO_x})_{total} = \sum f_{grid\,(i)} \times \delta^{15}N_{grid(i)} \qquad \text{Eq. (2.7)}$$

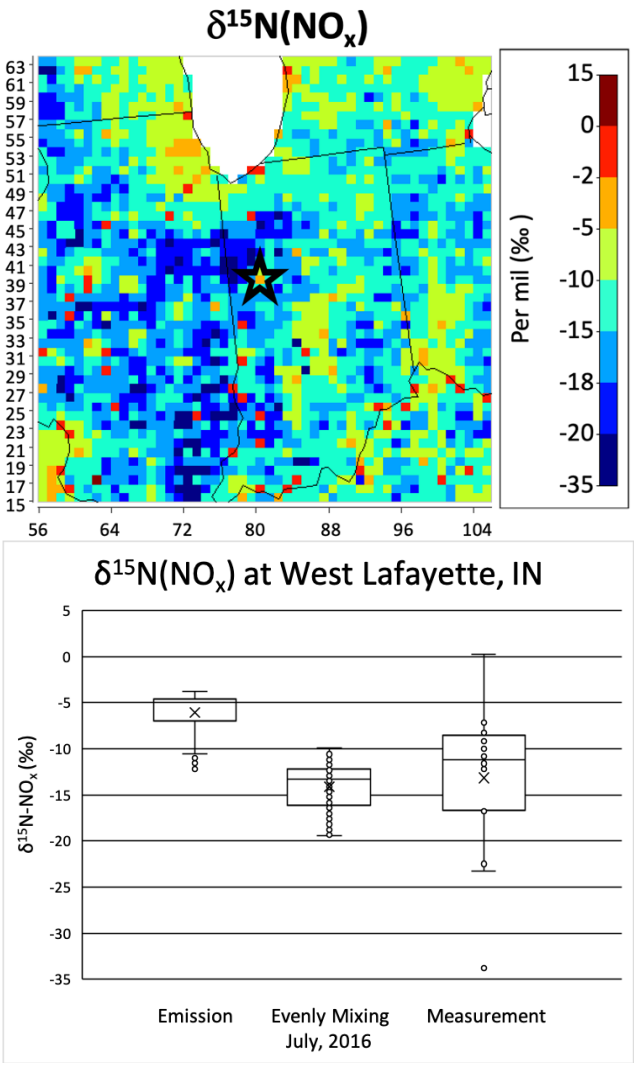

Figure 2.3.10: The $\delta^{15}N$ value of annual total NO_x emissions in 12 km^2 grids (top), center on West Lafayette, IN (☆). The modeled (with and without mixing) and measured $\delta^{15}N(NO_x)$ distributions for West Lafayette between from July 8 to August 5 (bottom). (box: lower quartile, median, upper quartile; whisker: lower extreme, upper extreme; dots outside the whisker: outliers)

Finally, we compared the emission model's predicted NO_x $\delta^{15}N$ values at 82 NADP sites in the Midwest (Fig. A.8) with measurements of NO_3^- $\delta^{15}N$ values (Elliott et al., 2009; Garten, 1992; Hall et al., 2016; Occhipinti, 2008; Russell et al., 1998). The $\delta^{15}N$ values of NO_x simulated by SMOKE at these sites show large monthly variations and a seasonal trend (Fig. 2.12, top). The monthly boxes are the 1st and 3rd quantiles of the simulated monthly $\delta^{15}N$ of NO_x emissions at the 82 sites. The whiskers represent the minimum and maximum values without outliers. There is a wide range of $\delta^{15}N(NO_x)$ values within each month, with a minimum during March (-17.1~ -1.9

‰) and the maximum during September (-26.5~-1.9 ‰). The seasonal trend shows low $\delta^{15}N(NO_x)$ during summer, with the median around -12 ‰, and high $\delta^{15}N(NO_x)$ during winter, with the median around -8 ‰. The SPSS analysis result shows the monthly change of $\delta^{15}N$ values is dominantly affected by biogenic emission. The effect from point sources is minimal since most of the NADP sites are more than 12 km (grid size of SMOKE) away from power plants. The NADP sites are not in big cities but close to soil emission. Thus, biogenic emission has the strongest effect on the $\delta^{15}N$ values of NO_x emission, account for 86.6% of the change on $\delta^{15}N(NO_x)$.

Comparing with the SMOKE simulation, the measurements of $\delta^{15}N$ values of NO_3^- in the United States from previous researches (Elliott et al., 2009; Garten, 1992; Hall et al., 2016; Occhipinti, 2008; Russell et al., 1998) shows the similar monthly variations and seasonal trend (Fig. 2.12, bottom). There is a wide range of $\delta^{15}N(NO_3^-)$ values within each month, with a minimum during June (-4.6~ 1.5 ‰) and a maximum during December (-1.0~12.5 ‰). The seasonal trend shows low $\delta^{15}N(NO_3^-)$ during summer, with the median around -2 ‰, and high $\delta^{15}N(NO_3^-)$ during winter, with the median around 2 ‰. The measured $\delta^{15}N$ values of NO_3^- has the same seasonal trend as the SMOKE simulated $\delta^{15}N$ values of NO_x. However, the measured $\delta^{15}N$ values of NO_3^- is about 10 ‰ higher than the SMOKE simulated $\delta^{15}N$ values of NO_x. This is because of the photochemical and equilibrium isotope effects that occur during the transformation of NO_x into NO_3^-, which enriches the ^{15}N isotopes in NO_3^-, as a more oxidized form of NO_y (Walters & Michalski, 2015; Walters et al., 2016). The 10‰ difference between the measured $\delta^{15}N(NO_3^-)$ and the SMOKE simulated $\delta^{15}N$ (NO_x) agree well with the previous study (Chang et al., 2018). The effect of tropospheric photochemistry, including the net N isotope effect during the conversion of NO_x to NO_3^-, will be addressed in Chapters 4~5.

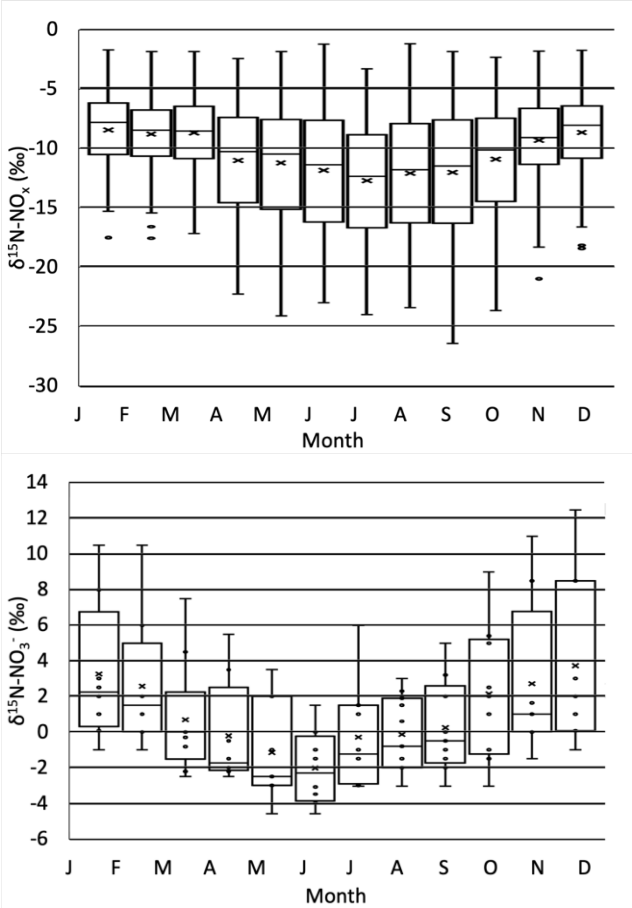

Figure 2.3.11: The SMOKE predicted the $\delta^{15}N$ value of total NO_x at 82 NADP sites (top) using NEI-2002 compared to the measured $\delta^{15}N$ of rain NO_3^- (bottom) from prior studies.

2.4 Conclusion

The $\delta^{15}N$ of atmospheric NO_x was simulated by SMOKE, by considering the NO_x emissions from NEI emission sectors and the corresponding $\delta^{15}N$ values from previous researches. $\delta^{15}N$ is a decent tool to present the spatial and temporal composition of atmospheric NO_x, as well as the corresponding variation in NO_x emission sources. The simulation indicates that the NO_x emission from biogenic sources is the key driver for the variation of $\delta^{15}N$, especially among the NADP sites. Comparing with the measurements of $\delta^{15}N(NO_3^-)$ from NADP sites within the Midwest region, the simulated $\delta^{15}N$ agreed well with the seasonal trend and monthly variation. While, the simulated NO_x is slightly heavier than the corresponding measurements in West Lafayette, IN, taken from July to August 2016. According to the previous researches, the uncertainty of NO_x emission is 71-250% from soil and 10-15% from vehicles. The variations among the removal efficiency of

different emission control technologies vary from 30% to 90%, also causes the uncertainty of power plant NO_x emission. In addition, in this study, due to the lack of measurements, the $\delta^{15}N$ of coal-fired and natural gas non-EGUs (industrial boilers, commercial and residential fuel combustions) were assumed to be the same as the $\delta^{15}N$ of coal-fired and natural gas EGUs respectively. Thus, detailed measurements of the $\delta^{15}N$ of non-EGUs are necessary for future study. Besides this, the non-road vehicles (aircrafts, ships, and trains) also need to be included in the future study.

If we only consider the effects from NO_x emission sources, the emission from soil, livestock waste, off-road vehicles, and natural gas power plant in West Lafayette, IN are possible to be underestimated, and the emission from the on-road vehicle and coal-fired power plant in West Lafayette, IN are possible to be overestimated. Another reason causing the estimated NO_x isotopically heavier than measured NO_x is the mixing caused by atmospheric processes, since the NO_x emission from the surrounding region of West Lafayette, IN is lighter. In addition, the tropospheric photochemistry could also alter the $\delta^{15}N$ values during the processes that convert NO_x to NO_y. Chapters 3~5 will explore the impacts of atmospheric processes and tropospheric photochemistry by incorporating ^{15}N into CMAQ and comparing the simulations with the corresponding measurements.

CHAPTER 3. SIMULATING Δ 15N OF ATMOSPHERIC NOX IN CMAQ VERSION 5.2.1, BASED ON 15N INCORPORATED SMOKE VERSION 4.6 AND WRF VERSION 4.0 FOR ASSESSING THE ROLE ATMOSPHERIC PROCESSES PLAYS IN CONTROLLING THE ISOTOPIC COMPOSITION OF NOX, NOY, AND ATMOSPHERIC NITRATE

The following chapter is a reprint from an article currently in press (Fang, H. and Michalski, G. Simulating $\delta^{15}N$ of atmospheric NO_x in CMAQ version 5.2.1, based on ^{15}N incorporated SMOKE version 4.6 and WRF version 4.0 for assessing the role atmospheric processes plays in controlling the isotopic composition of NO_x, NO_y, and atmospheric nitrate. *Geoscientific Model Development*)

3.1 Introduction

NO_x (NO_x = NO + NO_2) are important trace gases that affect atmospheric chemistry, air quality, and climate. The NO_x could be converted into NO_y (NO_y = NO_x + HONO + HNO_3 + HNO_4 + N_2O_5 + other N oxides) in the atmospheric NO_x cycle. During this process, the ground-level concentration of O_3 is elevated and secondary particles are generated. Secondary aerosols in turn affect cloud physics, enhancing the reflection of solar radiation (Schwartz, S. E., 1996) and are hazardous to human health (Lighty et al., 2000). Due to its impacts on air quality, climate, human health, and the environment, understanding the spatial and temporal variation in the sources of NO_x is a vital scientific question. However, there are still a number of significant uncertainties in the NO_x budget despite years of research. These include a). soil NO_x emissions caused by the application of N fertilizers (Shepherd, 1991; Ludwig et al., 2001; Galloway et al., 2004; Hudman, 2012; Houlton et al., 2013; Pilegaard, 2013) and the role of vegetation (Johansson, 1987; Jacob & Wofsy, 1990; Hanson & Lindberg, 1991; Yienger & Levy II, 1995; Thoene, Rennenberg & Weber, 1996; Slovik et al., 1996; Webber & Rennenberg, 1996; Almaraz et al., 2018); b). emissions from on-road vehicles estimated by different algorithms (Pierson et al., 1996; Singer & Harley, 1996; Cicero-Fernandez et al., 1997; Dreher & Harley, 1998; Dreher & Harley, 1998; Sawyer et al., 2000; Parrish, 2006); and c). power plant NO_x emissions due to the implementation of different NO_x emission control technologies (Felix et al., 2012; Srivastava et al., 2005; Xing et al., 2013).

Previous research has shown that there are distinctive differences in $\delta^{15}N$ values for NO_x from different emission sources (Fig. 3.1), such as soil (Li & Wang, 2008; Felix & Elliott, 2014; Yu & Elliott, 2017; Miller et al., 2018), wastes (Felix & Elliott, 2014), vehicles (Moore, 1977; Heaton,

1990; Ammann et al., 1999; Pearson et al., 2000; Savard et al., 2009; Redling et al., 2013; Fibiger, 2014; Felix & Elliott, 2014; Walters et al., 2015a; Walters et al., 2015b), and power plants (Heaton, 1987; Heaton, 1990; Snape, 2003; Felix et al., 2012; Felix et al., 2015; Walters et al, 2015a; Savard et al., 2017). Thus, the nitrogen stable isotope composition ($\delta^{15}N$) of NO_x could be an effective tracer of atmospheric NO_x sources. The $\delta^{15}N(NO_x)$ is determined by

$$\delta^{15}N(NO_x)\ (‰) = [(^{15}NO_x/^{14}NO_x) / (^{15}N_2/^{14}N_2)_{\ air} - 1] \times 1000) \quad \text{Eq. (3.1)}$$

where $^{15}NO_x/^{14}NO_x$ is the measurement of relative abundance of ^{15}N to ^{14}N in atmospheric NO_x, compared with the ratio of nitrogen in the air, which has a $^{15}N_2/^{14}N_2 = 0.0036$.

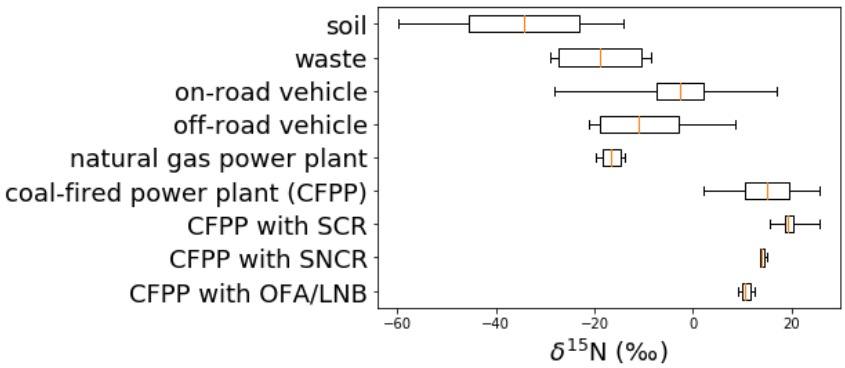

Figure 3.1.1: Box (lower quartile, median, upper quartile) and whisker (lower extreme, upper extreme) plot of the distribution of $\delta^{15}N$ values for NO_x emission sources

Here we have simulated the $\delta^{15}N$ values of atmospheric NO_x within the Midwestern United States, under different scenarios, and compared them with the recent measurements. The factors required to account for the processes that alter $\delta^{15}N$ of atmospheric NO_x during the NO_x chemical lifetime are a). The variability of the $\delta^{15}N$ values of NO_x emissions in time and space; b). The transport and mixing of tropospheric NO_x by meteorology; c.) The wet and dry deposition of NO_x/NO_y; and d). The isotope effects occurring during the tropospheric photochemistry that transforms NO_x into NO_y. In a companion paper (Fang & Michalski, 2020), we discussed the effects due to the variation of the $\delta^{15}N$ value of different NO_x emission sources and their variation in time and space. In this previous study (Fang & Michalski, 2020), ^{15}N was incorporated into the US EPA trace gas emission model SMOKE (Sparse Matrix Operator Kernel Emissions), in order

to simulate the spatiotemporal patterns in the isotopic composition NO_x and compare them with corresponding atmospheric measurements. However, the variability in NO_x emissions over time and space is not sufficient to resolve the spatial and temporal changes in the measured $\delta^{15}N$ values, due to the bias of the static SMOKE output files. For example, NO_x emitted from a single grid cell dominated by a coal-fired power plant would result in a NO_x $\delta^{15}N$ around +12‰. If this grid cell were surrounded by a large array of grid cells dominated by agricultural land-use with a $\delta^{15}N$ of -30‰, the impression is that the region would have a $\delta^{15}N$ value close to -30‰. However, since the power plant emits much more NO_x than the surrounding agricultural fields what would be expected for the actual regional NO_x $\delta^{15}N$ value is biased by the finer emission grid scale. This bias was reduced by weighting each grid cell's NO_x emission relative to the regional total (Fang & Michalski, 2020). In other words, the fine-scale grids were expanded to larger grids, based on assumptions about the NO_x lifetime and transport length scales. This is an unsatisfactory method since the transport of atmospheric NO_x is not controlled by radial diffusion, rather by meteorology/eddy diffusion driven by pressure gradients.

In this work, we explore the effects from the second and third factors, the impacts from atmospheric transport and deposition processes, by incorporating an input dataset of ^{15}N emissions used in simulations by the Chemistry-Transport Model (CTM) used in CMAQ (The Community Multiscale Air Quality Modeling System). We have previously explored the isotope effects arising from tropospheric photochemistry using a 0D box model (Michalski et al., 2020). This ^{15}N isotope reaction scheme will be incorporated into CMAQ as a new chemical mechanism in order to use CMAQ to simulate the $\delta^{15}N$ of NO_y compounds in the subsequent research. The goal of this chapter is to explore how atmospheric processes alter the $\delta^{15}N$ of atmospheric NO_x in time and space in the Midwestern US in the absence of isotope effects occurring during the photochemical transformation of NO_x (source and mixing hypothesis).

3.2 Methodology

In this study, we investigate the role of meteorological transport and removal processes play in the spatiotemporal distribution of NO_x $\delta^{15}N$ values. The ^{15}N emission dataset previously developed (Fang & Michalski, 2020) was used as input for CMAQ to simulate the meteorological transport effects (advection, eddy diffusion, etc). In addition, CMAQ simulated the effect of NO_x (nitrate) removal by dry and wet deposition rate is assessed to determine the role of chemistry and

deposition might play in the $\delta^{15}N$ of NO_x and atmospheric nitrate. The isotope effects associated with the photochemical transformation of NO_x into HNO_3 and other higher N oxides are ignored, therefore, this chapter only focuses on mixing effects and "lifetime chemistry", which blur the grid specific NO_x $\delta^{15}N$ value across the regional scale. The simulations using the same 2002 National Emission Inventory (NEI) but different meteorology conditions (2002 and 2016) were compared, in order to explore how meteorology condition impacts the atmospheric $\delta^{15}N(NO_x)$. Then simulations using the same meteorology condition (2016) but different emission inventories (2002 NEI and 2016 NEI) were compared, in order to explore how emission inventory impacts the atmospheric $\delta^{15}N(NO_x)$. The simulations cover the full domain and nested domain were conducted, in order to explore and eliminate the bias near the domain boundary.

3.2.1 The domain of the study

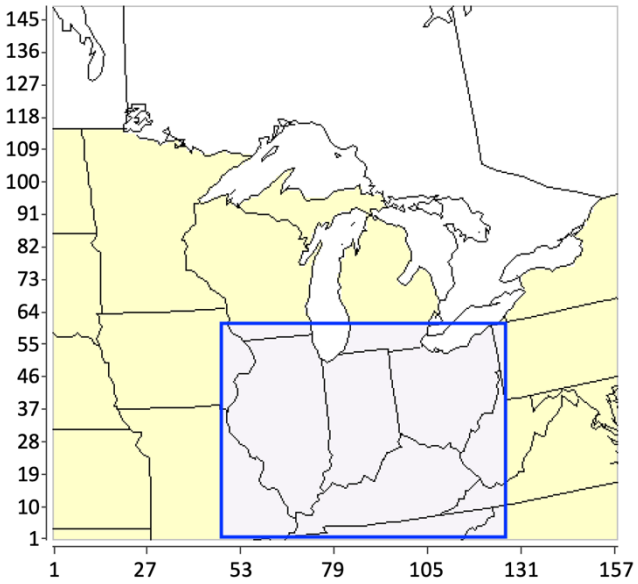

Figure 3.2.1: The full geographic domain (yellow) and nested domain (light purple) for the study.

Two domains were used, a larger domain encompassing the Midwestern region of the United States and a smaller nested domain of the central portion of the Midwest domain (Fig. 3.2). The larger Midwestern domain coordinates ranged from 37 N to 45 N in latitudes, and 98 W to 78 W in longitude. This fully covers the states of Minnesota, Iowa, Missouri, Wisconsin, Illinois,

Michigan, Indiana, Kentucky, Ohio, and West Virginia, and partially covers North Dakota, South Dakota, Nebraska, Kansas, Tennessee, North Carolina, Virginia, Maryland, Pennsylvania, and New York (Fig. 3.2, in yellow). A nested domain, which fully covers the states of Indiana, Illinois, Ohio, and Kentucky was extracted (Fig. 3.2, in light purple), in order to reduce the model bias near the borders that include boundary conditions (details in section 2.6). The horizontal grid resolution for both domains was 12 km x 12 km. The vertical grid resolution is isobaric dependent, which increases with height, from 50 m near the surface (bottom layer) to 600 m near the 50 mb pressure level (top layer).

3.2.2 $^{15}NO_x$ and $^{14}NO_x$ emission input dataset

The NO_x emission input dataset used by the CTM in CMAQ was prepared, based on the steps described by Fang & Michalski (2020), and are briefly discussed below. The EPA SMOKE model was used to simulate $^{14}NO_x$ emissions. SMOKE converts the annual NO_x emission from county-level emission data contained in the NEI, into hourly emissions and partitions the emission into the gridded format. The emission input datasets were prepared using both the 2002 and 2016 versions of the NEI. The main sources of NO_x emissions in the NEI's are on-road gasoline, on-road diesel, off-road gasoline, off-road diesel, coal-fired power plant, natural gas power plant, soil, and livestock wastes, were categorized into four SMOKE processing categories: Biogenic, Mobile, Point, and Area (Table 3.1).

The ^{15}N was incorporated into SMOKE outputs, based on NO_x emissions from NEI emission sectors and the corresponding $\delta^{15}N$ values previously discussed (Fang & Michalski, 2020; Table 3.1). The $^{15}NO_x$ emitted by each SMOKE processing category was calculated based on the definition of $\delta^{15}N$ (‰).

$$^{15}NO_x(i) = {}^{14}NO_x(i) \times {}^{15}R_{NO_x}(i) \qquad \text{Eq. (3.2)}$$

where $^{14}NO_x(i)$ is the NO_x emissions for each category (i) obtained from NEI and $^{15}R_{NOxi}$ is a ^{15}N emission factor ($^{15}NO_{Xi}/^{14}NO_{xi}$) calculated by:

$$^{15}R_{NO_x}(i) = \left(\frac{\delta^{15}N_{NO_x(i)}}{1000} + 1\right) \times 0.0036 \qquad \text{Eq. (3.3)}$$

$\delta^{15}N_{NOx(i)}$ is the $\delta^{15}N$ value of each NO_x source category (i = area, biogenic, mobile, and point) (Table 3.1) and 0.0036 is the $^{15}N/^{14}N$ of air N_2, the reference point for $\delta^{15}N$ measurements. The $\delta^{15}N$ of total NO_x emission was calculated by

$$\delta^{15}N_{NO_x\,(total)} = \left(\frac{\frac{^{15}NO_x\,(area)+{}^{15}NO_x\,(biog)+{}^{15}NO_x\,(mobile)+{}^{15}NO_x\,(point)}{^{14}NO_x\,(area)+{}^{14}NO_x\,(biog)+{}^{14}NO_x\,(mobile)+{}^{14}NO_x\,(point)}}{0.0036} - 1\right) \times 1000 \quad \text{Eq. (3.4)}$$

Where

$$^{15}NO_x\,(area) = \left(\frac{\delta^{15}N_{NO_x\,(waste)}}{1000} + 1\right) \times 0.0036 \times {}^{14}NO_x\,(waste) + \left(\frac{\delta^{15}N_{NO_x\,(off-road\,gas)}}{1000} + 1\right) \times 0.0036 \times {}^{14}NO_x\,(off-road\,gas) + \left(\frac{\delta^{15}N_{NO_x\,(off-road\,diesel)}}{1000} + 1\right) \times 0.0036 \times {}^{14}NO_x\,(off-road\,diesel) \quad \text{Eq. (3.5)}$$

$$^{15}NO_x\,(mobile) = \left(\frac{\delta^{15}N_{NO_x\,(on-road\,gas)}}{1000} + 1\right) \times 0.0036 \times {}^{14}NO_x\,(on-road\,gas) + \left(\frac{\delta^{15}N_{NO_x\,(on-road\,diesel)}}{1000} + 1\right) \times 0.0036 \times {}^{14}NO_x\,(on-road\,diesel) \quad \text{Eq. (3.6)}$$

where $\delta^{15}N_{NO_x\,(on-road\,gas)} = -12.35 + 3.02 \times \ln(t + 0.455)$

The biogenic is NO_x emission from by-products of microbial nitrification and denitrification occurring in the soil; the mobile is NO_x emission from the on-road vehicle; the point is NO_x emission from power plants or industry; and the area is all other stationary anthropogenic NO_x emissions, which spread over a spatial extent and individually too small in magnitude to report as point source These include off-road vehicles (utility vehicles for agricultural and residential purposes), residential combustion, industrial processes, agriculture production (livestock waste, fertilizer, etc), etc. Using Eq. (3.2-6) and $\delta^{15}N$ values from previous research (Table 3.1), $^{15}NO_x$ emission files were generated from the SMOKE $^{14}NO_x$ output files. The $\delta^{15}N$ of on-road gasoline vehicles was based on the average vehicle travel time (t) within each region with the same zip code (Walters et al., 2015a). The average $\delta^{15}N$ of on-road gasoline vehicles within the study area is -2.7 ± 0.8‰.

Table 3.2.1: $\delta^{15}N$ values for NO_x emission sources by SMOKE processing category and NEI sector

SMOKE Category	NEI Sector	$\delta^{15}N$-NO_x (‰) in this study
Biogenic	Soil	-34.3 (Felix & Elliott, 2014)
Area	Livestock Waste	-18.8 (Felix & Elliott, 2014)
	Off-road Gasoline	-11.5 (Walters et al., 2015b)
	Off-road Diesel	-10.5 (Walters et al., 2015b)
Mobile	On-road Gasoline	-2.7 (Walters et al., 2015b)
	On-road Diesel	-2.5 (Walters et al., 2015b)
Point	Coal-fired EGUs	+15 (Felix et al., 2012)
	Natural Gas EGUs	-16.5 (Walters et al., 2015)

Since the isotope effects associated with the photochemical transformation of NO_x into NO_y are ignored, ^{15}N was not incorporated into the chemical mechanism of CMAQ for the simulations of this research. Therefore, the $^{15}NO_x$ in the emission input dataset acts as a nonreactive chemical. Since $^{14}NO_x$ will go through and be removed in CMAQ's chemical mechanism, the $^{14}NO_x$ in the emission input dataset was replicated and set as a nonreactive chemical. As a result, the mixing effects on the $\delta^{15}N$ of atmospheric NO_x were explored, through the analysis of the time evolution of nonreactive $^{14}NO_x$ and $^{15}NO_x$ concentrations.

3.2.3 Meteorology input dataset

To explore the impact of atmospheric processes, the meteorology input datasets for the year 2002 and 2016 were prepared and compared. The preparation of the meteorology input datasets for the simulation using CMAQ CTM (CCTM) requires multiple steps. The first step is to generate the input for the CTM meteorological model using the NARR (North American Regional Reanalysis) and NAM (North American Mesoscale Forecast System). Both NARR and NAM Analyses are regional weather model datasets covering North America and were obtained from the National Centers for Environmental Information (2019). NARR and NAM were used to convert the weather observations (every 3 hours for NARR, every 6 hours for NAM Analyses) into gridded

meteorological elements, such as temperature, wind field, and precipitation, with the horizontal resolution of 12 km, and 34 vertical layers, with the thickness, increases with height, from 50 m near the surface to 600 m near the 50 mb pressure level. The simulation years were 2002 and 2016 and were selected based on the same timeframe as selected NO_y $\delta^{15}N$ measurements. These include measurements of $\delta^{15}N(NO_3^-)$ at 8 NADP (National Atmospheric Deposition Program) sites within Indiana, Illinois, Ohio, and Kentucky in 2001-03, and the direct measurements of $\delta^{15}N(NO_x)$ between July and August 2016 (Mase, 2010; Riha, 2013).

The second step was to generate the gridded meteorology files on an hourly basis, using the Weather Research and Forecasting Model (WRF) using the input files prepared by the NARR and NAM analyses. To maintain consistency between the NO_x emission dataset and the meteorology, the same coordinate system, spatial domain, and grid size used in the SMOKE model were used in the WRF simulation. The same as the emission dataset, the projection type of WRF output is Lambert Conformal, with the standard parallel of 33 N and 45 N, the central meridian of 97 W. The output dataset of WRF has the same spatial domain as the emission dataset with a horizontal resolution of 12 km.

The last step is to prepare the CMAQ-ready meteorology input dataset based on WRF outputs, by running MCIP (the Meteorology-Chemistry Interface Processor), one of the major components of CMAQ. The MCIP first obtains the necessary parameters (Table B.1) from WRF outputs. Then the MCIP extracts the data of the necessary parameters for the appropriate geographic domain, which are slightly smaller than the domain of WRF outputs since the cells near the boundary are inadequate for CMAQ simulation. For example, the geographic domain of WRF outputs for this research is 160 grids in the east-west direction and 151 grids in the north-south direction. Therefore, MCIP extracts the WRF outputs into 157 grids in the east-west direction and 148 grids in the north-south direction, which are exactly the same as the emission input dataset prepared from the previous companion research (Fang & Michalski, 2020), and are adequate for CMAQ simulation. After that, MCIP converts the units of the parameters into the units, which are consistent with the CMAQ simulation. For example, the 10-meter wind is displayed as u (east-west) and v (north-south) component of wind vector in WRF but is displayed as wind speed and wind direction in CMAQ. If the parameters, which are necessary for running CMAQ, are not available from the WRF output, MCIP will diagnose and compute them, such as PBL (planetary boundary layer) parameters and cloud information (cloud top, cloud base, liquid water content, cloud coverage).

The MCIP also conducts the interpolation and mass-weighted averaging of data, if the grid resolutions of WRF and CMAQ are different. Finally, MCIP organizes the parameters into seven netCDF files that embedded with I/O API (input/output applications programming interface): 2-D time-independent fields at cell centers, 2-D time-independent fields on domain perimeter, 2-D time-independent fields at cell corners, 2-D time-dependent fields at cell centers, 3-D time-dependent fields at cell centers, 3-D time-dependent fields on domain perimeter, and 3-D time-dependent fields at cell corners (Table B.2).

3.2.4 The role of deposition

The dry and wet deposition rates of nonreactive $^{14}NO_x$ and $^{15}NO_x$ were varied to assess their role in the spatiotemporal distribution of NO_x $\delta^{15}N$ value. First, the dry and wet deposition rate of $^{14}NO_x$ and $^{15}NO_x$ was set to zero to test the effect of transport and mixing only. This no-deposition simulation was based on 2002 NEI and 2016 meteorology. Next, the dry and wet deposition rate of nonreactive $^{14}NO_x$ and $^{15}NO_x$ was set equal to the CMAQ default (reactive) $^{14}NO_x$ rate in the simulation under the same scenario as the preliminary simulation. An additional simulation under the same scenario, with the amplified dry and wet deposition rate, was conducted, to utilize as the "pseudo tropospheric photochemistry" that removes atmospheric NO_x. To determine the deposition rate of nonreactive $^{14}NO_x$ and $^{15}NO_x$, the initial concentration of NO_x was first magnified to 20 times of the initial concentration derived from the ASCII vertical profiles to represent a relatively polluted atmospheric chemical condition. At the same time, the emission rate of nonreactive $^{14}NO_x$ and $^{15}NO_x$ was set to zero, in order to explore the removal of nonreactive $^{14}NO_x$ and $^{15}NO_x$ by deposition. After the multiple tuning trials, the deposition velocity of nonreactive $^{14}NO_x$ and $^{15}NO_x$ was set to 30 times of the deposition rate of reactive $^{14}NO_x$, of which more than 90% of the nonreactive $^{14}NO_x$ and $^{15}NO_x$ were removed in the simulation period of 2 days. This is in effect the same as simulating the conversion of NO_x into HNO_3, without any isotope effect, without having to alter the chemical mechanism to include ^{15}N. This "pseudo HNO_3" is then removed by wet/dry deposition and the 2-day criteria is the estimated lifetime of NO_x in the atmosphere. By comparing the CMAQ simulation with different settings of NO_x deposition rate, how the removal of atmospheric NO_x by dry and wet deposition impacts the $\delta^{15}N$ of atmospheric NO_x was explored.

3.2.5 Initial condition and boundary condition for the simulation

The meteorological fields generated by MCIP were used as the inputs for Initial Conditions Processor (ICON) and Boundary Conditions Processor (BCON), used for running CCTM of CMAQ. The ICON program prepares the initial chemical/isotopic concentrations in each of the 3D grid cells for use in the initial time step of the CCTM simulation. For this study, the initial condition was derived from the ASCII vertical profiles to create a "clean" atmospheric chemical condition within the domain at the beginning of the simulation, of which the background concentration of NO_x in each grid is lower than 0.25 ppb. The BCON program prepares the chemical/isotopic boundary condition for throughout the CCTM simulation. Similarly, the boundary condition was derived from the ASCII vertical profiles for this study, which assume a "clean" atmospheric chemical condition (NO_x concentration lower than 0.25 ppb at surface layer) outside the domain.

The $^{14}NO_x$ in the outputs of ICON and BCON were replicated and set as nonreactive chemical. The same technique was applied to the emission input dataset as well. The nonreactive $^{15}NO_x$ were added to the outputs of ICON and BCON, with the concentration equals to 0.0036 of the concentrations of reactive $^{14}NO_x$, which assumes $\delta^{15}N = 0$ at the initial time step and outside the domain of the simulation (calculated based on Eq. (3.1-3)). The nonreactive $^{14}NO_x$ and $^{15}NO_x$ do not go through the chemical mechanism within CMAQ so that the effects from tropospheric photochemistry are excluded, thus only atmospheric processes are explored.

3.2.6 Different versions of the NO_x emission inventory

The simulated $\delta^{15}N$ of atmospheric NO_x based on different emission inventories varies. In order to explore how the difference in $\delta^{15}N$ of NO_x emission impacts the simulated atmospheric NO_x, under the same meteorology conditions, and keep the consistency of the simulation at the same time, two different emission input datasets were prepared. The first dataset was solely based on NEI-2002. The ^{15}N was incorporated into the pre-merged SMOKE output, simulated from each sector of NEI-2002 that contains NO_x emission, based on the corresponding $\delta^{15}N$ values, before merging into the emission input dataset for CCTM simulation. The second dataset, as a comparison, directly obtain the emission rates from the first dataset, except for $^{15}NO_x$. The emission rate of $^{15}NO_x$ was determined by the emission rate of $^{14}NO_x$, obtained from the first dataset, and $\delta^{15}N$ of

total NO_x emission, simulated from NO_x emissions from each emission sector based on NEI-2016 and the corresponding $\delta^{15}N$ values determined by the previous companion research (Fang & Michalski, 2020). Thus, the only difference between the two emission input datasets is the $\delta^{15}N$ of the NO_x emission over each grid within the domain.

3.2.7 The simulation over the nested domain

As mentioned in section 2.5, atmospheric NO_x $\delta^{15}N = 0‰$ for initial condition and boundary condition. As a result, the bias occurs near the border of the research area, mainly under the following two circumstances: a). When the air mass transports out of the research area (Fig. B.1) since Canada is considered as "emission-free zone", the atmospheric NO_x is diluted, which impacts its $\delta^{15}N$ values, especially for those with extreme $\delta^{15}N$ values ($\delta^{15}N < -15‰$ or $\delta^{15}N > 5‰$); b). When the air mass with $\delta^{15}N(NO_x)=0$ transports from "emission-free zone" to the research area (Fig. B.2), the atmospheric $\delta^{15}N(NO_x)$ is flattened. Therefore, to avoid the bias near the border, the nested domain that only covers Indiana, Illinois, Ohio, and Kentucky was determined, where the measurements of $\delta^{15}N$ values at NADP sites are available (Mase, 2010; Riha, 2013). The boundary condition for the simulation over the nested domain is extracted from the CCTM output of the full-domain simulation.

3.3 Results and Discussion

3.3.1 Simulated spatial variability in δ15N of atmospheric NOx

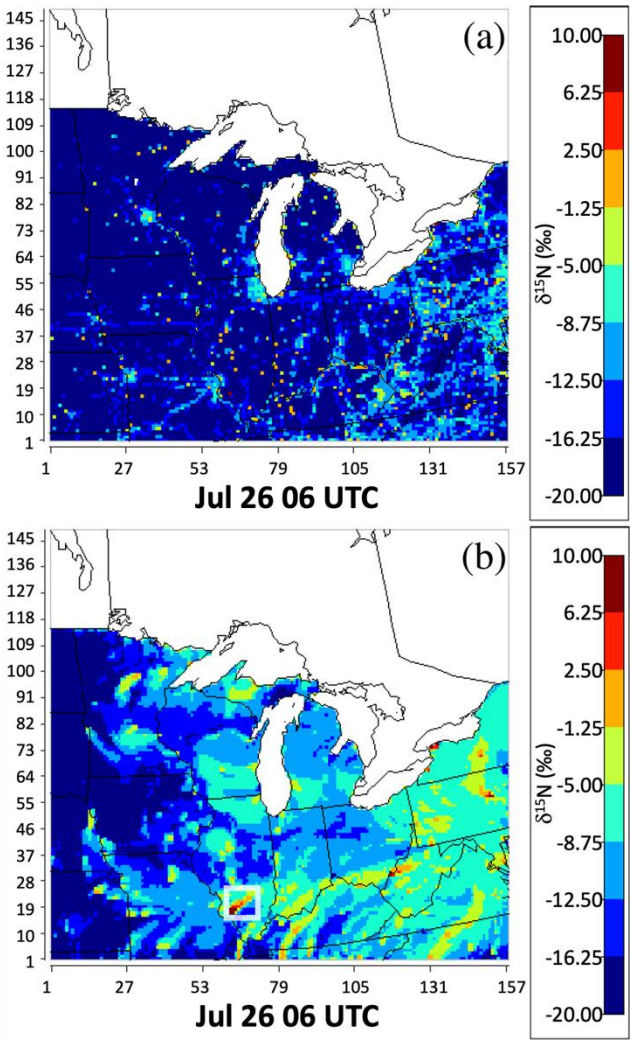

Figure 3.3.1: The $\delta^{15}N$ values of NO_x emission, based on NEI-2002 (a: "no transport" scenario) and the $\delta^{15}N$ values of atmospheric NO_x based on NEI-2002 and 2016 meteorology (b: "with transport" scenario), at 06 UTC on July 26, are presented by color in each grid. The warmer the color, the higher $\delta^{15}N$ values of atmospheric NO_x.

We first examine the spatial heterogeneity of NO_x $\delta^{15}N$ values at a specific time within the Midwestern domain and explore how atmospheric processes alter the $\delta^{15}N$ values relative to the "no transport" simulation. The "no transport" simulation of NO_x $\delta^{15}N$ values (at 06 UTC on July 26) shows that the domain grids ranged from -34.3‰ to 14.9‰ (Figure 3a). The majority of the

grids within the domain have NO_x $\delta^{15}N$ values lower than -16.3‰. These low $\delta^{15}N$ values across most of the domain are due to the $\delta^{15}N$ of -34.3‰ for biogenic NO_x emission sources (nitrification and denitrification) in sparsely populated areas where intensive agriculture dominates the land use (Fig. 3.3a). The $\delta^{15}N$ values of NO_x emitted into grids within big cities mainly ranged between -8.75‰ and -5‰. This is due to the higher fraction of NO_x emission from on-road vehicles having a $\delta^{15}N$ of -2.7 ± 0.8‰. The fraction of NO_x emission from on-road vehicles at the grids resolve major highways is relatively lower, comparing to the grids within big cities, while still higher than most of the grids within the domain. Thus, the $\delta^{15}N$ values along the major highways ranged between -16.25‰ and -8.75‰. The highest value of $\delta^{15}N$ occurs at the grids, where the coal-fired EGUs (+15‰) and hybrid-fired EGUs (using both coal and natural gas (-16.5‰) for combustion) are dominant, showing gold (-1.25‰ ~ +2.5‰) and red/dark red (+2.50‰ and above) on the map (Fig. 3.3a).

The effect of atmospheric mixing and transport on the NO_x $\delta^{15}N$ spatial distribution were then taken into account by coupling the $^{15}NO_x$ emissions (Fang & Michalski, 2020) to the meteorology simulation. There are significant differences between $\delta^{15}N(NO_x)$ values in the "no transport" (Fig. 3.3a) and the "with transport" (Fig. 3.3b) simulations. For example, under the "no transport" scenario (Fig. 3.3a) the map of $\delta^{15}N(NO_x)$ values clearly shows the locations of big cities, major highways, and power plants, but these features are much less obvious in the "with transport" (Fig. 3.3b) simulations. The isotopically heavier NO_x emission from big cities, such as Chicago, Detroit, Minneapolis-St Paul, Kansas City, St. Louis, Indianapolis, and Louisville, disperses to the surrounding rural areas so that the $\delta^{15}N(NO_x)$ values in rural areas are elevated to values similar to nearby big cities. Similarly, the NO_x emitted along major highways is transported to the surrounding grids, so that the atmospheric NO_x at the grids around the major highways become isotopically heavier relative to the "no transport" scenario. The most obvious and interesting example is the influence of grids containing coal-fired EGUs on the surrounding region. For example, the EGU located in the southwestern border of the state of Illinois, Baldwin Energy Complex (marked with a transparent white box on Fig. 3.3b), using refined coal, subbituminous coal, and bituminous coal as its major energy source. The $\delta^{15}N(NO_x)$ in the regions is altered as a function of distance away from the EGU and in this time snapshot, the northeastwards propagating plume of NO_x emission from the EGU creates higher $\delta^{15}N(NO_x)$ over 103 km away. Overall, the "with transport" $\delta^{15}N(NO_x)$ map is indicating the emission source that impacts each grid the most,

after taking atmospheric mixing and transport into account. The domain average $\delta^{15}N$ increases from -20.23‰ under the "no transport" scenario, to -11.49‰ under the "with transport" scenario. The overall emission pattern of the $\delta^{15}N$ value shows that the biogenic emission dominates the spatial domain but after considering the atmospheric processes, anthropogenic emission, mainly from on-road vehicles, becomes dominant over most of the grids, especially for the grids located in the suburb of major cities.

3.3.2 Seasonal variation in δ15N of NOx

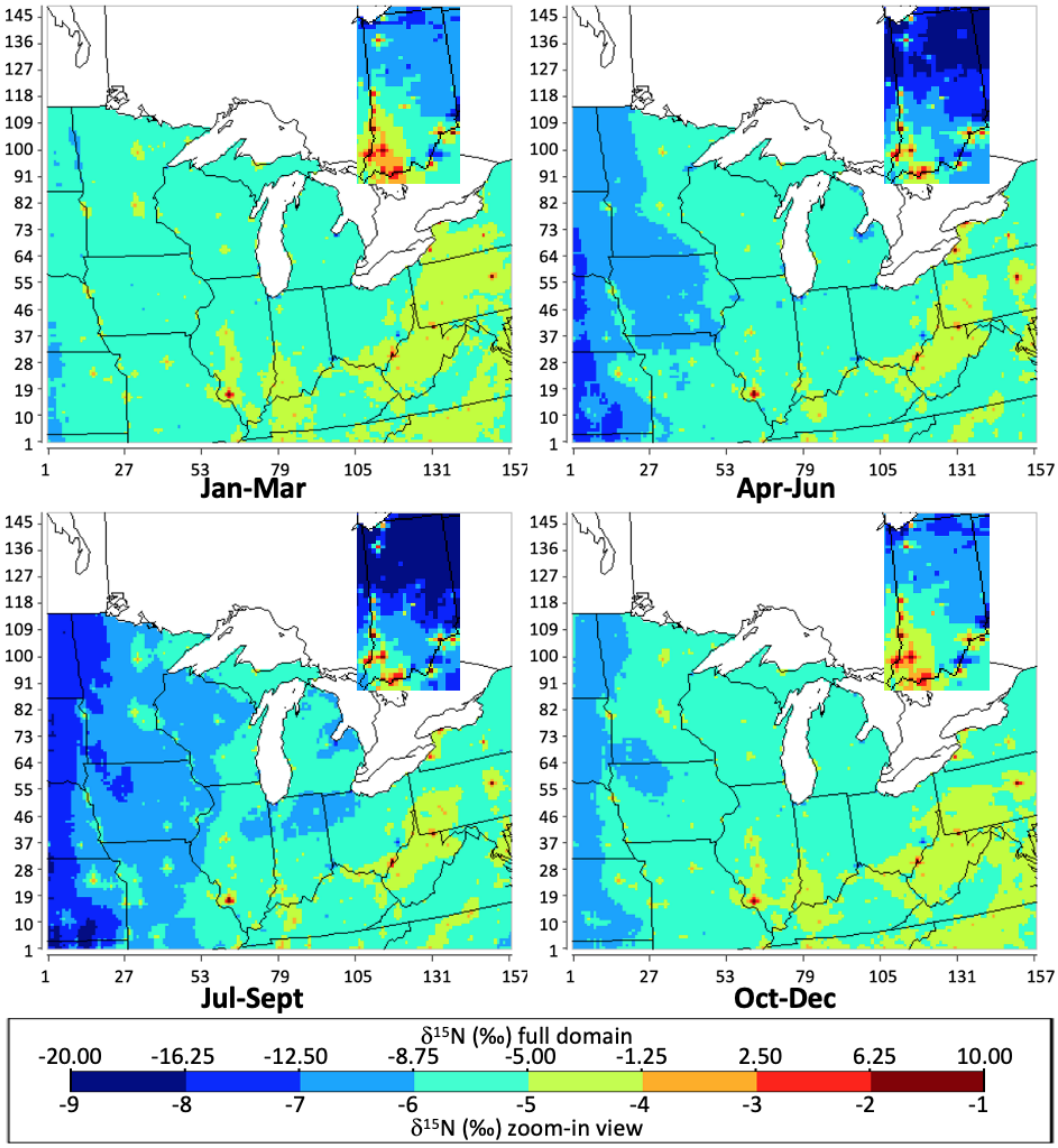

Figure 3.3.2: The geographical distribution of the $\delta^{15}N$ value of atmospheric NO_x in each season (Winter: Jan-Mar; Spring: Apr-Jun; Summer: Jul-Sep; Fall: Oct-Dec) in per mil (‰) throughout the Midwest (with zoom-in view focusing on Indiana) simulated by CMAQ, based on NEI-2002 and 2016 meteorology.

We next examine the temporal heterogeneity of atmospheric $\delta^{15}N(NO_x)$ under the "with transport" scenario over the domain and interpret them in terms of changes if the propagation of NO_x emission as a function of time. The predicted seasonal average $\delta^{15}N(NO_x)$ in the Midwest

shows significant variations (Fig. 3.4). On an annual basis, the $\delta^{15}N$ values of NO_x range from -19.2‰ to 11.6‰, with the annual average over the Midwest domain of -6.10‰, under the "with transport" scenario. Compared with the seasonal $\delta^{15}N(NO_x)$ under the "no transport" scenario (Fang & Michalski, 2020), the $\delta^{15}N(NO_x)$ under the "with transport" scenario has a similar overall average while narrower range, due to the transport and mixing of the air mass driven by the atmospheric processes. This could be clearly shown on the map, of which the color scheme is smoother, comparing with the seasonal $\delta^{15}N(NO_x)$ under the "no transport" scenario (Fig. B.3). The maps for different seasons show the obvious changes in $\delta^{15}N$ values over western regions of the Midwest, from -8.75 ~ -5‰ in Oct-Mar to -16.25 ~ -12.5‰ in Apr-Oct.

In addition to the variability of the NO_x emission source, which has been discussed in depth in the previous companion paper (Fang & Michalski, 2020), the significant temporal variation in the $\delta^{15}N$ value of atmospheric NO_x during different seasons is controlled by the transport and mixing of the air mass, under the different meteorology conditions that vary by season. The PBL height is an effective indicator showing whether the pollutant is under the synoptic condition, which is favorable for the disperse, mixing, and transport after being emitted into the atmosphere (Oke, 2002; Shu et al., 2017; Liao et al., 2018; Miao et al., 2019). In order to qualitatively analyze the changes in $\delta^{15}N$ values driven by atmospheric processes, the difference between the $\delta^{15}N$ value of atmospheric NO_x under the "with transport" scenario and "no transport" scenario ($\Delta\delta^{15}N_{transport}$) on the seasonal basis were shown (Fig. 3.5). The seasonal $\Delta\delta^{15}N_{transport}$ values range from -21.95‰ to 31.22‰, with an average of 4.93‰. The overall pattern of the $\Delta\delta^{15}N_{transport}$ values shows that after the NO_x being emitted into the atmosphere, it became isotopically heavier over the majority of the grids within the domain, and isotopically lighter over the grids that contain big cities, major highways, and power plants. This could be explained by the transport and disperse of biogenic emission and anthropogenic emission to the surrounding areas. Among the grids located in rural areas, where the biogenic emission dominates the NO_x budget, the $\delta^{15}N$ values increases from around -30‰ to around -10‰, due to transport and disperse of anthropogenic emission with relatively high emission rates from surrounding cities, highways, or power plants, which brings the isotopically heavier NO_x into the grids. On the other hand, among the grids located in urban areas, highways, or power plants, where anthropogenic emission dominates the NO_x budget, the changes in $\delta^{15}N$ values decrease is much less obvious, showing the $\Delta\delta^{15}N_{transport}$ values ranges between -5‰ and +5‰. This could be explained by the relatively high rates of anthropogenic

emission. Thus, the effects of the transport and disperse of biogenic emissions from the surrounding rural area are minimal.

Comparing the distributions of the difference in $\delta^{15}N$ values (Fig. 3.5) with the corresponding PBL height (Fig. B.4) among the maps of each season, the effects of PBL height on the propagation of the air mass are clearly shown. The PBL height changes significantly among each season within the geographic domain, especially over Minnesota, Wisconsin, and Iowa (Fig. B.4). The PBL height over these area increases from less than 250 meters above the ground level to more than 625 meters above the ground level, during spring (Apr-Jun) and summer (Jul-Sep), which creates a more favorable synoptic condition for the disperse, mixing, and transport of the pollutant after being emitted into the atmosphere. As a result, the difference in $\delta^{15}N$ values shifts to higher values, showing the stronger effect of atmospheric processes during spring and summer. The positive correlation between PBL height and propagation of air mass, indicated by the evolution of atmospheric $\delta^{15}N(NO_x)$ in this study, agrees well with the corresponding measurement in megacities in China from the previous studies (Shu et al., 2017; Liu et al., 2018; Liao et al., 2018).

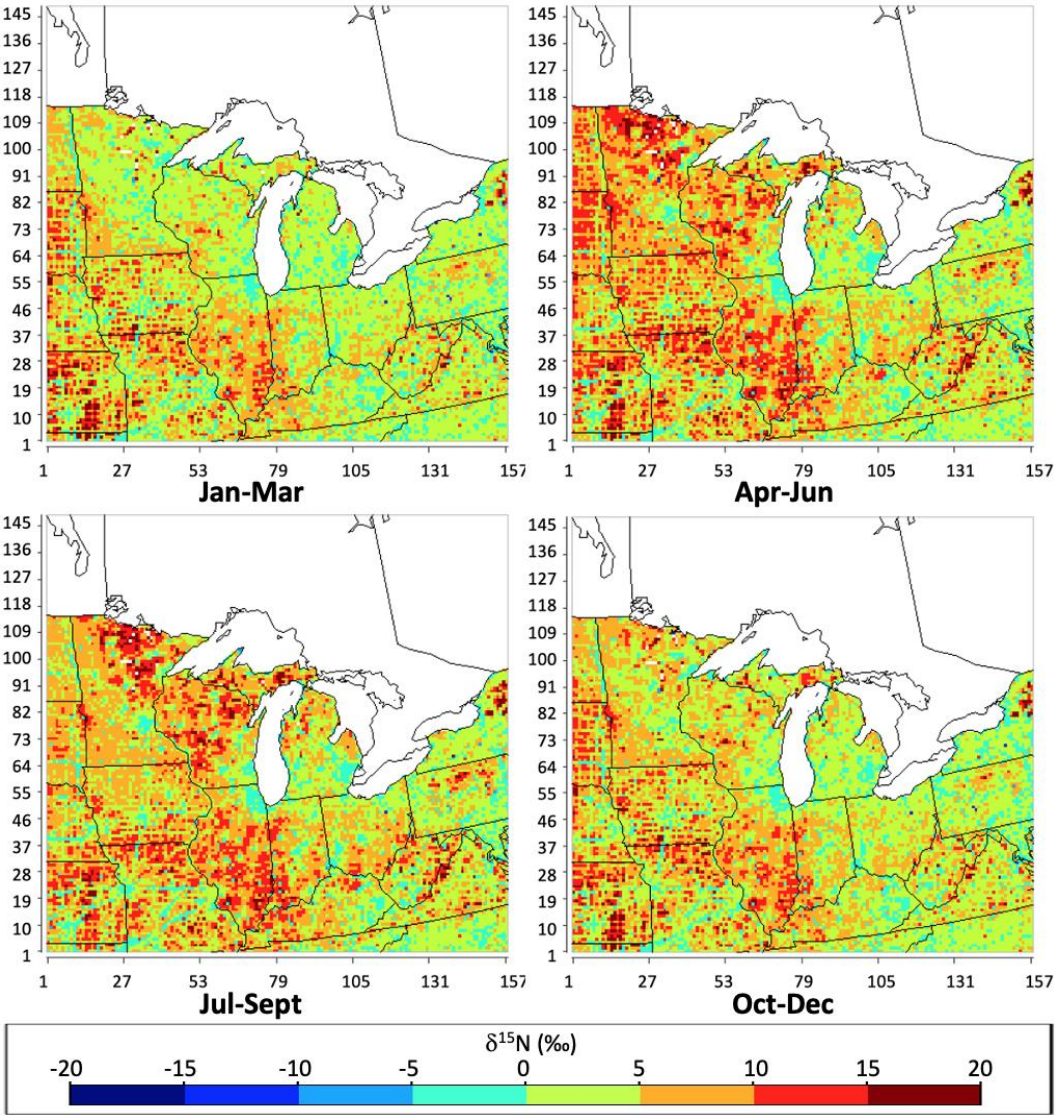

Figure 3.3.3: The difference between the $\delta^{15}N$ (‰) value of atmospheric NO_x under the "with transport" scenario and "no transport" scenario ($\Delta\delta^{15}N_{transport}$) during each season (Winter: Jan-Mar; Spring: Apr-Jun; Summer: Jul-Sep; Fall: Oct-Dec), throughout the Midwest simulated by CMAQ, based on NEI-2002 and 2016 meteorology.

3.3.3 Different meteorology conditions

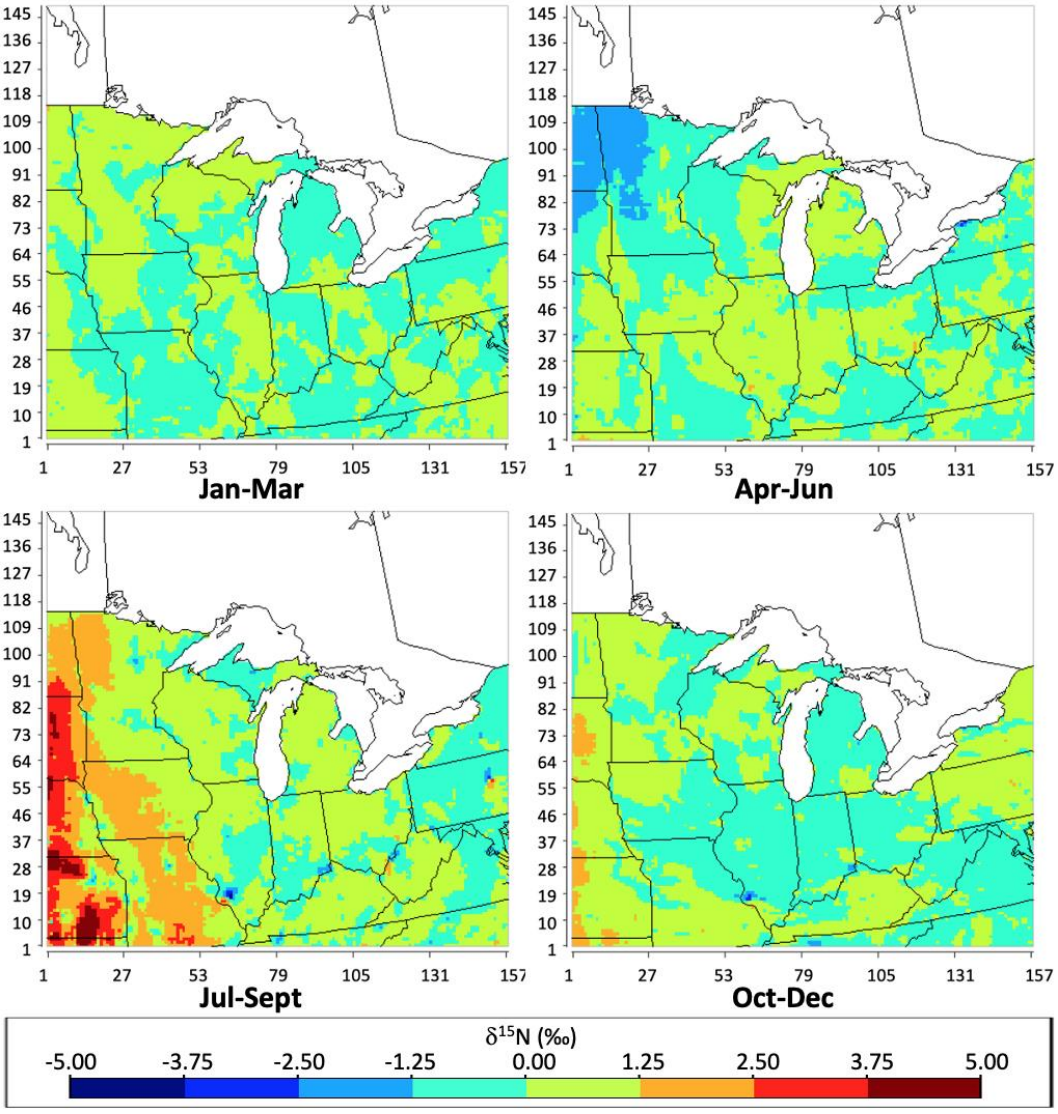

Figure 3.3.4: The geographical distribution of the difference between CMAQ simulated $\delta^{15}N$ value of atmospheric NO_x based on 2002 meteorology and 2016 meteorology in each season (Winter: Jan-Mar; Spring: Apr-Jun; Summer: Jul-Sep; Fall: Oct-Dec) in per mil (‰) throughout the Midwest.

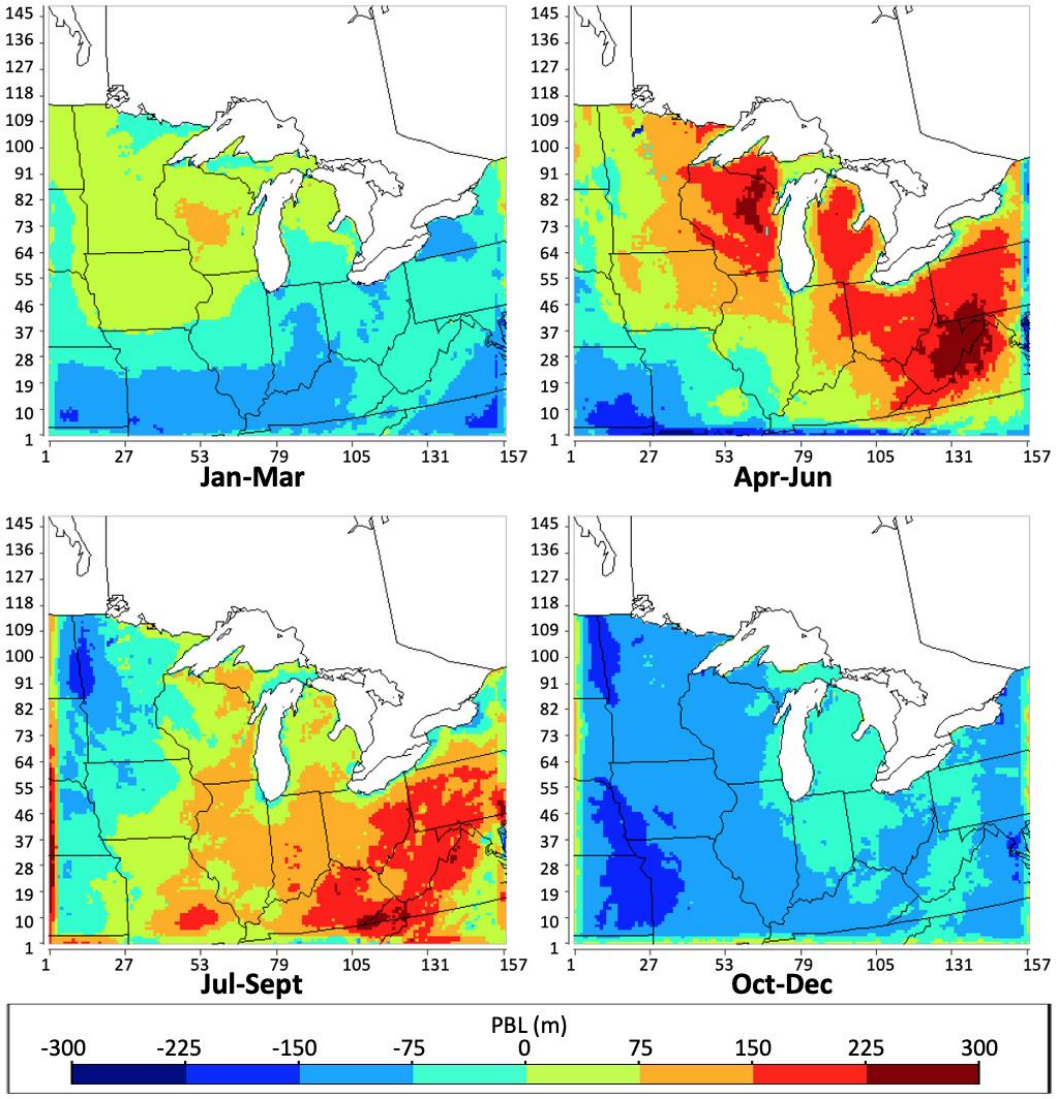

Figure 3.3.5: The geographical distribution of the difference between planetary boundary layer (PBL) height in meters based on 2002 meteorology and 2016 meteorology during each season (Winter: Jan-Mar; Spring: Apr-Jun; Summer: Jul-Sep; Fall: Oct-Dec) of 2016 throughout the Midwest.

The atmospheric $\delta^{15}N(NO_x)$ simulated based on different meteorology input dataset varies. In order to compare the spatial heterogeneity of the atmospheric $\delta^{15}N(NO_x)$ under different meteorology conditions, the same analysis was done on the simulation using 2002 meteorology (Fig. B.6). Overall, the simulated atmospheric NO_x under 2002 meteorology is isotopically heavier than under 2016 meteorology, especially in the western part of the domain during summer (Fig. 3.6). The dynamics of PBL height potentially cause the variation in the level of disperse, mixing, and transport of NO_x emission. Due to the significantly higher level of PBL during spring and summer (Fig. 3.7) comparing to the seasonal PBL height during 2016, the disperse, mixing, and transport of anthropogenic NO_x emission with higher $\delta^{15}N$ values alters the atmospheric $\delta^{15}N(NO_x)$ over the rural area further, under 2002 meteorology.

3.3.4 Different version of emission inventories

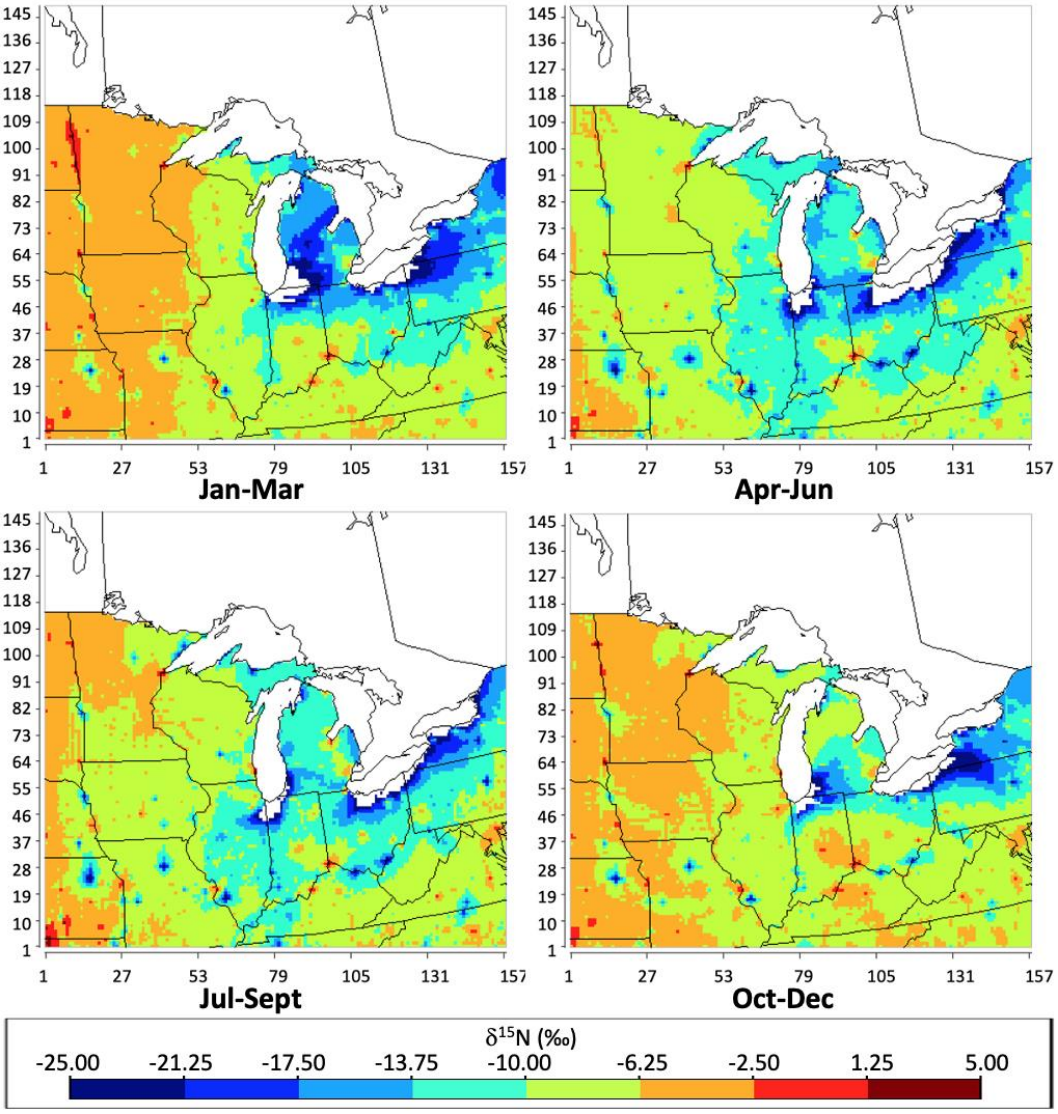

Figure 3.3.6: The geographical distribution of the difference between CMAQ simulated $\delta^{15}N$ value of atmospheric NO_x based on NEI-2016 and NEI-2002 in each season (Winter: Jan-Mar; Spring: Apr-Jun; Summer: Jul-Sep; Fall: Oct-Dec) in per mil (‰) throughout the Midwest.

There was a dramatic difference in the atmospheric $\delta^{15}N(NO_x)$ simulated depending on which NEI emission dataset was used. In order to compare the spatial heterogeneity of the atmospheric $\delta^{15}N(NO_x)$ generating from different NO_x emission budget, the same analysis was done on the simulation using the emission input dataset prepared from the 2016 version of NEI (Fig. B.7). In general, the simulated atmospheric NO_x based on 2016 NEI is significantly isotopically lighter than based on 2002 NEI, especially in the central and eastern parts of the domain (Fig. 3.8). According to Fang & Michalski (2020), the fraction of NO_x emission from the anthropogenic source in NEI-2016 was lower than in NEI-2002 for most of the grids within the domain. Therefore, the atmospheric $\delta^{15}N(NO_x)$ based on 2016 NEI was lower. According to US Energy Information Administration (2017b), from 2002 to 2016, 53 Giga Watts coal-fired and 54 Giga Watts natural gas EGU retired in the US. The EGU dominates the NO_x emission at the grids where it is located, accounts for up to 90% of the total NO_x emission (Fang & Michalski, 2020). Given the $\delta^{15}N$ value of the NO_x emitted from coal-fired EGU is +15‰ (Table 3.1), the $\delta^{15}N$ values of the atmospheric NO_x over the grids that contain the abandoned coal-fired EGU change dramatically during the period between 2002 and 2016. A similar pattern occurs at the grids that contain the EGU, which uses both coal and natural gas as its energy source ($\delta^{15}N$ = -0.75‰). As a result, the number of "hotspots" with high $\delta^{15}N$ values in 2016 is much less than in 2002. While, the change in $\delta^{15}N$ values of the atmospheric NO_x over the grids that contain the abandoned natural gas EGU is not that obvious under the scenario of "with transport" from 2002 to 2016, since the $\delta^{15}N$ value of the NO_x emitted from natural gas EGU is -16.5‰ (Table 3.1), which is similar to the $\delta^{15}N$ values at the surrounding grids after the mixture of NO_x emission from biogenic source and on-road vehicles. Besides this, the implementation of NO_x emission control technologies (SCR, SCNR, LNB, OFA) decreases the $\delta^{15}N$ of the NO_x emission from power plants and vehicles, thus decrease the atmospheric $\delta^{15}N(NO_x)$.

3.3.5 The role of deposition

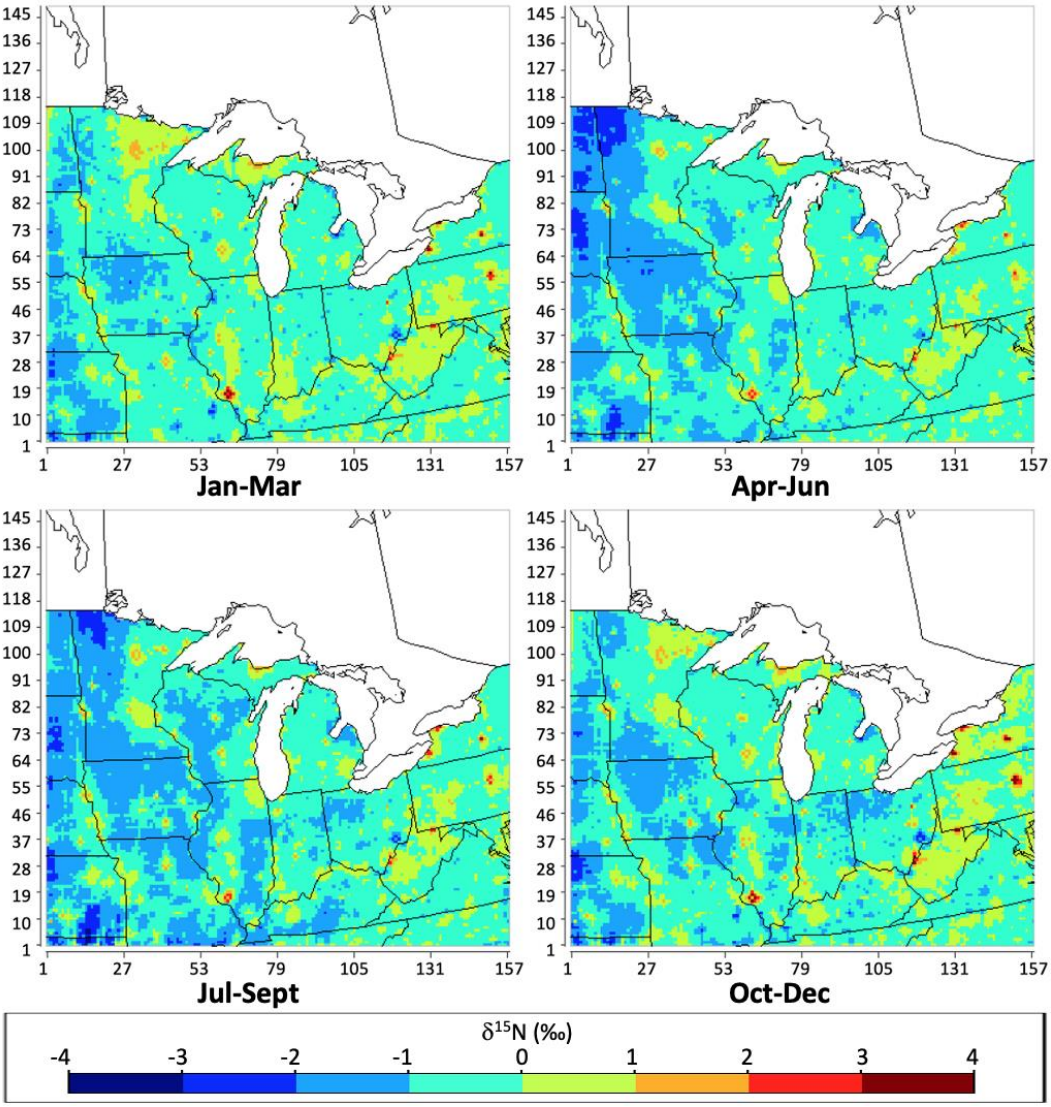

Figure 3.3.7: The difference between the $\delta^{15}N$ (‰) value of atmospheric NO_x under the "amplified deposition" scenario and "default deposition" scenario ($\Delta\delta^{15}N_{deposition}$) during each season (Winter: Jan-Mar; Spring: Apr-Jun; Summer: Jul-Sep; Fall: Oct-Dec), throughout the Midwest simulated by CMAQ, based on NEI-2002 and 2016 meteorology.

The deposition alters the $\delta^{15}N$ of atmospheric NO_x. In order to compare the spatial heterogeneity of the atmospheric $\delta^{15}N(NO_x)$ with different settings of NO_x deposition rate, the same analysis was done on the simulation using the amplified dry and wet deposition rates (Fig. B.8). In order to explore the impact of dry and wet deposition on the $\delta^{15}N$ of atmospheric NO_x, the

difference between the $\delta^{15}N$ values of atmospheric NO_x under the "amplified deposition" scenario and "default deposition" scenario ($\Delta\delta^{15}N_{deposition}$) on the seasonal basis were shown (Fig. 3.9). The seasonal $\Delta\delta^{15}N_{deposition}$ values range from -3.67‰ to 5.34‰, with an average of 0.51‰. The overall pattern of the $\Delta\delta^{15}N_{deposition}$ values shows that due to the impact of deposition, the atmospheric NO_x became isotopically lighter over the majority of the grids within the domain, and isotopically heavier over the grids, which contain or surround power plants and big cities. The amplified deposition simulation somehow presents the isotope effects associated with the "pseudo photochemical transformation" of NO_x into NO_y. The complete isotope effect of tropospheric photochemistry will be addressed in Chapter 4~5, which incorporates ^{15}N into the chemical mechanism of CMAQ for the simulation.

3.3.6 The simulation over the nested domain

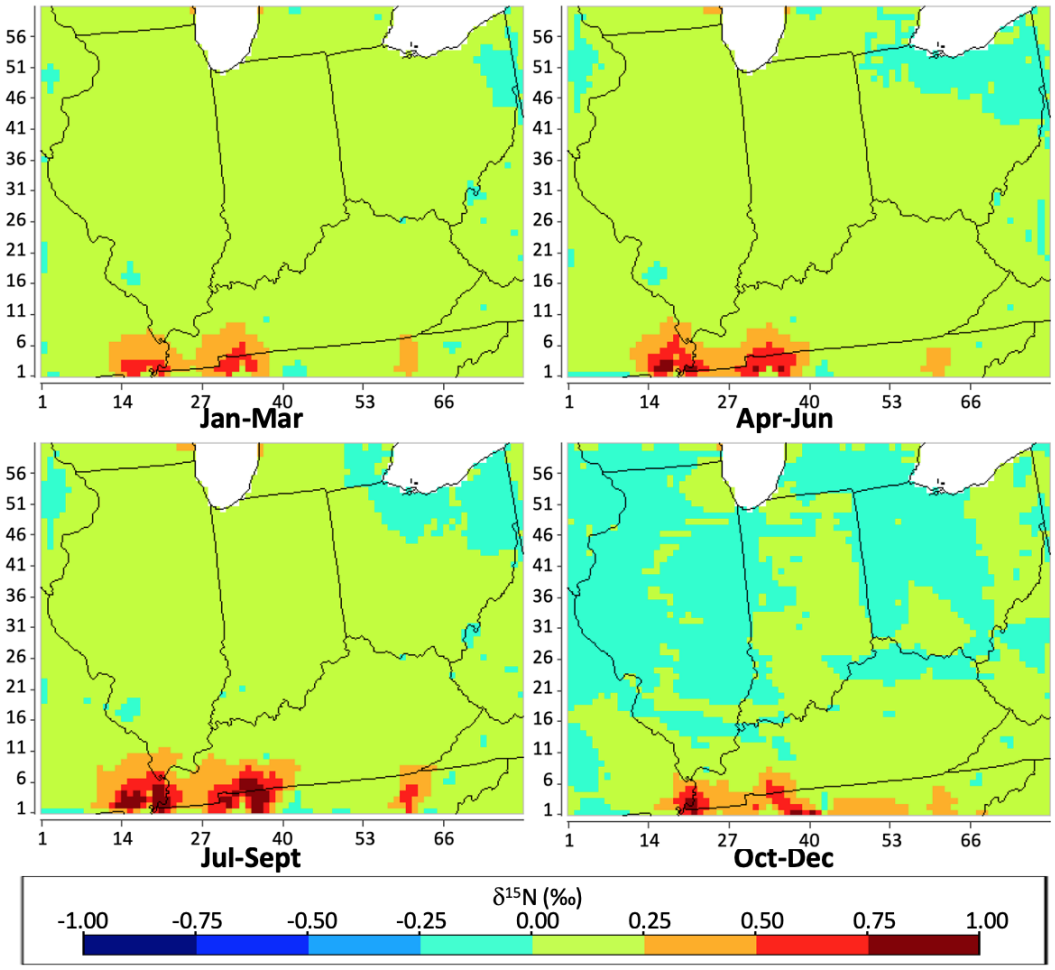

Figure 3.3.8: The geographical distribution of the difference between nested-domain simulation and full-domain simulation of $\delta^{15}N$ value of atmospheric NO_x ($\Delta\delta^{15}N_{nested\text{-}full}$) in each season (Winter: Jan-Mar; Spring: Apr-Jun; Summer: Jul-Sep; Fall: Oct-Dec) in per mil (‰) within IN, IL, OH, and KY, based on NEI-2002 and 2016 meteorology.

We next examine the temporal heterogeneity of difference in atmospheric $\delta^{15}N(NO_x)$ between nested-domain simulation and full-domain simulation ($\Delta\delta^{15}N_{nested\text{-}full}$), to explore the potential bias due to the motion of the air mass across the boundary of the geographic domain of the study (Fig. 3.10). The nested domain covers the states of Indiana, Illinois, Ohio, and Kentucky, where the measurements of $\delta^{15}N$ values at NADP sites are available. The predicted $\delta^{15}N$ of atmospheric NO_x over the nested domain shows a similar overall pattern as the $\delta^{15}N$ within the same domain from

the full-domain simulation, except over the southern border of the domain (Fig. B.9). In order to qualitatively analyze the effects from the initial boundary condition, the $\delta^{15}N$ of atmospheric NO_x within IN, IL, OH, and KY was extracted from the full-domain simulation (Fig. 3.4) and compare with the nested-domain simulation within the same region (Fig. 3.10). The $\Delta\delta^{15}N_{nested\text{-}full}$ values ranged between -0.25‰ and +0.25‰ over most of the grids within the nested domain, showing the difference between nested-domain simulation and full-domain simulation of $\delta^{15}N$ values are trivial. However, near the southern border of the nested domain, the obvious $\Delta\delta^{15}N_{nested\text{-}full}$ values closed to +0.75‰ during fall and winter, closed to +1.00‰ during spring and summer occur, which indicate the atmospheric NO_x from the nested-domain simulation is isotopically heavier. The values of $\Delta\delta^{15}N_{nested\text{-}full}$ become obvious near the southern border, which indicates the dilution of NO_x, after it transports out of the domain since the $\delta^{15}N$ on the boundary was set to zero. Unlike the southern border, the northern, western, and eastern border of the nested domain, located sufficient distance apart from the boundary of the full domain. As a result, the $\Delta\delta^{15}N_{nested\text{-}full}$ values are similar over the majority grids within the domain.

3.3.7 Model-observation comparison

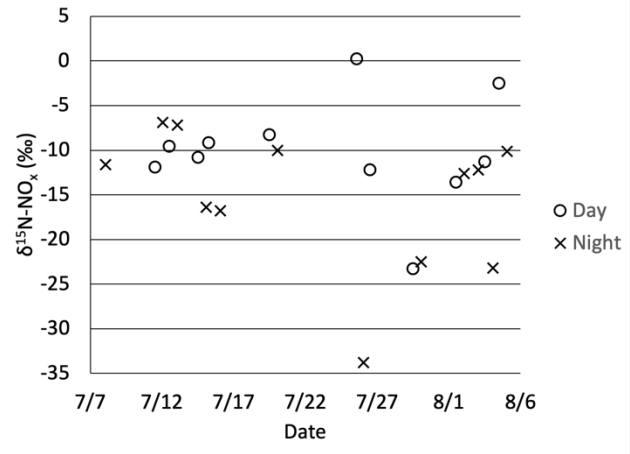

Figure 3.3.9: The $\delta^{15}N(NO_x)$ values measured at West Lafayette, IN between July 9 and August 5, 2016, from 8 am to 4 pm during the daytime (○), and from 9:30 pm to 5:30 am during the nighttime (×)

In order to evaluate the CMAQ simulation of atmospheric $\delta^{15}N(NO_x)$, several existing datasets of measurements were utilized to compare with the simulations. As the only direct

measurements of $\delta^{15}N(NO_x)$ within the domain, NO_x samples collected between July 8 and August 5, 2016 (Fig. 3.11; Walters, Fang, & Michalski, 2018) was first used for the validation of the CMAQ simulation. 30 NO_x samples were collected from 8 am to 4 pm during the daytime, and from 9:30 pm to 5:30 am during the nighttime in West Lafayette, IN, an NADP (National Atmospheric Deposition Program) site in the northwest part of Indiana and home to Purdue University. The measured $\delta^{15}N(NO_x)$ ranged from -23.3 to 0.2‰ for the daytime samples and -33.8 to -6.9‰ for the nighttime samples.

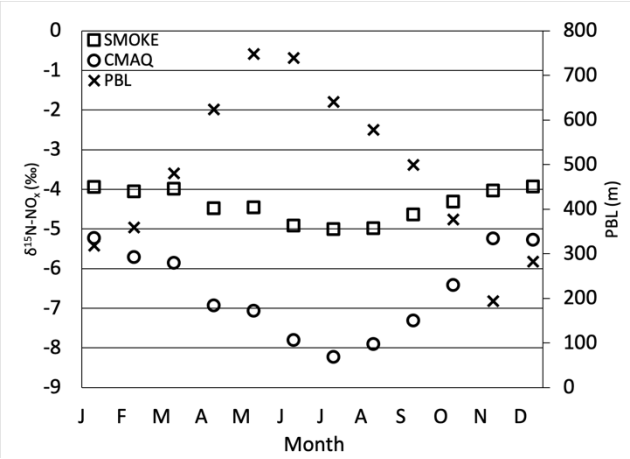

Figure 3.3.10: The monthly $\delta^{15}N$ values of total NO_x emission simulated by SMOKE (□) based on NEI-2002, the monthly $\delta^{15}N$ values of atmospheric NO_x simulated by CMAQ (○) based on NEI-2002 and 2016 meteorology, the monthly average of PBL height (×, right axis) over the 12-km grid that covers West Lafayette, IN.

The CMAQ simulated $\delta^{15}N$ values of atmospheric NO_x in West Lafayette show more obvious monthly variations and seasonal trend, comparing to the $\delta^{15}N$ values of NO_x emission (Fig. 3.12, in circles (○)). The simulation shows that the $\delta^{15}N$ of atmospheric NO_x starts around -5‰ in January, which is about 1‰ lower than $\delta^{15}N$ of NO_x emission (Fig. 3.12, in squares (□)). During winter (Jan-Mar), the $\delta^{15}N$ of atmospheric NO_x decrease slightly, and the difference between the $\delta^{15}N$ of NO_x emission gradually increases. During spring (Apr-June), a more obvious decreasing trend of the $\delta^{15}N$ of atmospheric NO_x occurs, and the difference between the $\delta^{15}N$ of NO_x emission is larger than during winter. The $\delta^{15}N$ value reaches the minimum around -8‰ in July. During summer (Jul-Sept), the $\delta^{15}N$ of atmospheric NO_x starts to increase, and the difference between the $\delta^{15}N$ of NO_x emission decreases. During fall (Oct-Dec), the $\delta^{15}N$ of atmospheric NO_x increases,

and the difference between the $\delta^{15}N$ of NO_x emission decreases, but with a slighter trend than during summer. The $\delta^{15}N$ of atmospheric NO_x ends at -5‰, 1‰ lower than $\delta^{15}N$ of NO_x emission. In addition to the change in the fractions of NO_x emission sources from April to September, which has been discussed in the previous companion paper (Fang & Michalski, 2020), the monthly variations and seasonal trend of the simulated atmospheric $\delta^{15}N(NO_x)$ are mainly driven by the strength of disperse, mixing, and transport of the atmospheric NO_x emitted from different sources, indicated by the PBL height. The PBL height during the period from April to September is 90% higher than during the period from October to March, which is favorable for the mixture of isotopically lighter NO_x from the surrounding area (Fig. 3.12, in crosses (×)). Thus, the $\delta^{15}N$ of atmospheric NO_x diverges further from the $\delta^{15}N$ of NO_x emission.

Table 3.3.1: Performance of $\delta^{15}N(NO_x)$ simulation for West Lafayette, IN

	measurement	NEI 2002	NEI 2016	NEI-2002 +WRF2016	NEI-2002 +WRF2002	NEI-2016 +WRF2016	NEI-2002 +WRF2016 nested
min	-33.800	-12.180	-18.439	-15.824	-14.779	-31.149	-15.858
max	0.200	-3.753	-4.410	-3.360	-3.726	5.458	-3.187
median	-11.250	-4.993	-7.049	-8.094	-8.355	-13.975	-8.108
stdev	8.023	2.168	2.388	2.081	1.881	4.122	2.099

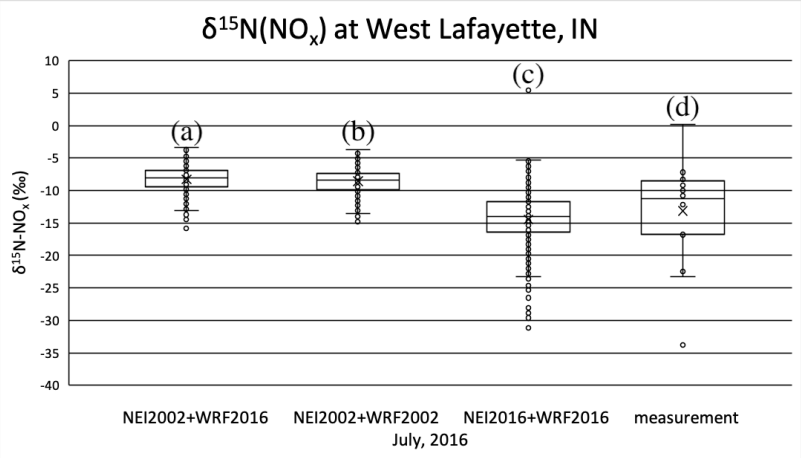

Figure 3.3.11: The distributions of $\delta^{15}N(NO_x)$ values over the 12-km grid that covers West Lafayette, IN from July 8 to August 5, simulated by CMAQ, based on NEI-2002 and 2016 meteorology (a), NEI-2002 and 2002 meteorology (b), NEI-2016 and 2016 meteorology (c), compared with the corresponding measurement (d) taken on July to August in 2016 (box: lower quartile, median, upper quartile; whisker: lower extreme, upper extreme; dots outside the whisker: outliers)

The CMAQ simulation of the $\delta^{15}N$ of atmospheric NO_x under different scenarios of NEI and WRF was compared with the measurement (Walters, Fang, & Michalski, 2018) from July 8 to August 5, 2016 (Fig. 3.13). The $\delta^{15}N$ of atmospheric NO_x simulated based on NEI-2002 and 2016 meteorology ranges from -15.8‰ to -3.4‰, with the medium of -8.1 ± 2.1‰; the $\delta^{15}N$ of atmospheric NO_x simulated based on NEI-2002 and 2002 meteorology ranges from -14.8‰ to -3.7‰, with the medium of -8.4 ± 1.9‰; the $\delta^{15}N$ of atmospheric NO_x simulated based on NEI-2016 and 2016 meteorology ranges from -31.1‰ to -5.5‰, with the medium of -14.0 ± 4.1‰. The $\delta^{15}N$ of the corresponding measurement ranges from -33.8‰ to 0.2‰, with the medium of -11.2 ± 8.0‰. In general, the CMAQ simulations of $\delta^{15}N(NO_x)$ under most of the scenarios conducted in this study, except the simulation based on NEI-2016 and 2016 meteorology, perform better than the SMOKE simulation of $\delta^{15}N(NO_x)$, which only take the variability of NO_x emission source into account (Table 3.2). On the other hand, the simulation based on NEI-2016 and 2016 meteorology capture the isotopically light NO_x better than the simulations under the other scenarios of emission and meteorology input datasets.

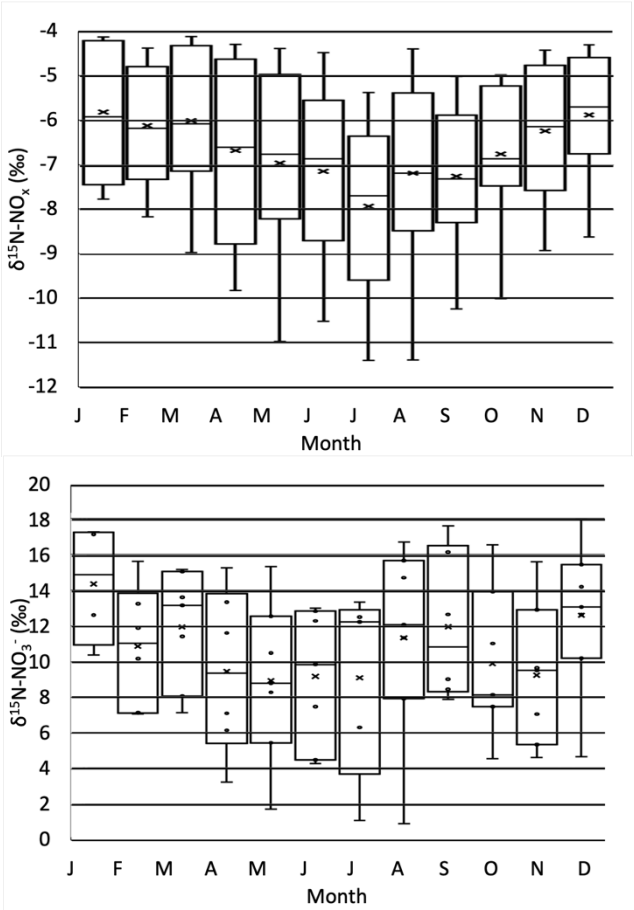

Figure 3.3.12: The CMAQ predicted $\delta^{15}N$ value of atmospheric NO_x at NADP sites within IN, IL, OH, and KY (top) using NEI-2002 and 2002 meteorology compared to the measured $\delta^{15}N$ of rain NO_3^- (bottom) from prior studies.

Finally, we compared the CMAQ predicted $\delta^{15}N(NO_x)$, under the scenario of NEI-2002+WRF2002 at NADP sites within Indiana, Illinois, Ohio, and Kentucky (Table B.3) with the measurements of $\delta^{15}N(NO_3^-)$ from 2001 to 2003. The $\delta^{15}N$ values of atmospheric NO_x simulated by CMAQ at these sites show obvious monthly variations and seasonal trends (Fig. 3.14, top). The monthly boxes are the 1st and 3rd quantiles of the simulated monthly $\delta^{15}N$ of atmospheric NO_x at the NADP sites. The whiskers represent the minimum and maximum values without outliers. There is a wide range of $\delta^{15}N(NO_x)$ values within each month, with a minimum during January (-7.8~ -4.1‰) and a maximum during August (-11.4~-4.4‰). The seasonal trend shows low $\delta^{15}N(NO_x)$ during summer, with the median around -7.4‰, and high $\delta^{15}N(NO_x)$ during winter, with the median around -6.0‰.

Comparing with the CMAQ simulation, the measurements of $\delta^{15}N$ values of NO_3^- at NADP sites from prior studies (Mase, 2010; Riha, 2013) shows the similar monthly variations and seasonal trend (Fig. 3.14, bottom). There is a wide range of $\delta^{15}N(NO_3^-)$ values within each month, with a minimum during January (10.4~17.2‰) and a maximum during August (1.0~16.7‰). The seasonal trend shows low $\delta^{15}N(NO_3^-)$ during spring, with the median around 9.3‰, and high $\delta^{15}N(NO_3^-)$ during winter, with the median around 13.0‰. The measured $\delta^{15}N$ values of NO_3^- has the same seasonal trend as the CMAQ simulated $\delta^{15}N$ values of NO_x. However, the measured $\delta^{15}N$ values of NO_3^- is about 17‰ higher than the CMAQ simulated $\delta^{15}N$ values of NO_x. The difference between CMAQ simulated $\delta^{15}N$ values of NO_x and measured $\delta^{15}N$ values of NO_3^- is caused by the following two factors: a). the mixture of isotopically lighter NO_x from the surrounding area discussed in section 3.2, and b). the net N isotope effect during the conversion of NO_x to NO_3^-, which will be addressed in Chapters 4~5.

3.4 Conclusion

The $\delta^{15}N$ of atmospheric NO_x was simulated by CMAQ, based on the emission input datasets prepared from the previous companion research (Fang & Michalski, 2020) and the meteorology input dataset simulated from WRF and MCIP. $\delta^{15}N$ is an effective tool to track the atmospheric NO_x, in term of its evolution of spatial and temporal composition, altered by atmospheric processes. The simulation indicates that the PBL height is the key driver for the mixture of anthropogenic and natural NO_x emission, which deepens the gap between $\delta^{15}N$ of atmospheric NO_x and NO_x emission. Comparing with the measurements of $\delta^{15}N(NO_3^-)$ from NADP sites within Indiana, Illinois, Ohio, and Kentucky, the simulated $\delta^{15}N$ agreed well with the seasonal trend and monthly variation. The performance of CMAQ simulated $\delta^{15}N(NO_x)$ is better than SMOKE $\delta^{15}N(NO_x)$ from the previous companion research (Fang & Michalski, 2020), due to the consideration of mixing, disperse, and transport of NO_x emission from different sources.

After considering the effects of NO_x emission sources and atmospheric processes, there is still an obvious gap between the simulated $\delta^{15}N(NO_x)$ and the corresponding measurements. Therefore, before adjusting the NO_x emission inventory, the future work is to explore how tropospheric photochemistry alters $\delta^{15}N(NO_x)$ by incorporating ^{15}N into the chemical mechanism of CMAQ and comparing the simulation with the corresponding measurements. With the

validation of our nitrogen isotopes incorporated CMAQ, the NO_x emission inventories could be effectively evaluated and improved.

CHAPTER 4. INRACM: INCORPORATING 15N INTO THE REGIONAL ATMOSPHERIC CHEMISTRY MECHANISM (RACM) FOR ASSESSING THE ROLE PHOTOCHEMISTRY PLAYS IN CONTROLLING THE ISOTOPIC COMPOSITION OF NOX, NOY, AND ATMOSPHERIC NITRATE

The following chapter is a reprint from an article currently in press (Fang, H.; Michalski, G.; Walters, W. W.; and Mase, D. i_NRACM: Incorporating ^{15}N into the Regional Atmospheric Chemistry Mechanism (RACM) for assessing the role photochemistry plays in controlling the isotopic composition of NO_x, NO_y, and atmospheric nitrate. *Geoscientific Model Development*)

4.1 Introduction

Nitrogen oxides are an integral part of atmospheric chemistry, controlling the oxidation state of the troposphere, influencing aerosol formation, altering the pH of rainwater, and facilitating the movement of nitrogen through the N cycle. Nitrogen oxides are classified as NO_x (nitric oxide (NO) + nitrogen dioxide (NO_2)) and NO_y (NO_x + NO_3, N_2O_5 HNO_3, + HNO_4 + HONO + Peroxyacetyl nitrate (PAN) + organic nitrates + any oxidized N compound) (Day et al., 2003; Harrison et al., 1999; Hegglin et al., 2006; Ma et al., 2013). NO_x produces ozone (O_3) through NO_2 photolysis, and NO acts as a catalyst in O_3 production when volatile organic compounds (VOCs) are present. In turn, O_3 photolysis generates OH radicals, which initiates a radical chain reaction involving HO_2 and organic peroxide propagators that result in the oxidation of chemically reduced compounds in the troposphere making them more soluble (Finlayson-Pitts and Pitts, 2000; Seinfeld and Pandis, 1998). Thus, NO_x facilitates the cleansing of the atmosphere through the production of O_3 and OH_x (OH + HO_2), which together define the troposphere's oxidation state (Bloss et al., 2005; Lelieveld et al., 2008; Prinn, 2003). These oxidants play an important role in the formation of particulate matter (PM) (Bauer et al., 2007; Pye et al., 2010), forming secondary organic aerosols (SOA) via VOC oxidation (Hoyle et al., 2011; Shrivastava et al., 2017). They also generate secondary inorganic PM through NO_x, sulfur oxides (SO_x), and ammonia (NH_3) neutralization, which leads to ammonium nitrate (NH_4NO_3) and ammonium sulfate ($(NH_4)_2SO_4$) production (Cao et al., 2017; Pan et al., 2018; Pusede et al., 2016). The production of PM has important consequences for air quality aerosols (Andreae and Crutzen, 1997), human health (Bruningfann and Kaneene, 1993; Hall et al., 1992), and radiative forcing (Charlson et al., 1992;

Chen et al., 2007). Termination reactions in NO_y cycling produce HNO_3, and facilitates the production of sulfuric acid (H_2SO_4), two strong acids that decrease the pH of rain, known colloquially as acid rain and impact aerosol pH, both of which triggers a number of negative impacts on the environment (Brimblecombe et al., 2007; Lajtha and Jones, 2013). When NO_y is deposited to the surface by wet and dry deposition, it transfers bioavailable N to ecosystems that may be bereft of or saturated with, bioavailable N. This process can shift the balance of both terrestrial and aquatic ecosystems and impact the goods and services that those ecosystems can normally deliver (Du et al., 2019; E. M. Elliott et al., 2019; Fowler et al., 2013). Thus, understanding NO_y sources and their chemistry is important for an array of scientific disciplines and evaluating their social, economic, and cultural impact on the environment.

Despite this importance, there are numerous knowledge gaps in the understanding of the cycling of NO_y in the atmosphere. The NO_x emission budget is still poorly constrained. Most emission inventories rely on fixed emission factors for some sources that may, in fact, be variable. For example, power plant NO_x emissions are based on the assumed efficiency of catalytic converters that may not be accurate (Srivastava et al., 2005; Felix et al., 2012). Soil NO emissions are highly dependent on soil moisture, redox conditions, fertilizer application rates, type, and timing making them challenging to constrain (Shepherd, 1991; Galloway et al., 2004; Hudman et al., 2012; Houlton et al., 2013; Pilegaard, 2013). There are several unresolved issues with the heterogeneous uptake coefficients of N_2O_5 (Brown et al., 2001; Brown et al., 2006; Chang et al., 2011) and the formation of organic nitrates in urban forests (Lee et al., 2016; Romer et al., 2016; Kastler and Ballschmiter, 1998). The relative importance and mechanism of HONO formation versus HONO emissions are also hotly debated. Likewise, reactions of NO_y in the aqueous phase and mixed aerosols are not fully understood. Chemical transport models (CTMs) do not accurately predict aerosol nitrate concentrations or other NO_y mixing ratios (Spak and Holloway, 2009; Zhang et al., 2009). Therefore, it is important that these uncertainties in NO_y cycling be resolved if we aim to have accurate air quality forecasts and accurate chemistry-climate models that use CTMs.

It has been suggested that stable N isotopes can provide clues as to the origin of NO_x (Elliott et al., 2009; Felix and Elliott, 2014; Walters et al., 2015b) and the oxidation pathways that transform in NO_y (Walters and Michalski, 2015; 2016). Isotopic measurements of NO_y compounds show a wide range of $\delta^{15}N$ values (Eq. (4.1)), which has been suggested to indicate variability in

NO_x emission sources, chemical processing, and/or a combination of these effects. $\delta^{15}N$ is defined by the relative difference between the $^{15}N/^{14}N$ ratio in a NO_y compound and the ratio in air N_2 (the arbitrary reference compound) and is typically reported in parts per thousand e.g. per mil (‰)

$$\delta^{15}N_{NOy}\,(‰) = (({}^{15}NO_y/{}^{14}NO_y) / ({}^{15}N_2/{}^{14}N_2) - 1)*1000 \qquad \text{Eq. (4.1)}$$

A number of studies have measured the $\delta^{15}N$ values of NO_x collected from NO_x sources such as power plants (Felix et al., 2012), automobiles (Walters et al., 2015a), biomass burning (Fibiger and Hastings, 2016), and non-road sources (Felix and Elliott, 2014).

Many studies have measured the $\delta^{15}N$ values of various NO_y compounds collected from the troposphere. Most of the NO_y $\delta^{15}N$ data is for nitrate that has been collected on filters ($PM_{2.5}$, PM_{10}, TSP) (Moore, 1977; Savard et al., 2017), as the dissolved NO_3^- anion in rain (Heaton, 1987; Hastings et al., 2003; Felix et al., 2015; Yu & Elliott, 2017), or as gas-phase HNO_3 (Elliott et al., 2009; Savard et al., 2017). The range of tropospheric NO_y $\delta^{15}N$ values span -50 to +15‰ but the average is ~0‰. Two hypotheses have been offered to explain these ranges: Source and Photochemistry. The source hypothesis (Elliott et al., 2007; Hastings et al., 2013) suggesting that the tropospheric NO_y $\delta^{15}N$ value range reflects the spatial and temporal mixing of NO_x sources with different $\delta^{15}N$ values that are then converted into NO_y. The photochemistry hypothesis (Freyer, 1978; Freyer et al., 1993; Walters et al., 2018) suggests that the observed NO_y $\delta^{15}N$ variations arise via isotope effects occurring when photochemical cycling partitions N into the myriad of NO_y compounds. These two hypotheses are not mutually exclusive. Indeed, it is likely to be a combination of both processes, but their relative importance likely shifts depending on environmental conditions such as a region's NO_x source diversity, plume versus dispersed chemistry, photolysis intensity, and oxidant load. In turn, the $\delta^{15}N$ data might be a new key to reconciling some of the current uncertainties in NO_y sources and chemistry, if it can be properly interpreted.

What has become clear is that the temporal-spatial heterogeneity of NO_x sources and the complex photochemistry of NO_y presents a serious challenge to deciphering the observed NO_y $\delta^{15}N$ values. Except for a few isolated cases, a proper assessment of NO_y $\delta^{15}N$ values will require incorporating isotope effects into 3-D chemical transport models. This will include emission modeling of $^{15}NO_x$, meteorological mixing, factoring in isotope effects during NO_y removal

processes, and developing chemical mechanisms that incorporate ^{15}N compounds and their relative rate constants. Here we take the first step in this endeavor by developing a chemical mechanism (0-D photochemical box model) that explicitly includes $^{15}NO_y$ compounds and the isotope effects that occur during their cycling through photolysis, equilibrium, and kinetic reactions.

4.2 Methods

4.2.1 Chemical and isotopic compounds and reactions included in i_NRACM

The basis of the i_NRACM model is incorporating ^{15}N into the Regional Atmospheric Chemistry Mechanism (RACM) detailed in Stockwell et al. (Stockwell et al., 1997). RACM is an extension of the chemical mechanism used in the Regional Acid Deposition Model (RADM2) (Stockwell et al., 1990), but with updated inorganic and organic chemistry. There are 17 stable inorganic compounds, 4 inorganic intermediates, 32 stable organic compounds, including 4 biogenic organics, and 24 organic intermediates in the RACM mechanism. The RACM mechanism uses 237 chemical reactions, including 23 photolysis reactions (Atkinson, 1990; Atkinson et al., 1992). The rate constants, photolysis cross-sections, and quantum yields for the inorganic compounds were taken from (DeMore et al., 1994). The RACM mechanism aggregates the thousands of VOCs in the atmosphere into 16 anthropogenic and 3 biogenic organic compounds. Part of the aggregation criteria is based on the reactivity of a VOC towards the hydroxyl radical (•OH). Full details on how •OH reacts with alkanes, alkenes, aromatics, and other VOCs, and the aggregation rationale, can be found in Stockwell et al. (1997). The actinic flux model used in RACM was developed by Madronich (1987) and calculates the wavelength-dependent photon flux as a function of solar zenith angle, which is a function of time (hourly), date, latitude, and longitude. Inputs to the model include temperature, water vapor content, pressure, initial gas mixing ratios, and primary pollutant emission rates. Complete details on the RACM mechanism can be found in Stockwell et al. (1997).

Our i_NRACM (isotope N in RACM) mechanism was generated by adding ^{15}N isotopologues for the 2 primaries (NO, NO_2) and the 14 secondary N pollutants found in the original RACM mechanism (Table C.1a). By definition, an isotopologue is a compound with the same chemical formula but a different mass (e.g. NO = 30 amu and ^{15}NO = 31 amu, with N = ^{14}N). This is different from isotopomers, which are isotopic isomers, compounds with the same mass but a different

structure caused by isotopic substitution (e.g. $^{15}NNO_5$ = 109 amu and $N^{15}NO_5$ = 109 amu). Of all the reactive N compounds only N_2O_5 has multiple possible ^{15}N substitutions and 2 isotopologues were defined in the i_NRACM: $^{15}NNO_5$ and $^{15}N^{15}NO_5$. The ^{15}N compounds are numbered (Table C.1a) and subscripted (a, b) in order to maintain a compound numbering scheme that is consistent with that in Stockwell et al. (1997). The non-N compounds found in both RACM and i_NRACM mechanisms have been excluded from Table C.1a for the sake of brevity but can be found in Stockwell et al. (1997). The 16 ^{15}N compounds (Table C.1a) were added to the original RACM FORTRAN code provided by Stockwell by using Z =^{15}N (e.g. ^{15}NO is defined as ZO).

The 96 chemical reactions involving N compounds (Table C.2a-f) were inspected and replicated for ^{15}N based on classification as the reaction being either "N only" or "multiple N" reactions. Single N reactions are those where only one N compounds were found in the products and reactants, for example, NO + O_3 → NO_2+O_2. Multiple N reactions could have multiple N compounds in the reactants, the products, or both. Examples of these possible multiple N reactions are NO_2+NO_3 → N_2O_5, N_2O_5 → NO_2 + NO_3, and NO_3 + NO → NO_2 + NO_2 respectively. For these multiple N reactions, a reaction probability was factored into the isotopologue/isotopomer rate constants (discussed below). For example, the N isotopologue/isotopomer equivalent of the N_2O_5 →NO_2 + NO_3 reaction has two isotopomer reactions: $^{15}NNO_5$ →$^{15}NO_2$ + NO_3 and $^{15}NNO_5$→NO_2 + $^{15}NO_3$. These two isotopologue rate constants (R54a, R54b) are multiplied by a factor of 1/2 to account for this statistical probability. Similar statistical factors were considered when N compounds or intermediates decomposed or reacted to form multiple N products (R52a, R52b, R52c, R52d). All N isotopologue reaction stoichiometry is given in Table C.2a-f.

4.2.2 Isotope effects included in i_NRACM

The main challenge for developing realistic isotopologue chemistry in i_NRACM is quantifying the differences in rate constants caused by isotopic substitution. These isotope effects can be classified into four general types: Equilibrium isotope effects (EIE), kinetic isotope effects (KIE), photo-induced isotope fractionation effects (PHIFE), and vapor pressure isotope effects (VPIE). For this study, the most up-to-date isotope fractionations were used when establishing the framework for modeling their effect associated with NO_x oxidation chemistry. The established framework will easily enable an adjustment of isotope effects as we improve our understanding of isotope fractionation factors.

Urey (1947) and Bigelesien and Mayer (1947) showed that EIEs are driven by the sensitivity of molecular and condensed-phase vibrational frequencies to isotopic substitutions (Bigeleisen and Mayer, 1947; Urey, 1947). Because vibrations are used in the molecular partition function (Q) to calculate equilibrium constants, isotopic substitution results in isotopologues having different equilibrium constants. Urey (1947) defined the reduced partition function ratio for two isotopologues of the same compound as a β value. For example, the reduced partition function ratio of nitric oxide N isotopologues is $Q_{15NO}/Q_{NO} = \beta_{NO}$, with the heavy isotope placed in the numerator by convention. The ratio of two β values is denoted as $\alpha_{\beta 1/\beta 2}$ the isotope fractionation factor. For example, $\alpha_{NO/NO2}$ is the temperature-dependent isotope fractionation factor (EIE) for the NO + $^{15}NO_2$ $\leftrightarrow$ ^{15}NO + NO_2. In this case, at 298K β_{NO} = 1.0669 and β_{NO2} = 1.1064 and $\alpha_{NO/NO2} = \beta_{NO}/\beta_{NO2}$ = 0.9643 (Walters and Michalski, 2015).

A KIE is a relative change in the rate of a unidirectional chemical reaction when one of the atoms of the reactants is substituted with an isotope (Bigeleisen and Wolfsberg, 1958). KIEs are driven by the change in energy required to proceed over the reaction barrier (transition state) as well as changes in the probability of quantum mechanical tunneling (Wolfsberg et al., 2010). This generally results in a lighter isotopologue reacting faster than a heavier isotopologue. Much of the early research on KIEs were investigations of the KIE in reactions containing hydrogen isotopes and these studies usually defined a KIE = $k_L/k_H = \alpha_{L/H}$, where the k's are the rate constants for the light and heavy isotopologues. This is the inverse of the definition of α usually used in research dealing with EIE, VPIE, PHIFE, and this inversion can lead to confusion. In this paper, in order to maintain consistency between the α values for EIE, KIE, VPIE, and PHIFE, α will be defined as heavy/light for all four effects.

The α values for EIE and KIE can be determined using a number of approaches. The α values for EIE can be calculated if molecular constants (e.g. harmonic frequencies and anharmonicity constants) of the isotopologue pair are known. Accurate molecular constants are difficult to accurately measure for large molecules and as a result, they primarily exist only for diatomic and triatomic isotopologues (Richet et al., 1977). The only experimental EIE values for ^{15}N isotopologues of NO_y are for the EIE between NO and NO_2 (Sharma et al., 1970; Walters et al., 2016). To determine the EIE in other NO_y compounds we must rely on quantum chemistry computation methods to estimate the molecular constants and anharmonicity constants. Recent

works utilizing these methods have estimated the EIE for most non-organic NO_y compounds (Walters and Michalski, 2015). For KIE, in addition to molecular constants, the transition state vibrational frequencies are also needed. The only ^{15}N KIE calculation to date for an NO_y compound is for the KIE for the NO + O_3 reaction (Walters and Michalski, 2016).

These EIE and KIE values have been incorporated in i_NRACM in this study Table C.2a-c. If there is no isotope effect associated with any of the NO_y reactions, then α is set equal to 1. The ^{15}N isotopologue rate constant for any reaction is then $\alpha^{14}k$ where ^{14}k is the rate constant for any ^{14}N reaction in RACM and these are given in Table C.2a-f. It is useful to define the magnitude of EIE and KIE in the same per mil (‰) notation used to quantify a $\delta^{15}N$ values by defining an enrichment factor ε(‰) = (α-1)1000. For example, in the NO_x isotope exchange equilibrium mentioned above, the $\varepsilon_{NO/NO2}$ = -35.7‰. This means that the $^{15}NO/NO$ ratio would be 35.7‰ smaller than the $^{15}NO_2/NO_2$ ratio if the isotopes in two gases were statistically distributed (Table C.2b).

PHIFE is the relative change in photolysis rates of isotopologues due to the substitution of a heavier isotope (Yung and Miller, 1997). In the atmospheric N cycle, NO_2, NO_3, N_2O_5, and HONO readily undergo photolysis at wavelengths of light that penetrate into the troposphere. The PHIFE can be estimated using a simple zero-point energy shift model (ΔZPE). In this approximation, the absorption spectra of the heavier isotopologue are generated by applying a uniform blue shift (equal to ΔZPE) to the measured spectral absorbance of the light (major) isotopologue (Blake et al., 2003; Liang et al., 2004; Miller and Yung, 2000). This results in isotopic fractionation because the wavelength (λ) dependent photolysis rate constant (J(λ)) is dependent on the convolution of the absorption cross-section ($\sigma(\lambda)$), actinic flux (F(λ)), and quantum yield ($\phi(\lambda)$) (Eq. (4.2)):

$$^{x}J(\lambda) = {}^{x}\sigma(\lambda)F(\lambda)\phi(\lambda) \qquad \text{Eq. (4.2)}$$

The overall photolysis rate constant (^{z}J) can be calculated by integrating σ, F, and ϕ over a range of wavelengths that can cause dissociation (λ_1 and λ_2):

$$^{x}J = \int_{\lambda_1}^{\lambda_2} {}^{x}\sigma(\lambda)F(\lambda)\phi(\lambda)d\lambda \qquad \text{Eq. (4.3)}$$

The N isotopologue fractionation (α) resulting from photolysis (of NO_2 isotopologues) is calculated by (Eq. (4.4)).

$$\alpha_{47/46} = \frac{^{47}J}{^{46}J} \qquad \text{Eq. (4.4)}$$

It is important to note that there are limitations in the ΔZPE-shift model (Blake et al., 2003; Liang et al., 2004; Miller and Yung, 2000). These include the failure to account for changes in shape and intensity of absorption spectra upon isotopic substitution and the same quantum yield (as a function of wavelength) is assumed for all isotopologues. Despite these limitations, this approach should still give a rough estimate of photolytic fractionation until experimentally determined PHIFE's become available (Blake et al., 2003; Liang et al., 2004; Miller and Yung, 2000).

Isotopologues partition differently between phases giving rise to the VPIE. This is most notable in gas-liquid systems (Van Hook et al., 2001), but also can occur in gas-solid equilibrium. Both of these may ultimately be important for understanding $\delta^{15}N$ variability in NO_y compounds. For example, solid-gas VPIE may be relevant for the $HNO_{3(g)} + NH_{3(g)} \leftrightarrow NH_4NO_{3(s)}$ reaction, whose temperature-dependent equilibrium can shift dramatically diurnally (Morino et al., 2006) and seasonally (Paulot et al., 2016). It is likely that this VPIE will result in the particle phase NO_3^- having a different $\delta^{15}N$ value compared to the gas phase HNO_3 (Heaton, 1987). Additionally, possible VPIE occurring during wet and dry deposition, such as $HNO_{3(g)} \rightarrow HNO_{3(aq)}$ may be relevant for $\delta^{15}N$ variations NO_3^- in precipitation (Freyer et al., 1993). Multiphase reactions are not included in RACM since it is only concerned with gas-phase reactions. These effects may be important for accurate $\delta^{15}N$ predictions and should be addressed in more complex models, but this is a limitation in any "gas phase only" photochemical box model. Similarly, NO_y aqueous phase reactions, such as $2NO_2 + H_2O \rightarrow HNO_3 + HNO_2$, are not included in RACM, which may limit i_NRACM's ability to accurately predict the $\delta^{15}N$ values of dissolved NO_3^- in rainfall samples.

4.2.3 Sensitivity analysis: Determining the "reaction relevance" of NO_y isotopologues

The objective of the i_NRACM model is to make predictions about the temporal and spatial variation of $\delta^{15}N$ value in various N compounds caused by EIE, KIE, and PHIFE, and compare

them to observations. Currently, the $\delta^{15}N$ observations are largely limited to HNO_3, as either particulate or dissolved NO_3^-, but there are a few recent measurements of the $\delta^{15}N$ values of NO_x (Walters et al., 2018) and HONO (Chai and Hastings, 2018). The $\delta^{15}N$ values of organic nitrates and PAN may be made in the not so distant future, but there is no published data to date. Thus, a given isotopologue reaction pair in i_NRACM was considered "relevant" if it significantly changed the $\delta^{15}N$ value (±1‰) of NO_x, HONO, or HNO_3. This relevance was determined by conducting a sensitivity analysis on the PHIFE, KIE, and EIE effects for all N reactions. This was done by arbitrarily setting $\alpha = 0.98$ ($\varepsilon = -20‰$) for one isotopologue reaction and $\alpha = 1.0$ for all others, then running a test case. This test case is a 5-day simulation, beginning at 3 AM on March 1 (2007), and simulates mid-latitude suburban chemistry using the trace gas and meteorology parameters given in Table C.3a-b. This simulation was repeated 96 times until every N containing reaction was tested. For example, NO_x, HONO, or HNO_3 $\delta^{15}N$ values are not sensitive to R51 (Fig. 4.1). The following section discusses which i_NRACM reactions are relevant and the approaches used to determine the appropriate α values for those reactions.

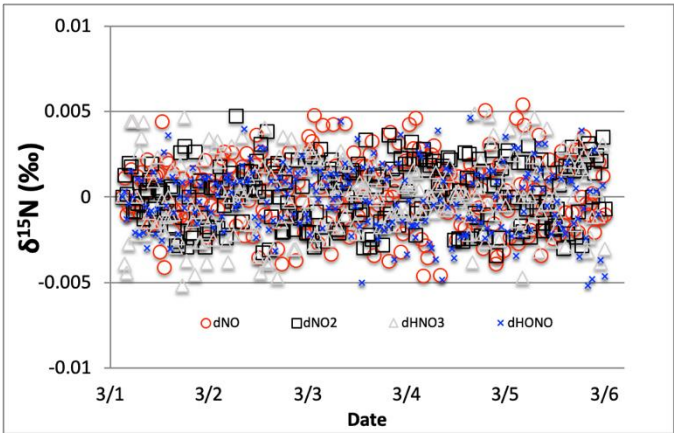

Figure 4.2.1: The time evolution of $\delta^{15}N$ values of NO, NO_2, HONO, and HNO_3, caused by the $NO_3 + NO \rightarrow NO_2 + NO_2$ reaction (R 51, 51_a).

4.2.3.1 PHIFE relevant in the i_NRACM mechanism

Only one of the 6 photolysis reactions involving N compounds was found to be relevant. NO_2 photolysis (R1) had a significant impact on the $\delta^{15}N$ value of NO_x, HONO, and HNO_3 (Fig. 4.2). The initial difference between the $\delta^{15}N$ of NO and NO_2 values is roughly equal to the arbitrarily

set -20‰ enrichment factor. The nature of the diurnal oscillation in $\delta^{15}N$ values on the three relevant NO_y compounds and the dampening effect over time will be discussed in the results section.

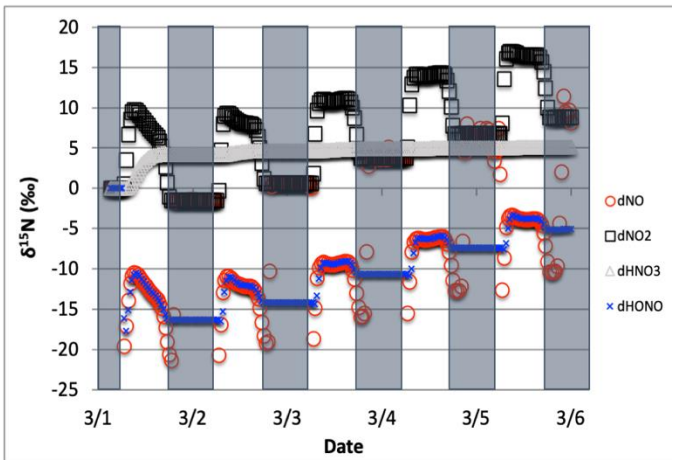

Figure 4.2.2: The time evolution of $\delta^{15}N$ values of NO, NO_2, HNO_3, and HONO, caused by PHIFE during NO_2 photolysis.

When there is sufficient photolysis of any single NO_y compound, then the $\delta^{15}N$ value of that compound tends to significantly change, but often neither the HNO_3, HONO, nor NO_x $\delta^{15}N$ values are affected. For example, the arbitrary α for NO_3 photolysis (R7 and R8) alters the $\delta^{15}N$ value of HNO_3 and NO_x by less than 0.1‰ (not shown), but it induces a large diurnal change in the $\delta^{15}N$ value of NO_3 and N_2O_5, with sharp transitions occurring during sunrise and sunset (Fig. 4.3). This is easily understood. For our test case, during the day $^{15}NO_3$ would be left behind because $^{14}NO_3$ is preferentially being photolyzed. The daytime N_2O_5 formed from this NO_3 (positive $\delta^{15}N$) and NO_2 ($\delta^{15}N \sim 0$) thus has a $\delta^{15}N$ values halfway between these two reactants (isotope mass balance). However, there is so little NO_3 and N_2O_5 during the day that essentially no HNO_3 is being formed through these precursors and the NO_3 PHIFE is not manifested in the NO_x or HNO_3 $\delta^{15}N$ value. During the night, photolysis and the PHIFE ceases and any NO_3 and N_2O_5 formed by NO_2 oxidation have $\delta^{15}N$ values equal to the NO_2.

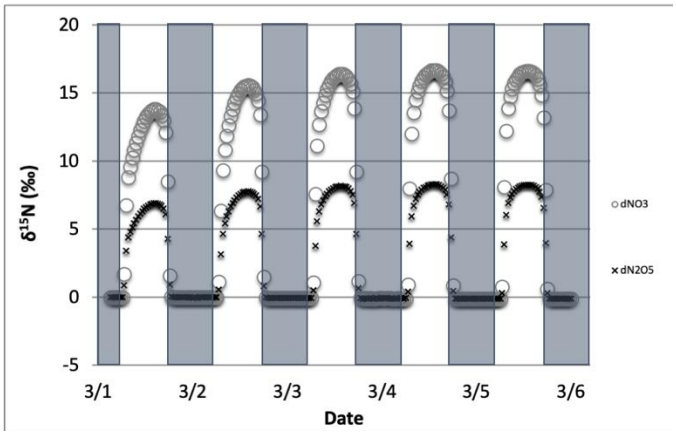

Figure 4.2.3: The time evolution of $\delta^{15}N$ values of NO_3, and N_2O_5, caused by PHIFE during NO_3 photolysis.

NO_x, HONO, and HNO_3 are not sensitive to the other NO_y photolysis reactions because of this isotope mass balance effect.

$$\delta^{15}N_{NOy} = \Sigma\, f_{NOyi} \bullet \delta^{15}N_{NOyi} \qquad \text{Eq. (4.5)}$$

Where f_{NOyi} is the mole fraction of any NO_{yi} compound relative to total NO_y, $\delta^{15}N_{NOyi}$ is the $\delta^{15}N$ value of that compound, and $\delta^{15}N_{NOy}$ is the value of total N, which in these simulations is arbitrarily set to 0‰. For an ε = -20‰ and a threshold of "importance" set to ± 1‰, isotope mass balance requires that f_{NOyi}>0.05. Only NO, NO_2, HONO, and HNO_3 compounds meet this threshold (Fig. 4.4). All other f_{NOyi} values are an order of magnitude smaller, the largest being f_{HNO4} and it only reaches a maximum value of 0.005. By the end of the second simulation day, the f_{HNO3} has approached 1 and effectively minimizes the other f_{NOyi} values because it is the only stable N compound because the other NO_y compounds are very photochemically active. If we exclude this build up in HNO_3 from the sum of NO_y, then f_{NO}, and f_{NO2} (and HONO during some hours, see discussion) become the dominant fractions (Fig. 4.4) and they control the other $f_{NOyi.}$ Even under this constraint, the f_{HNO4} only reaches 0.001 (Fig. 4.4). Thus, in i_NRACM, the α values of α_{R4}- α_{R8} were set equal to 1, and only the α_{R1} was assigned a non-1 value, which was determined using a PHIFE theory (discussed below).

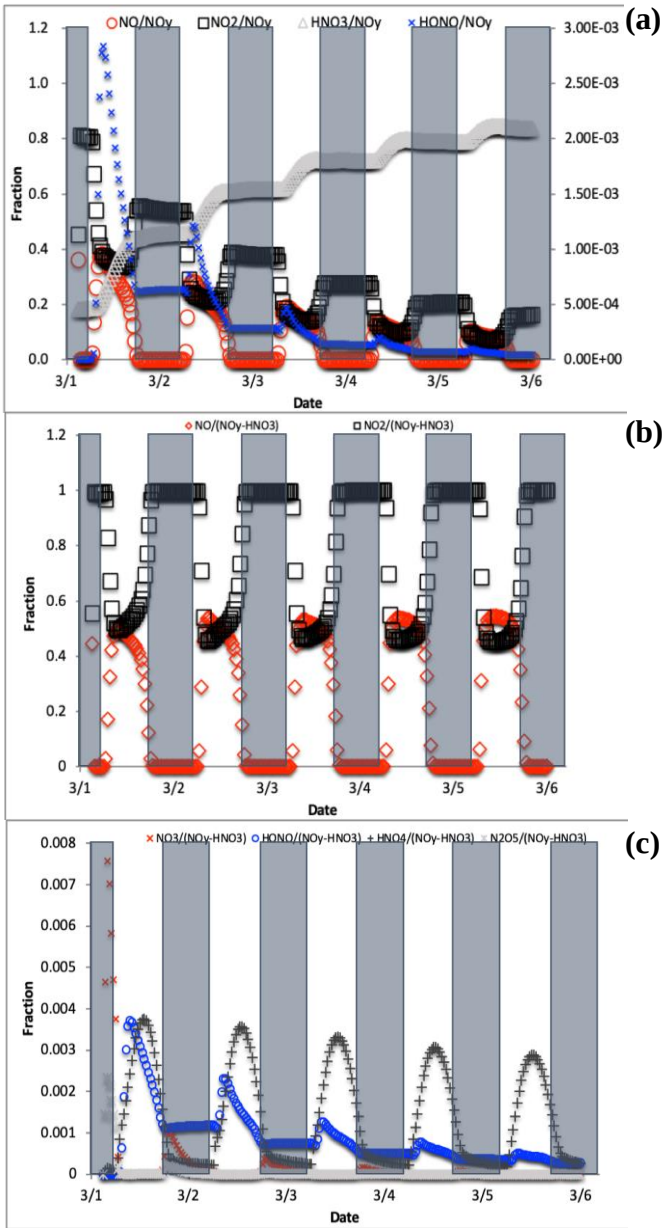

Figure 4.2.4: The change in f_{NO}, f_{NO2}, f_{NO3}, and f_{HONO} (right axis) over the 5-day simulation shows the transition from NO_y as mostly NO_x to predominately HNO_3 (top, a). For reactive NO_y (NO_y – HNO_3) large diurnal changes in f_{NO} and f_{NO2} (middle, b) caused by photolysis minimize the other f_{NOy} values, none of which exceeds 0.01 (bottom, c).

4.2.3.2 KIE relevant in i$_N$RACM mechanism

The KIE for 12 N containing compounds and their 96 reactions were evaluated using the same sensitivity analysis. The vast majority of reactions had little influence on the $\delta^{15}N$ values of NO_x, HONO, and HNO_3 (Fig. 4.1). Similar to the photolysis sensitivity, either reaction proximity or

isotope mass balance were controlling $\delta^{15}N$ relevance. For example, NO_2 + OH is a reaction that directly produces a significant fraction of HNO_3, and therefore R39 is relevant in the i_NRACM mechanism. In contrast, R95 produces very little HNO_3 so it has a negligible influence on the predicted HNO_3 $\delta^{15}N$ value. Therefore, the only relevant KIE reactions that have $\alpha \neq 1$ in i_NRACM mechanism are R39, R91-R97, R48 (Table C.2b).

4.2.3.3 EIE relevant in i_NRACM mechanism

While some EIE is naturally handled in the i_NRACM mechanism, such as the NO_2–NO_3–N_2O_5 equilibrium, other potentially important N isotope exchange reactions are not directly expressed in RACM and must be considered. From a thermodynamic perspective, the EIE for any two N containing compounds can be calculated. The rate at which these compounds can achieve equilibrium, however, needs careful consideration. For example, the EIE for the isotope exchange reaction NO + $^{15}HNO_3$ ←→ ^{15}NO + HNO_3 has been calculated and measured (Brown and Begun, 1959). Yet, steric considerations would suggest it would be very improbable for a gas-phase reaction pathway or transition state to exist where two O atoms and hydrogen from an HNO_3 could quickly migrate to a NO molecule during a collision. The result is that isotope exchange for this gas-phase reaction is likely kinetically too slow to be relevant but is valid in a highly concentrated liquid phase (Brown and Begun, 1959). The larger the N-containing molecule the more difficult it is to envision gas-phase EIE occurring on a timescale comparable to the residence time tropospheric N of about a week. On the other hand, the isotope exchange reaction NO + $^{15}NO_2$ ←→ ^{15}NO + NO_2 rapidly occurs (Sharma et al., 1970) because it can form an ONONO (N_2O_3) stable intermediate. As such, i_NRACM only considers N isotope equilibrium between NO, NO_2, NO_3, and N_2O_5. Since the latter 3 compounds are already chemically equilibrated in RACM, they are by default isotopically equilibrated in i_NRACM. Therefore, the only new isotope exchange reaction added to i_NRACM was NO + $^{15}NO_2$ ←→ ^{15}NO + NO_2 (R238, R238a).

4.2.4 Isotopologue fraction factors (α) used in i_NRACM

In this section, we discuss the methodology used to determine the values for the relevant PHIFE, KIE, and EIE. These are reactions R1, R39, R48, R91-R97, and R238.

4.2.4.1 PHIFE derived α used in the i_NRACM mechanism

The PHIFE for R1 was calculated using the existing NO_2 experimental photolysis cross-section of $^{14}NO_2$ for tropospheric relevant wavelengths (300 to 450 nm) (Vandaele et al., 2002). Using the experimentally determined ΔZPE for the $^{15}NO_2$ isotopologue of 29.79 cm^{-1} (Michalski et al., 2004), the $^{47}\sigma(\lambda)$ was blue-shifted by roughly 0.3 nm from the experimentally measured $^{46}\sigma(\lambda)$ (Vandaele et al., 2002) (Fig. 4.5). The wavelength-dependent actinic flux, F(λ), was taken from the TUV model (NCAR) for solar zenith angles from 0 to 90° in 15° increments. The ϕ(λ) values were taken from experimental data at 298 K (Roehl et al., 1994), and it was assumed that there is no significant quantum yield isotope effect. Based on these assumptions the $^{46}J(\lambda)$ and $^{47}J(\lambda)$ values were calculated (Fig. 4.5). An important feature of NO_2 the wavelength-dependent J includes a peak near 390-400 nm that subsequently decreases at longer wavelengths until NO_2 photolysis ceases beyond 420 nm due to a ϕ = 0 beyond this wavelength (Roehl et al., 1994). Overall, the NO_2 PHIFE α value was found to be consistent for the wide range of solar zenith angles, ranging between 1.002 to 1.0042 with higher values occurring at lower solar zenith angles. We used an α = 1.0042 for daylight hours.

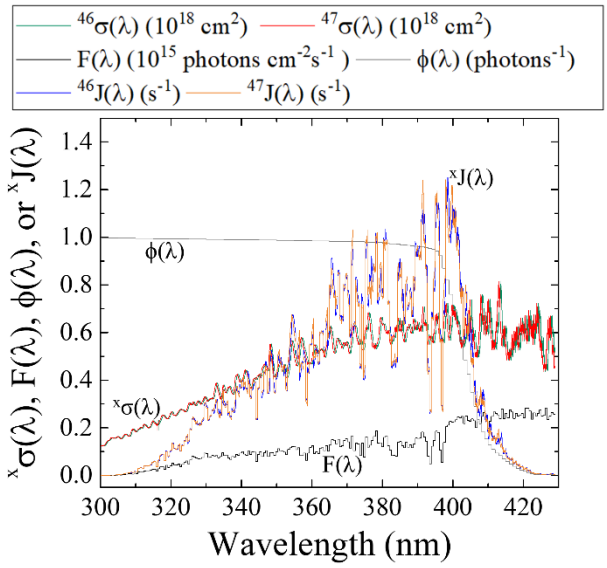

Figure 4.2.5: Literature reported $^{46}\sigma(\lambda)$ (Vandaele et al., 2002) F(λ) (at SZA of 60°; TUV model), and NO_2 ϕ(λ) (Roehl et al., 1994) and calculated $^{47}\sigma(\lambda)$ derived from the ZPE shift model for wavelengths relevant for tropospheric conditions for NO_2 photolysis. From these parameters, both $^{46}J(\lambda)$ and $^{47}J(\lambda)$ have been calculated (Eq. (4.2)).

4.2.4.2 KIE derived α used in the i_NRACM mechanism

4.2.4.2.1 KIE for the NO + O3 reaction

The $^{15}\alpha_{48}$ for the reaction NO + O_3 → NO_2 +O_2 reaction was determined by ab initio calculations (Walters and Michalski, 2016). Generally, in a normal KIE, the heavy ^{15}NO would react with O_3 slower than the light ^{14}NO, which consistent with the calculated effect, however, it is relatively small (ε = -6.7‰ at 298 K). The $^{15}\alpha_{48}$ was determined to have the following temperature-dependent relationship (Walters and Michalski, 2016) over the temperature range of 220 to 320 K (Eq. (4.6)):

$$\alpha_{48} = (0.9822*\exp(3.3523/T) \quad \text{Eq. (4.6)}$$

4.2.4.2.2 KIE for the NO3 + VOC reactions

The most influential reactions that impacted the $\delta^{15}N$ of HNO_3 were the three reaction pathways that generate HNO_3. This is because the isotope effect associated with this last step is largely retained in the product HNO_3 because photolysis of HNO_3 back into photochemically active compounds that could re-scramble N isotopes is slow, effectively "locking in" these final isotope effects. Two gas-phase reaction groups are important for HNO_3 production. Nitric acid is produced mainly by R39 during the daytime (Seinfeld and Pandis, 1998) but this reaction is treated as an EIE as discussed below in the EIE section. During the nighttime, when the photolysis sink for NO_3 vanishes, NO_3 can react with VOCs to form HNO_3 via hydrogen abstraction reactions (Atkinson, 2000). Any individual NO_3 + VOC reaction had a small "relevance" for the $\delta^{15}N$ values of NO_x, and HNO_3, but given there are 7 such reactions (R91-R97) their sum may be important.

The KIE for each of the NO_3 +VOC→ HNO_3 reaction (R91-R97) was determined by assuming collisional frequency was the key KIE factor in such reactions. In these reactions (R91-R97) NO_3 abstracts hydrogen from a hydrocarbon, acting through a transition state involving the oxygen atoms in the nitrate radical C--H--ONO_2. Since N is not directly participating in the bond formation it is classified as a secondary KIE (Wolfsberg, 1960). Secondary KIE is typically much smaller than primary KIEs that occur at bond breaking/forming positions within a molecule

(Wolfsberg, 1960). Therefore, we assumed that the secondary KIE was negligible and did not factor into the α values for these 7 reactions. On the other hand, isotope substitution does change the relative rate of collisions for N isotopologues because of the change in molecular mass. The collisional frequency (Eq.7) for any of the NO_3 + VOC reaction pair was calculated assuming a hard-sphere approximation via

$$A = \left[\frac{8kT}{\pi\mu}\right]^{1/2} \pi d^2 \qquad \text{Eq. (4.7)}$$

where μ is the reduced mass of either NO_3 or $^{15}NO_3$ and the specific hydrocarbon in a given reaction (R91-R97). When taking the isotopologue collision ratio, the constants, collision cross-section (d^2), and temperature cancel out giving a temperature-independent KIE of

$$\alpha = \frac{k_{15}}{k_{14}} = \frac{A_{15}}{A_{14}} = \sqrt{\frac{\mu_{15}}{\mu_{14}}} \qquad \text{Eq. (4.8)}$$

The α for each NO_3 + VOC reaction (R91-R97) as calculated using the hydrocarbon mass (Table C.1b) and the NO_3 isotopologue masses (62, 63 amu) and using Eq. (4.8).

4.2.4.3 EIE derived α used in the i_NRACM mechanism

4.2.4.3.1 EIE of NO + NO2 exchange

The NO + NO_2 exchange was added to i_NRACM by defining a forward and reverse reaction (R238, R238a) and an equilibrium constant $K_{238} = k_{238}/k_{238a} = \alpha$. The forward rate constant (k_{238}) was based on the NO-NO_2 isotope exchange rate determined by Sharma et al. (1970) ($3.6*10^{14}$ cm^3 s^{-1} $molecule^{-1}$). The reverse rate was calculated using $k_{238} = k_{238a}/\alpha_{238}$. The temperature-dependent for EIE of NO + NO_2 exchange (Eq. 9) was calculated using quantum mechanical techniques (Walters and Michalski, 2015) that matched well with recent experimental values (Walters et al., 2016).

$$\alpha_{238} = 0.9771*\exp(18.467/T) \qquad \text{Eq. (4.9)}$$

4.2.4.3.2 EIE used in the NO2 + OH reaction

The $^{15}\alpha_{39}$ for the NO_2+OH+M → HNO_3 reaction (R39) was determined by assuming equilibrium between NO_2 and HNO_3. The third body and the negative temperature dependence of the rate constant show that similar to O_3 formation, this reaction is an association reaction (Golden and Smith, 2000). It proceeds through an excited intermediate, $*HNO_3$, that can undergo collisional deactivation by a third body M (Eq.10).

$$NO_2 + OH \leftarrow k_r\ k_f \rightarrow *HNO_3\ k_d \rightarrow HNO_3 \qquad \text{Eq. (4.10)}$$

in which k_f and k_r are the forward and reverse rate constants for the association step and k_d is the rate constant for collisional deactivation. The HNO_3 production rate constant is then $k_f k_d(M)/k_r = K_{eq} k_d(M)$. This general form can be used to write two isotopologue equilibrium constants K

$$K_{39} = [*HNO_3]/([NO_2][OH]) = k_{39f}/k_{39r} \qquad \text{Eq. (4.11)}$$

$$K_{39a} = [*H^{15}NO_3]/([^{15}NO_2][OH]) = k_{39af}/k_{39ar} \qquad \text{Eq. (4.12)}$$

Since •OH is not participating in the N isotope chemistry, these two EIE effectively reduces the isotope chemistry to the temperature-dependent ^{15}N EIE

$$^{15}NO_2 + *HNO_3 \leftarrow\rightarrow NO_2 + *H^{15}NO_3 \qquad \text{Eq. (4.13)}$$

$$K_{39a}/K_{39} = \alpha_{HNO3/NO2} = \beta_{HNO3}/\beta_{NO2} \qquad \text{Eq. (4.14)}$$

The fundamental vibration frequencies for HNO_3* were taken to be the same as ground state HNO_3, similar to RRKM theory approaches used to calculate the uni-molecular decay rate of HNO_3* (Golden and Smith, 2000). The temperature-dependent β_{HNO3} and β_{NO2} values for this exchange were taken from (Walters and Michalski, 2015). Since the reaction has negative activation energy and has a fairly rapid rate constant at 101 kPa, (1×10^{11} cm^{-3} s^{-1}) and the isotope effect due to the collisional deactivation frequency (Eq. 7) is minimal (~2‰) compared to the equilibrium effect (~40‰), the deactivation rate constants k_d were set equal (k_{d14}/k_{d15}=1). Setting k_{r14}= k_{r15}, and using the $\alpha_{HNO3/NO2}$ equilibrium value the k_{39a} for the $^{15}NO_2$ + OH → $H^{15}NO_3$ reaction is

$$K_{39a} = \alpha_{HNO3/NO2} (K_{39}) \quad \text{Eq. (4.15)}$$

The temperature dependence of $\alpha_{HNO3/NO2}$ is derived from the tables in (Walters and Michalski, 2015) and α_{39} is then:

$$\alpha_{39} = (0.973*\exp(19.743/T) \quad \text{Eq. (4.16)}$$

For typical tropospheric temperatures the $\alpha_{HNO3/NO2}$ 1.040 suggesting the $\delta^{15}N$ of HNO_3 produced by the NO_2 + OH reaction will be +40‰ relative to tropospheric NO_2. This α value is larger and opposite the sign of the $^{15}\alpha = 0.9971$ assumed by Freyer et al. (1993). Freyer's α was approximated by using the reduced mass of the OH-NO_2 activated complex. There two problems with this approach. First, the activation complex's reduced mass approximation should be viewed in terms as the decomposition rate constant, not the product formation rate constant as assumed by Freyer, because transition state theory assumes equilibrium between the stable reactants and the transition state (Bigeleisen and Wolfsberg, 1958; Wolfsberg et al., 2010). In other words, Freyer's $\alpha = 0.9971$ should indicate that the $^{15}NO_2$-OH decomposes more slowly than $^{14}NO_2$-OH and therefore more likely to form HNO_3 at +2.9‰ (not -2.9‰ determined in Freyer). Secondly, the reduced mass approximation of the complex pair ignores the thermodynamic contribution of the reactants and the vibrations in the transitions state other than the bond-forming (imaginary) vibration. Our approach overcomes both of these assumptions and incorporates the temperature dependence of the EIE for this reaction.

4.2.4.3.3 EIE used in heterogeneous reactions of N2O5

During the nighttime, the heterogeneous HNO_3 formation pathway becomes important (Chang et al., 2011; Dentener and Crutzen, 1993; Riemer et al., 2003). During the night, NO is nearly completely oxidized to NO_2 leading to the build-up of the NO_3 radical (R48), the formation of N_2O_5 (R53), and heterogeneous N_2O_5 hydrolysis becomes a major source of HNO_3 production (discussed below). This is particularly true in regions that have high NO_x mixing ratios and large aerosol surface areas such as urban centers (Chang et al., 2011; Riemer et al., 2003). In order to assess the ^{15}N partitioning of this reaction pathway, both EIE and KIE were considered.

It was assumed that the fractionation factor for the $N_2O_5 \rightarrow 2HNO_3$ reaction was mainly controlled by the nighttime equilibrium between N_2O_5 and NO_2/NO_3 (R53, R54). When factoring the isotopologue dynamics, this equilibrium can be viewed as an EIE via

$$^{15}NO_2 + NO_3 \leftrightarrow O_2{}^{15}N\text{--}O\text{--}NO_2 \leftrightarrow NO_2 + {}^{15}NO_3 \qquad \text{Eq. (4.17)}$$

here $^{15}N_2O_5$ is represented as the transition state $O_2{}^{15}N\text{--}O\text{--}NO_2$ to highlight the relative ease of N isotope exchange via oxygen migration during N_2O_5 formation and decomposition. The symmetry of $^{15}NNO_5$ and $N^{15}NO_5$ is also why they were not treated as isotopomers since they are structurally identical.

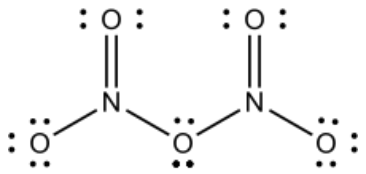

The N_2O_5 equilibrium in the RACM model is dealt with as a forward reaction R53 (k_{53}) and a decomposition reaction R54 (k_{54}) that are derived from the measured equilibrium constant (K_{53}) = (k_{53}/k_{54}). In i_NRACM, the N_2O_5 isotopologue has 2 formation pathways, with two forward rate constants ($k_{53\ a,b}$) and two decomposition rate constants ($k_{54\ a,b}$) that were used to write their respective equilibrium constants K

$$^{15}NO_2 + NO_3 \leftrightarrow {}^{15}NNO_5 \ (K_{53a} = k_{53a}/k_{54a}) \qquad \text{Eq. (4.18)}$$

$$NO_2 + {}^{15}NO_3 \leftrightarrow {}^{15}NNO_5 \ (K_{53b} = k_{53b}/k_{54b}) \qquad \text{Eq. (4.19)}$$

Dividing K_{53a} and K_{53b} by K_{53} yields isotopologue product and reactant ratios that can be evaluated using $\beta(\alpha)$ values from Walters and Michalski (2015). These were used to determine the α value for the N_2O_5 isotopologue equilibrium, which are simply a function of the formation and decomposition rate constants and temperature

$$K_{53a}/K_{53} = (^{15}NNO_5/N_2O_5)(NO_2/^{15}NO_2)(NO_3/NO_3) = \beta_{N2O5}/\beta_{NO2}$$
$$= \alpha_{N2O5/NO2} = k_{53a}/k_{53} \times k_{54}/k_{54a} \qquad \text{Eq. (4.20)}$$

$$K_{53b}/K_{53} = (^{15}NNO_5/N_2O_5)(NO_3/^{15}NO_3)(NO_2/NO_2) = \beta_{N2O5}/\beta_{NO3}$$
$$= \alpha_{N2O5/NO3} = k_{53b}/k_{53} \times k_{54}/k_{54b} \qquad \text{Eq. (4.21)}$$

The N_2O_5 decomposition rate constants were arbitrarily set to be equal ($k_{54} = k_{54a} = k_{54b}$) and the decomposition rate constants were then derived using the temperature-dependent α values

$$k_{53a} = k_{53}(\alpha_{N2O5/NO2})\ \alpha_{N2O5/NO2} = 1.0266\ (298\ K) \qquad \text{Eq. (4.22)}$$

$$k_{53b} = k_{53}(\alpha_{N2O5/NO3})\ \alpha_{N2O5/NO3} = 1.0309\ (298\ K) \qquad \text{Eq. (4.23)}$$

The α for doubly substituted $^{15}N_2O_5$ isotopologue was determined using $\alpha = \beta_{15N2O5}/\beta_{NO2}\beta_{NO3}$ and the value for β_{15N2O5} (1.272) was approximated using the principle of the geometric mean (Bigeleisen, 1958; Snyder et al., 1999), yielding a temperature-independent $\alpha = 1.057$. However, the N_2O_5 system is insensitive to this α value because of the low probability of a $^{15}N + ^{15}N$ reaction (1.5×10^{-5}) relative to a $^{14}N + ^{15}N$ reaction (4×10^{-3}), thus the small temperature dependence was also ignored.

Because RACM is a gas phase chemical mechanism, it does not include heterogeneous reactions of N_2O_5 on aerosols, which would limit i_NRACM to accurately predict the $\delta^{15}N$ values, particularly at night. Gas chemical mechanisms are often used in larger 1, 2, and 3-D chemical transport models that usually also include aerosol modules that calculate heterogeneous chemistry using inputs from the gas phase chemical mechanism (i.e. N_2O_5 concentrations). However, if the objective is to use a 0-D chemical box model to simulate local chemistry the N_2O_5 heterogeneous hydrolysis will need to be included. i_NRACM was modified to use a first-order rate constant to calculate N_2O_5 heterogeneous hydrolysis (Yvon et al. 1996; Riemer et al., 2003). The rate constant is a function of N_2O_5 molecular speed (c), the N_2O_5 uptake coefficient (γ), and the aerosol surface area density S.

$$-dN_2O_5/dt = d0.5HNO_3/dt = k_{N2O5}(N_2O_5) = R239 \qquad k_{N2O5} = ¼c\ \gamma\ S \qquad \text{Eq. (4.24)}$$

The k_{N2O5} values were assessed based on the different pollutant loadings and emission scenarios (Fig. 4.6). The k_{N2O5} was calculated as a function of γ (Anttila et al, 2006; Bertram & Thornton. 2009; Davis et al., 2008; Riemer et al., 2003; Riemer et al., 2009) and S (Cai et al., 2018; Kuang et al., 2010; McMurry et al., 2005; Petäjä et al., 2009; Qi et al., 2015) values that span clean to highly polluted environments. This range yielded $k_{N2O5} = 1$, 0.1, and 0.01 for high, medium, and low polluted environments (Fig. 4.6).

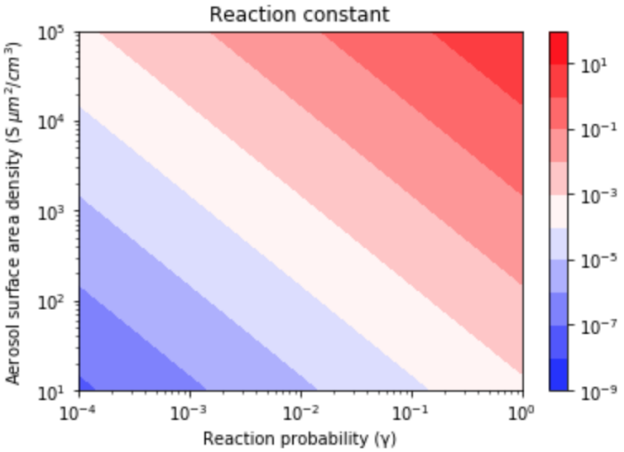

Figure 4.2.6: Contour lines of the same k_{N2O5} values as a function of γ and S values. The γ values depend on aerosol composition and range from 3.8 x 10^{-5} (relatively dry sulfuric acid) to 1 (aqueous aerosol in the winter polar stratosphere). S values are a function of aerosol number density and size distribution and range from 52 (low scavenging rate, low particle growth rate) to 1140.1 (high scavenging rate, high particle growth rate).

Only the uptake coefficient (γ) and molecular speed (c) could have a KIE during aerosol uptake of N_2O_5 (R239, R239a, R239b). The γ term was ignored because ab initio work suggests that N_2O_5 hydrolysis activates through hydrogen bonding between water molecules on the aerosol surface and O atom in the N_2O_5 (Snyder et al., 1999) making it a secondary (small) KIE for N. The c term is a function of the root of the N_2O_5 molecular mass and when the ratio is taken there is no temperature dependence yielding $\alpha_{239a} = (108/109)^{0.5} = 0.995$ and $\alpha_{239b} = (108/110)^{0.5} = 0.9909$.

4.2.4.4 i_NRACM simulations

A number of i_NRACM simulations were run with two different purposes. The first set of simulations iteratively changed the α values from 1 to their values discussed above. These simulations aimed at investigating the importance of each α as they aggregated together. These include photolysis only, Leighton cycle, daytime chemistry, night-time chemistry, and full chemistry using the same test case (Table C.3a-f). The second set of simulations replicated the test case simulations (Table C.4a-b, 5a-b) detailed in Stockwell (1997) and other pollution scenarios (Table C.8). These were run with all α's activated but with varied initialized chemistry and primary pollutant emissions.

4.3 Results and Discussion

It is important to first test i_NRACM by turning on and off individual relevant isotope effects and then combining their cumulative effects. This is advantageous relative to simply running the full mechanism under different pollution scenarios because it would be a challenge to disentangle which isotope effects in the full mechanism were mainly responsible for $\delta^{15}N$ change in NO_x, HONO, or HNO_3 without such a systematic investigation. For example, it is likely that the $\delta^{15}N$ value of NO_2 will be a significant factor in the $\delta^{15}N$ value of HNO_3 because it is the reactant in R39 and R239. Thus, understanding which isotope effects control the $\delta^{15}N$ of NO_2 helps with interpreting the $\delta^{15}N$ value of HNO_3 and vice versa. Thus, this discussion section is divided into 3 sections. The first is the examination of the relevant isotope effects occurring during daytime photochemistry and their impact on NO_x, HONO, and HNO_3 $\delta^{15}N$ values. Secondly, is the examination of the relevant isotope effects occurring during nighttime chemistry (EIE and KIE) and their effect on NO_x, HONO, and HNO_3 $\delta^{15}N$ values. These first two discussion sections focus mainly on the relative importance of each isotope effect when the photochemical conditions are constant. Finally, the full i_NRACM mechanism will be tested under different atmospheric conditions such as variations in trace gas concentrations, aerosol loading, and hours of sunlight. This tests how changes in photochemical oxidation pathways result in a difference in the $\delta^{15}N$ values of NO_x, HONO, and HNO_3.

4.3.1 The $\delta^{15}N$ of NO_x, HONO, and HNO_3 due to daytime chemistry

The role that daytime chemistry plays in determining the $\delta^{15}N$ values of NO_x, HONO, and HNO_3 was investigated by iteratively adding relevant fractionation factors to i_NRACM. The sensitivity of NO_x, HONO, and HNO_3 $\delta^{15}N$ values to NO_2 photolysis (R1a) was tested. The initial trace gas concentrations and emissions were set to the March 1 test cases (Table C.3 a-f) and simulations were run with, and without, NO emissions. All subsequent test simulations will also use the March 1 test case in order to have a consistent comparison of $\delta^{15}N$ values between different simulations. It is noted that the initial HNO_3 and O_3 mixing ratios are set to zero and that the start time of the simulations is 3 a.m. The main daytime only effects will be NO_2 photolysis (R1), O_3 oxidation (R8), and reaction OH (R39) since both photolysis and OH chemistry is only relevant

during the daytime. However, NO_x isotope exchange and $NO + O_3$ will also play a vital role despite no being exclusively daytime reactions.

4.3.1.1 The $\delta^{15}N$ values of NO_x, HONO, and HNO_3 due to the photolysis only

The simulations with only R1 isotope effect activated (with NO_x emissions) shows a clear diurnal cycle in NO_x and HONO $\delta^{15}N$ values and a multiday trend moving towards an approximate steady-state for HNO_3 $\delta^{15}N$ values, which can be explained by the PHIFE (Fig. 4.7a). Initially, all NO_y has $\delta^{15}N$ of zero (by default) and there is no photolysis at 3 am. At sunrise the $\delta^{15}N$ value of NO_2 goes negative and NO value positive since $^{15}NO_2$ is preferentially photolyzed ($\alpha_{R1} = 1.0042$). The difference between the $\delta^{15}N$ values of NO and NO_2 ($\Delta\delta^{15}N_{NO\text{-}NO2} = \delta^{15}N$ NO - $\delta^{15}N$ NO_2) at all times during the day is 4‰, which is the ε_{R1a} value. During the night both the NO and NO_2 $\delta^{15}N$ values approach 0‰ because most NO is oxidized to NO_2 and NO emissions (0‰) dominate the NO nighttime budget (relative to residual day NO). Over the weeklong simulation, the NO_x $\delta^{15}N$ value slowly increases by about one per mil. This is because ^{15}N depleted NO_2 is converted into HNO_3 leaving the residual NO_x ^{15}N enriched. This is also the reason for the $\delta^{15}N$ values of HNO_3 that initially mimic the daytime NO_2 values and trends towards 0‰ by the end of the simulation week. The $\delta^{15}N$ values of HONO mimics the NO values during the daytime since the main reaction pathway forming HONO is OH + NO, which peaks in the morning (~10:00). HONO retains the evening $\delta^{15}N$ values through the night since most of the HONO is destroyed in the afternoon via photolysis and again follows NO $\delta^{15}N$ the next morning as its production again reaches a maximum (Fig. 4.7).

The simulation without NO emissions shows a similar behavior but with some clear differences relative to the emission case. The NO_x and HONO $\delta^{15}N$ values exhibit the same diurnal $\Delta\delta^{15}N_{NO\text{-}NO2} = 4‰$ value. Unlike the emission case, however, the diurnal NO_x $\delta^{15}N$ value peaks and troughs trend downward during the week-long simulation, with NO approaching 0‰ and NO_2 approaching -4‰. The HNO_3 $\delta^{15}N$ values reach roughly a steady-state value of -1.7‰ after about a day and NO_x is ~ -1.8‰ (Fig. 4.7b). This difference between the emission and non-emission case is a consequence of isotope mass balance (f_x = mole fraction of compound x relative to total NO_y).

$$\delta^{15}N_{total} = 0 = f_{NOx} \bullet \delta^{15}N_{NOx} + f_{HNO3} \bullet \delta^{15}N_{NHNO3} + f_{ONIT} \bullet \delta^{15}N_{ONIT} \quad \text{Eq. (4.25)}$$

The positive $\delta^{15}N$ NO_y compound that effectively offsets the -1.7‰ in HNO_3 and -1.8‰ in NO_x is organic nitrate that is +2‰ and makes about half the NO_y pool and is roughly equal to HNO_3 + NO_x (f_{NOx} = 0.11, f_{HNO3}= 0.36, f_{ONIT} = 0.53). In the NO_x emission case, only about 5% of NO_y is as organic nitrate (f_{NOx} = 0.17, f_{HNO3}= 0.78, f_{ONIT} = 0.05) indicating a shift in oxidation pathways when NO and VOCs are emitted during the simulation relative to when they are not. In the emissions case, the NO_x mixing ratios at the end of the simulation is actually slightly higher than their initial ratios, in contrast to the no NO_x emission case where 90% of NO_x has been lost via oxidization into organic nitrate and HNO_3. This loss of N in the no emission scenario effectively shuts down the oxidation chemistry. For example, the day 5 mixing ratio of O_3 is 45 ppb_v (reasonable) for the emission case but only 2 ppb_v for the non-emission case (unreasonable). Therefore, we exclude no-emission simulations for the chemistry analysis discussed in this section and restrict them to the no emission simulations to 48 hours in the final test case analysis (See section 4.4).

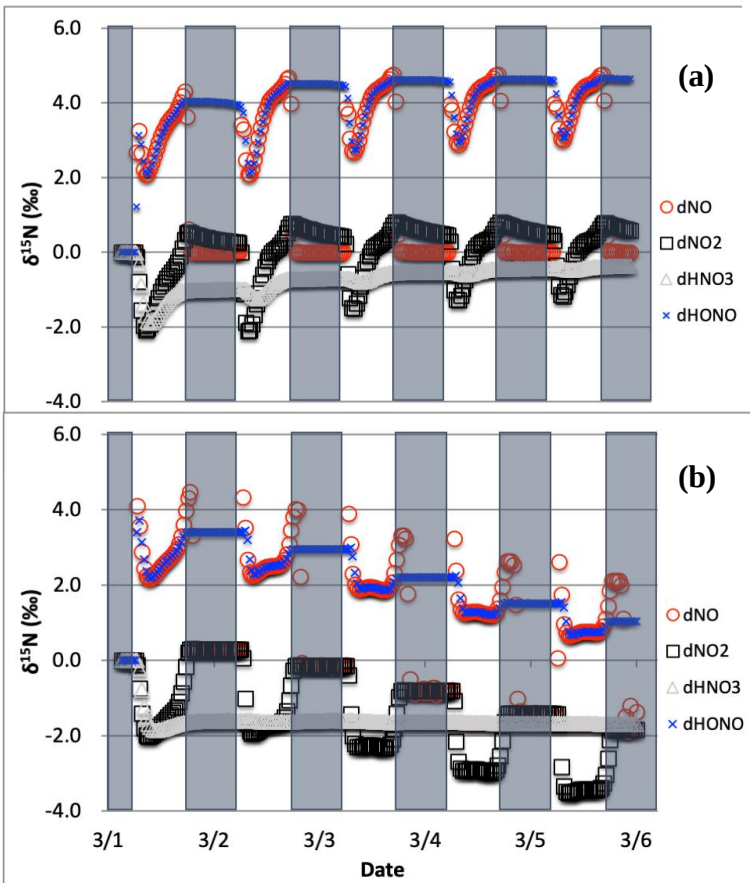

Figure 4.3.1: The $\delta^{15}N$ values of NO (O), NO_2, (□) HONO (x), and HNO_3 (△) with only the photolysis isotope fractionations active. The 5-day simulation was under the conditions list in Table C.3a-b. The gray boxes span night hours and the white span daytime. The top (a) is the simulation with NO_x emissions and the bottom (b) is without NO_x emissions.

4.3.1.2 The $\delta^{15}N$ values of NO_x, HONO, and HNO_3 due to the combined Leighton cycle

The simulations with both NO_2 photolysis (R1) and O_3 + NO (R48) isotope effects active shows similar diurnal and multiday trends as the photolysis only simulations, they are just slightly amplified (Fig. 4.8). The daytime $\Delta\delta^{15}N_{NO\text{-}NO2}$ is now ~ 9.5‰, which is close to the additive of the two isotope effects (ε_{48a} = -6.7‰, ε_{R1a} = 4.2‰). This is logical since ^{15}NO is reacting with O_3 slower than ^{14}NO, preferentially leaving behind ^{15}NO and thus the higher NO $\delta^{15}N$ value. The HNO_3 $\delta^{15}N$ values reach the mean of the daytime NO_2 $\delta^{15}N$ values via the NO_2 + OH reaction. The slight (1‰) upward trend of NO_x and HNO_3 are due to isotope mass balance as detailed in the photolysis only case. Similar to the photolysis only case the $\delta^{15}N$ of HONO is mimicking daytime NO $\delta^{15}N$ values.

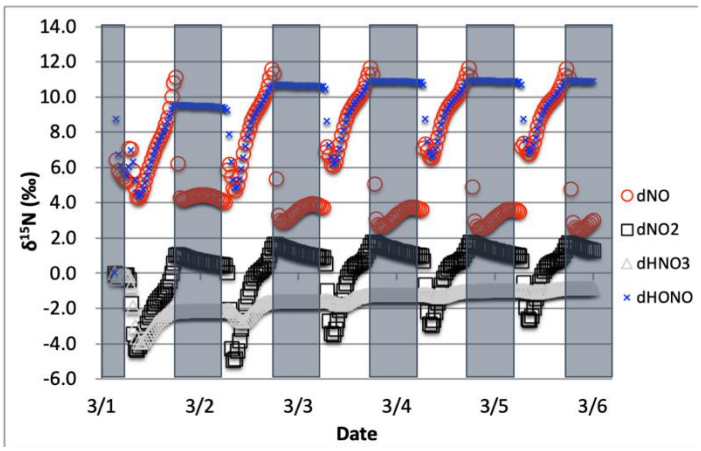

Figure 4.3.2: The $\delta^{15}N$ values of NO_x, HONO, and HNO_3 when isotope effects associated R1 and R48 are combined, with NO_x emission. The 5-day simulation was under the conditions list in Table C.3a-b. The diurnal patterns are reflecting the relative importance of photolysis and O_3 chemistry during the day and night.

4.3.1.3 The $\delta^{15}N$ values of NO_x, HONO, and HNO_3 due to the combined Leighton cycle and NO_x isotope exchange

The $\delta^{15}N$ values of NO_x produced when both the Leighton cycle and NO_x isotope exchange are active exhibit a very dynamic diurnal range that is a function of the NO_x mixing ratios. At high NO_x mixing ratios (150 ppb, 1/3 NO, 2/3 NO_2, Fig. 4.9a) the $\Delta\delta^{15}N_{NO\text{-}NO2}$ is -40‰ at night as expected for NO_x isotopic equilibrium ($\varepsilon_{NO/NO2}$ = -40‰ at 298K). During the daytime the $\Delta\delta^{15}N_{NOx}$ shifts -30 to -35‰ as the photolysis and O_3 isotope effects begin to influence the $\Delta\delta^{15}N_{NO\text{-}NO2}$. HNO_3 $\delta^{15}N$ values during the high NO_x mixing ratio simulation initially follow the $\delta^{15}N$ of NO_2 (via NO_2 + OH) before approaching 0‰, the defined NO_x source values.

At low NO_x mixing ratios (1.5 ppb, 1/3 NO, 2/3 NO_2, Fig. 4.9c) the $\Delta\delta^{15}N_{NO\text{-}NO2}$ and HNO_3 $\delta^{15}N$ is very different from the high NO_x simulation. The nighttime $\Delta\delta^{15}N_{NO\text{-}NO2}$ ranges from -15 to -20‰ and during the daytime, it is around +7‰, while the HNO_3 $\delta^{15}N$ values hover around zero throughout the simulation. The difference between the NO_y $\delta^{15}N$ values in the high and low NO_x cases can be explained as a competition between the NO_x EIE and the Leighton isotope effect. At high NO_x mixing ratios, the NO_x EIE achieves equilibrium quickly at night ($\Delta\delta^{15}N_{NO\text{-}NO2}$ = -40) because the rate of NO_x isotope exchange (R238) is proportional to its concentration. In contrast, isotope exchange is slow in the low NO_x case and the time scale to reach equilibrium is much

longer. Indeed, at the low NO_x mixing ratios, the nighttime equilibrium only reaches about 40-50% of completion by 6:30. Afterward, sunlight begins to erase the NO_x EIE effect until around noon when the $\delta^{15}N$ values of NO is mostly due to the Leighton effect and only a small contribution from EIE (about 5%). For intermediate NO_x mixing ratio case (15 ppb, 1/3 NO, 2/3 NO_2, Fig. 4.9b) the diurnal and week-long NO_y $\delta^{15}N$ trends fall somewhere in between the high and low NO_x simulations.

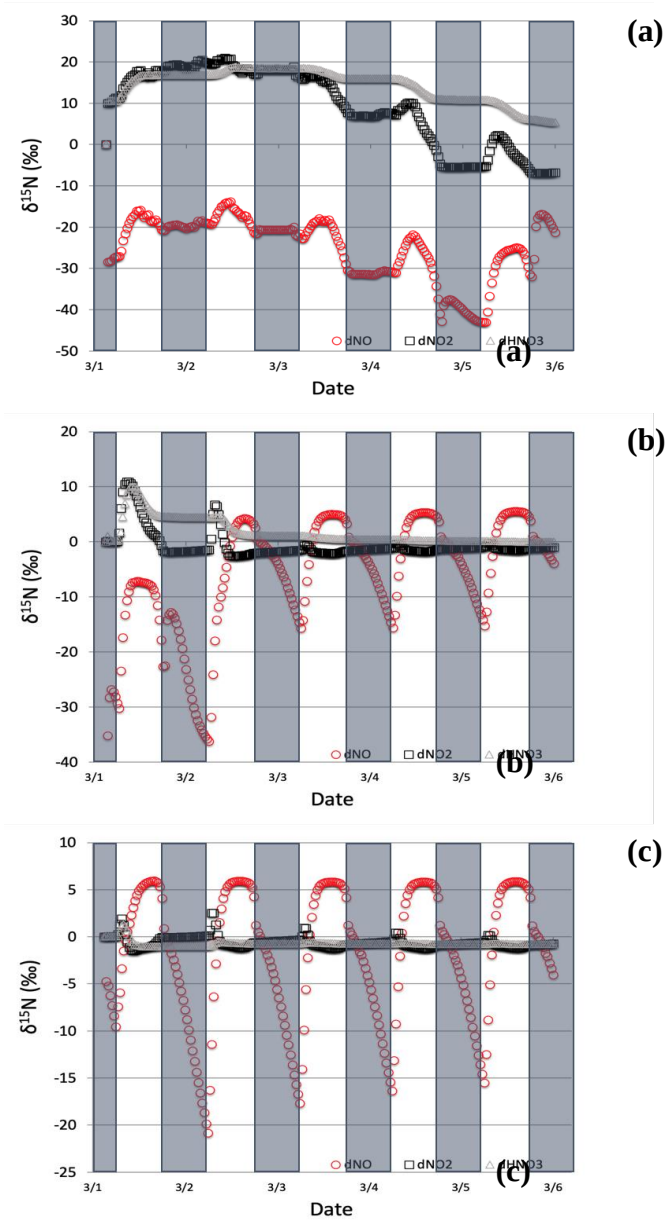

Figure 4.3.3: The $\delta^{15}N$ values of NO_x and HNO_3 when isotope effects in R1, R48, and R238 are included under high (top, a), medium (middle, b), and low (bottom, c) NO_x scenarios. The 5-day simulation was under the conditions list in Table C.3d-f. The NO_y $\delta^{15}N$ values are mainly controlled by NO_x isotope exchange (R238) under high NO_x conditions and Leighton (R1 + R58) under low NO_x conditions.

The changes in $\delta^{15}N$ values of HNO_3 during the March 1 simulations at differing NO_x mixing ratios can be explained in terms of HNO_3 production pathways. Over the course of day 1 the $\delta^{15}N$ of HNO_3 mirrors that of NO_2 because HNO_3 is produced by NO_2 + OH (R39), thus the product

HNO_3 $\delta^{15}N$ values are similar to those in NO_2. This varies depending on the NO_x mixing ratio scenario for two reasons. First, as the NO_x mixing ratio gets bigger, the closer the NO_x gets to achieving the EIE and the bigger the split between NO and NO_2 $\delta^{15}N$ values (40‰ versus 10‰ for Leighton+O_3). Secondly, differences in the amount of NO_x result in different NO/NO_2 ratios as the progress of the simulations. For example, under low NO_x mixing ratios the nighttime $NO/NO_2 < .001$, which means the $\delta^{15}N$ value of NO_2 will be close to that of total NO_x, which will be close to 0‰. At the same time the $\delta^{15}N$ value of NO will be close to the fraction of the EIE achieved, which is about 50% under low NO_x conditions, resulting in a NO $\delta^{15}N$ of about -15‰. These two effects control the $\delta^{15}N$ of NO_2 and that in turn controls the $\delta^{15}N$ value of HNO_3. In all scenarios, the diurnal cycle repeats itself over the subsequent 4 days and a greater fraction of total NO emitted has been turned into HNO_3, so that by the end of the 5-day simulation the HNO_3 $\delta^{15}N$ values converge towards 0‰, the defined value of NO_x emissions in the simulations.

The modeled $\delta^{15}N$ values of HONO also have a diurnal pattern that can also be traced to diurnal chemistry and isotope mass balance. Similar to the photolysis and photolysis + O_3 cases, the HONO $\delta^{15}N$ values mirror the oscillation of the NO $\delta^{15}N$ values (data not shown). This is a result of HONO production by the NO + OH reaction (R38). In contrast, the HONO $\delta^{15}N$ values at night remain nearly constant despite the fact that the $\delta^{15}N$ of NO is changing dramatically. This is because the absence of OH at night halts R38 and thus HONO production ceases and the $\delta^{15}N$ values are simply the same as the residual daytime HONO reservoir. There is a repeated minimum in HONO $\delta^{15}N$ values occurring each morning at 7:00 over the subsequent 4 days. This is a result of the fact that, unlike HNO_3, HONO is effectively destroyed by photolysis (R4) and OH (R45). Thus, HONO does not build up in the model over the 5-day simulation, but rather mixing ratio peaks daily (30 ppb) at around 9:00 each day. This is when the HONO production–destruction rate is greatest, and its mixing ratio then decreases to a low of 2 ppt by sunset. Since the nighttime HONO, with $\delta^{15}N \sim +5.5$‰, only contributes about 7% ($f = 0.07$) of the morning HONO spike, it does not greatly impact the control that NO $\delta^{15}N$ has on the HONO $\delta^{15}N$ value. This daily isotope effect should be contrasted with the HNO_3 $\delta^{15}N$ trends with time. Initially HNO_3 $\delta^{15}N$ values are influenced by NO_2 $\delta^{15}N$ variations by NO_2-OH-HNO_3 coupling, similar to the NO-OH-HONO coupling. But since there is no significant photochemical sink of HNO_3, the control on HNO_3 $\delta^{15}N$

values by HNO_3 accumulation increases with time, so that by day 5 the diurnal changes in NO_2 $\delta^{15}N$ have almost no impact on the HNO_3 $\delta^{15}N$ values (Fig. 4.9).

4.3.1.4 The $\delta^{15}N$ values of NO_x, HONO, and HNO_3 due to the combined Leighton cycle, NO_x isotope exchange, and NO_2 + OH

The effect of the NO_2 + OH reaction has on $\delta^{15}N$ values of NO_x and HNO_3 associated was then examined (Table C.3c). Since R39 is the last step in HNO_3 production, the instantaneous $\delta^{15}N$ $HNO_3 = \delta^{15}N(NO_2) + \varepsilon_{39}$, thus the $\delta^{15}N_{HNO3}$ is initially 40‰ higher than the NO_2 (Fig. 4.10). This in turn depletes ^{15}N in the residual NO_2 leading to more negative $\delta^{15}N$ values in NO_2 relative to the Leighton + exchange simulations. These latter two effects are still in play as evident by the diurnal NO_x $\delta^{15}N$ cycling and $\Delta\delta^{15}N_{NO\text{-}NO2}$. As the 5-day simulation progresses, the HNO_3 $\delta^{15}N$ value approaches 0‰, approaching the $\delta^{15}N$ of NO emissions, as expected based on isotope mass balance. We point out that this convergence to the source NO_x $\delta^{15}N$ value is much slower in this case than the Leighton and exchanges cases. This highlights the importance of knowing the correct ε_{48}. If $\varepsilon_{48} \sim 0$ as suggested by Freyer (1993) then daytime the $\delta^{15}N$ $HNO_3 \cong \delta^{15}N$ NO_2, demonstrably lower than the $\varepsilon_{48} \sim 40$‰ case. In the end the average daytime $\delta^{15}N$ value of HNO_3 for the entire simulation is about 10‰ higher than the $\delta^{15}N$ of the NO_x source (here defined as 0‰).

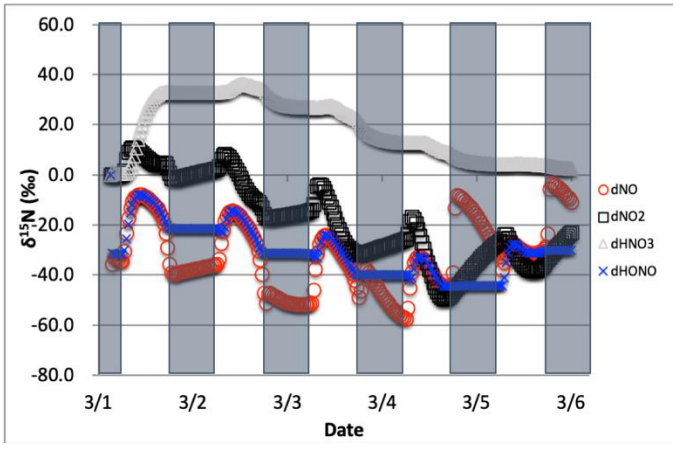

Figure 4.3.4: The time evolution of $\delta^{15}N$ values of NO, NO_2, HNO_3, and HONO caused by isotope effects of Leighton reactions, NO_x isotope exchange, and NO_2 + OH reaction, with NO emission, simulation starts from Mar 1. The 5-day simulation was under the conditions list in Table C.3c.

4.3.2 The $\delta^{15}N$ values of NO_x, HONO, and HNO_3 due to nighttime chemistry

The role that nighttime chemistry plays in determining the $\delta^{15}N$ values of NO_x, HONO, and HNO_3 was investigated by iteratively adding relevant fractionation factors to iRACM. The nighttime chemistry effect was assessed by separating the effects of NO_3 radical chemistry and N_2O_5 heterogeneous hydrolysis. NO_3 radical chemistry is only relevant at night because of its short daytime lifetime with respect to photolysis, which keeps its daytime mixing ratios at the sub ppt_v levels (Platt et al., 1984). At night NO_3 builds up and produces HNO_3 (Aldener et al., 2006; Finlayson-Pitts and Pitts, 1997; Horowitz et al., 1998) via reactions with hydrocarbons (R91-97). The magnitude of this isotope effect was tested by adding NO_3 the isotope fractionation factors for R91-97 (see methods) and altering VOC emission rates to simulate clean, moderate, and extreme VOC pollution environments. Likewise, N_2O_5 only accumulates at night when it begins producing HNO_3 on aerosol surfaces (Chang et al., 2011). The magnitude of this isotope effect was tested by adding the N_2O_5 EIE (see methods) and adding the first order N_2O_5 heterogeneous pathway (see methods) to i_NRACM. The first-order rate constant was adjusted to simulate clean, polluted, and extreme pollution environments where aerosol surface area density largely controls the rate constant (Riemer et al., 2003 Chang et al., 2011).

4.3.2.1 The $\delta^{15}N$ values of NO_x, HONO, and HNO_3 due to NO_3 + VOC reactions

The effect on the $\delta^{15}N$ values of NO_x, HNO_3, HONO associated with the KIE occurring during NO_3 + VOC nighttime reactions (R91-R97) were first examined. Four simulations were run that included the isotope effects (α values in Table C.6) of the Leighton cycle (R1 and R48), NO_x isotope exchange (R238), NO_2 + OH production of HNO_3 (R39), and the KIE effects (R91-R97), as well as NO emissions. The simulation tested first was the March test case (medium VOC ~360 ppb_v). Then, two simulations were run for June 1 (extended sunlight, warm temperatures), one with a high initial of VOC concentrations and a high VOC emission rate (2 $ppb_v\ h^{-1}$) and one with a low emission rate of VOCs (0.4 $ppb_v\ h^{-1}$). The same two initial conditions were used in the Jan. 1 test case to assess if the extended nighttime and cold temperatures significantly affected the NO_x of HNO_3 $\delta^{15}N$ values produced by NO_3 radicals. The impact of NO_3 reactions on NO_y $\delta^{15}N$ values was determined by subtracting these simulated $\delta^{15}N$ values from those same simulations when only the Leighton cycle, exchange, and OH + NO_2 reaction was considered (Section 4.3.1).

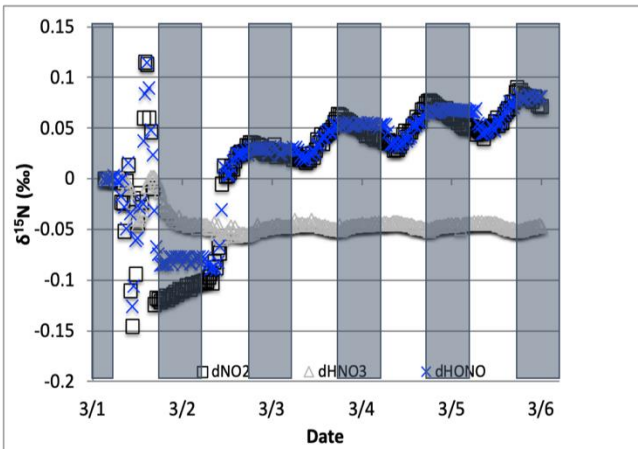

Figure 4.3.5: The difference between the $\delta^{15}N$ values of NO_2, HONO, and HNO_3 when NO_3 + VOC → HNO_3 reactions are included and excluded (NO was omitted for clarity). The 5-day simulation was under the conditions list in Table C3e. Total VOC mixing ratios during the last day of the March 1 simulation was 550-670 ppb C.

The NO_3 + VOC KIE induced a minor diurnal pattern on the $\delta^{15}N$ values of NO_x, and HONO, and a trend for HNO_3 for the March test case, but the size of the effect was relatively small (e.g., < 0.4‰; Fig. 4.11). At the start of the simulation (3 am), there is no HNO_3, therefore the initial HNO_3 is produced via OH production of HNO_3 (R39),

$\delta^{15}N$ values of HNO_3 decreased from 0.35 to 0.2‰ during the night. The pattern is because of increasing the importance of R91-R97 in HNO_3 production at night. The smallness of the effect is because α values are all relatively small, the average δ for the NO_3 + VOC is about -4‰, and the relatively small amount of HNO_3 produced via these pathways (around 2.6 % of 24-hour HNO_3). The first source of the HNO_3 in the simulation (3 to 6 am) is the NO_3 + VOC reactions and results in a slight negative $\delta^{15}N$ in HNO_3 value (-0.01‰). This leaves the residual NO_3^- ^{15}N enriched that is then photolyzed into NO_2 at sunrise and used NO_2 + OH → HNO_3 production resulting in slight positive $\delta^{15}N$ values (+0.35‰) (Fig. 4.11). The range of the diurnal HNO_3 $\delta^{15}N$ oscillation dampens as the fraction of emitted NO that has been converted to HNO_3 has increased over time. The diurnal and multiday change in $\delta^{15}N$ of HNO_3 changes did not significantly change during the winter and summer simulations (Fig. 4.12) run with and without the KIE for R91-R97 show negligible differences, similar to those in Fig. 4.11. In conclusion, although there is some $\delta^{15}N$ effect associated with NO_3 + VOC chemistry, it is much smaller than the effects associated with the Leighton cycle, NO_2 + OH, and NO_x equilibrium.

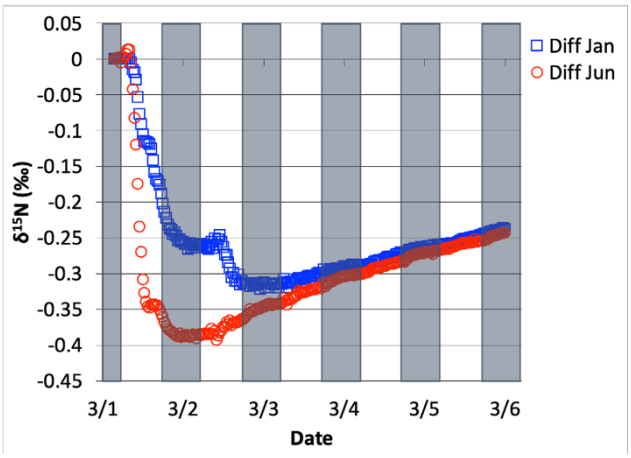

Figure 4.3.6: The difference in $\delta^{15}N(HNO_3)$ values when NO_3 + VOC → HNO_3 reactions are included and excluded, for Mar 1 simulation, relative to Jun 1 simulation (☐) and Jan 1 simulation (o). The 5-day simulation was under the conditions list in Table C.3e.

4.3.2.2 The $\delta^{15}N$ values of NO_x, HONO, and HNO_3 due to N_2O_5 reactions

The effect on the $\delta^{15}N$ values of NO_x, HNO_3, HONO associated with the EIE of N_2O_5 heterogeneous hydrolysis was also tested. March 1 simulations with N emissions and k_{N2O5} = 0.1 s^{-1} were run that included the isotope effects of the Leighton cycle (R1 and R48), NO_x isotope exchange (R238), OH production of HNO_3 (R39), and the N_2O_5 EIE (R53-54) KIE (R239) (Table C.7), as well as NO emissions. These simulations were compared to an identical simulation but where the α_{N2O5} was set equal to 1.0. This ensured that the NO_y chemistry was not altered when comparing the two simulations (i.e., α_{N2O5} = 1.029 vs. α_{N2O5} = 1.0). The effect of N_2O_5 chemistry on the $\delta^{15}N$ values of NO_2 and HNO_3 was investigated. Similar to the March 1 NO_3 + VOC tests, simulations with R1, R39, R48, R238, and R239 isotope effects active were run and then compared to simulations with the same conditions but with R239 turned off. In addition, March simulations were run using three different k_{N2O5} values (.01, 0.1, and 1) and compared to each other in order to test the range of NO_2 and HNO_3 $\delta^{15}N$ values that could be generated solely by heterogeneous N_2O_5 hydrolysis.

The average daily $\delta^{15}N$ values of HNO_3 exhibit some diurnal oscillations that roughly reach a steady-state average value after simulation day 2. At that point, HNO_3 has a $\delta^{15}N$ = +2.5‰ relative to the α_{N2O5} = 1.0 simulation. In contrast the NO_2 $\delta^{15}N$ values oscillate diurnally by about +/- 2‰ around an average daily difference of about -8‰. This change is due to the R53-54

equilibrium, which predicts ^{15}N enrichment in N_2O_5 (and thus HNO_3) and depletion in NO_3 and NO_2. The N_2O_5 produces HNO_3 with the highest $\delta^{15}N$ difference (~ +29‰) during the first simulation morning. This is because all of the initial HNO_3 is produced by N_2O_5 due to the 3 am simulation start time. The roughly steady state HNO_3 $\delta^{15}N$ value of +2.5‰ is a consequence of the fact that when α_{N2O5} = 1.0 HNO_3 is being produced by N_2O_5 at 0‰ and when α_{N2O5} =1.029 it is being produced at +29‰. The ratio of this simulated +2.5‰ value and N_2O_5 enrichment factor of +29‰ yields 0.086, the fraction of HNO_3 produced by N_2O_5. This is similar to the fraction of HNO_3 produced in simulations when the N_2O_5 reaction was active and where it is inactive, which yielded a fraction of 0.064. The difference in these fractions is because deactivating N_2O_5 chemistry changes overall NO_y chemistry and HNO_3 production (Dentener and Crutzen, 1990).

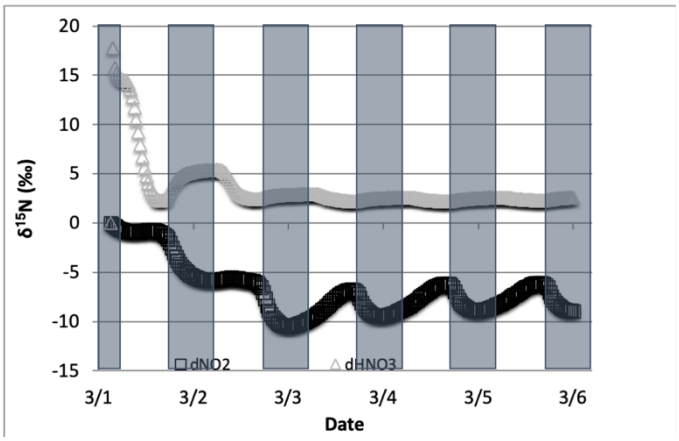

Figure 4.3.7: The difference in $\delta^{15}N$ values of NO_2 and HNO_3 when the isotopic effect during N_2O_5 heterogeneous reactions (R53-54, R239) is included (α_{N2O5} =1.029) and when it is excluded (α_{N2O5} = 1.0). The 5-day simulation was under the conditions list in Table C.3e.

The effect of N_2O_5 chemistry on the $\delta^{15}N$ values of NO_2 is more dynamic than HNO_3 (Fig. 4.13). This is mainly due to the fact that HNO_3 is continually building up over time and thus its $\delta^{15}N$ is less susceptible to change by small additions. The oscillation in the NO_2 $\delta^{15}N$ value becomes more negative at night, which corresponds to the increase in the HNO_3 $\delta^{15}N$ values. This is a reflection of ^{15}N preferentially incorporating into N_2O_5 resulting in NO_2 depleted in ^{15}N. Similar oscillations are found in NO and HONO (data not shown) as they are connected to NO_2 build-up and decay diurnally. This suggests that night-time partitioning of NO_y will have a small but measurable influence on daytime NO_y $\delta^{15}N$ values. The effect of using different k_{N2O5} values

had a small but measurable effect on the NO_2 and HNO_3 $\delta^{15}N$ values. Simulations that used a k_{N2O5} = 1.0 resulted in HNO_3 $\delta^{15}N$ values that were about 2‰ lower than those run at k_{N2O5} = 0.01 and 1‰ heavier than when k_{N2O5} = 1.0. This makes sense because the mean EIE for N_2O_5 (29‰) is lower than that for NO_2 + OH (40‰), therefore as N_2O_5 produces more HNO_3 its $\delta^{15}N$ value would decrease with respect to that of daytime HNO_3 production. Thus, the model predicts lower HNO_3 $\delta^{15}N$ values in cold, dark polluted regions (relative to the tropics where) where N_2O_5 heterogeneous hydrolysis may be the main HNO_3 production pathway (Dentener and Crutzen, 1990).

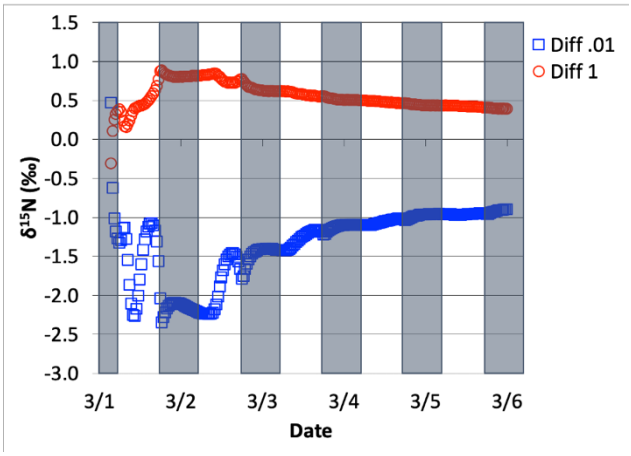

Figure 4.3.8: The difference in $\delta^{15}N(HNO_3)$ values when the isotopic effect during N_2O_5 heterogeneous reactions is included and when it is excluded, for the simulation of k_{N2O5} = 0.1, relative to 0.01 (□) and 1.0 (o). The 5-day simulation was under the conditions list in Table C.3e.

4.3.3 Case studies

The completed i_NRACM was tested using different simulation conditions that had various initial trace gas concentrations and emission rates. These test cases were labeled urban, rural, forest, and marine due to their initial conditions that were designed to mimic those environments. Initially, i_NRACM simulations were run using the 18 test cases without emission (9 for urban condition, 9 for rural condition), and 2 test cases with emission (1 for polluted atmosphere, 1 for clean atmosphere) provided in Stockwell (1997). However, we found that trace gas concentrations in these simulations do not agree with atmospheric observations (See SI) when simulations were run for several days (Altshuller, 1989; Baugues, 1986; Greenberg & Zimmerman, 1984; Logan, 1989; National Research Council, 1992; Torres & Buchan, 1988; Zimmerman et al., 1988). Thus, instead

of replicating Stockwell's cases (See SI), we set up four conditions that mimic urban, rural, forest, and marine, with the initial concentrations based on various measurements from previous studies. The emission rates of NO and total VOCs were tuned until the simulation results satisfied with the following features: a). The concentration of NO_x changes diurnally and stabilized through time; b). The concentration of O_3 changes diurnally and stabilized through time; c). VOCs are slowly consumed during nighttime (Fig. C.2-5). The molar fraction of each VOC species with respect to the total VOC emission rate was obtained from Stockwell's (1997) emission cases. It is noted that the conditions were chosen for the urban, rural, forest, and marine may not be representative of all of these environments in different countries or regions (i.e all urban environments are not the same) but was devised to bracket extremes of trace gases for most tropospheric conditions (we have ignored any polar environment simulations due to isotope effects occurring during snowpack photolysis).

4.3.3.1 The simulated $\delta^{15}N$ value under the urban conditions

The simulated $\delta^{15}N$ values of NO_x under the urban conditions have extreme diurnal oscillations and almost no multiday trend. The most striking feature is the extreme diurnal oscillations in NO and NO_2 $\delta^{15}N$ values. During the early nighttime (1/2, 6/2) the NO and NO_2 $\delta^{15}N$ values are similar (~ -5‰, $\Delta\delta^{15}N_{NO\text{-}NO2}$ =+20 ‰), but they diverge over about a 6 hour period until reaching a maximum $\Delta\delta^{15}N_{NO\text{-}NO2}$ = -35 +/- 5% (Fig. C.6). At this point, the NO $\delta^{15}N$ value has reached its minimum values of -47‰ (Jan 2) and -46‰ (June 2), which corresponds to minimums in the f_{NO} and NO mixing ratio (Fig. C.7). Meanwhile, the $\delta^{15}N$ values of NO_2 approach 0‰ as its mixing ratio and f_{NO2} have reached maximums. This indicates that the NO_x isotopic exchange ($\varepsilon_{NO/NO2}$ = -35‰ at 298K) is dominating the NO_x isotopic effects during the night and that under these conditions it requires about 6 hours for NO_x to achieve full isotopic equilibrium.

In contrast, during the daytime, the NO and NO_2 $\delta^{15}N$ values are influenced by photolysis and Leighton cycle isotope effects. In the morning, the split between NO and NO_2 $\delta^{15}N$ values is eliminated as NO_2 is photolyzed. This is, in large part, a simple isotope mass balance effect because isotopically heavy (nighttime) NO_2 is now producing isotopically heavy NO causing the NO $\delta^{15}N$ values to increase, closely following the f_{NO} (Fig. C.7). The NO_2 PHIFE (ε_{R1a} = 2.3‰ at 45 degrees of solar zenith angle), however, must also be in play otherwise NO_2 $\delta^{15}N$ values would not decrease

in the early morning. The NO_2 PHIFE, however, cannot account for the roughly 20‰ decrease in the NO_2 $\delta^{15}N$ values over the course of the mid-morning. This extra decrease is the result of NO_2 + OH (ε_{39a} = 40‰) which depletes the residual NO_2 $\delta^{15}N$ values and results in an HNO_3 $\delta^{15}N$ increase, which maximizes around noon each day (Fig. 4.15). This ε_{39a} effect reduces in importance in the late afternoon as OH mixing ratios decrease and the rate of R39 decreases to zero. The NO_x $\delta^{15}N$ equivalence point (NO_2 $\delta^{15}N \approx$ NO $\delta^{15}N$) occurs around noon in June and early evening in January, and corresponds to the NO_2 $\delta^{15}N$ minimum values of ~ -15 to -20 ‰. This highlights the fact that actinic flux plays a key role in controlling the rate of NO_x $\delta^{15}N$ oscillation rates. The combined Leighton cycle isotope effects eventually push NO $\delta^{15}N$ values above the NO_2 values, which occurs sooner in the June simulation than the Jan. because of higher NO_x Leighton cycle turnovers caused by higher photolysis rates and O_3 mixing ratios (maximums 316 ppb_v versus 236 ppb_v). Thus, unlike nighttime, when NO_x isotope exchange controls NO_x $\delta^{15}N$ values, photolysis and Leighton cycle and R39 isotope effects control daytime NO_x $\delta^{15}N$ values that in turn control HONO and HNO_3 $\delta^{15}N$ values.

The $\delta^{15}N$ values of HONO mimic the $\delta^{15}N$ values of NO during the daytime because of the production by the NO + OH reaction (R38). This mimicking is most obvious in the non-urban simulations where daytime HONO and NO $\delta^{15}N$ values are the same during the day, afterward, the HONO $\delta^{15}N$ decouples and remains constant during the night when OH is absent (Fig. 4.16-18). Interestingly, unlike the non-urban simulations, the urban nighttime HONO $\delta^{15}N$ does not remain constant. There is a slight increase in HONO $\delta^{15}N$ values earlier during the late evening, then the $\delta^{15}N$ values of HONO decrease dramatically to approach the $\delta^{15}N$ values of NO after midnight (Fig. 4.15). Since no HONO isotope effects are included in the current i_NRACM, this nighttime effect was traced to nighttime OH production under high pollution conditions. During the daytime, OH is produced by the reaction of water vapor with O^1D, which arises from ozone photolysis. In contrast, during the night, due to the absence of photolysis, the production of OH is usually assumed to be zero. However, under high VOCs, the i_NRACM model simulates OH production through a 2-step process. First, production of HO_2 by VOC + NO_3 reactions (R91, R93, R96) followed by the production of OH by HO_2 + NO_x reactions (R41-R44). Under the urban condition, the relatively high VOC concentration promotes the production of HO_2 by VOC + NO_3, and relatively high ozone concentration leads to higher NO_2 and NO_3 concentration during the

early evening, resulting in the production of OH by HO_2 + NO_x reactions (R41-R44). Because of the production of HONO by the NO + OH reaction (R38), the $\delta^{15}N$ values of HONO start approaching the nighttime $\delta^{15}N$ values of NO when the concentration of OH becomes sufficiently high. This effect can be seen in the changing OH mixing ratios during the urban night (Fig. C.7).

The daily HNO_3 $\delta^{15}N$ values reach a daily maximum around noon each simulation day and trend toward 0‰ at night and by the end of the week. The initial HNO_3 $\delta^{15}N$ values are near 0‰ because the initial HNO_3 is set to 0‰ (Table C.8). Afterward, the daily HNO_3 $\delta^{15}N$ values reach midday maximums, ~4‰ for Jan 1 and 3‰ for June 1 simulations, which corresponds to the maximums in OH concentration and HNO_3 produced by the R38 pathway. The $\delta^{15}N$ values of HNO_3 decrease during the late afternoons and nighttime, as the $\delta^{15}N$ of the reacting NO_2 decreases and as isotope effects of NO_3 +VOCs and N_2O_5 become effective. During this 5-day simulation, the HNO_3 concentrations gradually reach quasi-equilibrium, as an increasing amount of NO_x is converted into HNO_3. As a result, the small diurnal cycle in HNO_3 $\delta^{15}N$ values becomes less obvious going from simulation day 1 to day 5 where it approaches 0‰, the default $\delta^{15}N$ of NO_x emissions, which obeys the N isotope mass balance. In June 1 simulation, the rate and duration of ozone photolysis are higher, thus more O^3P is produced, comparing to Jan 1 simulation. As a result, the concentration of NO_3 during the late afternoon is higher, causing the isotope effect of the NO_3 +VOCs reaction to be stronger. Therefore, the $\delta^{15}N$ values of HNO_3 in the June 1 simulation reach the maximum value and approach to 0‰ faster than in the Jan 1 simulation.

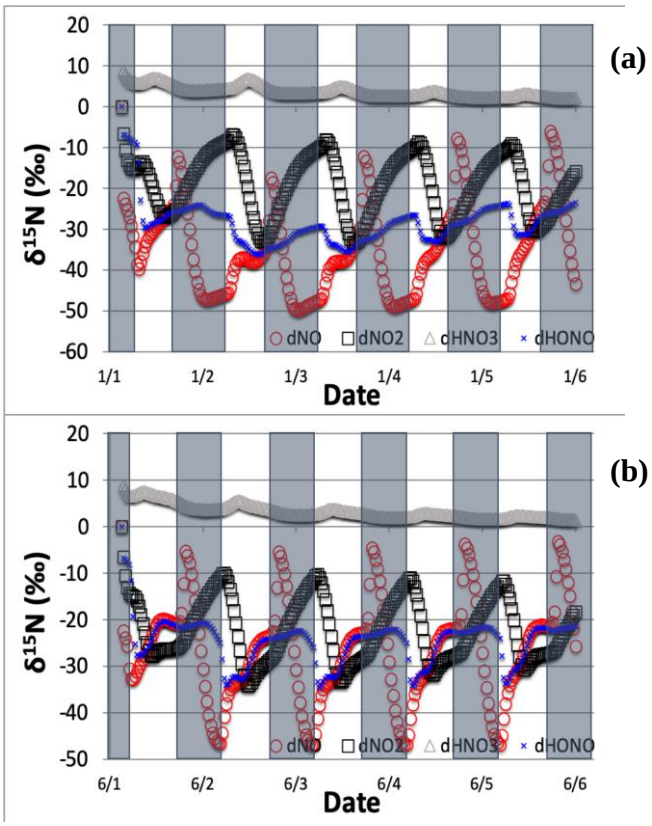

Figure 4.3.9: The $\delta^{15}N$ values of NO, NO_2, HNO_3, and HONO for the urban condition for Jan 1 (top, a) and Jun 1 (bottom, b) simulation. The 5-day simulation was under the conditions list in Table C.8.

4.3.3.2 The simulated $\delta^{15}N$ value under the rural conditions

The simulated $\delta^{15}N$ values of NO_x under the rural conditions shows similar, yet strikingly different, diurnal, and multiday trends compared to urban simulation. This difference is mainly due to the longer NO_x isotope equilibrium timescale under lower NO_x conditions. The $\Delta\delta^{15}N_{NO\text{-}NO2}$ decreases during the nighttime and reaches the -15.3‰ (June 1) just before sunrise indicating that NO_x isotopic exchange ($\varepsilon_{NO/NO2}$ = -40‰ at 298K) is not reaching full equilibration during the night.

Similar to urban simulation, $\Delta\delta^{15}N_{NO\text{-}NO2}$ in Jan 1 simulation is lower than in June 1 simulation, caused by the more remaining amount of NO_x after weaker NO_2 photolysis during the daytime. The NO_x isotopic exchange is weaker, comparing to the urban simulation, due to the lower NO_x concentrations. Therefore, the decrease of $\Delta\delta^{15}N_{NO\text{-}NO2}$ during the nighttime is less obvious than urban simulation. The $\Delta\delta^{15}N_{NO\text{-}NO2}$ gradually increases during the daytime, as the

photolysis (ε_{R1a} = 2.3‰ at 45 SZA), O_3 + NO (ε_{48a} = -6.7‰), and NO_2 + OH (ε_{39a} = 40‰) isotope effects become effective. The maximum daytime $\Delta\delta^{15}N_{NO\text{-}NO2}$ reaches at sunset, showing 5.5‰ for Jan 1 simulation and 8.5‰ for June 1 simulation. The $\Delta\delta^{15}N_{NO\text{-}NO2}$ increases by 37.6‰ and 23.8‰ during the daytime for the Jan 1 and June 1 simulation, respectively, which indicates the dominance of NO_2 + OH reaction (R39). Compared to urban simulation, the change of $\Delta\delta^{15}N_{NO\text{-}NO2}$ during the daytime is smaller, caused by weaker isotope effect from O_3 + NO (R48) reaction, because of lower ozone concentration. The change of $\Delta\delta^{15}N_{NO\text{-}NO2}$ during the daytime for the June 1 simulation is larger than that for the Jan 1 simulation, due to the higher rate and longer duration of NO_2 photolysis.

Similar to the urban simulation, the $\delta^{15}N$ values of HONO mimics the $\delta^{15}N$ values of NO during the daytime because of the production by the NO + OH reaction (R38), of which the fractionation factor (α) is zero. Unlike urban simulation, however, the $\delta^{15}N$ values of HONO remain constant at night since the concentration of HO_x (OH + HO_2) is not enough to produce HONO, due to the relatively low VOC (3.3% of urban value) and ozone (16.7% of urban value) concentration. A key caveat about the $\delta^{15}N$ values of HONO is that we have excluded any KIE associated with the NO + OH reaction because it has not been measured or calculated. Since this is the termination reaction, any isotope effect in this reaction would have a large influence on HONO $\delta^{15}N$ values. In the forest and ocean environment simulations, the $\delta^{15}N$ values of HONO also mimic the $\delta^{15}N$ values of daytime NO so they will not be discussed in the subsequent sections of this paper.

The $\delta^{15}N$ values of HNO_3 increases during the mornings and reaches the maximum of 7.5‰ for Jan 1 simulation and 8.4‰ for June 1 simulation, as the isotope effects of NO_2 + OH (ε_{39a} = 40‰) greater than NO_3 +VOCs ($\Sigma\varepsilon_{91a\sim\varepsilon97a}$ = -27.8‰). The maximum $\delta^{15}N$ value of HNO_3 is higher than that in urban simulation, as the lower VOC concentration weakens the NO_3 +VOCs reactions. The $\delta^{15}N$ values of HNO_3 decreases during the late afternoons and nighttime, as the isotope effects of NO_3 + VOCs are effective. The same as urban simulation, the diurnal trend of $\delta^{15}N(HNO_3)$ becomes less obvious from simulation day 1 to day 5 and approaches 0‰ at the end of the simulation, as an increasing amount of NO_x being converted into HNO_3. Again, the $\delta^{15}N$ values of HNO_3 in June 1 simulation approaches to 0‰ faster than in Jan 1 simulation, due to more $O(^3P)$ from stronger O_3 photolysis.

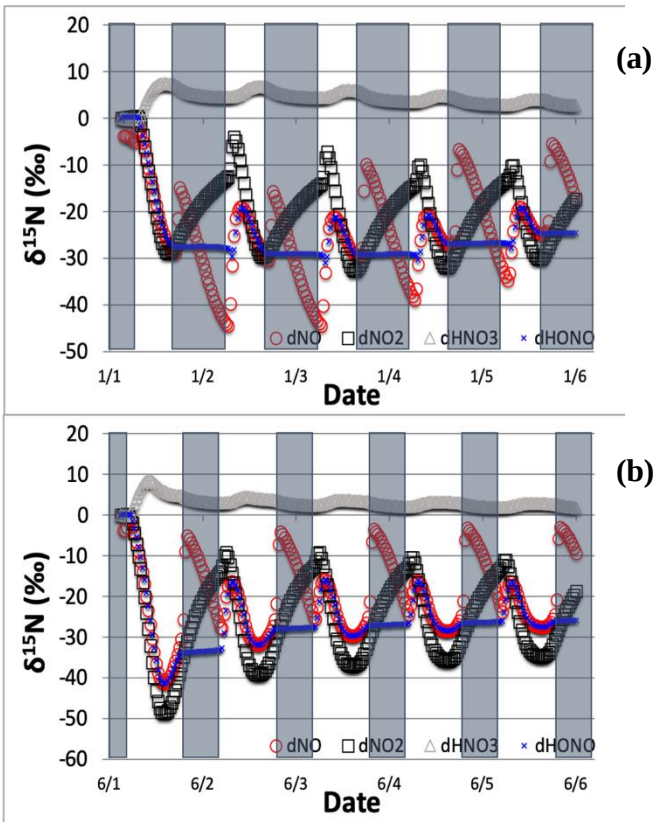

Figure 4.3.10: The $\delta^{15}N$ values of NO, NO_2, HNO_3, and HONO for the rural condition for Jan 1 (top, a) and Jun 1 (bottom, b) simulation. The 5-day simulation was under the conditions list in Table C.8.

4.3.3.3 The simulated $\delta^{15}N$ value under the forest conditions

The simulation of $\delta^{15}N$ values of NO_x under the forest conditions shows a similar, yet significantly different diurnal and multiday trend, compared to urban and rural simulation. There are obvious differences between the daily oscillations in NO_2 $\delta^{15}N$ values in the forest relative to urban simulations. In the cleaner atmosphere, NO_2 $\delta^{15}N$ values only change daily by only about 5‰, whereas they oscillate by 30 to 40‰ in the urban case. Likewise, daily oscillations in NO $\delta^{15}N$ values are weaker in the forest conditions (5-10‰) than in the urban and suburban conditions (30-40‰). This results in a decrease in the $\Delta\delta^{15}N_{NO\text{-}NO2}$ during the nighttime, reaching minimum values of -11.0‰ (Jan 1) and -4.5‰ (June 1) compared to roughly -40‰ in the urban case. This shows that under low NO_x conditions the NO_x isotopic exchange cannot occur fast enough to reach its full effect. This effect is more pronounced in June, due to the short night, relative to the January simulations that have about 14 hours of darkness at this latitude. This is similar to urban and rural

simulations, where $\Delta\delta^{15}N_{NO-NO2}$ in Jan 1 simulation is lower than in June 1 simulation, because of reduced NO_2 photolysis hours. The decrease of $\Delta\delta^{15}N_{NO-NO2}$ during the night time in the forest conditions is less obvious than urban and rural simulation. The $\Delta\delta^{15}N_{NO-NO2}$ gradually increases during the daytime, as the photolysis (ε_{R1a} = 4.2‰), O_3 + NO (ε_{48a} = -6.7‰), and NO_2 + OH (ε_{39a} = 40‰) isotope effects become effective. This results in daytime NO $\delta^{15}N$ values that are less negative than those in NO_2, opposite of the urban case where NO_2 $\delta^{15}N$ values are either higher or equal to NO. As a consequence, the daytime $\Delta\delta^{15}N_{NO-NO2}$ values are positive (as opposed to negative in the urban case) and reach a maximum at sunset (6.5‰ for Jan 1, 7.1‰ for June 1). The $\Delta\delta^{15}N_{NO-NO2}$ increases by 17.5‰ and 13.3‰ during the daytime for Jan 1 and June 1 simulation, respectively, which indicates the dominance of NO_2 + OH reaction (R39). The change of $\Delta\delta^{15}N_{NO-NO2}$ during the daytime is smaller than both urban and rural simulation, due to lower ozone concentration. The change of $\Delta\delta^{15}N_{NO-NO2}$ during the daytime for the June 1 simulation is larger than that for the Jan 1 simulation, due to the higher rate and longer duration of NO_2 photolysis.

The most striking difference between the "clean" and "polluted" simulations is the separation of HNO_3 $\delta^{15}N$ values from the initial (emission) NO_x $\delta^{15}N$ value (defined as 0‰). The $\delta^{15}N$ values of HNO_3 increases daily by about 1-4‰ due to the isotope effects of NO_2 + OH (ε_{39a} = 40‰) but are constant or slightly decrease throughout the night due to NO_3 +VOCs reactions under these conditions. This leads to a stepwise increase in HNO_3 $\delta^{15}N$ values that reach maximums of about +10‰ by the end of the 5-day simulation. This is in contrast to the urban and suburban simulations where HNO_3 $\delta^{15}N$ values reach minimums (~ 0‰) at the end of the simulation. This is an isotope mass balance effect driven by how N is partitioned into NO_y under different conditions. Under high NO_x and VOC conditions (urban, rural) over 90% of emitted NO_x has portioned into HNO_3 by the end of the 5-day simulation, thus the HNO_3 $\delta^{15}N$ value approaches that of the NO_x emissions. In contrast, under low NO_x and VOC conditions (forest, ocean) only about 33% of emitted NO_x has portioned into HNO_3, with the bulk of the remainder as NO_x (21%) and organic nitrate (42%) and PAN (4%). In this case, the isotope effects incorporated into the reactions that are responsible for this partitioning manifest themselves in the $\delta^{15}N$ of the individual NOy compounds. For example, i_NRACM predicts that forest conditions will produce $\delta^{15}N$ values in organic nitrate even though there are no isotope effects associated with organic nitrate production or loss in i_NRACM. This highlights how the $\delta^{15}N$ values are tracing shifts in NO_y oxidation pathways.

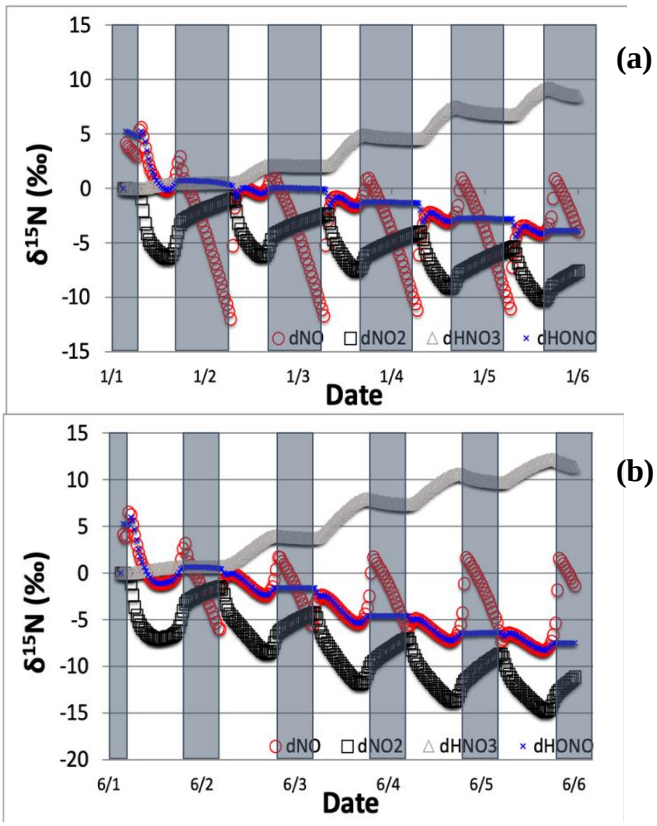

Figure 4.3.11: The $\delta^{15}N$ values of NO, NO_2, HNO_3, and HONO for forest condition for Jan 1 (top, a) and June 1 (bottom, b) simulation. The 5-day simulation was under the conditions list in Table C.8.

4.3.3.4 The simulated $\delta^{15}N$ value under the marine conditions

The simulation of $\delta^{15}N$ values of NO_y under the marine conditions is very similar to the forest simulation. The daily oscillations and multiday change in the $\delta^{15}N$ of NO_x, HONO, and HNO_3 all follow the same pattern as the forest simulations but with slight amplification in all compounds. The nighttime change in NO $\delta^{15}N$ is 15‰ (Jan) and 10‰ (June) is about 5‰ larger than in the forest simulation. Similarly, the ocean condition nighttime change in NO_2 $\delta^{15}N$ (9 to 12‰) is about 5‰ larger than in the forest simulation. The result is that the $\Delta\delta^{15}N_{NO\text{-}NO2}$ values decrease during the nighttime, reaching minimum values of -13.5‰ (Jan 1) and -3.6‰ (June 1). Again this shows that under low NO_x conditions the NO_x isotopic exchange is not occurring fast enough to reach its full effect ($\varepsilon_{NO/NO2}$ = -35‰ at 298K) and is more pronounced in the summer months due to the short night., relative to the January simulations that have about 14 hours of darkness at this latitude. Similar to the forest simulation the $\delta^{15}N$ values of HNO_3 increase stepwise during the daytime and

reach the maximum of 16‰ for both the Jan and June simulations. This is about 5‰ larger than in the forest simulation and 15‰ higher than the urban case. Similar to forest simulation, the emission rate of NO_x is higher than the conversion rate of NO_x to HNO_3. As a result, the amount of NO_x increases from simulation day 1 to day 5. The abundant NO_x promotes the production of HNO_3 during the daytime by NO_2 + OH reaction (R39), which leads to the overall increasing trend throughout the simulation period.

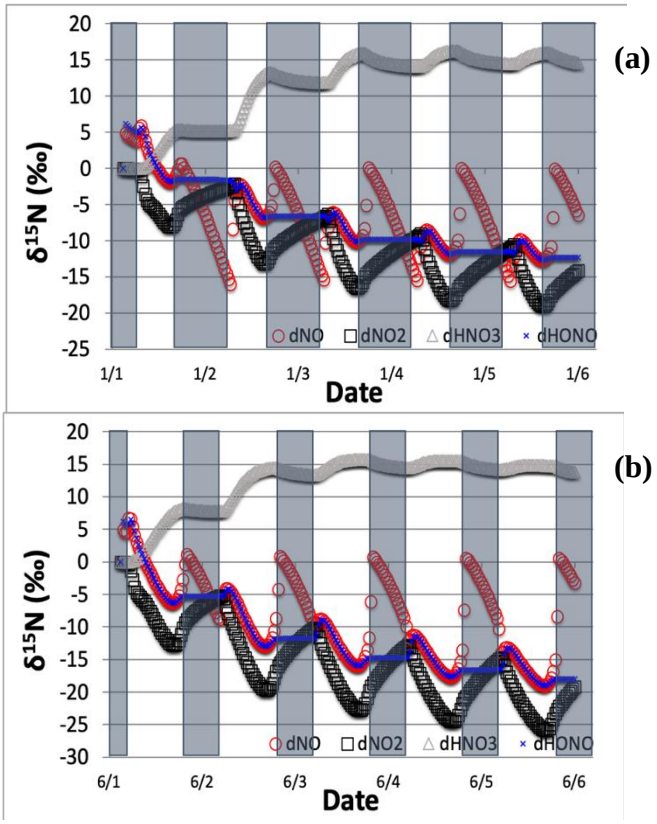

Figure 4.3.12. The $\delta^{15}N$ values of NO, NO_2, HNO_3, and HONO for the marine condition for Jan 1 (top, a) and Jun 1 (bottom, b) simulation. The 5-day simulation was under the conditions list in Table C.8.

4.3.4 Model comparison with observations

There are a number of challenges when trying to compare the i_NRACM model predictions of NO_y $\delta^{15}N$ values with observations in the real world. First, there has yet to be a study where the $\delta^{15}N$ values of NO, NO_2, and NO_3^- have been simultaneously measured. The most abundant data is on the $\delta^{15}N$ value of NO_3^- in aerosols or rainwater. Even with these studies, a direct comparison

is difficult because the $\delta^{15}N$ value of the source NO_x may be variable in space and time. The $\delta^{15}N$ value of NO_x sources can range from -40 to + 20 ‰ and both NO_x sources and NO_3^- deposition will be a strong function of the transport history of the air mass that is sampled. Without a 3-D chemical transport model that includes the i_NRACM mechanism, a direct comparison with most NO_3^- $\delta^{15}N$ studies would be tenuous. In addition, most NO_y $\delta^{15}N$ studies provide neither trace gas concentrations (NO_x, O_3, CO, VOC) nor local trace gas emissions that would be required to constrain i_NRACM for it makes an accurate prediction of secondary pollutants or $\delta^{15}N$ values.

The most complete dataset for which to evaluate the i_NRACM mechanism is from Riha (2013) in a study in Tucson AZ, USA. In that study, $PM_{2.5}$ and PM_{10} were collected weekly (24-hour period) for one year (2006) and the $\delta^{15}N$ value of water-soluble NO_3^- was determined (Fig. 4.19). Into PM mass and NO_3^- $\delta^{15}N$ data, local measurements of trace gases (accept VOCs) and meteorology (temperature, relative humidity, wind) were available. In addition, detailed local primary pollutant emission inventories have been developed (Diem and Comrie, 2001). Tucson is a city with little industry or power generation so roughly 80% of the NO_x is due to vehicles and the relative proportion of all NOx sources is invariant throughout the year. Further, Tucson is surrounded by a desert landscape and by and large not influences by regional pollution sources outside the city. These factors overcome some of the uncertainties discussed above. i_NRACM was initialized with observed trace gas concentrations and NO_x and VOC emissions were based on previous work (Riha, 2013) and the source NO_x $\delta^{15}N$ value was set to -3‰, typical of vehicle emissions (Walter et al., 2015) and run on the first day of each month. The predicted NO_3^- (as HNO_3) $\delta^{15}N$ values (After 48 hours) matched remarkably well with the observed values in $PM_{2.5}$ and PM_{10} (Fig. 4.19). Observed maximums were in the winter months, peaking January at 15‰ close to the model maximum in January of 17%. The minimum $\delta^{15}N$ values (-2‰) are measured in July, similar to model predictions of 0‰ during July. The model captures the seasonal trend quite well, including the Spring plateau. This suggests that at this location, the observed seasonal variation in PM NO_3^- $\delta^{15}N$ values can be explained by isotope effects associated with the photochemical conversion of NO_x into HNO_3.

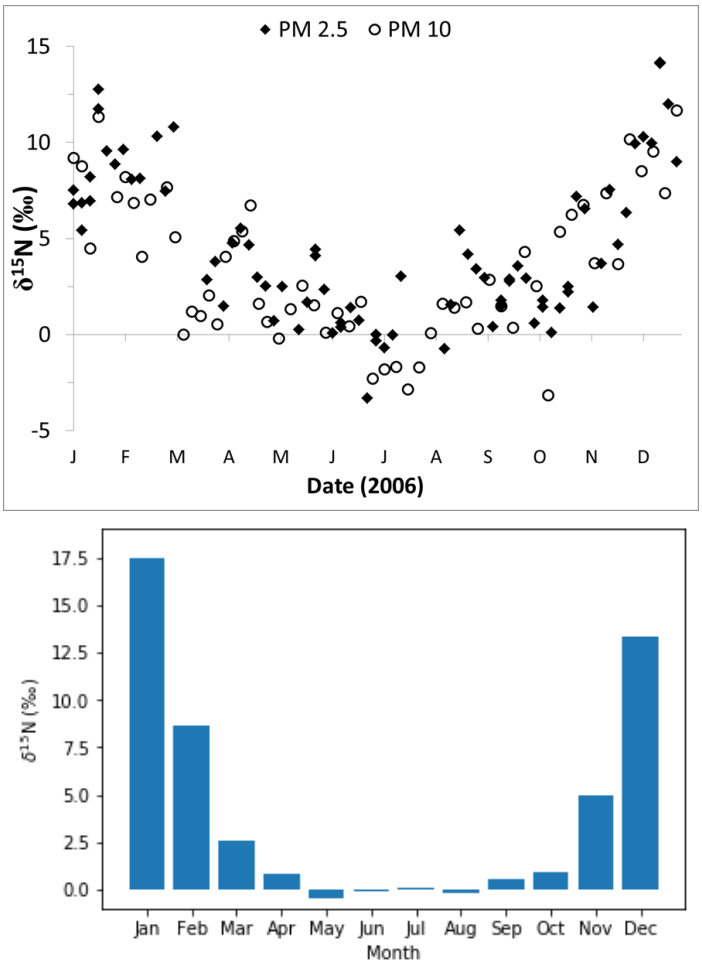

Figure 4.3.13: The upper panel is the observed NO_3^- $\delta^{15}N$ values of PM in the city of Tucson (Riha, 2013). The lower panel is the NO_3^- $\delta^{15}N$ values of HNO_3 predicted by the i_NRACM mechanism. Minimums, maximums, and seasonal change in $\delta^{15}N$ in PM NO_3^- can be explained by the EIE, KIE, and PHIFE occurring during NO_y cycling.

4.4 Conclusion

We have developed the first 0-D photochemical box model for ^{15}N compounds in the tropospheric NO_x-NO_y cycle. It was shown that of the 100's of N reactions in the RACM mechanism only a handful significantly impact the main NO_y compounds (NO_x, HONO, HNO_3). Primarily these are Leighton cycle reactions, NO_2 + OH, and NO_x isotope exchange, with N_2O_5 and nitrate radical reactions having a significant, but a minor influence on NO_y $\delta^{15}N$ values. It was also shown that there were two factors that can dramatically influence the simulated NO_y $\delta^{15}N$ values. The first is the size of the isotope fractions factors (KIE, EIE, PHIFE) for any given reaction. For example, the large EIE (assumed) for NO_2 + OH was much more important than the small KIE

associated with NO_3 + VOC reactions. This highlights the need for direct or computational measurements of KIE, EIE, PHIFE in NO_y reactions, particularly R39. The second is that shifts in oxidation pathways caused by pollutant loading are being reflected in the NO_y $\delta^{15}N$ values. In particular, high NO_x + VOC environments with aerosols tend to favor $\delta^{15}N$ that reflects NO_x isotope exchange and N_2O_5 uptake, while clean environments favor $\delta^{15}N$ that reflects NO_x cycle and OH oxidation reactions. This highlights that NO_y $\delta^{15}N$ values are not only related to NO_x sources but also affected by NO_y chemistry.

The i_NRACM model makes a number of predictions that could be tested by measuring the $\delta^{15}N$ values of various NO_y compounds in different environments and at different temporal scales. First, the model predicts very large diurnal changes in NO_x $\delta^{15}N$ values in all environments, ranging from 10 to 40‰, which could be easily be detected with even the crudest isotope methods (± 2‰). Second, it predicts that in highly polluted environments the $\delta^{15}N$ value of HNO_3 will be close to the $\delta^{15}N$ value of the NO_x sources in the area, but in clean environments, it will be 10 to 15‰ heavier. Third, it predicts seasonal and latitudinal trends in HNO_3 $\delta^{15}N$ values driven by sunlight and the shifting photochemical pathways associated with it. It predicts higher winter HNO_3 $\delta^{15}N$ values, as NO_x isotope exchange becomes more important relative to Leighton and OH reactions that become dominant in the summer. This effect should be more pronounced as a function of latitude. There should be relatively minor changes in equatorial HNO_3 $\delta^{15}N$ values since sunlight hours do not vary, significant changes at mid-latitudes (50% seasonal sunlight change) change, and essentially a bimodal change at the poles (ignoring snowpack recycling effects). Fourth, it predicts there will be $\delta^{15}N$ variations in key NO_y reservoirs yet to be measured such as organic nitrates and PAN. Finally, the i_NRACM model predicts that the most dramatic changes in NO_y $\delta^{15}N$ changes will occur after rain events where NO_y is largely removed from the atmosphere by wet depositions. Post rain, the NO_y $\delta^{15}N$ values effectively "reset", particularly HNO_3, and will have their biggest difference relative to the NO_x $\delta^{15}N$ before trending to the NO_x source over time. The i_NRACM model suggests that knowing how is NO_y partitioned and the $\delta^{15}N$ value of one (or more) compound that the $\delta^{15}N$ of the NO_x source can be determined. This, in turn, can be used as a constraint on NO_x budgets from the local to the regional and global scale.

This effect that tropospheric photochemistry has on NO_y $\delta^{15}N$ values was tested and shown to generally initially lead to higher $\delta^{15}N$ values in HNO_3 relative to the initial NO_x. The difference

between the $\delta^{15}N$ of HNO_3 relative to the initial (emitted) NO_x was typical ~ +10‰ by the 2nd and 3rd day of the simulation. This seems consistent with observations that show NO_3^- $\delta^{15}N$ values (positive $\delta^{15}N$) are typically higher than most NO_x sources (negative $\delta^{15}N$). This difference between NO_x source and HNO_3 $\delta^{15}N$ values tend to diminish as the simulation progresses as either all of the initial NO_x is oxidized to HNO_3 (no emission simulations) or the proportion of HNO_3 to total N approaches 1 (emission scenarios). This type of bias can be eliminated by incorporating i_NRACM into 3-D chemical transport models that account for time-dependent deposition and emission of NO_y.

The model accuracy and its validation could be improved with additional research. The i_NRACM model could be refined by additional theoretical and/or experimental determination of the isotope fractionation factors for the N reactions. First and foremost, the fractionation factor for the NO_2 + OH reaction needs evaluation in a more robust manner. Likewise, the fractionation factor for the NO + OH, another 3-body reaction, will have a large influence on HONO $\delta^{15}N$ values and determining its value will be key for interesting future HONO $\delta^{15}N$ data. The fractionation factor for NO_2 photolysis requires attention given the limitation of the ΔZPE PHIFE model (Blake et al., 2003; Liang et al., 2004; Miller and Yung, 2000). On the validation end, the simultaneous measurement of $\delta^{15}N$ in multiple NO_y compounds would expose the accuracy or limitations of the i_NRACM model in a quantitative way. Repeating these simultaneous measurements in a range of environments would test the predictions made by our test case simulations.

CHAPTER 5. SIMULATING Δ15N OF ATMOSPHERIC NOX IN CMAQ VERSION 5.2.1, BASED ON 15N INCORPORATED SMOKE VERSION 4.6, WRF VERSION 4.0, AS WELL AS 15N INCORPORATED RACM VERSION 2 AND CB VERSION 6, FOR ASSESSING THE ROLE GAS-PHASE TROPOSPHERIC PHOTOCHEMISTRY PLAYS IN CONTROLLING THE ISOTOPIC COMPOSITION OF NOX, NOY, AND ATMOSPHERIC NITRATE

The following chapter is a reprint from an article currently in press (Fang, H. and Michalski, G. Simulating $\delta^{15}N$ of atmospheric NO_x in CMAQ version 5.2.1, based on ^{15}N incorporated SMOKE version 4.6, WRF version 4.0, as well as ^{15}N incorporated RACM version 2 and CB version 6, for assessing the role gas-phase tropospheric photochemistry plays in controlling the isotopic composition of NO_x, NO_y, and atmospheric nitrate. *Geoscientific Model Development*)

5.1 Introduction

NO_x (NO_x = nitric oxide (NO) + nitrogen dioxide (NO_2)) are the important trace gases that affect atmospheric chemistry, air quality, and climate. The oxidation NO_x and subsequent deposition of atmospheric nitrate and other NO_y compounds have a number of negative impacts on the environment. Deposition of NO_y has been linked to acid rain, groundwater nitrate (EPA regulated), and the degradation of terrestrial and aquatic ecosystems (Galloway et al., 2004). NO_x oxidation in the presence of VOCs elevates the ground-level O_3 and generates secondary particulates, both of which affect the human respiratory system, causing health problems and mortality in susceptible populations (Lighty et al., 2000; Seinfeld & Pandis, 2006). Aerosols have a pronounced impact on cloud physics, enhancing the reflection of solar radiation (Schwartz, 1996). In addition, nitrate particles and secondary aerosols (sulfate, organics) generated by NO_x driven oxidation are the largest sources of uncertainty in current climate models that predict future warming due to greenhouse gases. It is therefore important to understand NO_x sources, how it is transported and mixed in the atmosphere, how it is removed from the atmosphere due to the conversion to NO_y and deposition, in order to make informed decisions regarding air quality policy and mitigation strategies for a sustainable future. To evaluate and constrain NO_x sources, atmospheric mixing and transport, and removal by chemistry and deposition, we developed a new model that incorporates N stable isotopes into a Chemical Transport Model (CTM) in a series of

studies and comparing the model simulation results under different scenarios with the corresponding isotopic measurements.

The atmospheric NO_x sources from both anthropogenic emissions, such as automobiles, power plants, agriculture, livestock waste, as well as natural processes, including by-product of nitrification and denitrification occurring in soil, and lightning (Galloway et al., 2004; Reis et al., 2009). The estimation of emissions from each source is called emission inventory, among which the most well-known and commonly used is the National Emission Inventory (NEI), updated by USEPA (the United States Environmental Protection Agency) every three years. The emissions from different sources are categorized into four categories: a) biogenic, the by-products of microbial nitrification and denitrification occurring in the soil; b) mobile, the emission based on on-road vehicle activity; c) point, the anthropogenic emissions that are located at a fixed, stationary position, significantly contribute from power plants; and d) area, the anthropogenic emissions that spread over a spatial extent and individually too small in magnitude to report as point sources, primarily from livestock and off-road vehicles.

The previous companion paper (Fang & Michalski, 2020) has discussed the uncertainties in NO_x emission inventories. To effectively trace NO_x sources in the atmosphere, nitrogen stable isotope composition ($\delta^{15}N$) of NO_x was used, due to the distinctive differences in $\delta^{15}N$ values of NO_x (Fig. 5.1), source from soil (Li & Wang, 2008; Felix & Elliott, 2014; Yu & Elliott, 2017; Miller et al., 2018), wastes (Felix & Elliott, 2014), vehicles (Moore, 1977; Heaton, 1990; Ammann et al., 1999; Pearson et al., 2000; Savard et al., 2009; Redling et al., 2013; Fibiger, 2014; Felix & Elliott, 2014; Walters et al., 2015a; Walters et al., 2015b), and power plants (Heaton, 1987; Heaton, 1990; Snape, 2003; Felix et al., 2012; Felix et al., 2015; Walters et al, 2015a; Savard et al., 2017).

The $\delta^{15}N$ of NO_x is determined by

$$\delta^{15}N(NO_x)\ (‰) = [(^{15}NO_x/^{14}NO_x) / (^{15}N_2/^{14}N_2)_{air} - 1] \times 1000) \quad \text{Eq. (5.1)}$$

where $^{15}NO_x/^{14}NO_x$ is the measurement of relative abundance of ^{15}N to ^{14}N in atmospheric NO_x, compared with the ratio of nitrogen in the air, which has a $^{15}N_2/^{14}N_2 = 0.0036$.

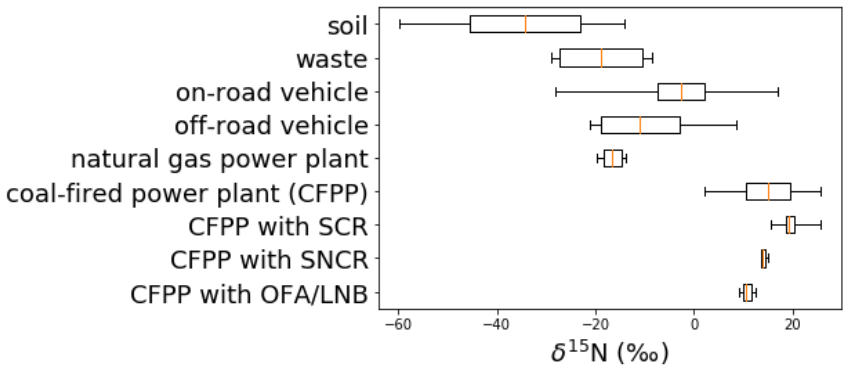

Figure 5.1.1: Box (lower quartile, median, upper quartile) and whisker (lower extreme, upper extreme) plot of the distribution of $\delta^{15}N$ values for NO_x emission sources

Here we have simulated the atmospheric $^{15}NO_x$ and compared the predicted $\delta^{15}N(NO_x)$ values under different scenarios with the corresponding measurements. The factors, which were taken into account for the simulation of the $\delta^{15}N$ of atmospheric NO_x during the NO_x chemical lifetime are: a). The spatiotemporal variability in the $\delta^{15}N$ values of NO_x emissions; b). The atmospheric mixing, dispersion, and transport of tropospheric NO_x from different sources; c) The isotope effects occurring during the tropospheric photochemistry that converts NO_x to NO_y and d). The wet and dry deposition of NO_x and NO_y. In the companion papers, we discussed the effects due to the variation of the $\delta^{15}N$ value by different NO_x emission sources in space and time (Fang & Michalski, 2020), as well as the effects due to the impacts from atmospheric processes, which are mixing, disperse, transport, and deposition (Fang & Michalski, 2021). In this paper, we explore the last factor, the impacts from the tropospheric photochemistry, by incorporating the ^{15}N isotope reaction scheme, which was developed previously in the 0D box model (Michalski et al., 2020), into CMAQ as a new chemical mechanism, to simulate the $\delta^{15}N$ of NO_y compounds. The goal of this paper is to explore how gas-phase tropospheric photochemistry alters the $\delta^{15}N$ of atmospheric NO_x in time and space in the Midwestern US. After the series of exploration of the changes in $\delta^{15}N$ values along the "journey" of atmospheric NO_x, the accuracy of the NO_x emission inventory could be evaluated using ^{15}N.

5.2 Methodology

In a previous companion paper (Fang & Michalski, 2020), CMAQ simulations of the $\delta^{15}N$ of atmospheric NO_x, based on the ^{15}N incorporated emission dataset, as well as meteorology condition generated from WRF (the Weather Research and Forecasting Model), were compared with the corresponding atmospheric measurements. However, the spatiotemporal variability in $\delta^{15}N$ of atmospheric NO_x with the consideration of atmospheric processes does not sufficiently resolve the changes in the corresponding measurements, due to the lack of isotope effects associated with tropospheric photochemistry. For example, NO_x emitted from a single grid cell dominated by a coal-fired power plant, with a NO_x $\delta^{15}N$ around +12‰, would propagate to the surrounding grids, causing the isotopically heavier NO_x, until the $\delta^{15}N$ along the plume being dissolved by the $\delta^{15}N$ over the surrounding grids. On the other hand, the period of the mixing, disperse, and transport of the atmospheric NO_x cannot exceed the lifetime, of which NO_x transforms into NO_y. Therefore, the effects of atmospheric transport and deposition processes were overestimated in the previous simulation in some circumstances. This bias was reduced by magnified the dry and wet deposition rate, for the substitution of the removal of atmospheric NO_x by chemistry, in addition to atmospheric deposition (the "fake chemistry" scenario, Fig. D.1, Fang & Michalski, 2020). However, this method is not satisfactory enough, since the conversion of NO_x into NO_y is dynamic and relative to the real-time concentration of reactants.

In this study, we investigate the role that tropospheric gas phase photochemistry plays in the spatiotemporal distribution of atmospheric $\delta^{15}N(NO_x)$ values. The previously developed ^{15}N emission dataset (Fang & Michalski, 2020) was used as input for the CMAQ simulation with the ^{15}N incorporated chemical mechanism (Michalski et al., 2020), to explore the isotope effects associated with the photochemical transformation of NO_x into HNO_3 and other higher N oxides. Therefore, this paper focuses on the removal effects of tropospheric photochemistry. The simulations using the same NEI and meteorology condition but the different chemical mechanism (Carbon Bond (CB) version 6 and Regional Atmospheric Chemistry Mechanism (RACM) version 2) were compared, in order to explore how different gas-phase tropospheric photochemistry alters the atmospheric $\delta^{15}N(NO_x)$ and impacts the atmospheric $\delta^{15}N(NO_y)$. The simulations over the full domain and nested domain were conducted, in order to explore and eliminate the bias near the domain boundary

5.2.1 The domain of the study

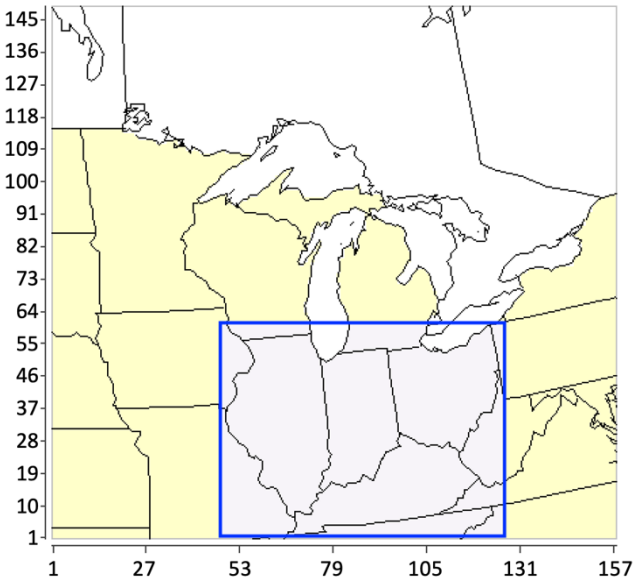

Figure 5.2.1: The full geographic domain (yellow) and nested domain (light purple) for the study.

Two domains were set for the CMAQ simulations, a larger domain encompassing the Midwestern region of the United States, which fully covers the states of Minnesota, Iowa, Missouri, Wisconsin, Illinois, Michigan, Indiana, Kentucky, Ohio, and West Virginia, and partially covers North Dakota, South Dakota, Nebraska, Kansas, Tennessee, North Carolina, Virginia, Maryland, Pennsylvania, and New York (Fig. 5.2, in yellow), and a smaller domain, nested from the central portion of the Midwestern domain, which fully covers the states of Indiana, Illinois, Ohio, and Kentucky was extracted (Fig. 5.2, in light purple). The simulations over both domains used a uniform 12 km x 12 km grid with 34 vertical layers, extends from surface to 50 mb level. The thickness of each layer increases with height, from 50 m at the bottom to 600 m near the top. The purpose of conducting the nested-domain simulation is to reduce the model bias near the border, for which the boundary conditions were extracted from the simulation results over the larger domain (Fang & Michalski, 2021).

5.2.2 The preparations for the simulations

The ^{15}N incorporated emission input dataset used by the CCTM (CMAQ's CTM) simulation was prepared from the previous companion research (Fang & Michalski, 2020), depending on the methods briefly discussed below. First, the US EPA trace gas emission model SMOKE (Sparse Matrix Operator Kernel Emissions) was used, to handle each source of NO_x emissions in NEI in order, so that the annual emission amounts (in tons) from each county based on 2002 NEI was converted into the emission rates (in moles/second or grams/second) on hourly basis and partitions into the gridded format. The main sources of NO_x emissions in the NEI, on-road gasoline, on-road diesel, off-road gasoline, off-road diesel, coal-fired power plant, natural gas power plant, soil, and livestock wastes, were processed in four different modules (Biogenic, Mobile, Point, and Area) of the SMOKE model (Table 5.1). Then, ^{15}N was incorporated into SMOKE outputs of each NEI emission sectors, based on the corresponding $\delta^{15}N$ values (Fang & Michalski, 2020; Table 5.1) and the definition of $\delta^{15}N$ (‰) (Eq. (5.2-3)).

$$^{15}NO_x(i) = {}^{14}NO_x(i) \times {}^{15}R_{NO_x}(i) \qquad \text{Eq. (5.2)}$$

where $^{14}NO_x$ (i) is the NO_x emissions for each source (i) obtained from NEI and $^{15}R_{NOxi}$ is a ^{15}N emission factor ($^{15}NO_{Xi}/^{14}NO_{xi}$) calculated by:

$$^{15}R_{NO_x}(i) = \left(\frac{\delta^{15}N_{NO_x(i)}}{1000} + 1\right) \times 0.0036 \qquad \text{Eq. (5.3)}$$

$\delta^{15}N_{NOx(i)}$ is the $\delta^{15}N$ value of each NO_x source (Table 5.1) and 0.0036 is the $^{15}N/^{14}N$ of air N_2, the reference point for $\delta^{15}N$ measurements.

Finally, the ^{15}N incorporated SMOKE outputs of each NEI emission sectors were merged into one netCDF file for each day (Eq. (5.4)).

$$^{15}NO_x(total) = \sum {}^{15}NO_x(i) \qquad \text{Eq. (5.4)}$$

The $\delta^{15}N$ of total NO_x emission was calculated by

$$\delta^{15}N_{NO_x\,(total)} = \left(\frac{\frac{^{15}NO_x\,(total)}{^{14}NO_x\,(total)}}{0.0036} - 1\right) \times 1000 \qquad \text{Eq. (5.5)}$$

SMOKE Category	NEI Sector	δ^{15}N-NO_x (‰) in this study
Biogenic	Soil	-34.3 (Felix & Elliott, 2014)
Area	Livestock Waste	-18.8 (Felix & Elliott, 2014)
	Off-road Gasoline	-11.5 (Walters et al., 2015b)
	Off-road Diesel	-10.5 (Walters et al., 2015b)
Mobile	On-road Gasoline	-2.7 (Walters et al., 2015b)
	On-road Diesel	-2.5 (Walters et al., 2015b)
Point	Coal-fired EGUs	+15 (Felix et al., 2012)
	Natural Gas EGUs	-16.5 (Walters et al., 2015)

Table 5.2.1: δ^{15}N values for NO_x emission sources by SMOKE processing category and NEI sector

The meteorology input dataset used by the CCTM simulation was prepared from the previous companion research (Fang & Michalski, 2021), depending on the methods briefly discussed below. First, the NARR (North American Regional Reanalysis) and NAM (North American Mesoscale Forecast System) was used to covert the weather observations into gridded meteorological elements, with the same vertical extent and resolution but slightly larger domain as the emission input dataset. Then, WRF (the Weather Research and Forecasting Model) was run to generate the gridded meteorology files on an hourly basis, with the same projection setting as the emission input dataset, which is Lambert Conformal, with the standard parallel of 33 N and 45 N, the central meridian of 97 W. Finally, the CMAQ-ready meteorology input dataset was prepared based on WRF output by running the CMAQ module MCIP (the Meteorology-Chemistry Interface Processor), after extracting the data of the necessary parameters for the same geographic domain as emission input dataset, converting the units and/or adjusting the resolution of the data if necessary, as well as organizing the parameters into seven netCDF files that embedded with I/O API (input/output applications programming interface) (Fang & Michalski, 2021).

The initial condition and boundary condition for the simulation were prepared, based on the steps described by Fang & Michalski (2021), and are briefly discussed below. The CMAQ module ICON (Initial Conditions Processor) and BCON (Boundary Conditions Processor) were used to simulate initial condition and boundary condition, respectively. The preparations of the initial condition and the boundary condition for the simulation over both the full domain and nested domain (Fig. 5.2) are slightly different. For the simulation over the full domain, the initial condition was derived from the CMAQ default ASCII vertical profiles, of which the NO_x background concentration at each grid is lower than 0.25 ppb, creating a "clean" atmospheric chemical condition within the domain in the initial time step of the simulation. The boundary condition for the simulation over the full domain was also derived from the CMAQ default ASCII vertical profiles, so that the "clean" atmospheric chemical condition outside the domain was consistently preserved, throughout the simulation. The $^{15}NO_x$ was incorporated into the outputs of ICON and BCON based on Eq. (5.1-3), assuming $\delta^{15}N = 0$ at the initial time step and outside the domain of the simulation. For the simulation over the nested domain, the preparation of the initial condition was the same, while the preparation of the boundary condition was different. For the nested domain, only the boundary condition at day 1 of the simulation was derived from the CMAQ default ASCII vertical profiles, starting on day 2, the boundary condition was extracted from the CCTM output of the full-domain simulation. The reason for treating the boundary condition differently is due to the bias near the boundary of the domain. Under the assumption of CMAQ simulation, the region out of the domain was regarded as the "emission-free zone". Therefore, when the air mass transporting out of the domain or transporting from the outside "emission-free zone" into the domain, the atmospheric NO_x is diluted, so that the atmospheric $\delta^{15}N(NO_x)$ is flattened. However, this assumption does not sufficiently reflect the reality. For example, a coal-fired power plant is located to the west of the western boundary of the domain. According to the model assumption, the NO_x emission from this power plant will be eliminated. Thus, the $\delta^{15}N$ of the atmospheric NO_x along the western domain boundary will be zero. While, in reality, the isotopically heavier NO_x emission from the coal-fired power plant would propagate across the western boundary. As a result, the atmospheric NO_x along the segment of the western domain boundary, which the plume of the coal-fired power plant intersects, will be obviously isotopically heavier than the CMAQ simulation. The representative circumstances showing the bias on the boundary of the domain were shown and discussed in detail in the previous companion

research (Fang & Michalski, 2021), which only focusing the atmospheric processes. After including the effects from tropospheric photochemistry on $\delta^{15}N$ of atmospheric NO_x, this bias becomes more obvious.

5.2.3 ^{15}N incorporated chemical mechanisms

To explore the impact of tropospheric photochemistry on the $\delta^{15}N$ of atmospheric NO_x, NO_3^-, and other higher N oxides, ^{15}N was incorporated into chemical mechanisms CB and RACM, so that new chemical mechanisms were created for CCTM simulation. The ^{15}N incorporated mechanism has been developed and tested in the 0D box model previously (Michalski et al., 2020). To build up the ^{15}N incorporated CB and RACM on CMAQ, several CMAQ utilities were conducted. The ^{15}N incorporated CB was developed from the preexisting cb6r3_ae6_aq mechanism (CB, version 6 revision 3 for the gas-phase mechanism, version 6 for the aerosol chemistry and aqueous chemistry). The CMAQ utility named chemmech (chemical mechanism compiler) was run to create the FORTRAN 90 modules for data and function of ^{15}N incorporated CB, for the compilation and simulation of CCTM. As the input files for chemmech simulation, the chemical mechanism definition file and species namelist files, divided into gas-phase, aerosol-phase, non-reactive, and tracer, was first replicated from the preexisting cb6r3_ae6_aq mechanism. Then, the N compounds in the species namelist files were replicated with ^{15}N. Similarly, the reactions involving N in the mechanism chemical definition file were replicated with ^{15}N, the isotope fractionation factors for the new reactions were assigned to the reaction rates based on the previous companion study (Michalski et al., 2020). The data module generated from chemmech requires the cross-sections and quantum yields (CSQY) data for the calculation of its photolysis rate, which was simulated by another CMAQ utility named inline_phot_preproc (inline photolysis preprocessor). In addition to the data module generated from chemmech, the simulation of inline_phot_preproc reads the CSQY data for the photolysis species, which are preexisting on CMAQ. Finally, the CMAQ utility named create_ebi was used, to generate an Euler Backward Iterative (EBI) solver for the ^{15}N incorporated CB, for the better accuracy and computational efficiency of CCTM simulation (Hertel et al., 1993). Similar to the ^{15}N incorporated CB, the ^{15}N incorporated RACM was developed from the preexisting racm2_ae6_aq mechanism (RACM, version 2 for the gas-phase mechanism, version 6 for the aerosol chemistry and aqueous chemistry), following the same step introduced above. The isotopic effects associated with tropospheric

photochemistry occur in the conversion of NO_x to NO_y, mainly controlled by the reactions with OH (Eq. (5.6)) and NO_3 (Eq. (5.7)), which lead to the isotopically lighter NO_x (Michalski et al., 2020). The conversion between the gas-phase NO_x, NO_3^-, and other higher N oxides to the corresponding aerosol phase chemicals potentially alters their $\delta^{15}N$ values. However, due to the lack of knowledge about the phase conversion rate of $^{15}NO_y$, with respect to the phase conversion rate of $^{14}NO_y$, the use of aerosol module on CMAQ was disabled in the driver routine function of EBI solver. Thus, this study only focuses on the isotope effects from the gas-phase tropospheric photochemistry, in order to verify the ^{15}N incorporated mechanism developed previously (Michalski et al., 2020) by the 3D CTM CMAQ.

$$^{15}NO_2 + OH \rightarrow H^{15}NO_3,\ \alpha=1.04 \qquad \text{Eq. (5.6)}$$

$$^{15}NO_2 + NO_3 \rightarrow N_2O_5,\ \alpha=1.0266 \qquad \text{Eq. (5.7)}$$

5.3 Result and Discussion

5.3.1 Simulated spatial variability in $\delta^{15}N$ of atmospheric NO_x

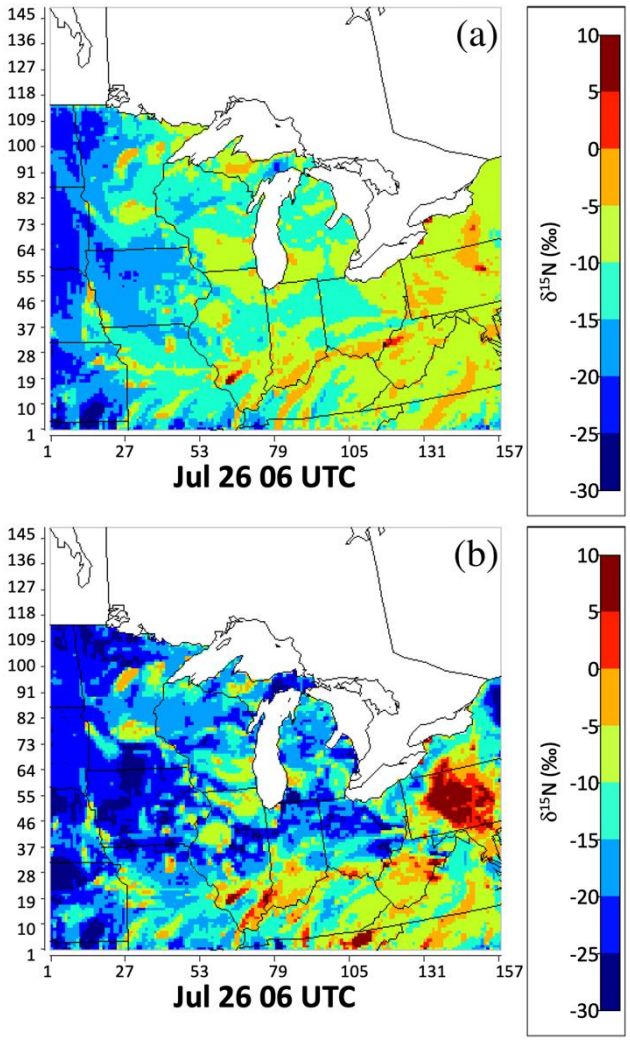

Figure 5.3.1: The $\delta^{15}N$ values of atmospheric NO_x based on NEI-2002 and 2016 meteorology (a: "no chemistry" scenario), based on NEI-2002, 2016 meteorology, and CB (b: "with chemistry" scenario), at 06 UTC on July 26, are presented by color in each grid. The warmer the color, the higher $\delta^{15}N$ values of atmospheric NO_x.

We first examine the spatial heterogeneity of simulated $\delta^{15}N(NO_x)$ values at a specific time (at 06 UTC on July 26) within the Midwestern domain and explore how gas-phase tropospheric photochemistry alters the $\delta^{15}N$ values relative to the previous simulation under the "no chemistry" scenario (emission + transport). The "no chemistry" simulation of $\delta^{15}N(NO_x)$ values ranged from

-33.5‰ to 12.4‰ over the grids within the domain (Fig. 5.3a). The geographic distribution of $\delta^{15}N(NO_x)$ values indicates the atmospheric mixing and transport of NO_x emission from different sources. The $\delta^{15}N$ values of NO_x among the grids within big cities mainly ranged between -10‰ and -5‰, as NO_x with a higher fraction of on-road vehicles ($\delta^{15}N$=-2.7‰) being emitted into grids. The NO_x from big cities was then transported to the surrounding rural areas, which alters the $\delta^{15}N(NO_x)$ to similar values (-10‰ ~ -5‰). The $\delta^{15}N$ values of NO_x among the grids resolve major highways mainly ranged between -15‰ and -10‰, as NO_x with a relatively lower fraction of on-road vehicles, comparing to the grids within big cities, being emitted into grids. The NO_x from major highways was then transported to the surrounding rural areas, which alters the $\delta^{15}N(NO_x)$ to similar values (-15‰ ~ -10‰). The $\delta^{15}N$ values of NO_x among the grids contain power plants are higher than -5‰, as NO_x dominated by coal-fired EGUs (+15‰) and hybrid-fired EGUs (using both coal and natural gas (-16.5‰) for combustion) being emitted into the grids. The NO_x from power plants was then transported to the surrounding rural area, which alters the $\delta^{15}N(NO_x)$ as a function distance away from the power plant, showing the propagation of the plume. The $\delta^{15}N$ values of NO_x among the grids with the distinct distance away from urban area are lower than -15‰, due to the higher fraction of biogenic NO_x emission (nitrification and denitrification), as well as the absence of the transport of anthropogenic source from big cities, major highways, or power plants.

The effect of gas-phase tropospheric photochemistry on the spatial distribution of $\delta^{15}N(NO_x)$ were then taken into account by incorporating ^{15}N into chemical mechanisms for the CCTM simulation. The $\delta^{15}N(NO_x)$ values under the "with chemistry" (Fig. 5.3b) scenario (emission + transport + chemistry) was compared with the $\delta^{15}N(NO_x)$ values under the "no chemistry" (Fig. 5.3a) scenario (emission + transport). The domain average $\delta^{15}N$ under the "with chemistry" scenario (-14.4‰) is lower than the domain average $\delta^{15}N$ under the "no chemistry" scenario (-11.5‰). The NO_x conversion to NO_y was taken into account for the simulation of atmospheric NO_x under the "with chemistry" scenario, in addition to the local NO_x emission, as well as the dispersing, transport, and mixing of atmospheric NO_x. Due to the conversion of NO_x to NO_y, which offsets the effect of local NO_x emission on the atmospheric $\delta^{15}N(NO_x)$, the NO_x transported from surrounding grids has a stronger impact on the local $\delta^{15}N(NO_x)$, comparing to under the "no chemistry" scenario. As a result, the $\delta^{15}N(NO_x)$ under the "with chemistry" (Fig. 5.3b) scenario is

lower than under the "no chemistry" (Fig. 5.3a) among the regions downstream of biogenic NO_x emission ($\delta^{15}N$=-34.3‰). Similarly, over the grids surrounding big cities and the grids resolve the plume of power plants, such as central Pennsylvania, the $\delta^{15}N$ under the "with chemistry" scenario is higher, due to the transport of the isotopically heavier NO_x from the surrounding grids. In the previous research, a simulation with the amplified deposition rates was conducted, in order to mimic the removal of atmospheric NO_x by chemistry. The amplified deposition simulation shows similar isotopic effects as the simulation under the "with chemistry" scenario, which strengthens the impact of NO_x transported from surrounding grids on the local atmospheric $\delta^{15}N(NO_x)$ (Fig. D.1). However, this is not an accurate assumption, since the conversion rates of NO_x depend on the dynamic concentration of the reactants in the atmosphere.

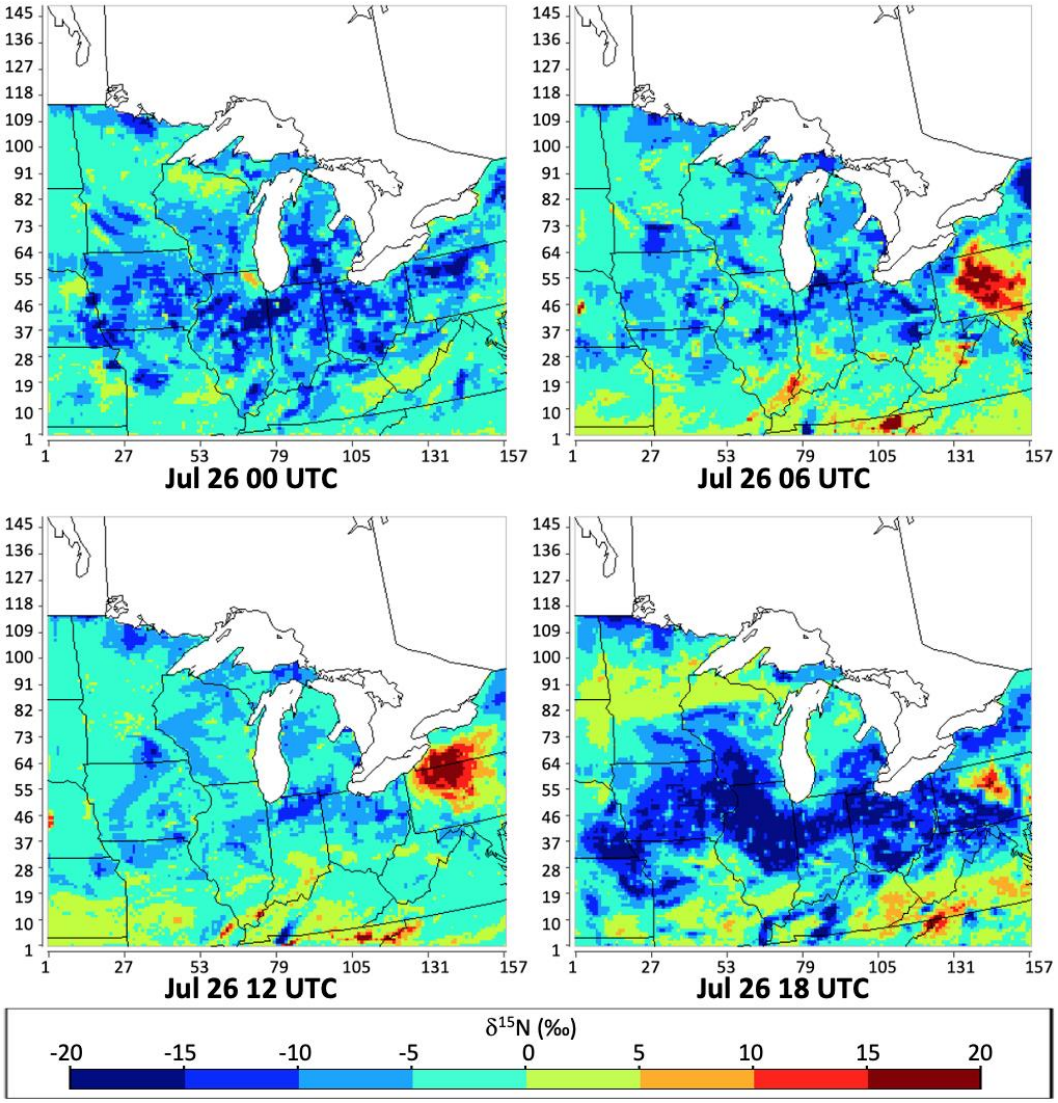

Figure 5.3.2: The difference between the $\delta^{15}N$ (‰) value of atmospheric NO_x under the "with chemistry" scenario and "no chemistry" scenario ($\Delta\delta^{15}N_{chem}$) from 00 UTC to 18 UTC on July 26, 2016, throughout the Midwest simulated by CMAQ, based on NEI-2002, 2016 meteorology, and CB.

In order to explore the time evolution of the effect of gas-phase tropospheric photochemistry on the spatial distribution of $\delta^{15}N(NO_x)$, we define $\Delta\delta^{15}N_{chem} = \delta^{15}N(NO_x)_{chem} - \delta^{15}N(NO_x)_{nochem}$, the difference between the $\delta^{15}N$ value of atmospheric NO_x under the "with chemistry" scenario and the "no chemistry" scenario. We arbitrarily select July 26 (Fig. 5.4) and examine diurnal effects by calculating $\Delta\delta^{15}N_{chem}$ at 00 UTC (local sunset), 06 UTC (local midnight), 12 UTC (local sunrise), and 18 UTC (local noon). The overall pattern of the hourly $\Delta\delta^{15}N_{chem}$ values shows a

decreasing trend of $\Delta\delta^{15}N_{chem}$ from local sunrise to noon. This is driven by the increase in ozone photolysis rate during this period (Eq. (5.8)). As a result, the mixing ratio of OH is increasing from local sunrise to noon (Eq. (5.9)). Since the $^{15}NO_2$ reacts faster with OH than $^{14}NO_2$ (Eq. (5.6)), the $\Delta\delta^{15}N_{chem}$ is negative. Furthermore, due to the increasing mixing ratio of OH, the isotope effect of the NO_2 + OH reaction was magnified. Thus, the $\Delta\delta^{15}N_{chem}$ decreases from local sunrise to noon. During the local afternoon, as the ozone photolysis rate decreases, the mixing ratio of OH decreases. Therefore, the $\Delta\delta^{15}N_{chem}$ increases. The $\Delta\delta^{15}N_{chem}$ continues to increase during the nighttime, due to the absence of ozone photolysis. The overall pattern of the hourly $\Delta\delta^{15}N_{chem}$ values, which shows a decreasing trend of $\Delta\delta^{15}N_{chem}$ from local sunrise to noon, and an increasing trend of $\Delta\delta^{15}N_{chem}$ from local noon to sunrise, agrees well with the previous study in the 0D box model (Michalski et al., 2020).

$$O_3 + h\nu \rightarrow O_2 + O^1D$$

Eq. (5.8)

$$O^1D + H_2O \rightarrow 2OH$$

Eq. (5.9)

$$NO_2 + O_3 \rightarrow NO_3 + O_2$$

Eq. (5.10)

5.3.2 Seasonal variation in $\delta^{15}N$ of NO_x

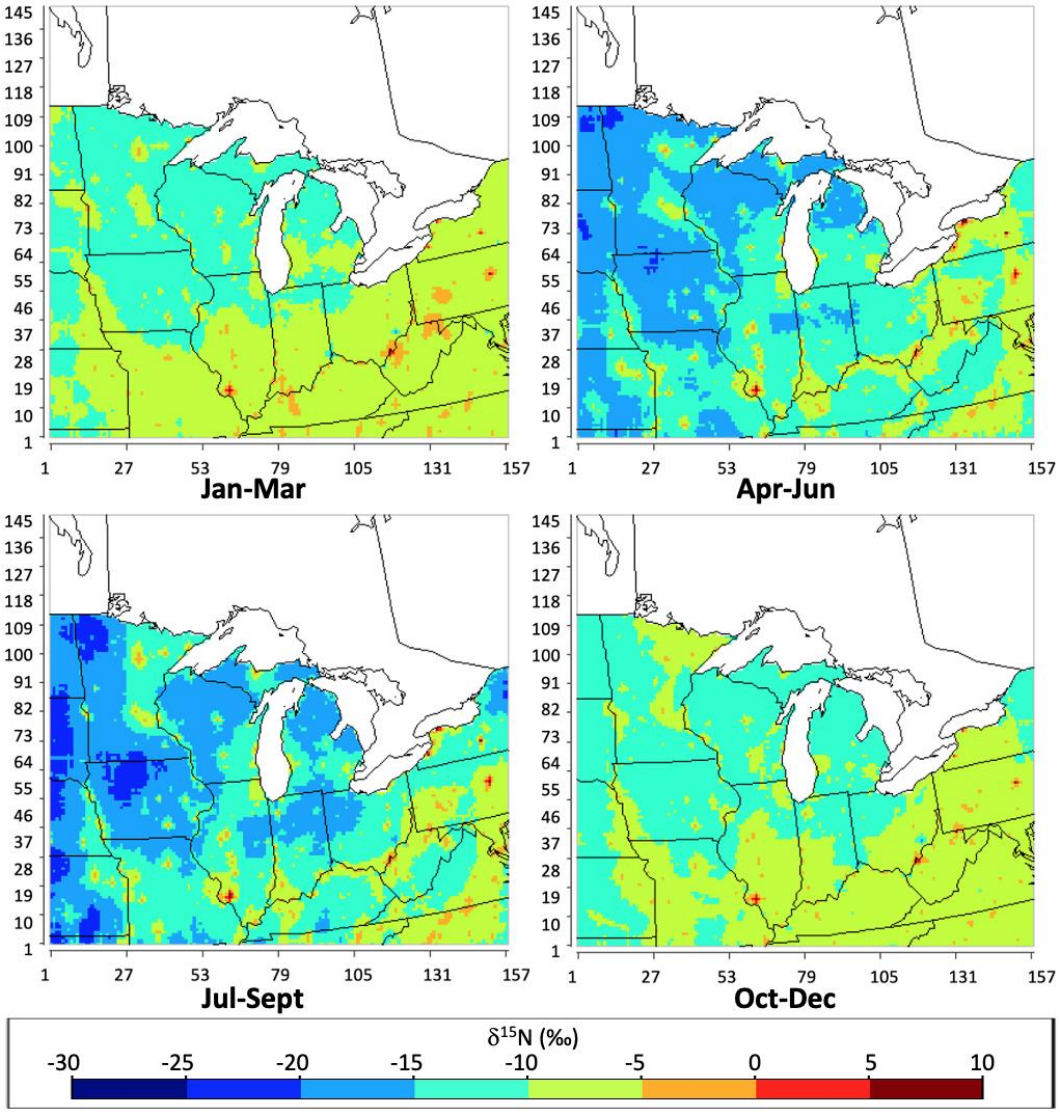

Figure 5.3.3: The geographical distribution of the $\delta^{15}N$ value of atmospheric NO_x in each season (Winter: Jan-Mar; Spring: Apr-Jun; Summer: Jul-Sep; Fall: Oct-Dec) in per mil (‰) throughout the Midwest simulated by CMAQ, based on NEI-2002, 2016 meteorology, and CB.

We next examine the temporal heterogeneity of atmospheric $\delta^{15}N(NO_x)$ under the "with chemistry" scenario over the domain and explore whether the effects of gas-phase tropospheric photochemistry changes seasonally (Fig. 5.5). The $\delta^{15}N(NO_x)$ under the "with chemistry" scenario ranged from -25.0‰ to 11.5‰, with the annual average over the Midwest domain of -11.1‰. Compared with the seasonal $\delta^{15}N(NO_x)$ under the "no chemistry" scenario (Fang & Michalski,

2021), the $\delta^{15}N(NO_x)$ under the "with chemistry" scenario has a lower overall average and wider range, due to the isotope effects associated with the tropospheric photochemistry, which cause the atmospheric NO_x becoming lighter. The maps for different seasons show the obvious changes in $\delta^{15}N$ values over western regions of the Midwest, from -15~ -10‰ in Oct-Mar to -25 ~ -20‰ in Apr-Oct.

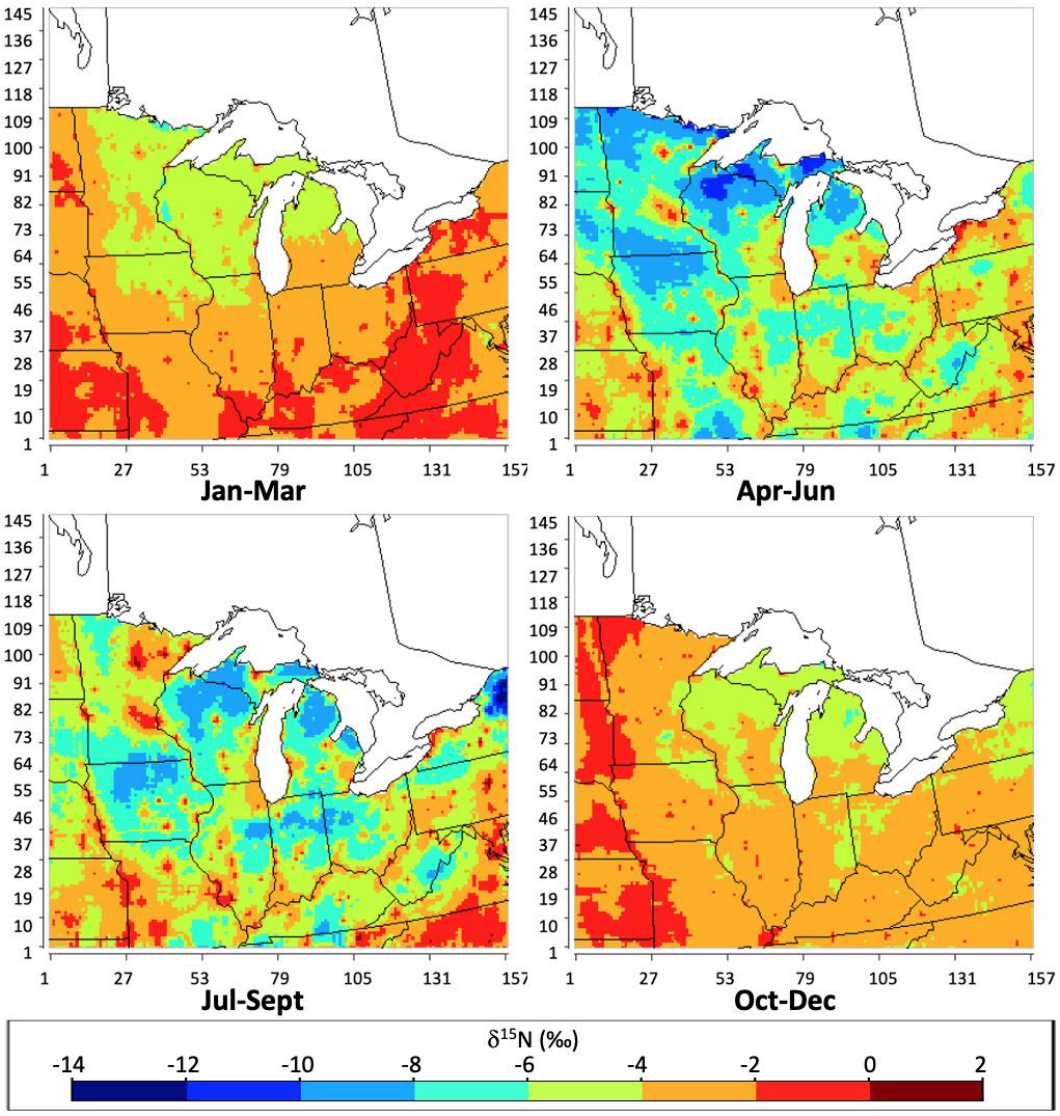

Figure 5.3.4: The difference between the $\delta^{15}N$ (‰) value of atmospheric NO_x under the "with chemistry" scenario and "no chemistry" scenario ($\Delta\delta^{15}N_{chem}$) during each season (Winter: Jan-Mar; Spring: Apr-Jun; Summer: Jul-Sep; Fall: Oct-Dec) in per mil (‰) throughout the Midwest simulated by CMAQ, based on NEI-2002, 2016 meteorology, and CB.

In order to qualitatively analyze the changes in $\delta^{15}N$ values driven by gas-phase tropospheric photochemistry, the difference between the $\delta^{15}N$ value of atmospheric NO_x under the "with chemistry" scenario and "no chemistry" scenario ($\Delta\delta^{15}N_{chem}$) on the seasonal basis were shown (Fig. 5.6). The seasonal $\Delta\delta^{15}N_{chem}$ values range from -13.90‰ to 1.61‰, with an average of -4.17‰. The overall pattern of the $\Delta\delta^{15}N_{chem}$ values indicates that the atmospheric NO_x became isotopically lighter over the majority of the grids. This could be explained by isotope effects occurring during the conversion of NO_x to NO_y. The isotope effects of the conversion of NO_x to NO_y are mainly controlled by $^{15}NO_2 + OH \rightarrow H^{15}NO_3$ reaction (Eq. (5.6)) during the daytime with the fractionation factor α=1.04, and by $^{15}NO_2 + NO_3 \rightarrow {}^{15}NNO_5$ (Eq. (5.7)) reaction during the nighttime with the fractionation factor α=1.0266. Thus, both reactions lead to the isotopically lighter NO_x. The isotope effects of gas-phase tropospheric photochemistry are stronger during spring and summer (Apr-Sep) than during fall and winter (Oct-Mar), showing the more negative $\Delta\delta^{15}N_{chem}$ during spring and summer, especially among the grids within the rural area. This could be explained by the relatively longer photolysis hours during the period from April to September. Due to the increased duration of O_3 photolysis, more OH (Fig. D.2) and NO_3 (Fig. D.3) were produced (Eq. (5.8-10)), which leads to the increase in the reaction rates of NO_x conversion to NO_y. Therefore, the isotope effects on atmospheric NO_x is stronger during spring and summer.

5.3.3 Different chemical mechanisms

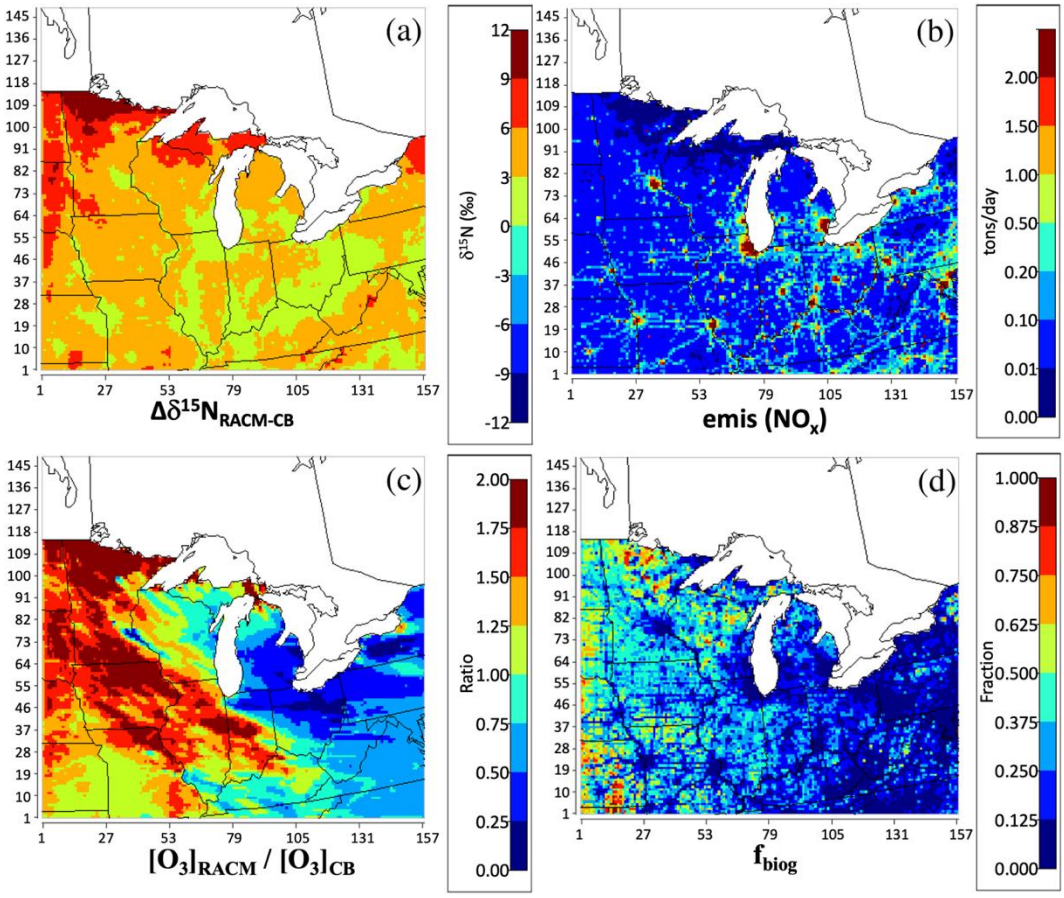

Figure 5.3.5: The difference between the CMAQ simulated $\delta^{15}N$ (‰) value of atmospheric NO_x using RACM and CB ($\Delta\delta^{15}N_{RACM-CB}$) in per mil (‰) (a); The daily average emission rate of NO_x (emis (NO_x)) simulated by SMOKE (b); The ratio between the CMAQ simulated ozone concentration using RACM and CB ($[O_3]_{RACM}$ / $[O_3]_{CB}$) (d) ; The fraction of NO_x emission from biogenic sources (f_{biog}) simulated by SMOKE (c), throughout the Midwest, based on NEI-2002 and 2016 meteorology.

The atmospheric $\delta^{15}N(NO_x)$ simulated using different chemical mechanisms varies. In order to compare the spatial heterogeneity of the atmospheric $\delta^{15}N(NO_x)$ under simulation from the different chemical mechanisms, the same analysis was done on the simulation using RACM (Fig. D.4). Overall, the simulated atmospheric NO_x using RACM is isotopically heavier than using CB (Fig. 5.7a). The isotopic effects associated with the conversion of NO_x to NO_y are mainly controlled by the reaction with OH during the daytime (Eq. (5.8)) and the reaction with NO_3 during the nighttime (Eq. (5.10)), of which the fractionation factors are greater than one. Thus, both

reactions lead to the isotopically lighter NO_x. As stated in section 5.3.1, atmospheric NO_x depends on local NO_x emission, NO_x conversion to NO_y, and NO_x transported from the surrounding area, in rural areas, where the local NO_x emission rate is relatively lower, the local $\delta^{15}N(NO_x)$ are dominated by NO_x transported from surrounding grids, after considering the tropospheric photochemistry (Fig. 5.7b). The difference in $\delta^{15}N$ between RACM and CB simulations are determined by the concentration of ozone (Fig. 5.7c). In the western part of the domain, where natural NO_x emissions are dominant among most of the grids (Fig. 5.7d), isotopically heavier NO_x transported from nearby cities or power plants has stronger impacts on the atmospheric NO_x in rural areas in RACM simulation, due to the relatively higher ozone concentration. Thus, the $\delta^{15}N(NO_x)$ in the RACM simulation is higher. In the eastern part of the domain, where anthropogenic NO_x emissions are dominant among most of the grids (Fig. 5.7d), the conversion of NO_x to NO_y is slower in RACM simulation, due to the relatively lower ozone concentration. Thus, the $\delta^{15}N(NO_x)$ in the RACM simulation is higher.

5.3.4 The simulation over the nested domain

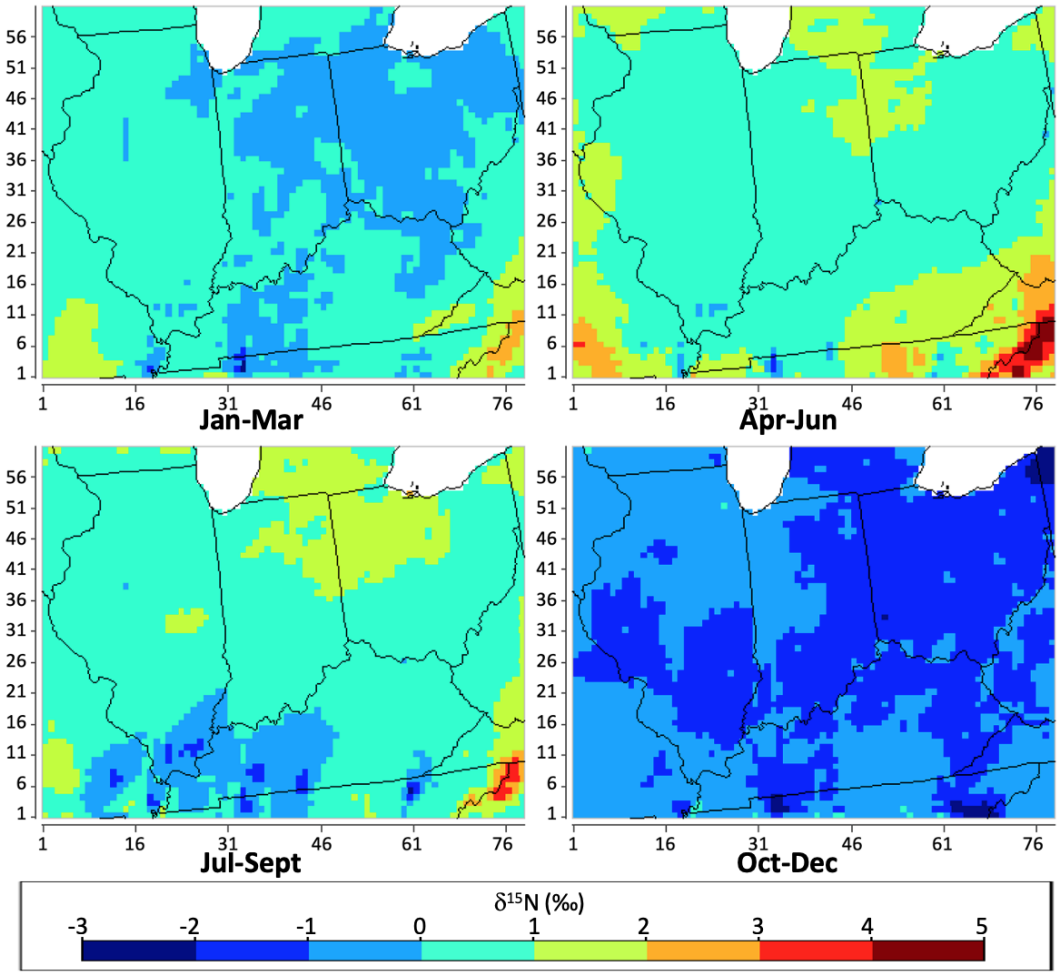

Figure 5.3.6: The geographical distribution of the difference between nested-domain simulation and full-domain simulation of $\delta^{15}N$ value of atmospheric NO_x ($\Delta\delta^{15}N_{nested\text{-}full}$) in each season (Winter: Jan-Mar; Spring: Apr-Jun; Summer: Jul-Sep; Fall: Oct-Dec) in per mil (‰) within IN, IL, OH, and KY, based on NEI-2002, 2016 meteorology, and CB.

We next examine the temporal heterogeneity of difference in atmospheric $\delta^{15}N(NO_x)$ between the simulation over the nested domain and over the full domain ($\Delta\delta^{15}N_{nested\text{-}full}$), to explore the bias in $\delta^{15}N(NO_x)$ values, caused by the transport of air mass from the research area to the "emission-free zone" outside the domain or vice versa. The nested domain overs the states of Indiana, Illinois, Ohio, and Kentucky, where the measurements of $\delta^{15}N$ values at NADP sites are available. The atmospheric $\delta^{15}N(NO_x)$ from nested-domain simulation has a similar overall pattern as the

atmospheric $\delta^{15}N(NO_x)$ from full-domain simulation within the same domain (Fig. D.5). In order to qualitatively analyze the effects from the motion of the air mass across the domain boundary, the difference between the $\delta^{15}N$ value of atmospheric NO_x from nested-domain simulation and from full-domain simulation ($\Delta\delta^{15}N_{nested\text{-}full}$) on the seasonal basis were shown (Fig. 5.8). The $\Delta\delta^{15}N_{nested\text{-}full}$ values ranged between -3‰ and +5‰ over most of the grids within the nested domain. The difference between the $\delta^{15}N$ from nested-domain simulation and full-domain simulation under the "with chemistry" scenario is more obvious than the same analysis for the "no chemistry" scenario in the previous work (Fang & Michalski, 2021). The atmospheric NO_x simulated over the nested domain is isotopically heavier during the period from January to September over most of the grids within the domain, while isotopically lighter during the period from October to December.

5.3.5 Model-observation comparison

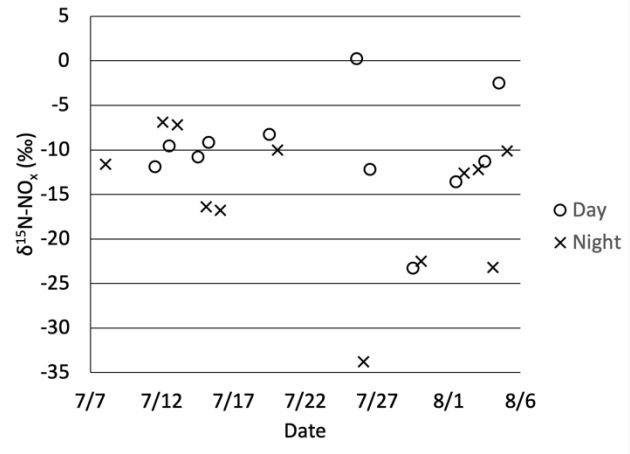

Figure 5.3.7: The $\delta^{15}N(NO_x)$ values measured at West Lafayette, IN between July 9 and August 5, 2016, from 8 am to 4 pm during the daytime (○), and from 9:30 pm to 5:30 am during the nighttime (×)

The simulated atmospheric $\delta^{15}N(NO_x)$ were compared with the corresponding measurements, for the evaluation of the CMAQ simulation under different scenarios of meteorology conditions and chemical mechanisms. Among several existing datasets of measurements, the only direct measurement of $\delta^{15}N(NO_x)$ within the domain was collected between July 8 and August 5, 2016

(Fig. 5.9; Walters, Fang, & Michalski, 2018), at an NADP (National Atmospheric Deposition Program) site located in West Lafayette, IN. The $\delta^{15}N$ of the NO_x samples were collected during the daytime (8 am-4 pm) ranged from -23.3 to 0.2‰, the $\delta^{15}N$ of the NO_x samples were collected during the nighttime (9:30 pm-5:30 am) ranged from -33.8 to -6.9‰.

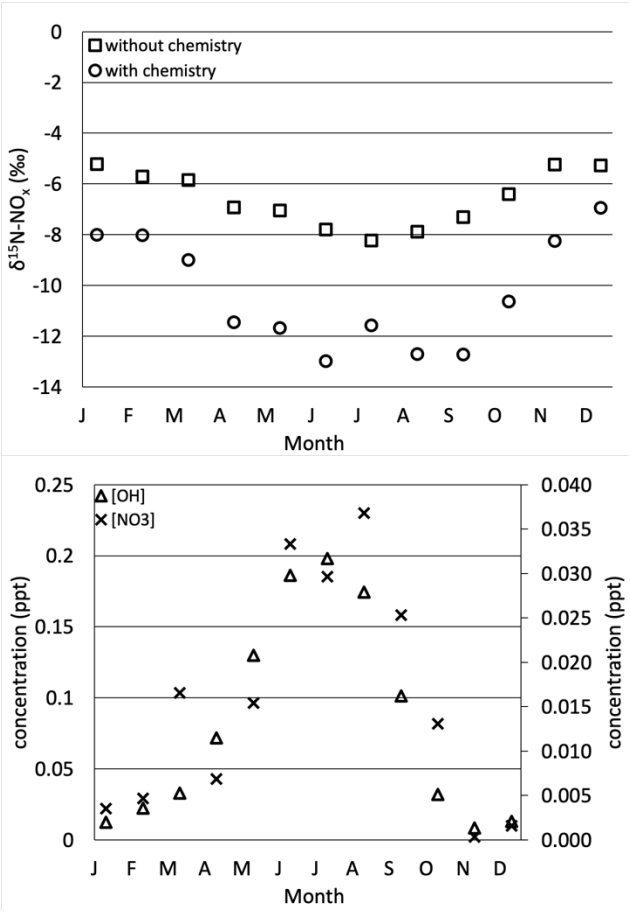

Figure 5.3.8: The monthly $\delta^{15}N$ values of atmospheric NO_x simulated by CMAQ based on 2016 meteorology only (□), based on 2016 meteorology and CB (○) (top), the monthly average of OH (Δ) and NO_3 (×, in right axis) concentration (bottom), over the 12-km grid that covers West Lafayette, IN.

The CMAQ simulations of atmospheric $\delta^{15}N(NO_x)$ in West Lafayette, IN with ^{15}N incorporated CB and RACM have more obvious monthly variation and seasonal trend than without considering the isotope effects from gas-phase tropospheric photochemistry. The monthly average of the simulated $\delta^{15}N$, which only considers atmospheric transport and mixing (Fig. 5.10 top in squares (□)), starts around -5‰ in January, then decreases slightly during winter (Jan-Mar). The

more obvious decreasing trend of $\delta^{15}N$ occurs during spring (Apr-June) until it reaches the minimum around -8‰ in July and starts to increase and ends around -5‰ in December. The increasing trend of $\delta^{15}N$ during summer (Jul-Sep) is more obvious than during fall (Oct-Dec). A similar but more obvious seasonal trend and monthly variation appear in the simulated $\delta^{15}N$ of atmospheric NO_x, after adding isotope effects from the chemical mechanism into the simulation. The monthly average of simulated $\delta^{15}N$ after considering isotope effects from CB mechanism (Fig. 5.10 top in circles (○)) starts around -8‰ in January, which is about 3‰ lower than simulated $\delta^{15}N(NO_x)$ under the "no chemistry" scenario. The $\delta^{15}N$ then decreases slightly, and the difference between $\delta^{15}N(NO_x)$ under the "no chemistry" scenario becomes more obvious since March. The $\delta^{15}N(NO_x)$ reaches the minimum around -13‰ in June, which is about 5‰ lower than simulated $\delta^{15}N(NO_x)$ under the "no chemistry" scenario. The $\delta^{15}N$ starts to increase since August, and the difference between $\delta^{15}N(NO_x)$ under the "no chemistry" scenario becomes less obvious gradually until it reaches the maximum around -7‰ in December. Similar to the $\delta^{15}N(NO_x)$ under the "no chemistry" scenario, the increasing trend of $\delta^{15}N(NO_x)$ under the "with chemistry" scenario during summer (Jul-Sep) is more obvious than during fall (Oct-Dec). The monthly variations and seasonal trend of the simulated $\delta^{15}N(NO_x)$ under the "with chemistry" are mainly driven by the isotope effects associated with the conversion of NO_x to NO_y, driven by the concentration of OH (Fig. 5.10 bottom in triangles (Δ)) and NO_3 (Fig. 5.10 bottom in crosses (×)). As good indicators to show the strength of isotope effects of NO_x conversion to NO_y, the concentration of OH and NO_3 during spring and summer (Apr-Sep) is on average 615% and 271% higher than the concentration during full and winter (Oct-Mar), respectively. The elevated OH and NO_3 concentration during spring and summer promotes the isotope effects and leads to a larger difference in $\delta^{15}N(NO_x)$ between the "with chemistry" scenario and "no chemistry" scenario. A decrease in NO_3 concentration in July could explain the increase of $\delta^{15}N(NO_x)$ under the "with chemistry" scenario during this period.

Table 5.3.1: Performance of $\delta^{15}N(NO_x)$ simulation for West Lafayette, IN

$\delta^{15}N(NO_x)$	Measured	WRF 2002	WRF 2016	WRF 2002 +CB6	WRF 2002 +RACM2	WRF 2016 +CB6	WRF 2016 +RACM2	WRF 2016 +CB6 nested
min	-33.800	-14.779	-15.824	-30.165	-27.071	-25.631	-22.041	-24.569
max	0.200	-3.726	-3.360	-3.449	-4.537	-1.418	14.553	6.058
median	-11.200	-8.355	-8.094	-15.372	-13.596	-11.261	-9.066	-9.677
stdev	8.023	1.881	2.081	5.166	4.186	4.154	6.187	4.924

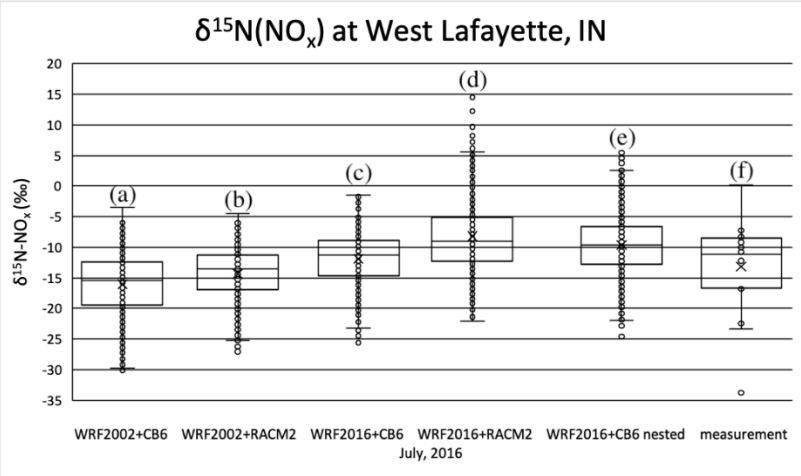

Figure 5.3.9: The distributions of $\delta^{15}N(NO_x)$ values over the 12-km grid that covers West Lafayette, IN from July 8 to August 5, simulated by CMAQ, based on 2002 meteorology and CB over the full domain (a), 2002 meteorology and RACM over the full domain (b), 2016 meteorology and CB over the full domain (c), 2016 meteorology and RACM over the full domain (d), 2016 meteorology and CB over the nested domain (e), compare with the corresponding measurement (f) taken on July to August in 2016 (box: lower quartile, median, upper quartile; whisker: lower extreme, upper extreme; dots outside the whisker: outliers)

The CMAQ simulated $\delta^{15}N$ values of atmospheric NO_x in West Lafayette, IN under different scenarios of the chemical mechanism was compared with the corresponding measurement (Walters, Fang, & Michalski, 2018) from July 8 to August 5, 2016 (Fig. 5.11). The $\delta^{15}N$ of atmospheric NO_x simulated based on NEI-2002 and 2016 meteorology ranges from -15.8‰ to -3.4‰, with the medium of -8.1 ± 2.1‰. The simulated NO_x became isotopically lighter, after taking the isotope effects of the chemical mechanism into account. The $\delta^{15}N$ of atmospheric NO_x simulated based on NEI-2002, 2002 meteorology, and CB ranges from -30.2‰ to -3.4‰, with the medium of -15.4 ± 5.2‰; the $\delta^{15}N$ of atmospheric NO_x simulated based on NEI-2002, 2002 meteorology, and RACM ranges from -27.1‰ to -4.5‰, with the medium of -13.6 ± 4.2‰; the $\delta^{15}N$ of atmospheric NO_x simulated based on NEI-2002, 2016 meteorology, and CB ranges from -25.6‰ to -1.4‰, with the medium of -11.3 ± 4.2‰; the $\delta^{15}N$ of atmospheric NO_x simulated based on NEI-2002, 2016 meteorology, and RACM ranges from -22.0‰ to 14.6‰, with the medium of -9.1 ± 6.2‰; the $\delta^{15}N$ of atmospheric NO_x simulated based on NEI-2002, 2016 meteorology, and CB over the nested domain ranges from -24.6‰ to 6.1‰, with the medium of -9.7 ± 4.9‰. Overall, the estimations of $\delta^{15}N(NO_x)$ are more accurate after including ^{15}N incorporated chemical mechanisms in the CMAQ simulation (Table 5.2). Among the CMAQ simulations under different scenarios, the simulation based on NEI-2002, 2016 meteorology, and CB has the best performance, in terms of median and maximum values of $\delta^{15}N(NO_x)$. On the other hand, the simulation based on NEI-2002, 2002 meteorology, and CB capture the isotopically light NO_x better than the simulations under the other meteorology conditions and chemical mechanisms.

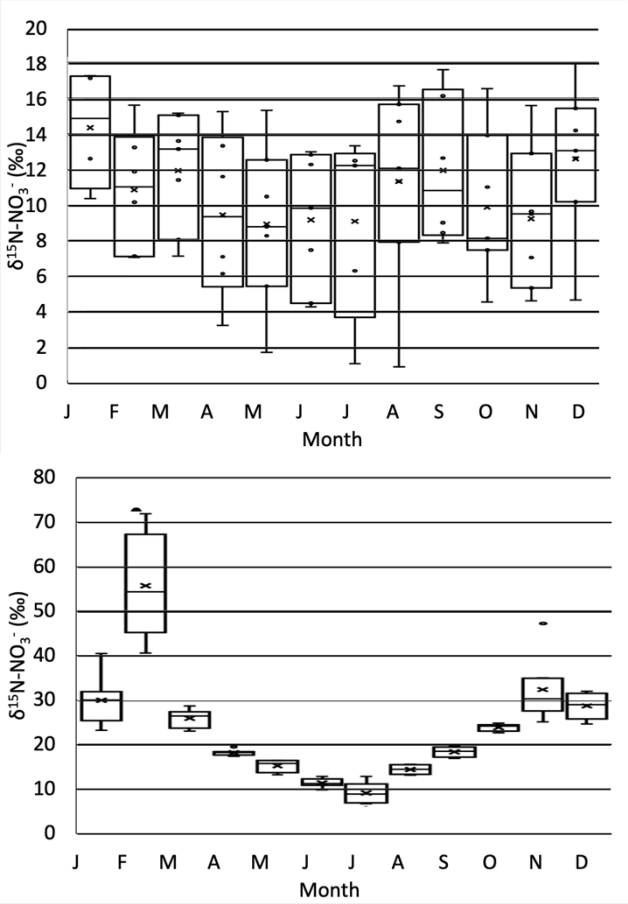

Figure 5.3.10: The measured $\delta^{15}N$ of rain NO_3^- (top) from prior studies; the CMAQ predicted $\delta^{15}N$ value of atmospheric NO_3^- at NADP sites within IN, IL, OH, and KY (bottom) using 2002 meteorology and RACM

Finally, we compared the CMAQ predicted $\delta^{15}N(NO_3^-)$, under the scenario of NEI-2002+WRF2002+CB at NADP sites within Indiana, Illinois, Ohio, and Kentucky (Table D.1) with the corresponding measurements from 2001 to 2003. The measurements of $\delta^{15}N$ values of NO_3^- at the NADP sites from prior studies (Mase, 2010; Riha, 2013) show obviously monthly variation and seasonal trend (Fig. 5.12 top). The monthly boxes are the 1st and 3rd quantiles of the simulated $\delta^{15}N(NO_3^-)$ at these sites. The whiskers represent the minimum and maximum values without outliers. The range of monthly $\delta^{15}N(NO_3^-)$ values, with a minimum during January (10.4~17.2‰) and maximum during August (1.0~16.7‰). The seasonal trend shows isotopically lighter NO_3^- during spring and summer, with the median of monthly $\delta^{15}N(NO_3^-)$ reaches the lowest value of 9.3‰ in May, and isotopically heavier NO_3^- during fall and winter, with the median of monthly $\delta^{15}N(NO_3^-)$ reaches the highest value of 14.3‰ on January.

The CMAQ simulated $\delta^{15}N$ values of NO_3^- at the NADP sites shows the similar monthly variations and seasonal trend (Fig. 5.12, bottom). The range of monthly $\delta^{15}N(NO_3^-)$ values, with a minimum during April (17.6~ 19.7‰) and the maximum during February (40.7~72.0‰). The seasonal trend shows isotopically lighter NO_3^- during spring and summer, with the median of monthly $\delta^{15}N(NO_3^-)$ reaches the lowest value of 9.1‰ in July, and isotopically heavier NO_3^- during fall and winter, with the median of monthly $\delta^{15}N(NO_3^-)$ reaches the highest value of 54.5‰ on February. At the same time, the performance of $\delta^{15}N(NO_3^-)$ simulation is better during spring and summer, with the smallest difference of 1.7‰ in June, than during fall and winter with the largest difference of 43.5‰ in February (Table 5.3). The monthly variation and seasonal trend of $\delta^{15}N(NO_3^-)$ mimic those of $\delta^{15}N(NO_x)$, except in February (Fig. D.6). The similar monthly variation and seasonal trend This could be explained by the conversion of NO_x to NO_3^- in section 5.3.2. The outlying $\delta^{15}N(NO_3^-)$ in February could be explained by the conversion between gas-phase NO_3^- to aerosol-phase, which will be addressed in future work.

Table 5.3.2: Performance of $\delta^{15}N(NO_3^-)$ simulation for West Lafayette, IN

$\delta^{15}N(NO_3^-)$	measured	simulated	difference
Jan	14.852	30.215	15.363
Feb	11.021	54.479	43.458
Mar	13.137	26.587	13.450
Apr	9.358	18.422	9.064
May	8.797	15.955	7.157
Jun	9.839	11.498	1.659
Jul	12.212	9.144	3.069
Aug	12.057	14.653	2.595
Sep	10.831	18.737	7.905
Oct	8.154	24.296	16.142
Nov	9.510	30.410	20.900
Dec	13.049	29.161	16.112

5.4 Conclusion

The new chemical mechanisms with the incorporation of ^{15}N were developed for the CMAQ simulation of atmospheric $\delta^{15}N(NO_x)$ and $\delta^{15}N(NO_3^-)$. The previously prepared emission datasets (Fang & Michalski, 2020) and meteorology dataset (Fang & Michalski, 2021) were used as the inputs for the CMAQ simulation. $\delta^{15}N$ is an effective tracer for the "journey" of atmospheric NO_x, in terms of its emission source, how it is transported and mixed in the atmosphere, and how it is removed from the atmosphere by the deposition and the conversion to NO_y. The simulation indicates the seasonal trend of the conversion of NO_x to NO_y, showing the larger difference between the $\delta^{15}N$ of atmospheric NO_x under the scenario of "with chemistry" and "no chemistry" during spring and summer, due to the increased duration of O_3 photolysis. The CMAQ simulation of $\delta^{15}N(NO_x)$ has better performance than previous companion research (Fang & Michalski, 2021), due to the consideration of gas-phase tropospheric photochemistry. Comparing the simulations of $\delta^{15}N(NO_3^-)$ for the NADP sites within Indiana, Illinois, Ohio, and Kentucky with the corresponding measurements, similar seasonal trends, and monthly variation was shown. However, the performance of the simulations of $\delta^{15}N(NO_3^-)$ during fall and winter still needs to improve. Therefore, the future work is to incorporate ^{15}N into the aerosol module of CMAQ and explore the associated isotope effects. After the series of exploration of the isotope effect on NO_x along its "journey" in the atmosphere, our nitrogen isotopes incorporated CMAQ will be validated and effectively used for the evaluation and improvement of the NO_x emission inventories.

CHAPTER 6. CONCLUSION

The oxidation NO_x and subsequent deposition of atmospheric nitrate and other NO_y compounds have a number of negative impacts on air quality, climate, human health, and the environment. Therefore, it is important to understand NO_x sources, how it is transported and mixed in the atmosphere, how it is removed from the atmosphere due to the conversion to NO_y and deposition, in order to make informed decisions regarding air quality policy and mitigation strategies for a sustainable future. However, there are still a number of significant uncertainties in the NO_x budget despite years of research, including the impacts of N fertilizers and vegetation on soil NO_x emission, different algorithms for the estimation of NO_x emission from on-road vehicles, the implementation of different NO_x emission control technologies on fossil fuel combustion. As a measurement of the relative abundance of ^{15}N, comparing with the air, the $\delta^{15}N$ values for NO_x from different emission sources have distinctive differences. In this research, the source, chemistry, and removal of atmospheric NO_x were evaluated and constrained by developing a new model that incorporates N stable isotopes into a Chemical Transport Model (CTM) in a series of studies and comparing the model simulation results under different scenarios with the corresponding isotopic measurements. The ^{15}N was first incorporated into the emission dataset (Chapter 2), based on the amount of NO_x emission from each source retrieved from the emission inventories, and the corresponding $\delta^{15}N(NO_x)$ values characterized from the prior studies. Then the ^{15}N incorporated emission dataset was used as input to run CMAQ, to trace how atmospheric processes alter the composition of NO_x, by using WRF (Weather Research and Forecasting) model to prepare meteorology conditions (Chapter 3). Finally, ^{15}N was incorporated into the chemical mechanisms of CMAQ to explore the gas phase isotope effects associated with NO_x oxidation (Chapter 5), by adding the ^{15}N of N compounds and replicate the chemical reactions involving N compounds, with the corresponding fractionation factors (α) based on prior experimental and theoretical studies (Chapter 4).

6.1 The variability in the $\delta^{15}N$ values of NO_x emission sources

The atmospheric NO_x sources from both anthropogenic emissions, such as automobiles, power plants, agriculture, livestock waste, as well as natural processes, including by-product of nitrification and denitrification occurring in soil, and lightning. In this research, the National Emission Inventory (NEI), the most well-known and commonly used estimation of emissions, was utilized as the NO_x budget to evaluate and constrain. The first scenario for the atmospheric $\delta^{15}N(NO_x)$ simulation is only considering the $\delta^{15}N$ of NO_x from different sources. The $\delta^{15}N$ simulation was generated by conducting the US EPA trace gas emission model SMOKE (Sparse Matrix Operator Kernel Emissions) to convert the NO_x emissions from each source based on NEI to CMAQ-ready netCDF file, then incorporating ^{15}N based on the fraction of each source and the corresponding $\delta^{15}N(NO_x)$ values. The simulation under this scenario reveals the dominant influence of the NO_x emission from biogenic sources on the variation of $\delta^{15}N$, especially among the NADP sites. In addition, the simulated $\delta^{15}N$ agreed well with the seasonal trend and monthly variation of the corresponding measurements from NADP sites within the Midwest region. Meanwhile, the simulated $\delta^{15}N(NO_x)$ is slightly heavier than the measured values in West Lafayette, IN. If only considering the variability in the $\delta^{15}N$ values of NO_x emission sources, this simulation indicates the potential underestimation of emission from soil, livestock waste, off-road vehicles, and natural gas power plants, as well as the potential overestimation of emission from on-road vehicles and coal-fired power plants in West Lafayette, IN.

6.2 The atmospheric mixing, dispersion, transport, and deposition of tropospheric NOx emitted from different sources

The effect of atmospheric mixing, dispersion, and transport was taken into account for the simulation of atmospheric $\delta^{15}N(NO_x)$ under the second scenario. The $\delta^{15}N$ simulation was generated by using the ^{15}N incorporated emission dataset as input for CMAQ simulation of the meteorological transport effects (advection, eddy diffusion, etc), and the effect of NO_x removal by dry and wet deposition. The CMAQ-ready meteorology input dataset was prepared by CMAQ's MCIP module, based on WRF output from NARR and NAM. The simulation under this scenario presents the mixture of anthropogenic and natural NO_x emission so that the $\delta^{15}N(NO_x)$ values over the grids resolving rural areas were elevated to values similar to nearby big cities, major highways, or power plants, while the atmospheric NO_x became isotopically lighter over the grids that contain

big cities, major highways, and power plants. Due to the consideration of mixing, disperse, and transport of NO_x emission from different sources, the performance of CMAQ simulated $\delta^{15}N(NO_x)$ improved from the simulation under the first scenario. However, the gap between the simulated $\delta^{15}N(NO_x)$ and the corresponding measurements is still obvious, after considering the effects from atmospheric processes, in addition to the variability in the $\delta^{15}N$ values of NO_x emission sources. Therefore, the isotope effects associated with the tropospheric photochemistry that converts NO_x to NO_y were then explored.

6.3 The isotope effects occurring during the gas-phase tropospheric photochemistry that transforms NO_x into NO_y

The isotope impact from the gas phase tropospheric photochemistry was incorporated into the third scenario, on the basis of the first and second scenarios. The $\delta^{15}N$ simulation was generated by CMAQ using a similar method but using the ^{15}N was incorporated chemical mechanisms CB and RACM instead. The CMAQ utility chemmech was used to generate the FORTRAN 90 modules for data and function of ^{15}N incorporated CB and RACM, for the compilation and simulation of CCTM. The CMAQ utility inline_phot_preproc was used to generate the cross-sections and quantum yields (CSQY) data for the calculation of its photolysis rate. The CMAQ utilitycreate_ebi was used to generate the Euler Backward Iterative (EBI) solver for the ^{15}N incorporated CB and RACM, for the better accuracy and computational efficiency of CCTM simulation. The simulation under this scenario indicates the seasonal trend of the conversion of NO_x to NO_y, showing the larger difference in atmospheric $\delta^{15}N(NO_x)$ between under the second scenario during spring and summer, due to the increased duration of O_3 photolysis. After taking the gas-phase tropospheric photochemistry into account, the CMAQ simulation of $\delta^{15}N(NO_x)$ has better performance than the second scenario. In addition, the simulations of $\delta^{15}N(NO_3^-)$ for the NADP sites within Indiana, Illinois, Ohio, and Kentucky agree well with the seasonal trend and monthly variation of the corresponding measurements. The simulated $\delta^{15}N(NO_3^-)$ has good performance during spring and summer, while the obvious gap between the simulated $\delta^{15}N(NO_3^-)$ and the corresponding measurements during fall and winter was shown. The isotope effects associated with the heterogeneous/aqueous phase tropospheric photochemistry that occurs during the multiphase oxidation of NO_x into NO_3^- potentially lead to the bias on $\delta^{15}N(NO_3^-)$ simulation.

6.4 Future outlook

This research constructs the 3-D CTM of ^{15}N in reactive N to trace the changes in $\delta^{15}N$ values along the "journey" of atmospheric NO_x. After the exploration of the effects of the spatiotemporal variability in the $\delta^{15}N$ values of NO_x emissions, atmospheric processes of tropospheric NO_x from different sources, and the isotope effects occurring during the gas-phase tropospheric photochemistry that converts NO_x to NO_y, the future work will be focusing on the heterogeneous/aqueous phase isotope effects, by incorporating ^{15}N into the aerosol module of CMAQ. After the series of exploration of the changes in $\delta^{15}N$ values along the "journey" of atmospheric NO_x, the accuracy of the NO_x emission inventory could be evaluated using ^{15}N.

6.5 Limitation and future needs

The accuracy and validation of our nitrogen isotopes incorporated CMAQ could be improved with additional research. The ^{15}N incorporated emission dataset could be refined by additional theoretical and/or experimental determination of the $\delta^{15}N$ values of NO_x from different emission sources. First, the detailed measurements of $\delta^{15}N$ of coal-fired and natural gas non-EGUs (industrial boilers, commercial and residential fuel combustions), which were assumed to be the same as the $\delta^{15}N$ of coal-fired and natural gas EGUs respectively in this study. In addition, the non-road vehicles (aircrafts, ships, and trains) also need to be included in the future study. Likewise, the ^{15}N incorporated chemical mechanisms (CB and RACM) could also be refined by additional theoretical and/or experimental determination of the isotope fractionation factors for the N reactions, especially, the fractionation factor for the NO_2 + OH reaction, the NO + OH, and NO_2 photolysis. The current limitation in terms of the reconstruction of CMAQ occurs in the isotope effect associated with the aerosol module, deposition rates of $^{15}NO_y$, and impacts from lightning. The ^{15}N will be incorporated into the aerosol module of CMAQ, so that the impacts on $\delta^{15}N$ values due to the conversion between the gas phase and aerosol phase NO_y will be considered in the simulation. Besides this, lightning also needs to include in the simulations. The determination of $\delta^{15}N$ values of NO_x from different emission sources, the isotope fractionation factors, isotope effects associated with the aerosol module, deposition rates of $^{15}NO_y$, as well as lightning effects, would be validated with massive measurements of $\delta^{15}N$ of NO_y in different space and time under a range of different environmental conditions.

REFERENCES

Aldener, M., Brown, S. S., Stark, H., Williams, E. J., Lerner, B. M., Kuster, W. C., ... & Ravishankara, A. R. (2006). Reactivity and loss mechanisms of NO_3 and N_2O_5 in a polluted marine environment: Results from in situ measurements during New England Air Quality Study 2002. *Journal of Geophysical Research: Atmospheres*, *111*(D23).

Almaraz, M., Bai, E., Wang, C., Trousdell, J., Conley, S., Faloona, I., & Houlton, B. Z. (2018). Agriculture is a major source of NO_x pollution in California. *Science advances*, *4*(1), eaao3477.

Altshuller, A. P. (1989). Nonmethane organic compound to nitrogen oxide ratios and organic composition in cities and rural areas. *JAPCA*, *39*(7), 936-943.

Ammann, M., Siegwolf, R., Pichlmayer, F., Suter, M., Saurer, M., & Brunold, C. (1999). Estimating the uptake of traffic-derived NO_2 from 15 N abundance in Norway spruce needles. *Oecologia*, *118*(2), 124-131.

Andreae, M. O., and P. J. Crutzen (1997), Atmospheric aerosols: biogeochemical sources and role in atmospheric chemistry, *Science*, *276*(5315), 1052-1058.

Anttila, T., Kiendler-Scharr, A., Tillmann, R., & Mentel, T. F. (2006). On the reactive uptake of gaseous compounds by organic-coated aqueous aerosols: Theoretical analysis and application to the heterogeneous hydrolysis of N_2O_5. *The Journal of Physical Chemistry A*, *110*(35), 10435-10443.

Atkinson, R. (1990), Gas-phase tropospheric chemistry of organic-compounds - a review, *Atmospheric Environment Part a-General Topics*, *24*(1), 1-41, doi:10.1016/0960-1686(90)90438-s.

Atkinson, R. (1994). Gas-phase tropospheric chemistry of organic compounds. *J. Phys. Chem. Ref. Data, Monograph, 2*, 1-216.

Atkinson, R. (2000), Atmospheric chemistry of VOCs and NO_x, *Atmospheric Environment*, *34*(12-14), 2063-2101.

Atkinson, R., Baulch, D. L., Cox, R. A., Crowley, J. N., Hampson, R. F., Hynes, R. G., ... & Wallington, T. J. (2008). Evaluated kinetic and photochemical data for atmospheric chemistry: Volume IV–gas phase reactions of organic halogen species. *Atmospheric chemistry and physics*, *8*(15), 4141-4496.

Atkinson, R., Baulch, D. L., Cox, R. A., Hampson Jr, R. F., Kerr, J. A., & Troe, J. (1992). Evaluated kinetic and photochemical data for atmospheric chemistry: Supplement IV. IUPAC subcommittee on gas kinetic data evaluation for atmospheric chemistry. *Journal of Physical and Chemical Reference Data*, *21*(6), 1125-1568.

Atkinson, R., Tuazon, E. C., Bridier, I., & Arey, J. (1994). Reactions of NO3-naphthalene adducts with O2 and NO2. *International journal of chemical kinetics*, *26*(6), 605-614.

Bauer, S. E., D. Koch, N. Unger, S. M. Metzger, D. T. Shindell, and D. G. Streets (2007), Nitrate aerosols today and in 2030: a global simulation including aerosols and tropospheric ozone, *Atmospheric Chemistry and Physics*, *7*(19), 5043-5059

Baugues, K. (1986). *Review of NMOC, NOx and NMOC/NOx ratios measured in 1984 and 1985* (No. PB-87-166963/XAB; EPA-450/4-86/015). Environmental Protection Agency, Research Triangle Park, NC (USA). Monitoring and Data Analysis Div..

Beirle, S., Spichtinger, N., Stohl, A., Cummins, K. L., Turner, T., Boccippio, D., ... & Wagner, T. (2006). Estimating the NO_x produced by lightning from GOME and NLDN data: A case study in the Gulf of Mexico. *Atmospheric Chemistry and Physics*, *6*(4), 1075-1089.

Bertram, T. H., & Thornton, J. A. (2009). Toward a general parameterization of N_2O_5 reactivity on aqueous particles: the competing effects of particle liquid water, nitrate and chloride. *Atmospheric Chemistry and Physics*, *9*(21), 8351-8363.

Bigeleisen, J., and M. G. Mayer (1947), Calculation of Equilibrium Constants for Isotopic Exchange Reactions, *The Journal of Chemical Physics*, *15*(5), 261-267.

Bigeleisen, J. (1958), Second-Order Sum Rule for the Vibrations of Isotopic Molecules and the Second Rule of the Mean, *The Journal of Chemical Physics*, *28*(4), 694-699.

Bigeleisen, J., and M. Wolfsberg (1958), Theoretical and experimental aspects of isotope effects in chemical kinetics, *Advances in Chem. Phys. (Prigogine, I. Interscience Publishers, Inc. , New York)*, *1*, 15-76.

Blake, G. A., M. C. Liang, C. G. Morgan, and Y. L. Yung (2003), A born-oppenheimer photolysis model of N_2O fractionation, *Geophysical Research Letters*, *30*(12), 58/51-58/54.

Bloss, W. J., M. J. Evans, J. D. Lee, R. Sommariva, D. E. Heard, and M. J. Pilling (2005), The oxidative capacity of the troposphere: Coupling of field measurements of OH and a global chemistry transport model, *Faraday Discussions*, *130*, 425-436.

Boersma, K. F., Eskes, H. J., Meijer, E. W., & Kelder, H. M. (2005). Estimates of lightning NO_x production from GOME satellite observations. *Atmospheric Chemistry and Physics*, *5*(9), 2311-2331.

Bottenheim, J. W., Gallant, A. G., & Brice, K. A. (1986). Measurements of NOy species and O3 at 82 N latitude. *Geophysical Research Letters*, *13*(2), 113-116.

Bradshaw, J., Davis, D., Grodzinsky, G., Smyth, S., Newell, R., Sandholm, S., & Liu, S. (2000). Observed distributions of nitrogen oxides in the remote free troposphere from the NASA global tropospheric experiment programs. *Reviews of Geophysics*, *38*(1), 61-116.

Brimblecombe, P., H. Hara, and D. Houle (2007), *Acid Rain - Deposition to Recovery*, Springer.

Brown, L. L., & Begun, G. M. (1959). Nitrogen isotopic fractionation between nitric acid and the oxides of nitrogen. *The Journal of Chemical Physics*, *30*(5), 1206-1209.

Brown, S. S., et al. (2006), Variability in nocturnal nitrogen oxide processing and its role in regional air quality, *Science*, *311*(5757), 67-70.

Brown, S. S., J. B. Burkholder, R. K. Talukdar, and A. R. Ravishankara (2001), Reaction of hydroxyl radical with nitric acid: insights into its mechanism, *Journal of Physical Chemistry A*, *105*(9), 1605-1614.

Brown, S. S., Ryerson, T. B., Wollny, A. G., Brock, C. A., Peltier, R., Sullivan, A. P., ... & Fehsenfeld, F. C. (2006). Variability in nocturnal nitrogen oxide processing and its role in regional air quality. *Science*, *311*(5757), 67-70.

Bruningfann, C. S., and J. B. Kaneene (1993), The Effects of Nitrate, Nitrite and N-Nitroso Compounds on Human Health - A Review, *Veterinary and Human Toxicology*, *35*(6), 521-538.

Byun, D. W., Pleim, J. E., Tang, R. T., & Bourgeois, A. (1999). Meteorology-chemistry interface processor (MCIP) for models-3 community multiscale air quality (CMAQ) modeling system. *Washington, DC, US Environmental Protection Agency, Office of Research and Development*.

Cantrell, C. A., Davidson, J. A., McDaniel, A. H., Shetter, R. E., & Calvert, J. G. (1990). Temperature-dependent formaldehyde cross sections in the near-ultraviolet spectral region. *Journal of Physical Chemistry*, *94*(10), 3902-3908.

Cao, Z. Y., X. H. Zhou, Y. J. Ma, L. P. Wang, R. D. Wu, B. Chen, and W. X. Wang (2017), The Concentrations, Formations, Relationships and Modeling of Sulfate, Nitrate and Ammonium (SNA) Aerosols over China, *Aerosol and Air Quality Research*, *17*(1), 84-97, doi:10.4209/aaqr.2016.01.0020.

Carroll, M. A., Ridley, B. A., Montzka, D. D., Hubler, G., Walega, J. G., Norton, R. B., ... & Grahek, F. E. (1992). Measurements of nitric oxide and nitrogen dioxide during the Mauna Loa Observatory Photochemistry Experiment. *Journal of Geophysical Research: Atmospheres*, *97*(D10), 10361-10374.

Chai, J. J., and M. G. Hastings (2018), Collection Method for Isotopic Analysis of Gaseous Nitrous Acid, *Analytical Chemistry*, *90*(1), 830-838, doi:10.1021/acs.analchem.7b03561.

Chameides, W. L., Davis, D. D., Bradshaw, J., Rodgers, M., Sandholm, S., & Bai, D. B. (1987). An estimate of the NO_x production rate in electrified clouds based on NO observations from the GTE/CITE 1 fall 1983 field operation. *Journal of Geophysical Research: Atmospheres*, *92*(D2), 2153-2156.

Chang, W. L., P. V. Bhave, S. S. Brown, N. Riemer, J. Stutz, and D. Dabdub (2011), Heterogeneous Atmospheric Chemistry, Ambient Measurements, and Model Calculations of N_2O_5: A Review, *Aerosol Science and Technology*, *45*(6), 665-695.

Chang, Y., Zhang, Y., Tian, C., Zhang, S., Ma, X., Cao, F., ... & Lehmann, M. F. (2018). Nitrogen isotope fractionation during gas-to-particle conversion of NO_x to NO_3^- in the atmosphere–implications for isotope-based NO x source apportionment. *Atmospheric Chemistry and Physics*, *18*(16), 11647-11661.

Charlson, R. J., S. E. Schwartz, J. M. Hales, R. D. Cess, J. A. Coakley, J. E. Hansen, and D. J. Hofmann (1992), Climate Forcing by Anthropogenic Aerosols, *Science*, *255*(5043), 423-430.

Chen, W. T., H. Liao, and J. H. Seinfeld (2007), Future climate impacts of direct radiative forcing of anthropogenic aerosols, tropospheric ozone, and long-lived greenhouse gases, *Journal of Geophysical Research-Atmospheres*, *112*(D14).

Christian, H. J., Blakeslee, R. J., Boccippio, D. J., Boeck, W. L., Buechler, D. E., Driscoll, K. T., ... & Stewart, M. F. (2003). Global frequency and distribution of lightning as observed from space by the Optical Transient Detector. *Journal of Geophysical Research: Atmospheres*, *108*(D1), ACL-4.

Cicero-Fernández, P., Long, J. R., & Winer, A. M. (1997). Effects of grades and other loads on on-road emissions of hydrocarbons and carbon monoxide. *Journal of the Air & Waste Management Association*, *47*(8), 898-904.

Cleveland, W. S., Kleiner, B., McRae, J. E., Warner, J. L., & Pasceri, R. E. (1977). Geographical properties of ozone concentrations in the northeastern United States. *Journal of the Air Pollution Control Association*, *27*(4), 325-328.

Cooper, O. R., Gao, R. S., Tarasick, D., Leblanc, T., & Sweeney, C. (2012). Long-term ozone trends at rural ozone monitoring sites across the United States, 1990–2010. *Journal of Geophysical Research: Atmospheres*, *117*(D22).

Dameris, M., Grewe, V., Ponater, M., Deckert, R., Eyring, V., Mager, F., ... & Brühl, C. (2005). Long-term changes and variability in a transient simulation with a chemistry-climate model employing realistic forcing. *Atmospheric Chemistry and Physics*, *5*(8), 2121-2145.

Davidson, E. A. (1992). Pulses of nitric oxide and nitrous oxide flux following wetting of dry soil: An assessment of probable sources and importance relative to annual fluxes. *Ecological Bulletins*, 149-155.

Davidson, E. A., & Kingerlee, W. (1997). A global inventory of nitric oxide emissions from soils. *Nutrient cycling in agroecosystems*, *48*(1-2), 37-50.

Davis, J. M., Bhave, P. V., & Foley, K. M. (2008). Parameterization of N_2O_5 reaction probabilities on the surface of particles containing ammonium, sulfate, and nitrate. *Atmospheric Chemistry and Physics*, *8*(17), 5295-5311.

Day, D. A., M. B. Dillon, P. J. Wooldridge, J. A. Thornton, R. S. Rosen, E. C. Wood, and R. C. Cohen (2003), On alkyl nitrates, O_3, and the "missing NO_y", *Journal of Geophysical Research-Atmospheres*, *108*(D16), doi:10.1029/2003jd003685.

de Foy, B., Lu, Z., Streets, D. G., Lamsal, L. N., & Duncan, B. N. (2015). Estimates of power plant NO_x emissions and lifetimes from OMI NO2 satellite retrievals. *Atmospheric Environment*, *116*, 1-11.

de Laeter, J. R., Böhlke, J. K., DeBièvre, P., Hidaka, H., Peiser, H. S., Rosman, K. J. R., & Taylor,P. D. P. (2003). Atomic weights of the elements. Review 2000 (IUPAC Technical Report). *Pure and applied chemistry*,*75*(6), 721.

DeCaria, A. J., Pickering, K. E., Stenchikov, G. L., & Ott, L. E. (2005). Lightning-generated NO_x and its impact on tropospheric ozone production: A three-dimensional modeling study of a Stratosphere-Troposphere Experiment: Radiation, Aerosols and Ozone (STERAO-A) thunderstorm. *Journal of Geophysical Research: Atmospheres*, *110*(D14).

DeMore, W. B., Hampson, S. S. D. G. R., & Ravishankara, M. K. C. H. A. (1994). CE Kolb MJ Molina. *Chemical Kinetics and Photochemical Data for Use in Stratospheric Modeling, JPL Publication*, 92-20.

DeMore, W. B., S. P. Sander,D. M. Golden, R. F. Hampson,M. J. Kurylo, C. J. Howard, A. R. Ravishankara,C. E. Kolb, and M. J. Molina, (1994), Chemical kinetics and photochemical data for use in stratospheric modeling, Eval. 11, *Natl. Aeronaut. and Space Admin., Jet Propul. Lab.*

DeMore, W. B., Sander, S. P., Golden, D. M., Hampson, R. F., Kurylo, M. J., Howard, C. J., ... & Molina, M. J. (1997). Chemical kinetics and photochemical data for use in stratospheric modeling, JPL Publication 97-4. *Jet Propulsion Laboratory, Pasadena, CA*.

Dentener, F. J., & Crutzen, P. J. (1993). Reaction of N2O5 on tropospheric aerosols: Impact on the global distributions of NO_x, O_3, and OH. *Journal of Geophysical Research: Atmospheres*, *98*(D4), 7149-7163.

Diem, J. E., & Comrie, A. C. (2001). Allocating anthropogenic pollutant emissions over space: application to ozone pollution management. *Journal of environmental management*, *63*(4), 425-447.

Dignon, J., & Hameed, S. (1989). Global emissions of nitrogen and sulfur oxides from 1860 to 1980. *Japca*, *39*(2), 180-186.

Dreher, D. B., & Harley, R. A. (1998). A fuel-based inventory for heavy-duty diesel truck emissions. *Journal of the Air & Waste Management Association*, *48*(4), 352-358.

Du, E. Z., M. E. Fenn, W. De Vries, and Y. S. Ok (2019), Atmospheric nitrogen deposition to global forests: Status, impacts and management options, *Environmental Pollution, 250*, 1044-1048, doi:10.1016/j.envpol.2019.04.014.

Duncan, B. N., Yoshida, Y., de Foy, B., Lamsal, L. N., Streets, D. G., Lu, Z., ... & Krotkov, N. A. (2013). The observed response of Ozone Monitoring Instrument (OMI) NO_2 columns to NO_x emission controls on power plants in the United States: 2005–2011. *Atmospheric Environment*, *81*, 102-111.

Elliott, E. M., C. Kendall, E. W. Boyer, D. A. Burns, G. G. Lear, H. E. Golden, K. Harlin, A. Bytnerowicz, T. J. Butler, and R. Glatz (2009), Dual nitrate isotopes in dry deposition: Utility for partitioning NO_x source contributions to landscape nitrogen deposition, *Journal of Geophysical Research-Biogeosciences, 114*.

Elliott, E. M., C. Kendall, S. D. Wankel, D. A. Burns, E. W. Boyer, K. Harlin, D. J. Bain, and T. J. Butler (2007), Nitrogen isotopes as indicators of NOx source contributions to atmospheric nitrate deposition across the Midwestern and northeastern United States, *Environmental Science & Technology, 41*(22), 7661-7667.

Elliott, E. M., Kendall, C., Boyer, E. W., Burns, D. A., Lear, G. G., Golden, H. E., … Glatz, R. (2009). Dual nitrate isotopes in dry deposition: Utility for partitioning NO_x source contributions to landscape nitrogen deposition. *JOURNAL OF GEOPHYSICAL RESEARCH-BIOGEOSCIENCES, 114*. https://doi.org/10.1029/2008JG000889

Elliott, E. M., Kendall, C., Wankel, S. D., Burns, D. A., Boyer, E. W., Harlin, K., … Butler, T. J. (2007). Nitrogen isotopes as indicators of NO_x source contributions to atmospheric nitrate deposition across the Midwestern and northeastern United States. *ENVIRONMENTAL SCIENCE & TECHNOLOGY, 41*(22), 7661–7667. https://doi.org/10.1021/es070898t

Elliott, E. M., Z. J. Yu, A. S. Cole, and J. G. Coughlin (2019), Isotopic advances in understanding reactive nitrogen deposition and atmospheric processing, *Science of the Total Environment, 662*, 393-403, doi:10.1016/j.scitotenv.2018.12.177.

Fahey, D. W., Hübler, G., Parrish, D. D., Williams, E. J., Norton, R. B., Ridley, B. A., ... & Fehsenfeld, F. C. (1986). Reactive nitrogen species in the troposphere: Measurements of NO, NO_2, HNO_3, particulate nitrate, peroxyacetyl nitrate (PAN), O_3, and total reactive odd nitrogen (NO_y) at Niwot Ridge, Colorado. *Journal of Geophysical Research: Atmospheres*, *91*(D9), 9781-9793.

Fang, H. & Michalski, G. (2020). Simulating $\delta^{15}N$ of NO_x emission within Midwestern United States. *Geoscientific Model Development (submitted)*

Farrell, A., Carter, R., & Raufer, R. (1999). The NOx Budget: market-based control of tropospheric ozone in the northeastern United States. *Resource and Energy Economics*, *21*(2), 103-124.

Fehr, T., Höller, H., & Huntrieser, H. (2004). Model study on production and transport of lightning-produced NO_x in a EULINOX supercell storm. *Journal of Geophysical Research: Atmospheres*, *109*(D9).

Felix, J. D., & Elliott, E. M. (2013). The agricultural history of human-nitrogen interactions as recorded in ice core $\delta 15N\text{-}NO_3^-$. *Geophysical Research Letters*, *40*(8), 1642-1646.

Felix, J. D., & Elliott, E. M. (2014). Isotopic composition of passively collected nitrogen dioxide emissions: Vehicle, soil and livestock source signatures. *Atmospheric environment*, *92*, 359-366.

Felix, J. D., E. M. Elliott, and S. L. Shaw (2012), Nitrogen Isotopic Composition of Coal-Fired Power Plant NO_x: Influence of Emission Controls and Implications for Global Emission Inventories, *Environmental Science & Technology*, *46*(6), 3528-3535.

Felix, J. D., Elliott, E. M., Avery, G. B., Kieber, R. J., Mead, R. N., Willey, J. D., & Mullaugh, K. M. (2015). Isotopic composition of nitrate in sequential Hurricane Irene precipitation samples: implications for changing NO_x sources. *Atmospheric Environment*, *106*, 191-195.

Fibiger, D. L., Hastings, M. G., Lew, A. F., & Peltier, R. E. (2014). Collection of NO and NO_2 for Isotopic Analysis of NO_x Emissions. *Analytical chemistry*, *86*(24), 12115-12121.

Fibiger, D. L., and M. G. Hastings (2016), First Measurements of the Nitrogen Isotopic Composition of NO_x from Biomass Burning, *Environmental Science & Technology*, *50*(21), 11569-11574, doi:10.1021/acs.est.6b03510.

Finlayson-Pitts, B. J., and J. N. Pitts, Jr. (2000), *Chemistry of the Upper and Lower Atmosphere*, Academic Press, San Diego.

Fowler, D., et al. (2013), The global nitrogen cycle in the twenty-first century, *Philosophical Transactions of the Royal Society B-Biological Sciences*, *368*(1621).

Fraser, A., Goutail, F., McLinden, C. A., Melo, S. M. L., & Strong, K. (2007). Lightning-produced NO_2 observed by two ground-based UV-visible spectrometers at Vanscoy, Saskatchewan in August 2004. *Atmospheric Chemistry and Physics*, *7*(6), 1683-1692.

Freyer, H. D. (1978), Seasonal Trends of NH_4^+ and NO_3^- Nitrogen Isotope Composition in Rain Collected at Julich, Germany, *Tellus*, *30*(1), 83-92.

Freyer, H. D., D. Kley, A. Volzthomas, and K. Kobel (1993), On the interaction of isotopic exchange processes with photochemical-reactions in atmospheric oxides of nitrogen, *Journal of Geophysical Research-Atmospheres*, *98*(D8), 14791-14796, doi:10.1029/93jd00874.

Fuentes, J. D., Chamecki, M., Nascimento dos Santos, R. M., Von Randow, C., Stoy, P. C., Katul, G., ... & Souza Freire, L. (2016). Linking meteorology, turbulence, and air chemistry in the Amazon rain forest. *Bulletin of the American Meteorological Society*, *97*(12), 2329-2342.

Fujita, E. M., Croes, B. E., Bennett, C. L., Lawson, D. R., Lurmann, F. W., & Main, H. H. (1992). Comparison of emission inventory and ambient concentration ratios of CO, NMOG, and NO_x in California's South Coast Air Basin. *Journal of the Air & Waste Management Association*, *42*(3), 264-276.

Fujita, E. M., Campbell, D. E., Zielinska, B., Sagebiel, J. C., Bowen, J. L., Goliff, W. S., ... & Lawson, D. R. (2003). Diurnal and weekday variations in the source contributions of ozone precursors in California's South Coast Air Basin. *Journal of the Air & Waste Management Association*, *53*(7), 844-863.

Fujita, E. M., Stockwell, W. R., Campbell, D. E., Keislar, R. E., & Lawson, D. R. (2003). Evolution of the magnitude and spatial extent of the weekend ozone effect in California's South Coast Air Basin, 1981–2000. *Journal of the Air & Waste Management Association*, *53*(7), 802-815.

Galbally, I. E., & Roy, C. R. (1978). Loss of fixed nitrogen from soils by nitric oxide exhalation. *Nature*, *275*(5682), 734.

Gallardo, L., & Rodhe, H. (1997). Oxidized nitrogen in the remote Pacific: The role of electrical discharges over the oceans. *Journal of atmospheric chemistry*, *26*(2), 147-168.

Galloway, J. N., & Cowling, E. B. (2002). Reactive nitrogen and the world: 200 years of change. *AMBIO: A Journal of the Human Environment*, *31*(2), 64-71.

Galloway, J. N., Dentener, F. J., Capone, D. G., Boyer, E. W., Howarth, R. W., Seitzinger, S. P., . & Karl, D. M. (2004). Nitrogen cycles: past, present, and future. *Biogeochemistry*, *70*(2), 153-226.

Ganzeveld, L. N., Lelieveld, J., Dentener, F. J., Krol, M. C., Bouwman, A. J., & Roelofs, G. J. (2002). Global soil-biogenic NO_x emissions and the role of canopy processes. *Journal of Geophysical Research: Atmospheres*, *107*(D16).

Gardner, E. P., Sperry, P. D., & Calvert, J. G. (1987). Photodecomposition of acrolein in oxygen-nitrogen mixtures. *Journal of Physical Chemistry*, *91*(7), 1922-1930.

Garten Jr, C. T. (1992). Nitrogen isotope composition of ammonium and nitrate in bulk precipitation and forest throughfall. *International Journal of Environmental Analytical Chemistry*, *47(1)*, 33-45.

Gauss, M., Myhre, G., Isaksen, I. S. A., Grewe, V., Pitari, G., Wild, O., ... & Hauglustaine, D. A. (2006). Radiative forcing since preindustrial times due to ozone change in the troposphere and the lower stratosphere. *Atmospheric Chemistry and Physics*, *6*(3), 575-599.

Geron, C., Guenther, A., Greenberg, J., Karl, T., & Rasmussen, R. (2006). Biogenic volatile organic compound emissions from desert vegetation of the southwestern US. *Atmospheric Environment*, *40*(9), 1645-1660.

Giguère, P. A., & Olmos, A. W. (1956). SUR LE SPECTRE ULTRAVIOLET DE L'ACIDE PERACÉETIQUE ET L'HYDROLYSE DES PERACÉTATES. *Canadian Journal of Chemistry*, *34*(5), 689-691.

Golden, D. M., and G. P. Smith (2000), Reaction of OH + NO_2 + M: A new view, *Journal of Physical Chemistry A*, *104*(17), 3991-3997.

Greenberg, J. P., & Zimmerman, P. R. (1984). Nonmethane hydrocarbons in remote tropical, continental, and marine atmospheres. *Journal of Geophysical Research: Atmospheres*, *89*(D3), 4767-4778.

Gregory, G. L., Browell, E. V., & Warren, L. S. (1988). Boundary layer ozone: An airborne survey above the Amazon Basin. *Journal of Geophysical Research: Atmospheres*, *93*(D2), 1452-1468.

Grell, G. A., Dudhia, J., & Stauffer, D. R. (1994). A description of the fifth-generation Penn State/NCAR mesoscale model (MM5).

Guenther, A., Geron, C., Pierce, T., Lamb, B., Harley, P., & Fall, R. (2000). Natural emissions of non-methane volatile organic compounds, carbon monoxide, and oxides of nitrogen from North America. *Atmospheric Environment*, *34*(12-14), 2205-2230.

Hagenbjörk, A., Malmqvist, E., Mattisson, K., Sommar, N. J., & Modig, L. (2017). The spatial variation of O_3, NO, NO_2 and NO_x and the relation between them in two Swedish cities. *Environmental monitoring and assessment*, *189*(4), 161.

Hall, J. V., A. M. Winer, M. T. Klienman, F. W. Lurmann, V. Brajer, and S. D. Colome (1992), Valuing the Health Benefits of Clean Air, *Science, V255*, 812-817.

Hall, S. J., Ogata, E. M., Weintraub, S. R., Baker, M. A., Ehleringer, J. R., Czimczik, C. I., & Bowling, D. R. (2016). Convergence in nitrogen deposition and cryptic isotopic variation across urban and agricultural valleys in northern Utah. *JOURNAL OF GEOPHYSICAL RESEARCH-BIOGEOSCIENCES*, *121*(9), 2340–2355. https://doi.org/10.1002/2016JG003354

Hanson, P. J., & Lindberg, S. E. (1991). Dry deposition of reactive nitrogen compounds: a review of leaf, canopy and non-foliar measurements. *Atmospheric Environment. Part A. General Topics*, *25*(8), 1615-1634.

Harley, R. A., McKeen, S. A., Pearson, J., Rodgers, M. O., & Lonneman, W. A. (2001). Analysis of motor vehicle emissions during the Nashville/Middle Tennessee Ozone Study. *Journal of Geophysical Research: Atmospheres*, *106*(D4), 3559-3567.

Harrison, R. M., J. L. Grenfell, S. Yamulki, K. C. Clemitshaw, S. A. Penkett, J. N. Cape, and G. G. McFadyen (1999), Budget of NO_y species measured at a coastal site, *Atmospheric Environment*, *33*(26), 4255-4272, doi:10.1016/s1352-2310(99)00176-4.

Hastings, M. G., K. L. Casciotti, and E. M. Elliott (2013), Stable Isotopes as Tracers of Anthropogenic Nitrogen Sources, Deposition, and Impacts, *Elements*, *9*(5), 339-344.

Hastings, M. G., Sigman, D. M., & Lipschultz, F. (2003). Isotopic evidence for source changes of nitrate in rain at Bermuda. *Journal of Geophysical Research: Atmospheres*, *108*(D24).

He, H., Stehr, J. W., Hains, J. C., Krask, D. J., Doddridge, B. G., Vinnikov, K. Y., ... & Dickerson, R. R. (2013). Trends in emissions and concentrations of air pollutants in the lower troposphere in the Baltimore/Washington airshed from 1997 to 2011. *Atmospheric Chemistry and Physics*, *13*(15), 7859-7874.

Heaton, T. H. E. (1987). 15N 14N ratios of nitrate and ammonium in rain at Pretoria, South Africa. *Atmospheric Environment (1967)*, *21*(4), 843-852.

Heaton, T. H. E. (1990). 15N/14N ratios of NO_x from vehicle engines and coal-fired power stations. *Tellus B*, *42*(3), 304-307.

Hegglin, M. I., D. Brunner, T. Peter, P. Hoor, H. Fischer, J. Staehelin, M. Krebsbach, C. Schiller, U. Parchatka, and U. Weers (2006), Measurements of NO, NO_y, N_2O, and O_3 during SPURT: implications for transport and chemistry in the lowermost stratosphere, *Atmospheric Chemistry and Physics*, *6*, 1331-1350, doi:10.5194/acp-6-1331-2006.

Hertel, O., Berkowicz, R., Christensen, J., & Hov, Ø. (1993). Test of two numerical schemes for use in atmospheric transport-chemistry models. *Atmospheric Environment. Part A. General Topics*, *27*(16), 2591-2611.

Hoering, T. (1957). The isotopic composition of the ammonia and the nitrate ion in rain. *Geochimica et Cosmochimica Acta*, *12*(1-2), 97-102.

Horowitz, L. W., J. Liang, G. M. Gardner, and D. J. Jacob (1998), Export of reactive nitrogen from North America during summertime: sensitivity to hydrocarbon chemistry, *Journal of Geophysical Research*, *103*(D11), 13451-13476.

Houlton, B. Z., Boyer, E., Finzi, A., Galloway, J., Leach, A., Liptzin, D., ... & Townsend, A. R. (2013). Intentional versus unintentional nitrogen use in the United States: trends, efficiency and implications. *Biogeochemistry*, *114*(1-3), 11-23.

Houyoux, M. (2005). Clean Air Interstate Rule Emissions Inventory Technical Support Document. *US EPA*.

Hoyle, C. R., et al. (2011), A review of the anthropogenic influence on biogenic secondary organic aerosol, *Atmospheric Chemistry and Physics*, *11*(1), 321-343, doi:10.5194/acp-11-321-2011.

Hudman, R. C., Moore, N. E., Mebust, A. K., Martin, R. V., Russell, A. R., Valin, L. C., & Cohen, R. C. (2012). Steps towards a mechanistic model of global soil nitric oxide emissions: implementation and space based-constraints. *Atmospheric Chemistry and Physics*, *12*(16), 7779-7795.

Huntrieser, H., Feigl, C., Schlager, H., Schröder, F., Gerbig, C., Van Velthoven, P., ... & Schumann, U. (2002). Airborne measurements of NO_x, tracer species, and small particles during the European Lightning Nitrogen Oxides Experiment. *Journal of Geophysical Research: Atmospheres*, *107*(D11).

Huntrieser, H., Schlager, H., Feigl, C., & Höller, H. (1998). Transport and production of NO_x in electrified thunderstorms: Survey of previous studies and new observations at midlatitudes. *Journal of Geophysical Research: Atmospheres*, *103*(D21), 28247-28264.

Ingalls, M. N. (1989). On-road vehicle emission factors from measurements in a Los Angeles area tunnel. *AIR & WASTE MANAGEMENT ASSOC, PITTSBURGH, PA, (USA).*, *8*, 1989.

Jacob, D. J., & Wofsy, S. C. (1990). Budgets of reactive nitrogen, hydrocarbons, and ozone over the Amazon forest during the wet season. *Journal of Geophysical Research: Atmospheres*, *95*(D10), 16737-16754.

Jaeglé, L., Steinberger, L., Martin, R. V., & Chance, K. (2005). Global partitioning of NO_x sources using satellite observations: Relative roles of fossil fuel combustion, biomass burning and soil emissions. *Faraday discussions*, *130*, 407-423.

Jaffe, D. A., Honrath, R. E., Zhang, L., Akimoto, H., Shimizu, A., Mukai, H., ... & Merrill, J. (1996). Measurements of NO, NO_y, CO and O_3 and estimation of the ozone production rate at Oki Island, Japan, during PEM-West. *Journal of Geophysical Research: Atmospheres*, *101*(D1), 2037-2048.

Janach, W. E. (1989). Surface ozone: trend details, seasonal variations, and interpretation. *Journal of Geophysical Research: Atmospheres*, *94*(D15), 18289-18295.

Jimenez, P., Baldasano, J. M., & Dabdub, D. (2003). Comparison of photochemical mechanisms for air quality modeling. *Atmospheric Environment*, *37*(30), 4179-4194.

Johansson, C. (1987). Pine forest: a negligible sink for atmospheric NO_x in rural Sweden. *Tellus B: Chemical and Physical Meteorology*, *39*(5), 426-438.

Kastler, J., & Ballschmiter, K. (1998). Bifunctional alkyl nitrates–trace constituents of the atmosphere. *Fresenius' journal of analytical chemistry*, *360*(7-8), 812-816.

Kim, S. W., Heckel, A., Frost, G. J., Richter, A., Gleason, J., Burrows, J. P., ... & Trainer, M. (2009). NO_2 columns in the western United States observed from space and simulated by a regional chemistry model and their implications for NO_x emissions. *Journal of Geophysical Research: Atmospheres*, *114*(D11).

Kirchhoff, V. W. (1988). Surface ozone measurements in Amazonia. *Journal of Geophysical Research: Atmospheres*, *93*(D2), 1469-1476.

Koike, M., Kondo, Y., Kita, K., Takegawa, N., Nishi, N., Kashihara, T., ... & Liley, B. (2007). Measurements of reactive nitrogen produced by tropical thunderstorms during BIBLE-C. *Journal of Geophysical Research: Atmospheres*, *112*(D18).

Kuang, C., Riipinen, I., Sihto, S. L., Kulmala, M., McCormick, A. V., & McMurry, P. H. (2010). An improved criterion for new particle formation in diverse atmospheric environments. *Atmospheric Chemistry and Physics*, *10*(17), 8469-8480.

Lajtha, K., and J. Jones (2013), Trends in cation, nitrogen, sulfate and hydrogen ion concentrations in precipitation in the United States and Europe from 1978 to 2010: a new look at an old problem, *Biogeochemistry*, *116*(1-3), 303-334, doi:10.1007/s10533-013-9860-2.

Lawrence, M. G., Chameides, W. L., Kasibhatla, P. S., Levy II, H., & Moxim, W. (1995). Lightning and atmospheric chemistry: The rate of atmospheric NO production. *Handbook of Atmospheric Electrodynamics*, *1*, 189-202.

Lee, S. H., Uin, J., Guenther, A. B., de Gouw, J. A., Yu, F., Nadykto, A. B., ... & Baumann, K. (2016). Isoprene suppression of new particle formation: Potential mechanisms and implications. *Journal of Geophysical Research: Atmospheres*, *121*(24), 14-621.

Lefohn, A. S., & Pinkerton, J. E. (1988). High resolution characterization of ozone data for sites located in forested areas of the United States. *JAPCA*, *38*(12), 1504-1511.

Lelieveld, J., et al. (2008), Atmospheric oxidation capacity sustained by a tropical forest, *Nature*, *452*(7188), 737-740.

Lerdau, M. T., Munger, J. W., & Jacob, D. J. (2000). The NO_2 flux conundrum. *Science*, *289*(5488), 2291-2293.

Levy, H., Moxim, W. J., & Kasibhatla, P. S. (1996). A global three-dimensional time-dependent lightning source of tropospheric NO_x. *Journal of Geophysical Research: Atmospheres*, *101*(D17), 22911-22922.

Li, D., & Wang, X. (2008). Nitrogen isotopic signature of soil-released nitric oxide (NO) after fertilizer application. *Atmospheric Environment*, *42*(19), 4747-4754.

Li, Y., Schichtel, B. A., Walker, J. T., Schwede, D. B., Chen, X., Lehmann, C. M., ... & Collett, J. L. (2016). Increasing importance of deposition of reduced nitrogen in the United States. *Proceedings of the National Academy of Sciences*, 201525736.

Liang, M. C., G. A. Blake, and Y. L. Yung (2004), A semianalytic model for photo-induced isotopic fractionation in simple molecules, *Journal of Geophysical Research-Atmospheres*, *109*(D10).

Liao, T., Gui, K., Jiang, W., Wang, S., Wang, B., Zeng, Z., ... & Sun, Y. (2018). Air stagnation and its impact on air quality during winter in Sichuan and Chongqing, southwestern China. *Science of the Total Environment*, *635*, 576-585.

Lighty, J. S., Veranth, J. M., & Sarofim, A. F. (2000). Combustion aerosols: factors governing their size and composition and implications to human health. *Journal of the Air & Waste Management Association*, *50*(9), 1565-1618.

Liu, L., Guo, J., Miao, Y., Li, J., Chen, D., He, J., & Cui, C. (2018). Elucidating the relationship between aerosol concentration and summertime boundary layer structure in central China. *Environmental Pollution*, *241*, 646-653.

Logan, J. A. (1989). Ozone in rural areas of the United States. *Journal of Geophysical Research: Atmospheres*, *94*(D6), 8511-8532.

Lu, Z., Streets, D. G., De Foy, B., Lamsal, L. N., Duncan, B. N., & Xing, J. (2015). Emissions of nitrogen oxides from US urban areas: estimation from Ozone Monitoring Instrument retrievals for 2005-2014. *Atmospheric Chemistry and Physics Discussions (Online)*, *15*(10).

Ludwig, J., Meixner, F. X., Vogel, B., & Förstner, J. (2001). Soil-air exchange of nitric oxide: An overview of processes, environmental factors, and modeling studies. *Biogeochemistry*, *52*(3), 225-257.

Ma, J. Z., Y. C. Liu, C. Han, Q. X. Ma, C. Liu, and H. He (2013), Review of heterogeneous photochemical reactions of NOy on aerosol - A possible daytime source of nitrous acid (HONO) in the atmosphere, *Journal of Environmental Sciences-China*, *25*(2), 326-334, doi:10.1016/s1001-0742(12)60093-x.

Ma, Z., Liu, C., Zhang, C., Liu, P., Ye, C., Xue, C., ... & Mu, Y. (2019). The levels, sources and reactivity of volatile organic compounds in a typical urban area of Northeast China. *Journal of Environmental Sciences*, *79*, 121-134.

Madronich, S. (1987). Photodissociation in the atmosphere: 1. Actinic flux and the effects of ground reflections and clouds. *Journal of Geophysical Research: Atmospheres*, *92*(D8), 9740-9752.

Martin, R. V., Sauvage, B., Folkins, I., Sioris, C. E., Boone, C., Bernath, P., & Ziemke, J. (2007). Space-based constraints on the production of nitric oxide by lightning. *Journal of Geophysical Research: Atmospheres*, *112*(D9).

Martinez, R. D., Buitrago, A. A., Howell, N. W., Hearn, C. H., & Joens, J. A. (1992). The near UV absorption spectra of several aliphatic aldehydes and ketones at 300 K. *Atmospheric Environment. Part A. General Topics*, *26*(5), 785-792.

Mase, D. F. (2010). *A coupled modeling and observational approach to understanding oxygen-18 in atmospheric nitrate* (Doctoral dissertation, Purdue University).

Mathur, R., Shankar, U., Hanna, A. F., Odman, M. T., McHenry, J. N., Coats Jr, C. J., ... & Byun, D. W. (2005). Multiscale Air Quality Simulation Platform (MAQSIP): Initial applications and performance for tropospheric ozone and particulate matter. *Journal of Geophysical Research: Atmospheres*, *110*(D13).

McMurry, P. H., Fink, M., Sakurai, H., Stolzenburg, M. R., Mauldin III, R. L., Smith, J., ... & Huey, L. G. (2005). A criterion for new particle formation in the sulfur-rich Atlanta atmosphere. *Journal of Geophysical Research: Atmospheres*, *110*(D22).

Miao, Y., Guo, J., Liu, S., Zhao, C., Li, X., Zhang, G., ... & Ma, Y. (2018). Impacts of synoptic condition and planetary boundary layer structure on the trans-boundary aerosol transport from Beijing-Tianjin-Hebei region to northeast China. *Atmospheric Environment*, *181*, 1-11.

Michalski, G., Fang, H., Walters, W. W., & Mase, D. (2020). i_N RACM: Incorporating ^{15}N into the Regional Atmospheric Chemistry Mechanism (RACM) for assessing the role photochemistry plays in controlling the isotopic composition of NO_x, NO_y, and atmospheric nitrate. *Geoscientific Model Development Discussions*, 1-47.

Michalski, G., R. Jost, D. Sugny, M. Joyeux, and M. Thiemens (2004), Dissociation energies of six NO_2 isotopologues by laser induced fluorescence and zero point energy of some triatomic molecules *Journal of Chemical Physics*, *121*(15), 7153-7161.

Miller, C. E., and Y. L. Yung (2000), Photo-induced isotopic fractionation, *Journal of Geophysical Research-Atmospheres*, *105*(D23), 29039-29051.

Miller, D. J., Chai, J., Guo, F., Dell, C. J., Karsten, H., & Hastings, M. G. (2018). Isotopic Composition of In Situ Soil NO_x Emissions in Manure-Fertilized Cropland. *Geophysical Research Letters*, *45*(21), 12-058.

Miller, D. J., Wojtal, P. K., Clark, S. C., & Hastings, M. G. (2017). Vehicle NO_x emission plume isotopic signatures: Spatial variability across the eastern United States. *Journal of Geophysical Research: Atmospheres*, *122*(8), 4698-4717.

Moore, H. (1977). The isotopic composition of ammonia, nitrogen dioxide and nitrate in the atmosphere. *Atmospheric Environment (1967)*, *11*(12), 1239-1243.

Moortgat, G. K., Klippel, W., Möbus, K. H., Seiler, W., & Warneck, P. (1980). *Laboratory Measurements of Photolytic Parameters for Formaldehyde*. MAX-PLANCK-INST FUER CHEMIE MAINZ (GERMANY FR).

Morino, Y., Y. Kondo, N. Takegawa, Y. Miyazaki, K. Kita, Y. Komazaki, M. Fukuda, T. Miyakawa, N. Moteki, and D. R. Worsnop (2006), Partitioning of HNO_3 and particulate nitrate over Tokyo: Effect of vertical mixing, *Journal of Geophysical Research-Atmospheres*, *111*(D15), doi:10.1029/2005jd006887.

Müller, J. F. (1992). Geographical distribution and seasonal variation of surface emissions and deposition velocities of atmospheric trace gases. *Journal of Geophysical Research: Atmospheres*, *97*(D4), 3787-3804.

Müller, J. F., & Stavrakou, T. (2005). Inversion of CO and NO_x emissions using the adjoint of the IMAGES model. *Atmospheric Chemistry and Physics*, *5*(5), 1157-1186.

Murray, L. T. (2016). Lightning NO_x and impacts on air quality. *Current Pollution Reports*, *2*(2), 115-133.

National Centers for Environmental Information. (2019). North American Mesoscale Forecast System (NAM). Retrieved from https://www.ncdc.noaa.gov/data-access/model-data/model-datasets/north-american-mesoscale-forecast-system-nam

National Centers for Environmental Information. (2019). U.S. Wind Climatology. Retrieved from https://www.ncdc.noaa.gov/societal-impacts/wind/

National Research Council. (1992). *Rethinking the ozone problem in urban and regional air pollution*. National Academies Press.

Occhipinti, C., Aneja, V. P., Showers, W., & Niyogi, D. (2008). Back-trajectory analysis and source-receptor relationships: Particulate matter and nitrogen isotopic composition in rainwater. *JOURNAL OF THE AIR & WASTE MANAGEMENT ASSOCIATION*, *58*(9, SI), 1215–1222. https://doi.org/10.3155/1047-3289.58.9.1215

Oke, T. R. (2002). *Boundary layer climates*. Routledge.

Ott, L. E., Pickering, K. E., Stenchikov, G. L., Huntrieser, H., & Schumann, U. (2007). Effects of lightning NO_x production during the 21 July European Lightning Nitrogen Oxides Project storm studied with a three-dimensional cloud-scale chemical transport model. *Journal of Geophysical Research: Atmospheres*, *112*(D5).

Pan, Y. P., S. L. Tian, D. W. Liu, Y. T. Fang, X. Y. Zhu, M. Gao, G. R. Wentworth, G. Michalski, X. J. Huang, and Y. S. Wang (2018), Source Apportionment of Aerosol Ammonium in an Ammonia-Rich Atmosphere: An Isotopic Study of Summer Clean and Hazy Days in Urban Beijing, *Journal of Geophysical Research-Atmospheres*, *123*(10), 5681-5689, doi:10.1029/2017jd028095.

Parrish, D. D., Trainer, M., Williams, E. J., Fahey, D. W., Hübler, G., Eubank, C. S., ... & Fehsenfeld, F. C. (1986). Measurements of the NO_x-O_3 photostationary state at Niwot Ridge, Colorado. *Journal of Geophysical Research: Atmospheres*, *91*(D5), 5361-5370.

Parrish, D. D. (2006). Critical evaluation of US on-road vehicle emission inventories.*Atmospheric Environment,40*(13), 2288-2300.

Paulot, F., P. Ginoux, W. F. Cooke, L. J. Donner, S. Fan, M. Y. Lin, J. Mao, V. Naik, and L. W. Horowitz (2016), Sensitivity of nitrate aerosols to ammonia emissions and to nitrate chemistry: implications for present and future nitrate optical depth, *Atmospheric Chemistry and Physics*, *16*(3), 1459-1477, doi:10.5194/acp-16-1459-2016.

Pearson, J., Wells, D. M., Seller, K. J., Bennett, A., Soares, A., Woodall, J., & Ingrouille, M. J. (2000). Traffic exposure increases natural 15 N and heavy metal concentrations in mosses. *The New Phytologist*, *147*(2), 317-326.

Petäjä, T., Mauldin Iii, R. L., Kosciuch, E., McGrath, J., Nieminen, T., Paasonen, P., ... & Kulmala, M. (2009). Sulfuric acid and OH concentrations in a boreal forest site. *Atmospheric Chemistry and Physics*, *9*(19), 7435-7448.

Pierce, T. E. (2001). Reconsideration of the Emission Factors assumed in BEIS3 for Three USGS Vegetation Categories: Shrubland, Coniferous Forest, and Deciduous Forest.

Pierson, W. R., Gertler, A. W., & Bradow, R. L. (1990). Comparison of the SCAQS tunnel study with other on road vehicle emission data. *Journal of the Air & Waste Management Association*, *40*(11), 1495-1504.

Pierson, W. R., Gertler, A. W., Robinson, N. F., Sagebiel, J. C., Zielinska, B., Bishop, G. A., ... & Ray, W. D. (1996). Real-world automotive emissions—summary of studies in the Fort McHenry and Tuscarora mountain tunnels. *Atmospheric Environment*, *30*(12), 2233-2256.

Pilegaard, K. (2013). Processes regulating nitric oxide emissions from soils. *Phil. Trans. R. Soc. B*, *368*(1621), 20130126

Platt, U. F., A. M. Winer, H. W. Biermann, R. Atkinson, and J. N. Pitts (1984), Measurement of Nitrate Radical Concentrations in Continental Air, *Environmental Science & Technology*, *18*(5), 365-369.

Potter, C. S., Matson, P. A., Vitousek, P. M., & Davidson, E. A. (1996). Process modeling of controls on nitrogen trace gas emissions from soils worldwide. *Journal of Geophysical Research: Atmospheres*, *101*(D1), 1361-1377.

Pouliot, G., & Pierce, T. E. (2009, April). Integration of the Model of Emissions of Gases and Aerosols from Nature (MEGAN) into the CMAQ Modeling System. In *18th International Emission Inventory Conference, Baltimore, Maryland* (pp. 14-17).

Prinn, R. G. (2003), The cleansing capacity of the atmosphere, *Annual Review of Environment and Resources*, *28*, 29-57.

Pusede, S. E., et al. (2016), On the effectiveness of nitrogen oxide reductions as a control over ammonium nitrate aerosol, *Atmospheric Chemistry and Physics*, *16*(4), 2575-2596, doi:10.5194/acp-16-2575-2016.

Pye, H. O. T., A. W. H. Chan, M. P. Barkley, and J. H. Seinfeld (2010), Global modeling of organic aerosol: the importance of reactive nitrogen (NO_x and NO_3), *Atmospheric Chemistry and Physics*, *10*(22), 11261-11276.

Qi, X. M., Ding, A. J., Nie, W., Petäjä, T., Kerminen, V. M., Herrmann, E., and Sun, J. N. (2015). Aerosol size distribution and new particle formation in the western Yangtze River Delta of China: 2 years of measurements at the SORPES station. *Atmospheric chemistry and physics*, *15*(21), 12445-12464.

Redling, K., Elliott, E., Bain, D., & Sherwell, J. (2013). Highway contributions to reactive nitrogen deposition: tracing the fate of vehicular NO_x using stable isotopes and plant biomonitors. *Biogeochemistry*, *116*(1-3), 261-274.

Reis, S., Pinder, R. W., Zhang, M., Lijie, G., & Sutton, M. A. (2009). Reactive nitrogen in atmospheric emission inventories-a review. *Atmospheric Chemistry & Physics Discussions*, *9*(3).

Richet, P., Y. Bottinga, and M. Javoy (1977), Review of hydrogen, carbon, nitrogen, oxygen, sulfur, and chlorine stable isotope fractionation among gaseous molecules, *Annual Review of Earth and Planetary Sciences*, *5*, 65-110

Ridley, B. A., Dye, J. E., Walega, J. G., Zheng, J., Grahek, F. E., & Rison, W. (1996). On the production of active nitrogen by thunderstorms over New Mexico. *Journal of Geophysical Research: Atmospheres*, *101*(D15), 20985-21005.

Ridley, B., Ott, L., Pickering, K., Emmons, L., Montzka, D., Weinheimer, A., ... & McGill, M. (2004). Florida thunderstorms: A faucet of reactive nitrogen to the upper troposphere. *Journal of Geophysical Research: Atmospheres*, *109*(D17).

Riemer, N., H. Vogel, B. Vogel, B. Schell, I. Ackermann, C. Kessler, and H. Hass (2003), Impact of the heterogeneous hydrolysis of N_2O_5 on chemistry and nitrate aerosol formation in the lower troposphere under photosmog conditions, *Journal of Geophysical Research*, *108*(D4), 4144-DOI: 4110.1029/2002JD002436.

Riemer, N., Vogel, H., Vogel, B., Anttila, T., Kiendler-Scharr, A., and Mentel, T. F. (2009). Relative importance of organic coatings for the heterogeneous hydrolysis of N_2O_5 during summer in Europe. *Journal of Geophysical Research: Atmospheres*, *114*(D17).

Riha, K. M. (2013). The use of stable isotopes to constrain the nitrogen cycle. Purdue University, West Lafayette, IN

Roehl, C. M., J. J. Orlando, G. S. Tyndall, R. E. Shetter, G. J. Vazquez, C. A. Cantrell, and J. G. Calvert (1994), Temperature-dependence of the quantum yields for the photolysis of NO_2 near the dissociation limit, *Journal of Physical Chemistry*, *98*(32), 7837-7843, doi:10.1021/j100083a015.

Romer, P. S., Duffey, K. C., Wooldridge, P. J., Allen, H. M., Ayres, B. R., Brown, S. S., ... & Feiner, P. A. (2016). The lifetime of nitrogen oxides in an isoprene-dominated forest. *Atmospheric Chemistry and Physics*, *16*(12), 7623-7637.

Russell, K. M., Galloway, J. N., Macko, S. A., Moody, J. L., & Scudlark, J. R. (1998). Sources of nitrogen in wet deposition to the Chesapeake Bay region. *ATMOSPHERIC ENVIRONMENT*, *32*(14–15), 2453–2465.

Saito, T., Yokouchi, Y., & Kawamura, K. (2000). Distributions of C^2–C^6 hydrocarbons over the western North Pacific and eastern Indian Ocean. *Atmospheric environment*, *34*(25), 4373-4381.

Sander, S. P., Friedl, R. R., Barker, J. R., Golden, D. M., Kurylo, M. J., Wine, P. H., ... & Huie, R. E. (2009). *Chemical kinetics and photochemical data for use in Atmospheric Studies Evaluation Number 16: supplement to Evaluation 15: update of key reactions*. Pasadena, CA: Jet Propulsion Laboratory, National Aeronautics and Space Administration, 2009.

Savard, M. M., Bégin, C., Smirnoff, A., Marion, J., & Rioux-Paquette, E. (2009). Tree-ring nitrogen isotopes reflect anthropogenic NO_x emissions and climatic effects. *Environmental science & technology*, *43*(3), 604-609.

Savard, M. M., Cole, A., Smirnoff, A., & Vet, R. (2017). δ15N values of atmospheric N species simultaneously collected using sector-based samplers distant from sources–Isotopic inheritance and fractionation. *Atmospheric environment*, *162*, 11-22.

Sawyer, R. F., Harley, R. A., Cadle, S. H., Norbeck, J. M., Slott, R., & Bravo, H. A. (2000). Mobile sources critical review: 1998 NARSTO assessment. *Atmospheric Environment*, *34*(12-14), 2161-2181.

Scholes, M. C., Martin, R., Scholes, R. J., Parsons, D., & Winstead, E. (1997). NO and N_2O emissions from savanna soils following the first simulated rains of the season. *Nutrient cycling in Agroecosystems*, *48*(1-2), 115-122.

Schumann, U., & Huntrieser, H. (2007). The global lightning-induced nitrogen oxides source. *Atmospheric Chemistry and Physics*, *7*(14), 3823-3907.

Schumann, U., Kurz, C., & Schlager, H. (2006, July). Towards a Robust Estimate of the Global Lightning Nitrogen Oxides Source Rate and its Error Bound. In *Atmospheric Science Conference* (Vol. 628).

Schwartz, S. E. (1996). The whitehouse effect—Shortwave radiative forcing of climate by anthropogenic aerosols: An overview. *Journal of Aerosol Science*,*27*(3), 359-382.

Schwede, D., Pouliot, G., & Pierce, T. (2005, September). Changes to the biogenic emissions inventory system version 3 (BEIS3). In *4th Annual CMAS Models-3 Users' Conference, September* (Vol. 26, p. 28).

Seinfeld, J. H., and S. N. Pandis (1998), *Atmospheric chemistry and physics : from air pollution to climate change*, 1 ed., New York : Wiley.

Seinfeld, J. H., & Pandis, S. N. (2016). *Atmospheric chemistry and physics: from air pollution to climate change*. John Wiley & Sons.

Selden, T. M., Forrest, A. S., & Lockhart, J. E. (1999). Analyzing the reductions in US air pollution emissions: 1970 to 1990. *Land Economics*, 1-21.

Sharma, H. D., R. E. Jervis, and K. Y. Wong (1970), Isotopic exchange reactions in nitrogen oxides, *Journal of Physical Chemistry*, *74*(4), 923-933.

Shepherd, M. F., Barzetti, S., & Hastie, D. R. (1991). The Production of Atmospheric NO_2 and N_2O from a Fertilized Agricultural Soil.

Shrivastava, M., Cappa, C. D., Fan, J., Goldstein, A. H., Guenther, A. B., Jimenez, J. L., ... & Petaja, T. (2017). Recent advances in understanding secondary organic aerosol: Implications for global climate forcing. *Reviews of Geophysics*, *55*(2), 509-559.

Shu, L., Xie, M., Gao, D., Wang, T., Fang, D., Liu, Q., ... & Peng, L. (2017). Regional severe particle pollution and its association with synoptic weather patterns in the Yangtze River Delta region, China. *Atmospheric Chemistry and Physics*, *17*(21), 12871.

Singer, B. C., & Harley, R. A. (1996). A fuel-based motor vehicle emission inventory. *Journal of the Air & Waste Management Association*, *46*(6), 581-593.

Singer, B. C., & Harley, R. A. (2000). A fuel-based inventory of motor vehicle exhaust emissions in the Los Angeles area during summer 1997. *Atmospheric Environment*, *34*(11), 1783-1795.

Sjostedt, S. J., Slowik, J. G., Brook, J. R., Chang, R. W., Mihele, C., Stroud, C. A., ... & Abbatt, J. P. D. (2011). Diurnally resolved particulate and VOC measurements at a rural site: indication of significant biogenic secondary organic aerosol formation. *Atmospheric Chemistry and Physics*, *11*(12), 5745-5760.

Skamarock, W. C., Dye, J. E., Defer, E., Barth, M. C., Stith, J. L., Ridley, B. A., & Baumann, K. (2003). Observational-and modeling-based budget of lightning-produced NO_x in a continental thunderstorm. *Journal of Geophysical Research: Atmospheres*, *108*(D10).

Slovik, S., Siegmund, A., FÜHRER, H. W., & Heber, U. (1996). Stomatal uptake of SO_2, NO_x and O_3 by spruce crowns (Picea abies) and canopy damage in Central Europe. *New phytologist*, *132*(4), 661-676.

Snape, C. E., Sun, C. G., Fallick, A. E., Irons, R., & Haskell, J. (2003). Potential of stable nitrogen isotope ratio measurements to resolve fuel and thermal NO_x in coal combustion. *Papers of the American Chemical Society*, *225*, U843-U843.

Snyder, J. A., D. Hanway, J. Mendez, A. J. Jamka, and F. M. Tao (1999), A density functional theory study of the gas-phase hydrolysis of dinitrogen pentoxide, *Journal of Physical Chemistry A*, *103*(46), 9355-9358.

Snyder, J. P. (1987). *Map projections--A working manual* (Vol. 1395). US Government Printing Office (pp. 104-110)

Spak, S. N., and T. Holloway (2009), Seasonality of speciated aerosol transport over the Great Lakes region, *Journal of Geophysical Research-Atmospheres*, *114*.

Spak, S., Holloway, T., Mednick, A., & Stone, B. (2007, December). Evaluation of Bottom-Up Mobile Emissions Inventories in the Upper Midwest. In *AGU Fall Meeting Abstracts*.

Srivastava, R. K., Neuffer, W., Grano, D., Khan, S., Staudt, J. E., & Jozewicz, W. (2005). Controlling NO_x emission from industrial sources. *Environmental progress*, *24*(2), 181-197.

Staffelbach, T. A., Orlando, J. J., Tyndall, G. S., & Calvert, J. G. (1995). The UV-visible absorption spectrum and photolysis quantum yields of methylglyoxal. *Journal of Geophysical Research: Atmospheres*, *100*(D7), 14189-14198.

Staudt, A. C., Jacob, D. J., Ravetta, F., Logan, J. A., Bachiochi, D., Krishnamurti, T. N., ... & Talbot, B. (2003). Sources and chemistry of nitrogen oxides over the tropical Pacific. *Journal of Geophysical Research: Atmospheres*, *108*(D2).

Stavrakou, T., Müller, J. F., Boersma, K. F., Van Der A, R. J., Kurokawa, J., Ohara, T., & Zhang, Q. (2013). Key chemical NO_x sink uncertainties and how they influence top-down emissions of nitrogen oxides.

Stehfest, E., & Bouwman, L. (2006). N_2O and NO emission from agricultural fields and soils under natural vegetation: summarizing available measurement data and modeling of global annual emissions. *Nutrient Cycling in Agroecosystems*, *74*(3), 207-228.

Stevenson, D. S., Dentener, F. J., Schultz, M. G., Ellingsen, K., Van Noije, T. P. C., Wild, O., ... & Bergmann, D. J. (2006). Multimodel ensemble simulations of present-day and near-future tropospheric ozone. *Journal of Geophysical Research: Atmospheres*, *111*(D8).

Stockwell, W. R., Kirchner, F., Kuhn, M., & Seefeld, S. (1997). A new mechanism for regional atmospheric chemistry modeling. *Journal of Geophysical Research: Atmospheres*, *102*(D22), 25847-25879.

Stockwell, W. R., Middleton, P., Chang, J. S., & Tang, X. (1990). The second generation regional acid deposition model chemical mechanism for regional air quality modeling. *Journal of Geophysical Research: Atmospheres*, *95*(D10), 16343-16367.

Stockwell, W. R., P. Middleton, J. S. Chang, and X. Y. Tang (1990), The 2nd Generation Regional Acid Deposition Model Chemical Mechanism for Regional Air-Quality Modeling, *Journal of Geophysical Research-Atmospheres*, *95*(D10), 16343-16367.

The Institute for the Environment - The University of North Carolina at Chapel Hill. (2017). SMOKE v4.5 User's Manual. Retrieved from https://www.cmascenter.org/smoke/documentation/4.5/html/

Thoene, B., Rennenberg, H., & Weber, P. (1996). Absorption of atmospheric NO_2 by spruce (Picea abies) trees: II. Parameterization of NO_2 fluxes by controlled dynamic chamber experiments. *New Phytologist*, *134*(2), 257-266.

Thomas, R. J., Krehbiel, P. R., Rison, W., Hamlin, T., Boccippio, D. J., Goodman, S. J., & Christian, H. J. (2000). Comparison of ground-based 3-dimensional lightning mapping observations with satellite-based LIS observations in Oklahoma. *Geophysical research letters*, *27*(12), 1703-1706.

Tie, X., Zhang, R., Brasseur, G., & Lei, W. (2002). Global NO_x production by lightning. *Journal of Atmospheric Chemistry*, *43*(1), 61-74.

Torres, A. L., & Buchan, H. (1988). Tropospheric nitric oxide measurements over the Amazon Basin. *Journal of Geophysical Research: Atmospheres*, *93*(D2), 1396-1406.

Tost, H., Jöckel, P., & Lelieveld, J. (2007). Lightning and convection parameterisations–uncertainties in global modelling. *Atmospheric Chemistry and Physics*, *7*(17), 4553-4568.

United States Census Bureau. (n.d.). 2007−2011 American Community Survey, 2011 American Community Survey 5-Year Estimate, travel time to work by zip code, table B08303. Retrieved from https://data.census.gov/cedsci/search

United States Energy Information Administration. (2017a). Electricity. Retrieved from https://www.eia.gov/electricity/data/eia860/

United States Energy Information Administration. (2017b). U.S. electric generating capacity increase in 2016 was largest net change since 2011. Retrieved from https://www.eia.gov/todayinenergy/detail.php?id=30112

United States Environmental Protection Agency. (2014). National Emissions Inventory (NEI). Retrieved from https://www.epa.gov/air-emissions-inventories/national-emissions-inventory-nei

United States Environmental Protection Agency. (2018). 2002 National Emissions Inventory (NEI) Booklet. Retrieved from https://archive.epa.gov/epa/air-emissions-inventories/2002-national-emissions-inventory-nei-booklet.html

United States Environmental Protection Agency. (2018). Biogenic Emissions Landuse Database. Retrieved from https://www.epa.gov/air-emissions-modeling/biogenic-emissions-landuse-database-version-3-beld3

Urey, H. C. (1947), Thermodynamic properties of isotopic substances, *J. Chem. Soc*, 562-581.

US Environmental Protection Agency. (2003). User's guide to MOBILE6. 1 and MOBILE6. 2 Mobile Source Emission Factor Model.

Van Hook, W. A., L. P. N. Rebelo, and M. Wolfsberg (2001), An interpretation of the vapor phase second virial coefficient isotope effect: Correlation of virial coefficient and vapor pressure isotope effects, *Journal of Physical Chemistry A*, *105*(40), 9284-9297, doi:10.1021/jp004305z.

Van Noije, T. P. C., Eskes, H. J., Dentener, F. J., Stevenson, D. S., Ellingsen, K., Schultz, M. G., ... & Bey, I. (2006). Multi-model ensemble simulations of tropospheric NO_2 compared with GOME retrievals for the year 2000. *Atmospheric chemistry and physics*, *6*(10), 2943-2979.

Vandaele, A. C., C. Hermans, S. Fally, M. Carleer, R. Colin, M. F. Merienne, A. Jenouvrier, and B. Coquart (2002), High-resolution Fourier transform measurement of the NO_2 visible and near-infrared absorption cross sections: Temperature and pressure effects, *Journal of Geophysical Research-Atmospheres*, *107*(D18), doi:10.1029/2001jd000971.

Vukovich, J., & Pierce, T. (2002, April). The implementation of BEIS3 within the SMOKE modeling framework. In *Proceedings of the 11th International Emissions Inventory Conference, Atlanta, Georgia* (pp. 15-18).

Walters, W. W., & Michalski, G. (2015). Theoretical calculation of nitrogen isotope equilibrium exchange fractionation factors for various NO_y molecules. *Geochimica et Cosmochimica Acta*, *164*, 284-297.

Walters, W. W., and G. Michalski (2016), Ab initio study of nitrogen and position-specific oxygen kinetic isotope effects in the NO + O_3 reaction, *Journal of Chemical Physics*, *145*(22), doi:10.1063/1.4968562.

Walters, W. W., B. D. Tharp, H. Fang, B. J. Kozak, and G. Michalski (2015b), Nitrogen Isotope Composition of Thermally Produced NOx from Various Fossil-Fuel Combustion Sources, *Environmental Science & Technology*, *49*(19), 11363-11371, doi:10.1021/acs.est.5b02769.

Walters, W. W., Fang, H., & Michalski, G. (2018). Summertime diurnal variations in the isotopic composition of atmospheric nitrogen dioxide at a small Midwestern United States city. *Atmospheric Environment*,*179*, 1-11.

Walters, W. W., Goodwin, S. R., & Michalski, G. (2015a). Nitrogen stable isotope composition ($\delta^{15}N$) of vehicle-emitted NO_x. *Environmental science & technology*, *49*(4), 2278-2285.

Walters, W. W., Tharp, B. D., Fang, H., Kozak, B. J., & Michalski, G. (2015b). Nitrogen isotope composition of thermally produced NO_x from various fossil-fuel combustion sources. *Environmental science & technology*, *49*(19), 11363-11371.

Walters, W. W., Simonini, D. S., & Michalski, G. (2016). Nitrogen isotope exchange between NO and NO_2 and its implications for $\delta^{15}N$ variations in tropospheric NO_x and atmospheric nitrate. *Geophysical Research Letters*, *43*(1), 440-448.

Wang, T., Xue, L., Brimblecombe, P., Lam, Y. F., Li, L., & Zhang, L. (2017). Ozone pollution in China: A review of concentrations, meteorological influences, chemical precursors, and effects. *Science of the Total Environment*, *575*, 1582-1596.

Wayne, R. P., Barnes, I., Biggs, P., Burrows, J. P., Canosa-Mas, C. E., Hjorth, J., ... & Restelli, G. (1991). The nitrate radical: Physics, chemistry, and the atmosphere. *Atmospheric Environment. Part A. General Topics*, *25*(1), 1-203.

Weber, P., & Rennenberg, H. (1996). Dependency of nitrogen dioxide (NO_2) fluxes to wheat (Triticum aestivum L.) leaves from NO_2 concentration, light intensity, temperature and relative humidity determined from controlled dynamic chamber experiments. *Atmospheric Environment*, *30*(17), 3001-3009.

Williams, E. J., Parrish, D. D., & Fehsenfeld, F. C. (1987). Determination of nitrogen oxide emissions from soils: Results from a grassland site in Colorado, United States. *Journal of Geophysical Research: Atmospheres*, *92*(D2), 2173-2179.

Wolfsberg, M. (1960), Note on secondary isotope effects in reaction rates, *Journal of Chemical Physics*, *33*(1), 2-6, doi:10.1063/1.1731078.

Wolfsberg, M., W. A. Van Hook, P. Paneth, L. P. N. Rebelo, M. Wolfsberg, W. A. VanHook, and P. Paneth (2010), *Isotope Effects on Equilibrium Constants of Chemical Reactions; Transition State Theory of Isotope Effects*, 77-137 pp., doi:10.1007/978-90-481-2265-3_4.

Wong, S., Wang, W. C., Isaksen, I. S., Berntsen, T. K., & Sundet, J. K. (2004). A global climate-chemistry model study of present-day tropospheric chemistry and radiative forcing from changes in tropospheric O3 since the preindustrial period. *Journal of Geophysical Research: Atmospheres*, *109*(D11).

Xing, J., Pleim, J., Mathur, R., Pouliot, G., Hogrefe, C., Gan, C. M.,&Wei, C. (2013). Historical gaseous and primary aerosol emissions in the United States from 1990 to 2010.*Atmospheric Chemistry and Physics*,*13*(15), 7531-7549.

Yan, X., Ohara, T., & Akimoto, H. (2005). Statistical modeling of global soil NO_x emissions. *Global Biogeochemical Cycles*, *19*(3).

Yang, J., Honrath, R. E., Peterson, M. C., Parrish, D. D., & Warshawsky, M. (2004). Photostationary state deviation–estimated peroxy radicals and their implications for HO_x and ozone photochemistry at a remote northern Atlantic coastal site. *Journal of Geophysical Research: Atmospheres*, *109*(D2).

Yarwood, G., Whitten, G. Z., Jung, J., Heo, G., & Allen, D. T. (2010). Texas Commission on Environmental Quality 12118 Park 35 Circle Austin, Texas 78753.

Yienger, J. J., & Levy, H. (1995). Empirical model of global soil-biogenic NO_x emissions. *Journal of Geophysical Research: Atmospheres*, *100*(D6), 11447-11464.

Yu, Z., & Elliott, E. M. (2017). Novel method for nitrogen isotopic analysis of soil-emitted nitric oxide. *Environmental Science & Technology*, *51*(11), 6268-6278.

Zhang, Y., K. Vijayaraghavan, X. Y. Wen, H. E. Snell, and M. Z. Jacobson (2009), Probing into regional ozone and particulate matter pollution in the United States: 1. A 1 year CMAQ simulation and evaluation using surface and satellite data, *Journal of Geophysical Research-Atmospheres*, *114*.

Zimmerman, P. R., Greenberg, J. P., & Westberg, C. E. (1988). Measurements of atmospheric hydrocarbons and biogenic emission fluxes in the Amazon boundary layer. *Journal of Geophysical Research: Atmospheres*, *93*(D2), 1407-1416.

Zörner, J., Penning de Vries, M., Beirle, S., Sihler, H., Veres, P. R., Williams, J., & Wagner, T. (2016). Multi-satellite sensor study on precipitation-induced emission pulses of NO_x from soils in semi-arid ecosystems. *Atmospheric Chemistry and Physics*, *16*(14), 9457-9487.

APPENDIX A. SUPPLEMENTARY DATA CHAPTER 2

Table 0.1: Categorization of emission sources

SMOKE Processing Category	Emission Source
Biogenic	By-products of microbial nitrification and denitrification occurring in soil
Area	Off-road vehicles Residential combustion: *anthracite coal, bituminous coal, distillate oil, residual oil, natural gas, liquified petroleum gas, and wood* Industrial processes: *chemical manufacturing, food, and kindred products, metal production, mineral processes, petroleum refining, wood products, construction, machinery, mining, and quarrying, etc.* Agriculture production: *crops, fertilizer application, livestock, animal waste, etc.* Solvent utilization Storage and transport Waste disposal, treatment, and recovery Forest wildfires Road dust and fugitive dust
Mobile	On-road vehicles
Point	Electric generating units (EGU) Commercial combustion and industrial combustion (non-EGU) Fugitive dust

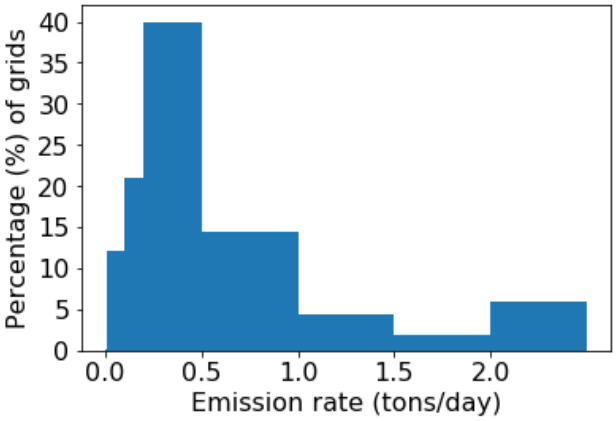

Figure 0.1: The histogram of total NO_x emission in the Midwest between April and June in tons/day.

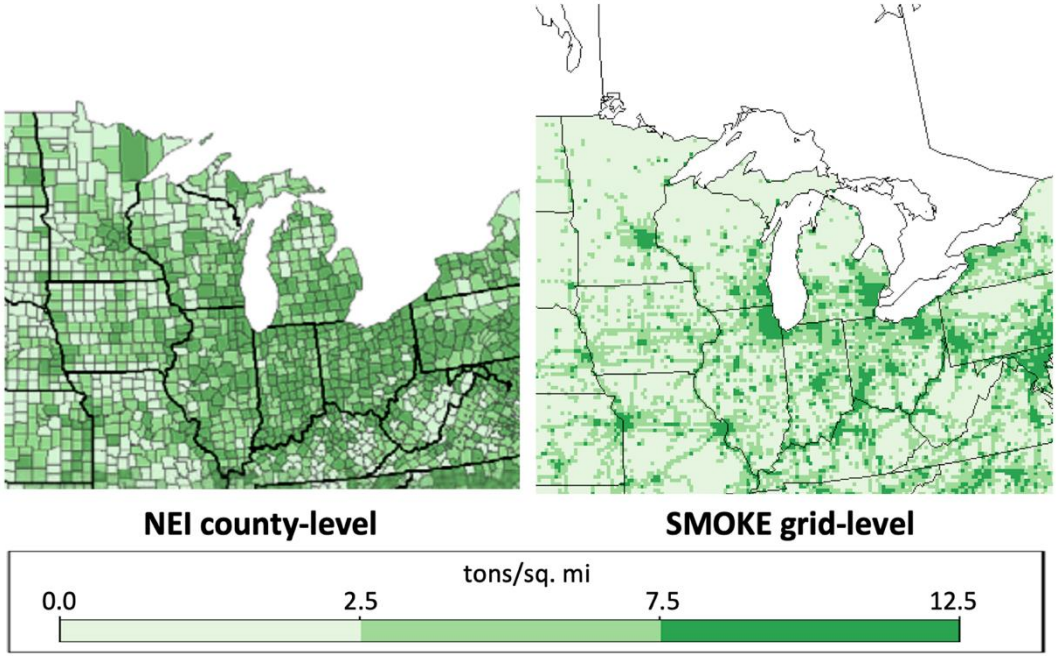

Figure 0.2: The geographical distribution of 2002 NO_x emission density estimated by NEI over each county (left) and simulated by SMOKE over each grid (right), throughout the Midwest.

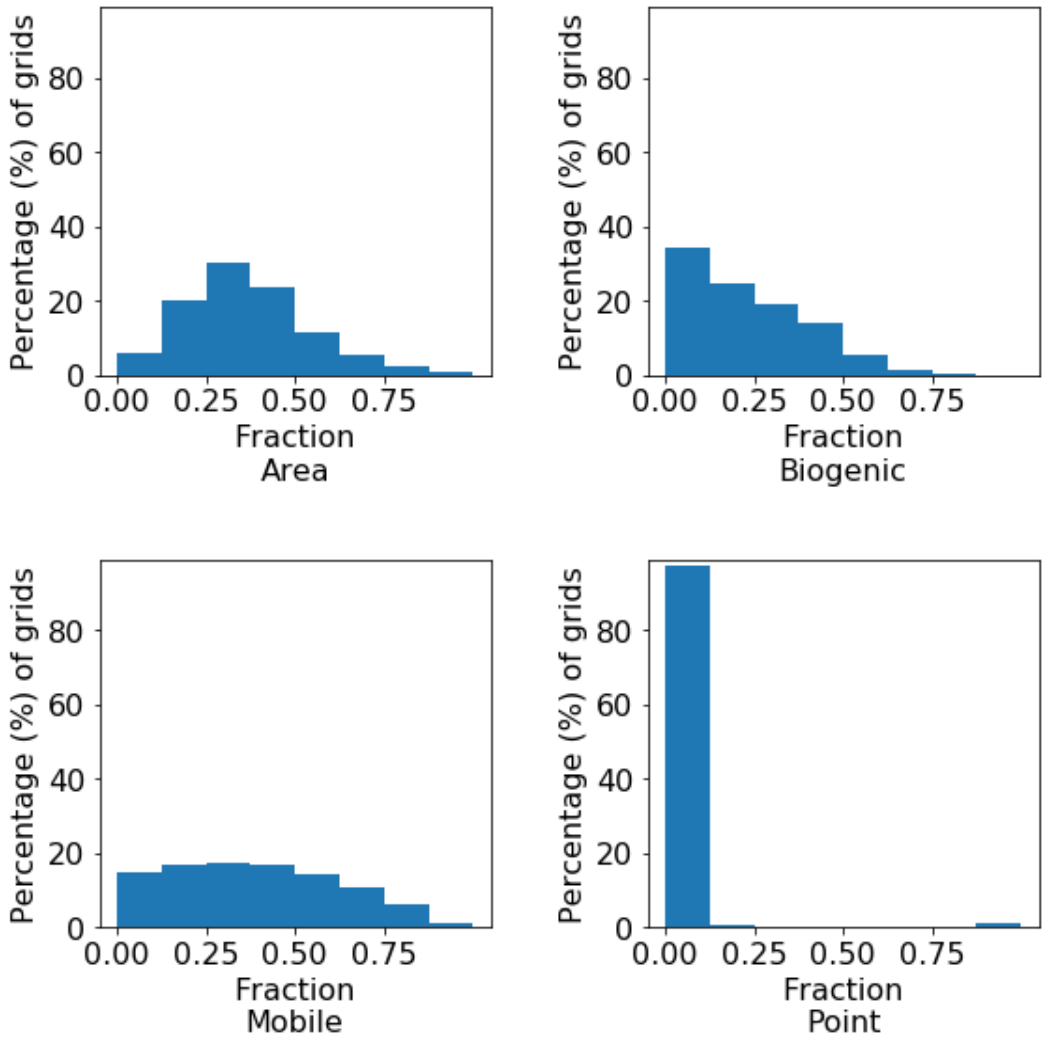

Figure 0.3: The histogram of the fraction of NO_x emission from each SMOKE processing category (area, biogenic, mobile, point) over each grid throughout the Midwest between April and June based on NEI-2002.

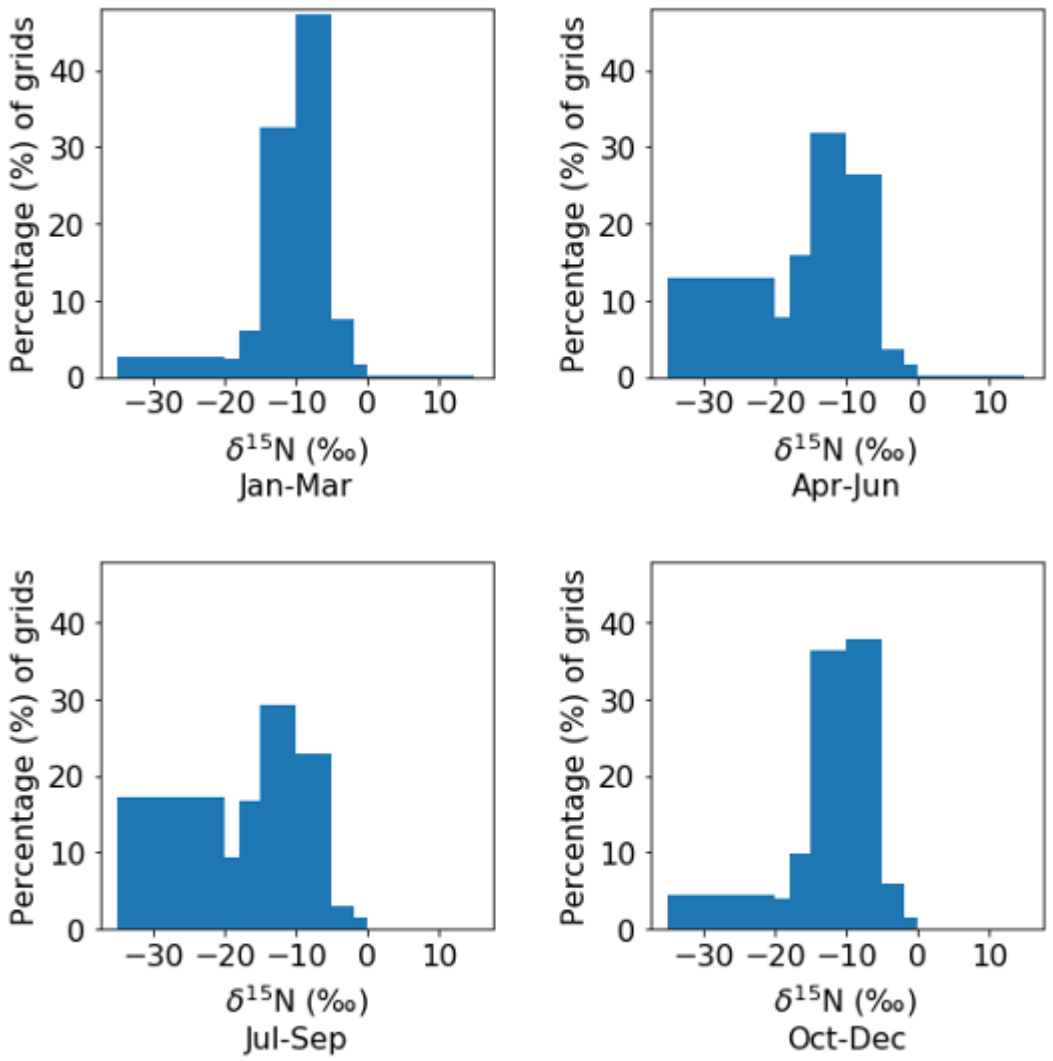

Figure 0.4: The histogram of the $\delta^{15}N$ of total NO_x emissions in each season (Winter: Jan-Mar; Spring: Apr-Jun; Summer: Jul-Sep; Fall: Oct-Dec) in per mil (‰) over the 12-km grids throughout the Midwest simulated by SMOKE, based on NEI-2002.

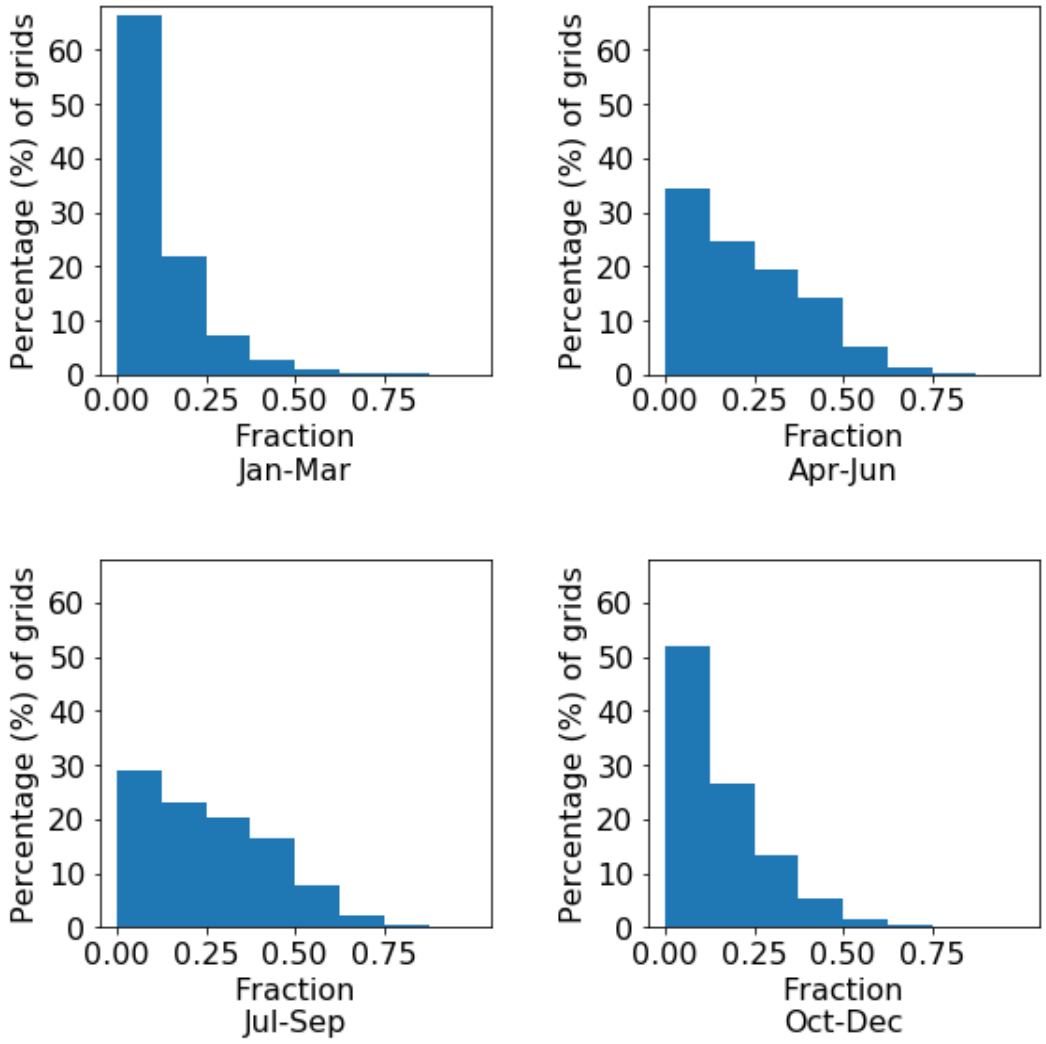

Figure 0.5: The histogram of the fraction of NO_x emission from biogenic sources over each grid in each season (Winter: Jan-Mar; Spring: Apr-Jun; Summer: Jul-Sep; Fall: Oct-Dec) throughout the Midwest simulated by SMOKE, based on NEI-2002.

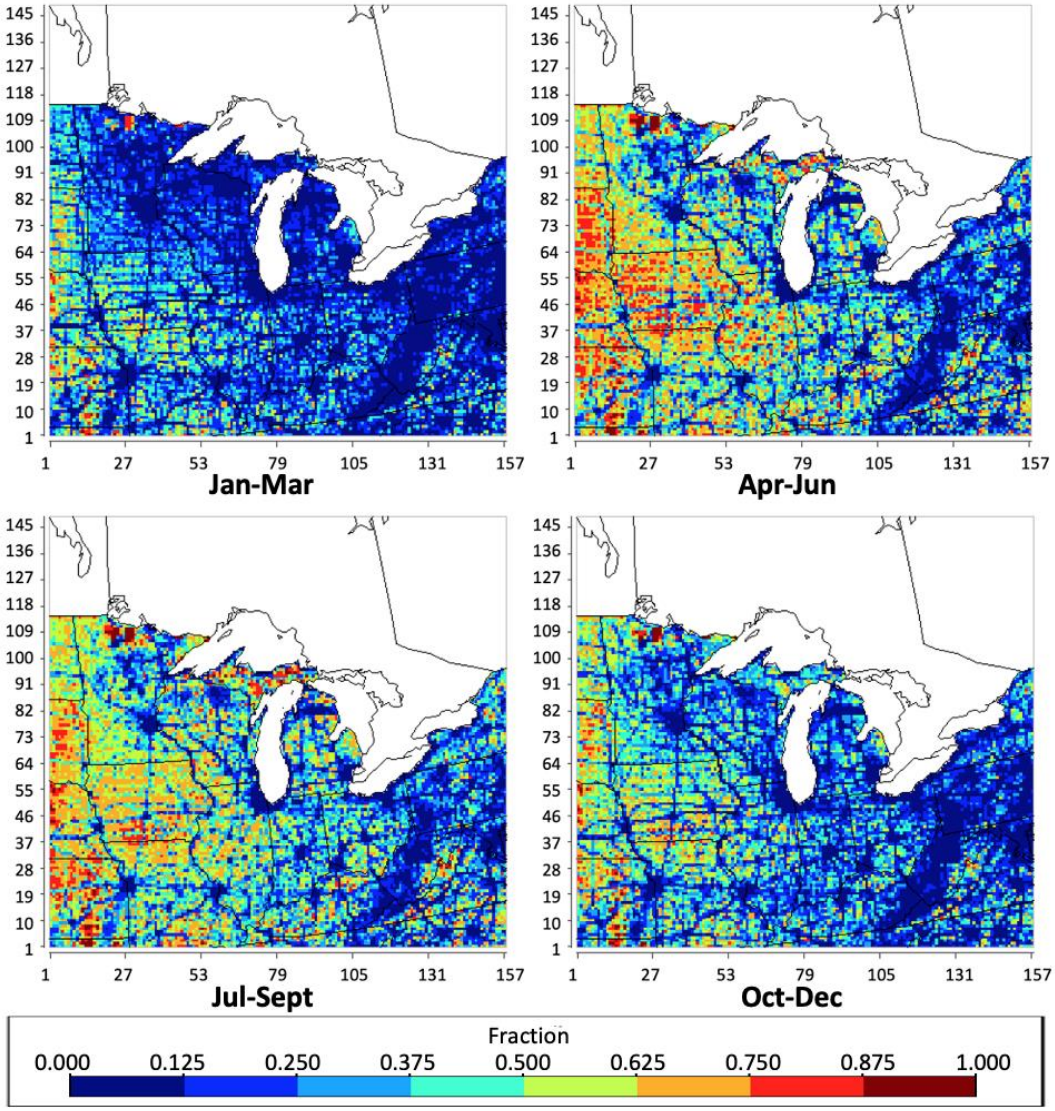

Figure 0.6: The geographical distribution of the fraction of NO_x emission from biogenic sources over each grid in each season (Winter: Jan-Mar; Spring: Apr-Jun; Summer: Jul-Sep; Fall: Oct-Dec) throughout the Midwest simulated by SMOKE, based on NEI-2016.

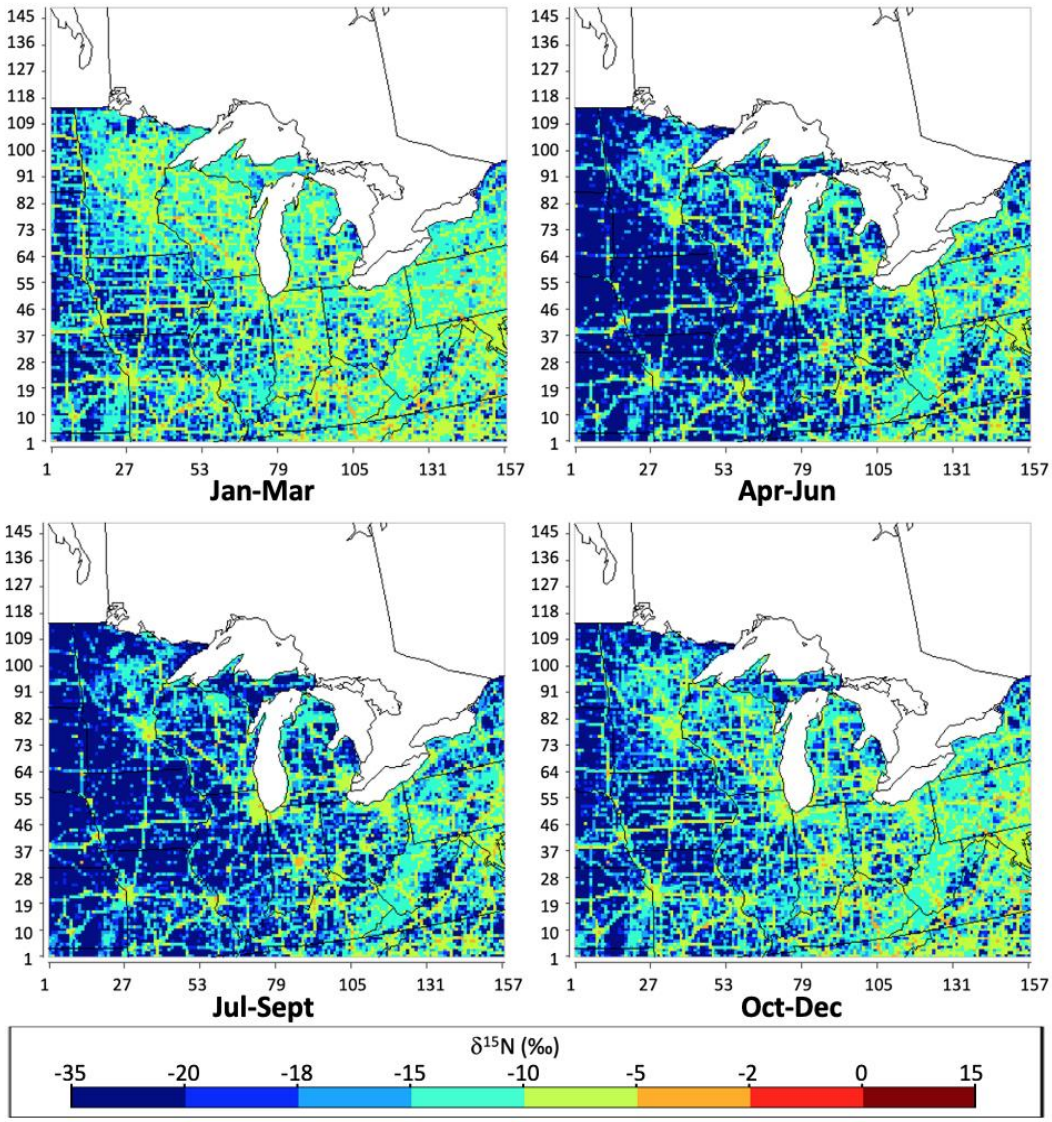

Figure 0.7: The geographical distribution of the $\delta^{15}N$ value of total NO_x emissions in each season (Winter: Jan-Mar; Spring: Apr-Jun; Summer: Jul-Sep; Fall: Oct-Dec) in per mil (‰) throughout the Midwest simulated by SMOKE, based on NEI-2016.

Figure 0.8: Locations of 82 NADP sites within Midwest © Google Maps

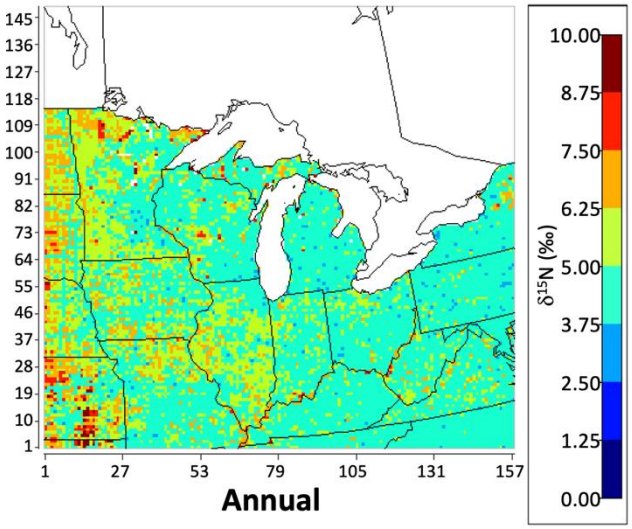

Figure 0.9: The uncertainties of $\delta^{15}N$ values based on NEI-2002 are presented by color in each grid. The warmer the color, the higher uncertainties of $\delta^{15}N$ values.

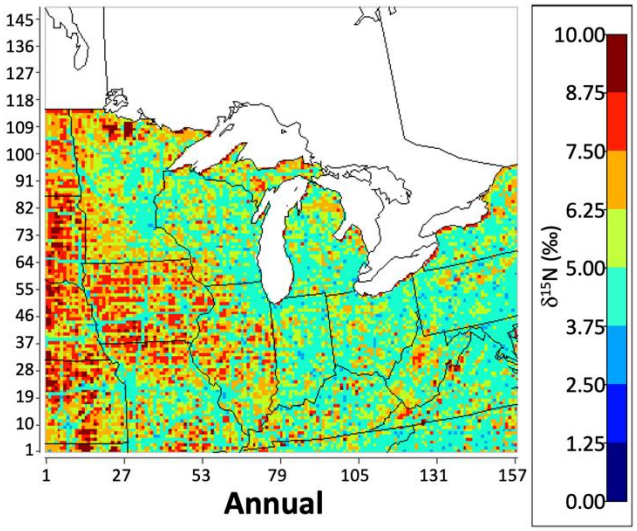

Figure 0.10: The uncertainties of $\delta^{15}N$ values based on NEI-2016 are presented by color in each grid. The warmer the color, the higher uncertainties of $\delta^{15}N$ values.

APPENDIX B. SUPPLEMENTARY DATA CHAPTER 3

Table 0.2: MCIP output variables

Variable Name	Description	Unit	File
LAT	latitude (cell centers)	degree	GRIDBDY2D, GRIDCRO2D
LON	longitude (cell centers)	degree	GRIDBDY2D, GRIDCRO2D
MSFX2	squared map-scale factor (cell centers)	$m^2\ m^{-2}$	GRIDBDY2D, GRIDCRO2D
HT	terrain elevation	m	GRIDBDY2D, GRIDCRO2D
DLUSE	dominant land use	category	GRIDBDY2D, GRIDCRO2D
LWMASK	land-water mask	category	GRIDBDY2D, GRIDCRO2D
PURB	urban percent of cell based on land coverage	percent	GRIDBDY2D, GRIDCRO2D
LUFRAC	fraction of land use by category	unitless	GRIDBDY2D, GRIDCRO2D
LATD	latitude (cell corners)	degree	GRIDDOT2D
LOND	longitude (cell corners)	degree	GRIDDOT2D
MSFD2	squared map scale factor (cell corners)	$m^2\ m^{-2}$	GRIDDOT2D
LATU	latitude (cell west-east faces)	degree	GRIDDOT2D
LONU	longitude (cell west-east faces)	degree	GRIDDOT2D
MSFU2	squared map scale factor (cell west-east faces)	$m^2\ m^{-2}$	GRIDDOT2D
LATV	latitude (cell south-north faces)	degree	GRIDDOT2D
LONV	longitude (cell south-north faces)	degree	GRIDDOT2D

Table B.1 continued

MSFV2	squared map scale factor (cell south-north faces)	$m^2\ m^{-2}$	GRIDDOT2D
JACOBF	total Jacobian (layer face)	m	METBDY3D, METCRO3D
JACOBM	total Jacobian (layer middle)	m	METBDY3D, METCRO3D
DENSA_J	Jacobian-weighted total air density	$kg\ m^{-2}$	METBDY3D, METCRO3D
WHAT_JD	Jacobian- and density-weighted vertical contravariant velocity	$kg\ m^{-1}\ s^{-1}$	METBDY3D, METCRO3D
TA	air temperature	K	METBDY3D, METCRO3D
QV	water vapor mixing ratio	$kg\ kg^{-1}$	METBDY3D, METCRO3D
PRES	air pressure	Pa	METBDY3D, METCRO3D
DENS	air density	$kg\ m^{-3}$	METBDY3D, METCRO3D
ZH	mid-layer height above ground	m	METBDY3D, METCRO3D
ZF	full layer height above ground	m	METBDY3D, METCRO3D
QC	cloud water mixing ratio	$kg\ kg^{-1}$	METBDY3D, METCRO3D
QR	rain water mixing ratio	$kg\ kg^{-1}$	METBDY3D, METCRO3D
CFRAC_3D	3D resolved cloud fraction	unitless	METBDY3D, METCRO3D
PRSFC	surface pressure	Pa	METCRO2D
USTAR	cell-averaged horizontal friction velocity	$m\ s^{-1}$	METCRO2D
WSTAR	convective velocity scale	$m\ s^{-1}$	METCRO2D
PBL	planetary boundary layer height	m	METCRO2D

Table B.1 continued

ZRUF	surface roughness length	m	METCRO2D
MOLI	inverse Monin-Obukhov length	m^{-1}	METCRO2D
HFX	sensible heat flux	W m^{-2}	METCRO2D
LH	latent heat flux	W m^{-2}	METCRO2D
RADYNI	inverse aerodynamic resistance	m s^{-1}	METCRO2D
RSTOMI	inverse bulk stomatal resistance	m s^{-1}	METCRO2D
TEMPG	skin temperature at ground	K	METCRO2D
TEMP2	2-m temperature	K	METCRO2D
Q2	2-m water vapor mixing ratio	m s^{-1}	METCRO2D
WSPD10	10-m wind speed	m s^{-1}	METCRO2D
WDIR10	10-m wind direction	degree	METCRO2D
GLW	longwave radiation at ground	W m^{-2}	METCRO2D
RGRND	solar radiation absorbed at ground	W m^{-2}	METCRO2D
RN	non-convective precipitation over interval	cm	METCRO2D
RC	convective precipitation over interval	cm	METCRO2D
CFRAC	total column integrated cloud fraction	unitless	METCRO2D
CLDT	cloud layer top height	m	METCRO2D
CLDB	cloud layer bottom height	m	METCRO2D
WBAR	average liquid water content of cloud	g m^{-3}	METCRO2D
SNOCOV	snow cover	category	METCRO2D
VEG	vegetation coverage	unitless	METCRO2D
LAI	leaf-area index	m^2 m^{-2}	METCRO2D
SEAICE	sea ice	unitless	METCRO2D
WR	canopy moisture content	m	METCRO2D
SOIM1	volumetric soil moisture in near-surface soil	m^3 m^{-3}	METCRO2D

Table B.1 continued

SOIM2	volumetric soil moisture in deep soil	$m^3\ m^{-3}$	METCRO2D
SOIT1	soil temperature in near-surface soil	K	METCRO2D
SOIT2	soil temperature in deep soil	K	METCRO2D
SLTYP	soil texture type	category	METCRO2D
UWIND	u-component of horizontal wind (cell corners)	$m\ s^{-1}$	METDOT3D
VWIND	v-component of horizontal wind (cell corners)	$m\ s^{-1}$	METDOT3D
UHAT_JD	contravariant U-component wind×density×Jacobian	$kg\ m^{-1}\ s^{-1}$	METDOT3D
VHAT_JD	contravariant V-component wind×density×Jacobian	$kg\ m^{-1}\ s^{-1}$	METDOT3D
UWINDC	u-component of horizontal wind (west-east cell faces)	$m\ s^{-1}$	METDOT3D
VWINDC	v-component of horizontal wind (south-north cell faces)	$m\ s^{-1}$	METDOT3D

Table 0.3: Output files of MCIP

File Name	Description	Time-Dependence	Spatial Dimensions
GRIDCRO2D	2-D time-independent fields at cell centers	Independent	X*Y
GRIDBDY2D	2-D time-independent fields on domain perimeter	Independent	Perimeter*Z
GRIDDOT2D	2-D time-independent fields at cell corners	Independent	(X+1)*(Y+1)
METCRO2D	2-D time-dependent fields at cell centers	Hourly	X*Y
METCRO3D	3-D time-dependent fields at cell centers	Hourly	X*Y*Z
METBDY3D	3-D time-dependent fields on domain perimeter	Hourly	Perimeter*Z
METDOT3D	3-D time-dependent fields at cell corners	Hourly	(X+1)*(Y+1)*Z

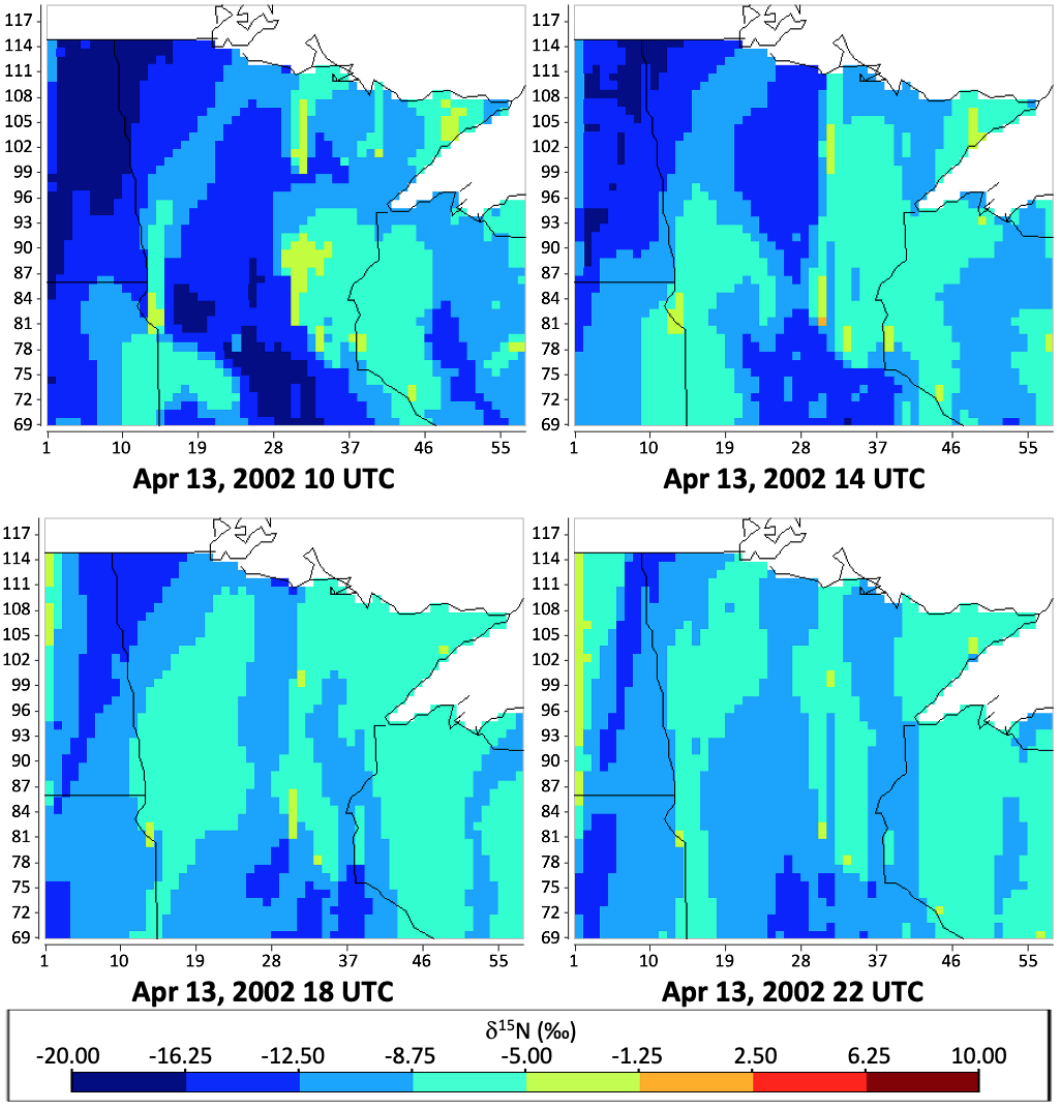

Figure 0.11: The geographical distribution of the $\delta^{15}N$ value of atmospheric NO_x in per mil (‰) from 10 UTC to 22 UTC on Apr 13, 2002, near the northwest corner of the study domain, simulated by CMAQ, based on NEI-2002 and 2016 meteorology.

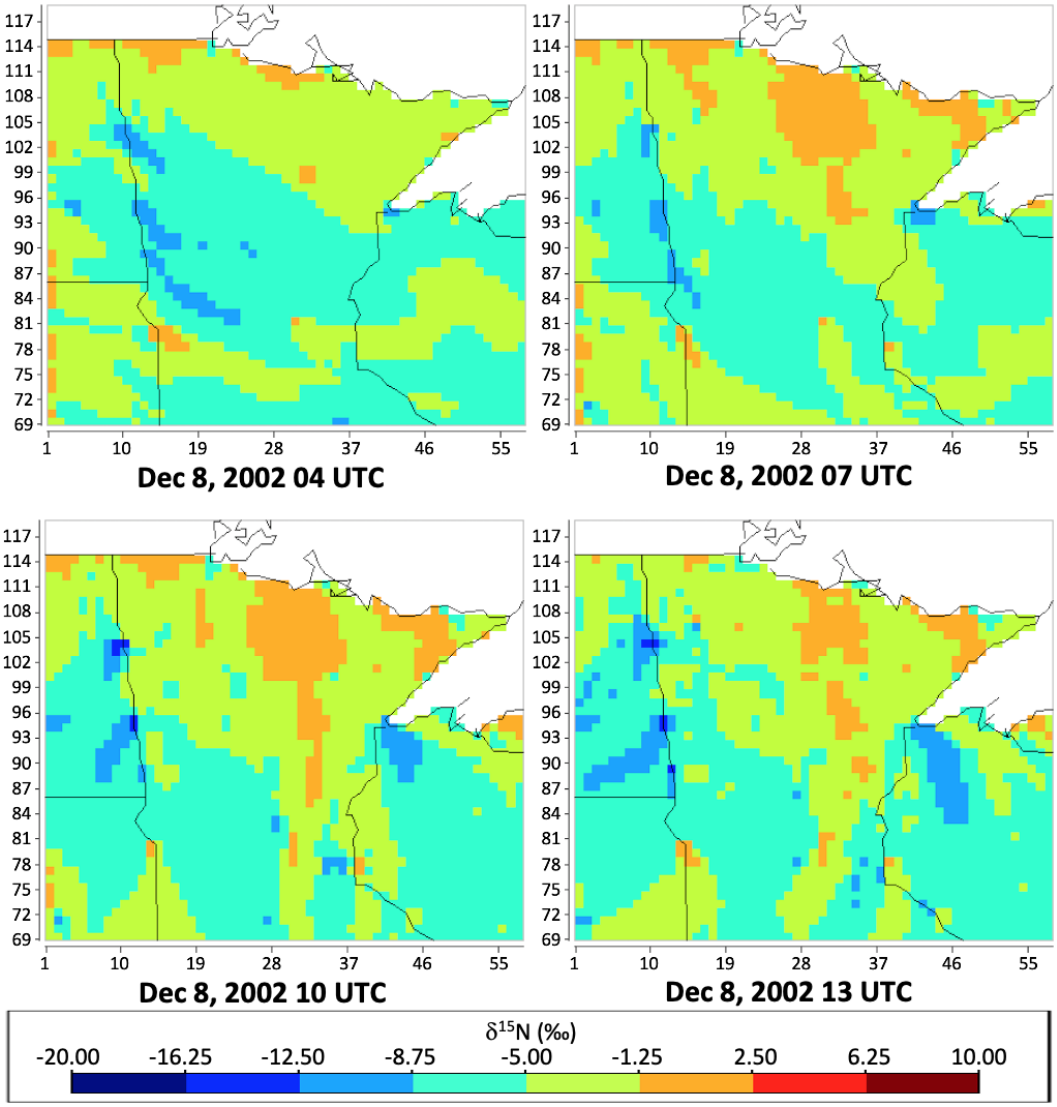

Figure 0.12: The geographical distribution of the $\delta^{15}N$ value of atmospheric NO_x in per mil (‰) from 04 UTC to 13 UTC on Dec 8, 2002, near the northwest corner of the study domain, simulated by CMAQ, based on NEI-2002 and 2016 meteorology.

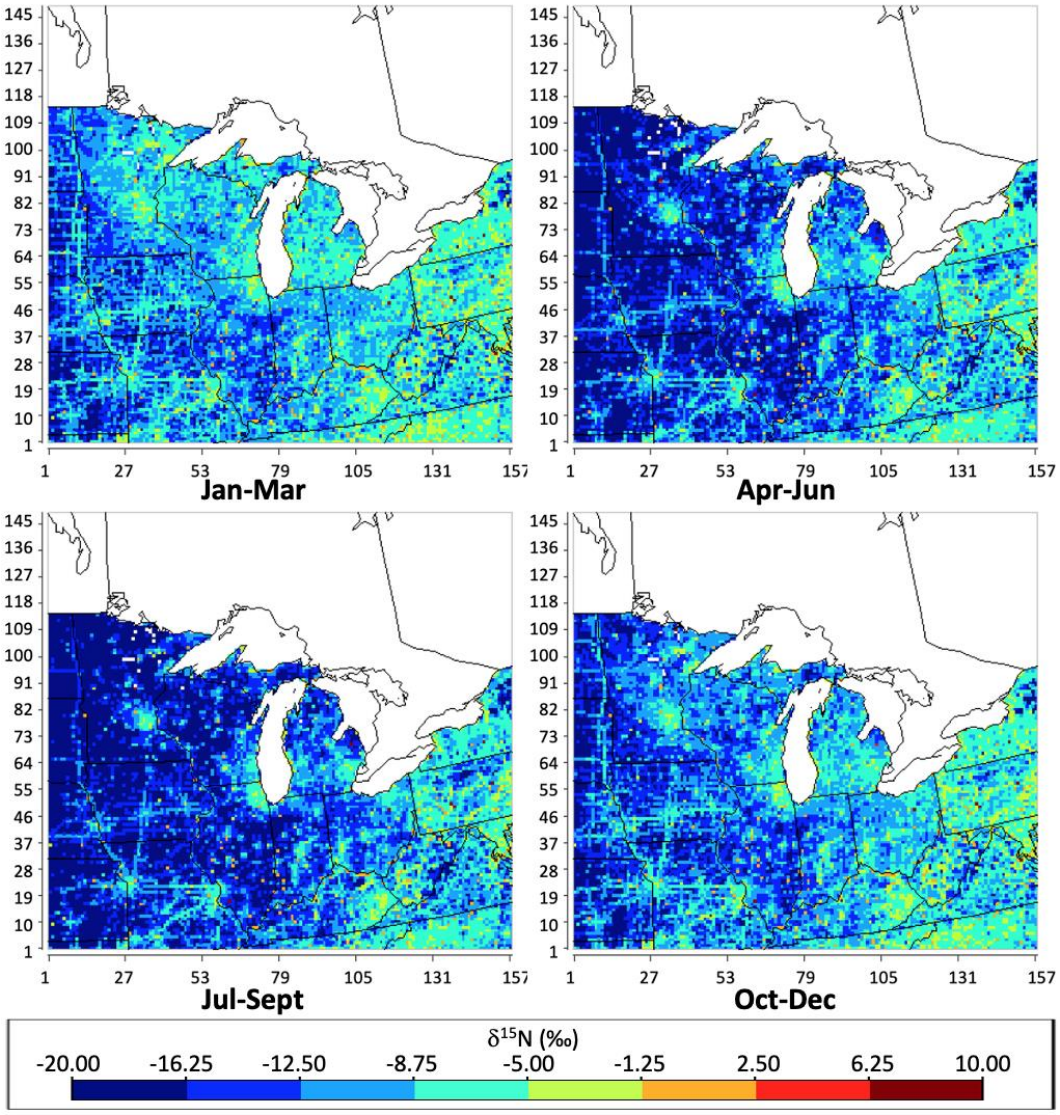

Figure 0.13: The geographical distribution of the $\delta^{15}N$ value of total NO_x emissions in each season (Winter: Jan-Mar; Spring: Apr-Jun; Summer: Jul-Sep; Fall: Oct-Dec) in per mil (‰) throughout the Midwest simulated by SMOKE, based on NEI-2002.

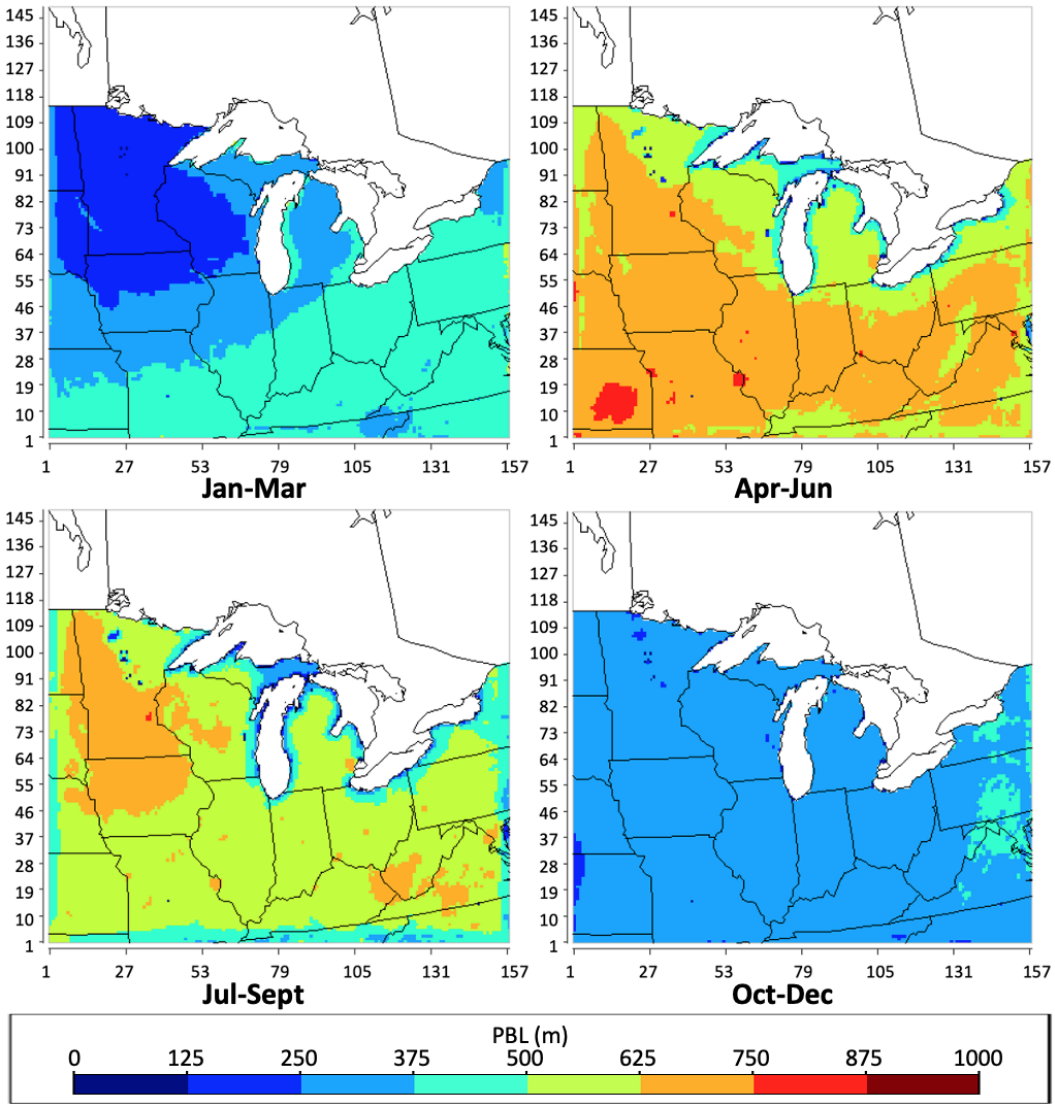

Figure 0.14: The geographical distribution of the planetary boundary layer (PBL) height in meters during each season (Winter: Jan-Mar; Spring: Apr-Jun; Summer: Jul-Sep; Fall: Oct-Dec) of 2016 throughout the Midwest.

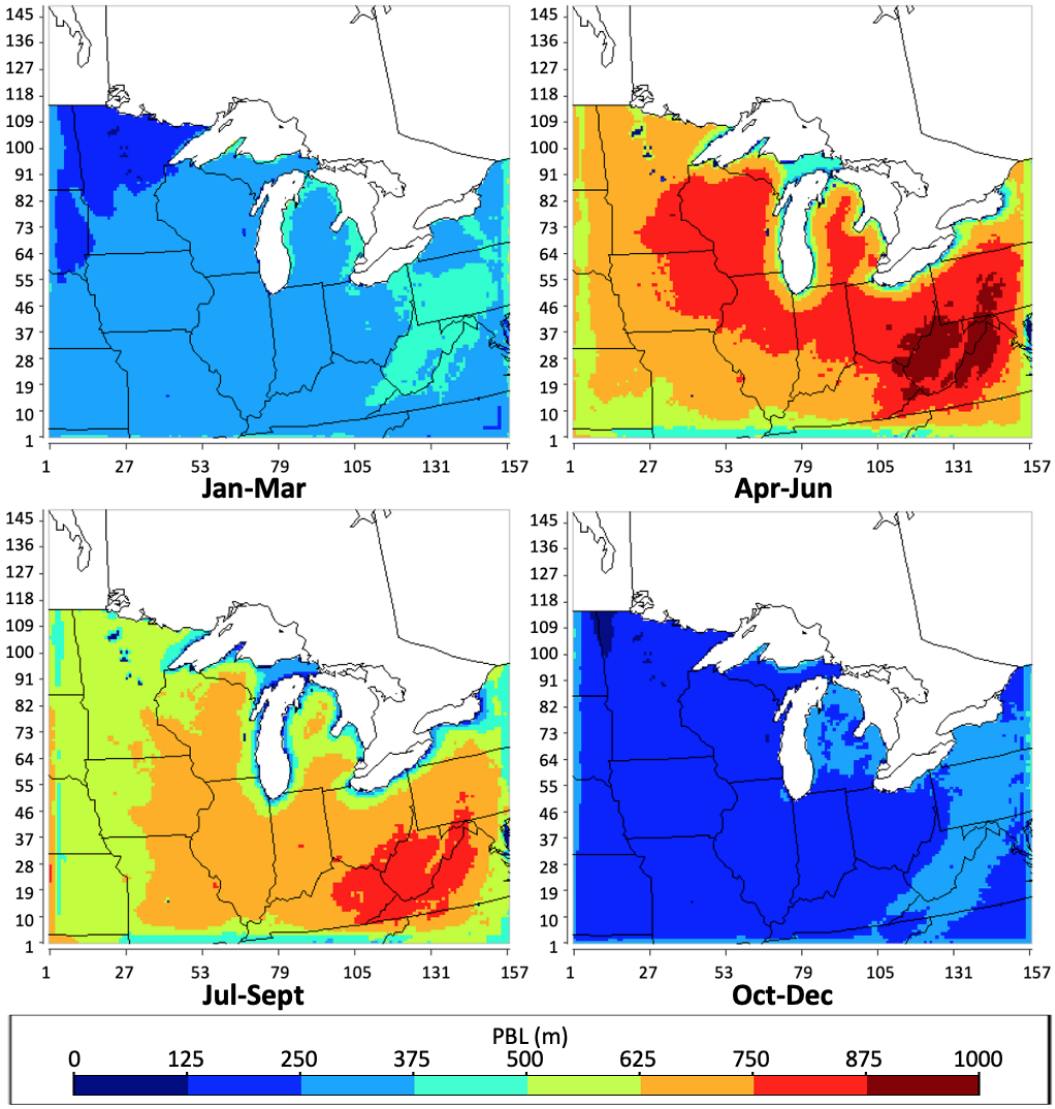

Figure 0.15: The geographical distribution of the planetary boundary layer (PBL) height in meters during each season (Winter: Jan-Mar; Spring: Apr-Jun; Summer: Jul-Sep; Fall: Oct-Dec) of 2002 throughout the Midwest.

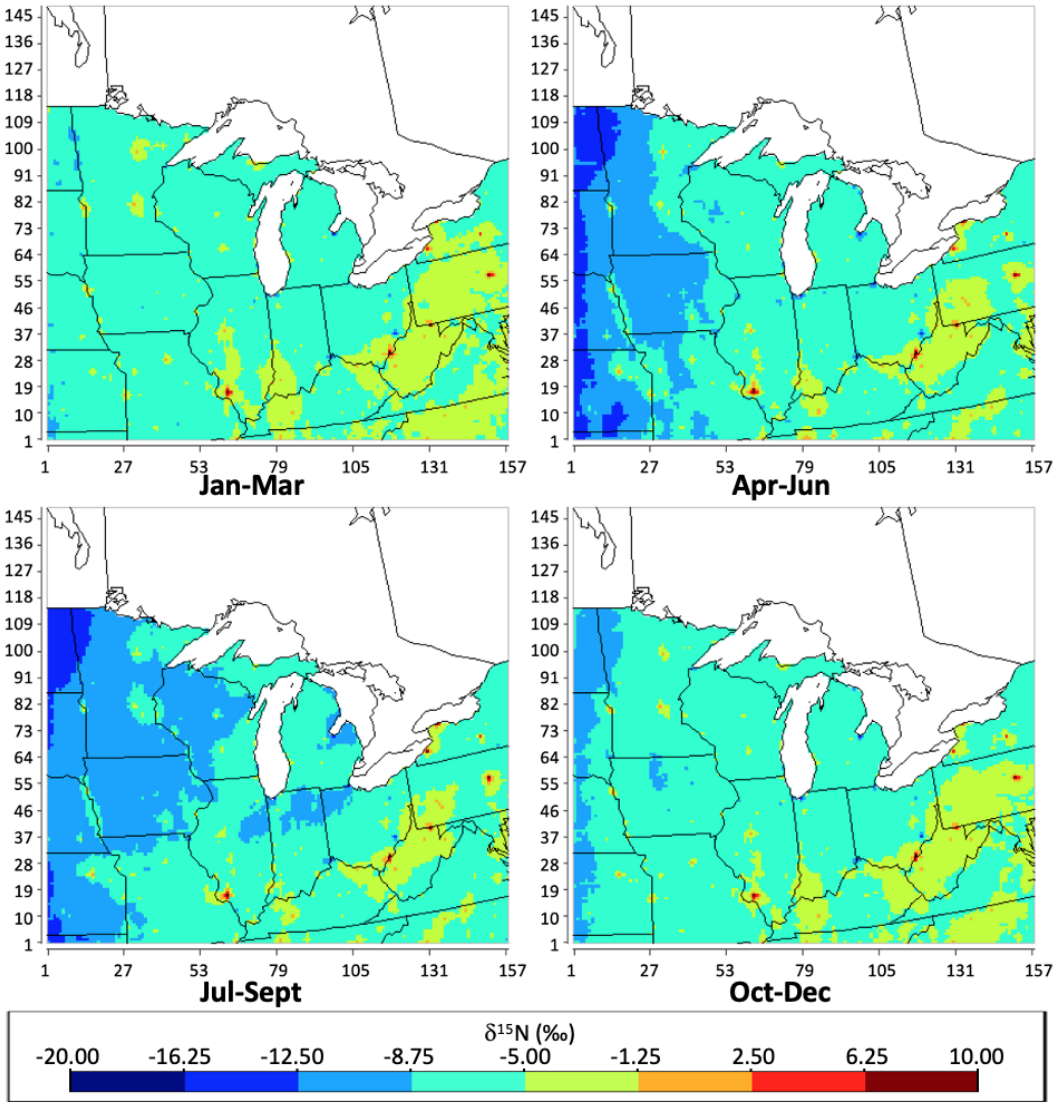

Figure 0.16: The geographical distribution of the $\delta^{15}N$ value of atmospheric NO_x in each season (Winter: Jan-Mar; Spring: Apr-Jun; Summer: Jul-Sep; Fall: Oct-Dec) in per mil (‰) throughout the Midwest simulated by CMAQ, based on NEI-2002 and 2002 meteorology.

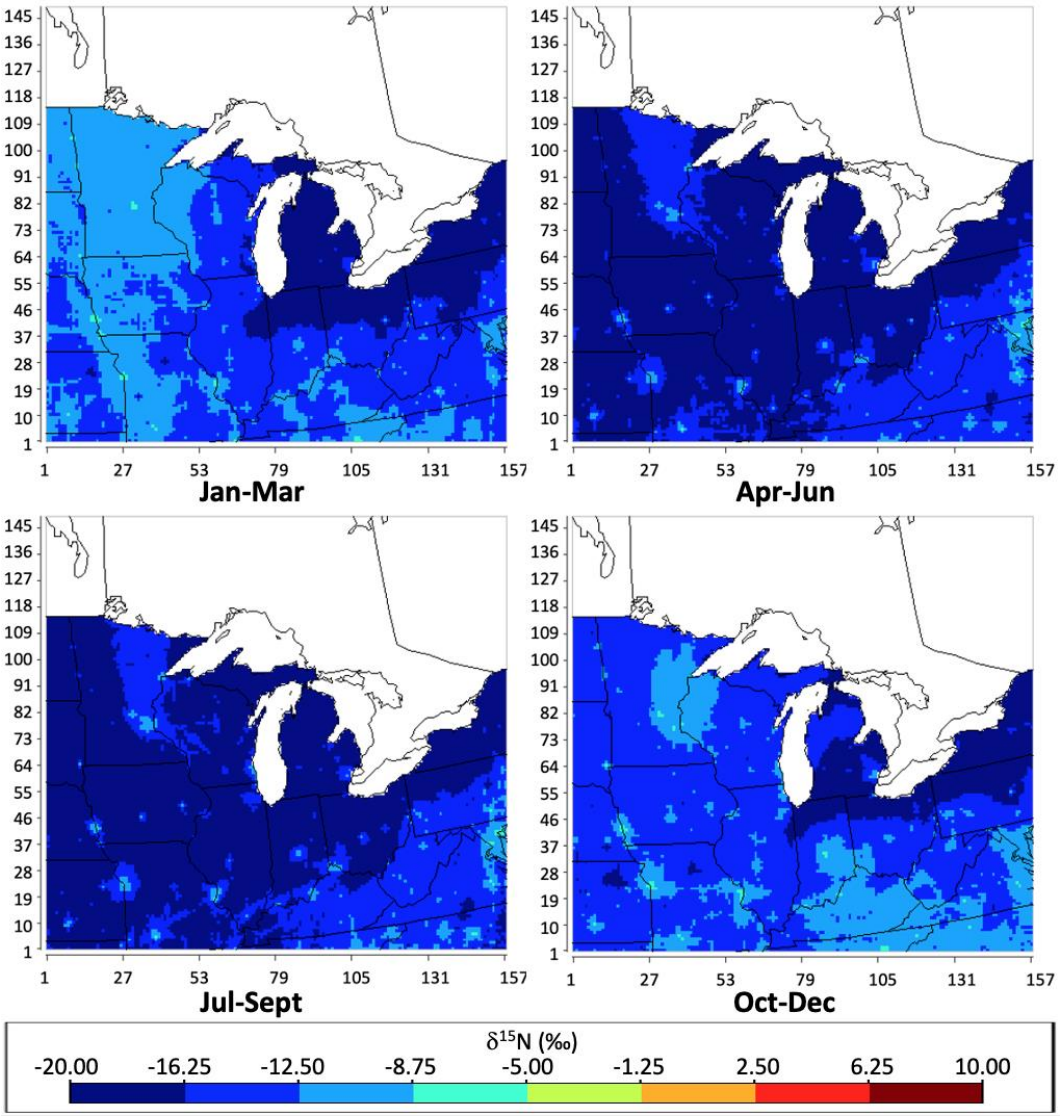

Figure 0.17: The geographical distribution of the $\delta^{15}N$ value of atmospheric NO_x in each season (Winter: Jan-Mar; Spring: Apr-Jun; Summer: Jul-Sep; Fall: Oct-Dec) in per mil (‰) throughout the Midwest simulated by CMAQ, based on NEI-2016 and 2016 meteorology.

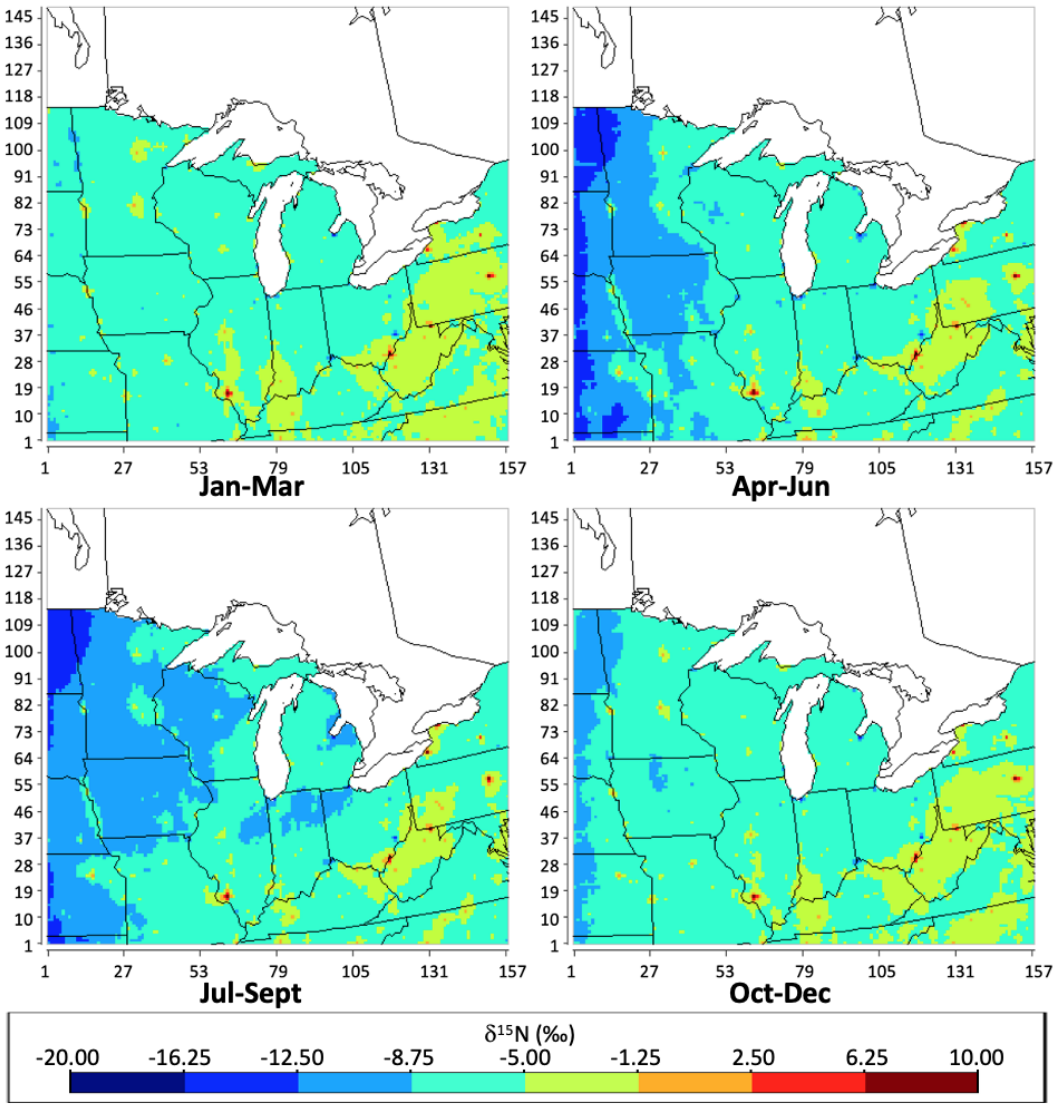

Figure 0.18: The geographical distribution of the $\delta^{15}N$ value of atmospheric NO_x in each season (Winter: Jan-Mar; Spring: Apr-Jun; Summer: Jul-Sep; Fall: Oct-Dec) in per mil (‰) throughout the Midwest simulated by CMAQ, based on NEI-2002 and 2016 meteorology,

under the "amplified deposition" scenario.

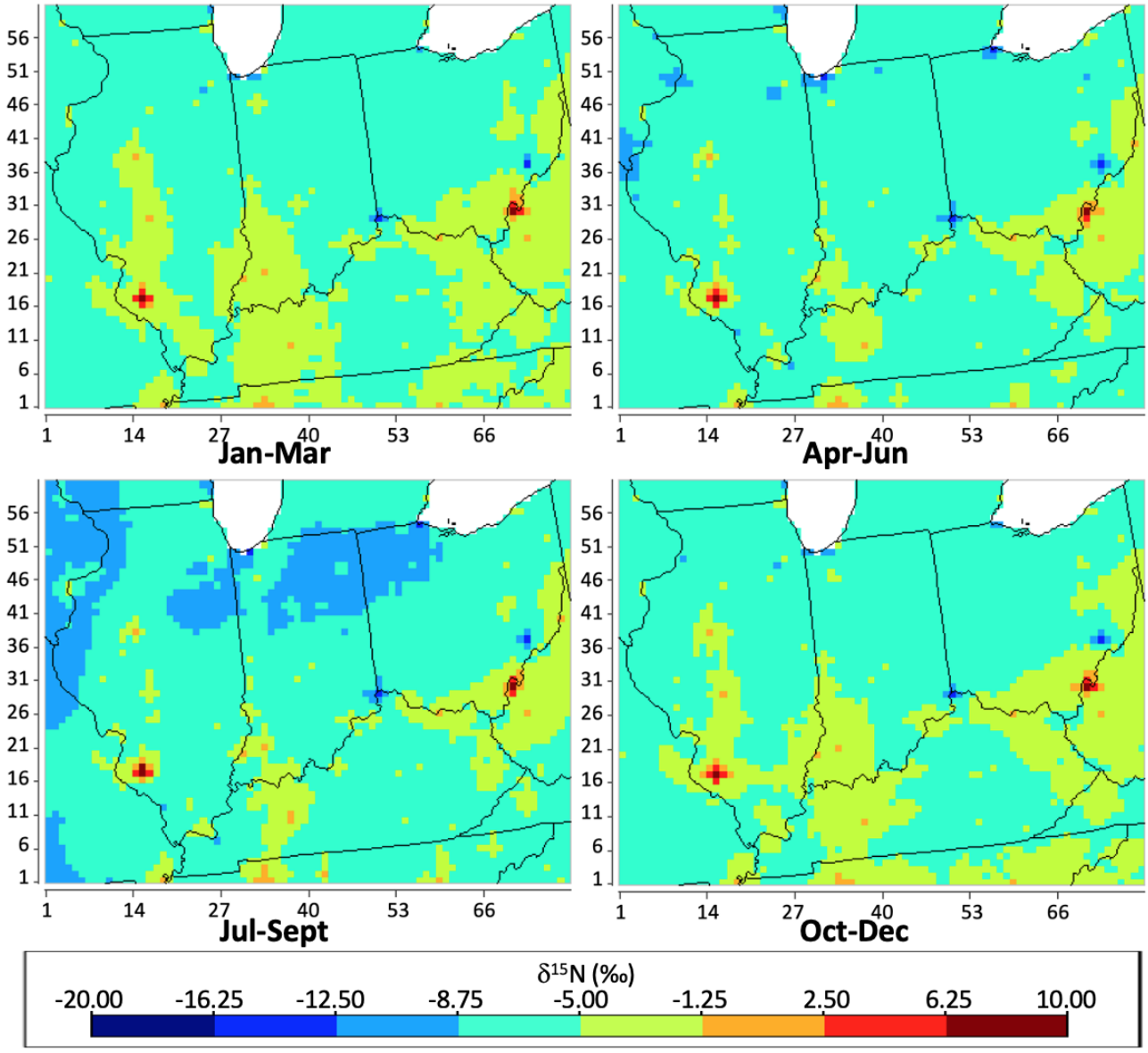

Figure 0.19: The nested-domain simulation of the $\delta^{15}N$ value of atmospheric NO_x in each season (Winter: Jan-Mar; Spring: Apr-Jun; Summer: Jul-Sep; Fall: Oct-Dec) in per mil (‰) within IN, IL, OH, and KY, based on NEI-2002 and 2016 meteorology.

Table 0.4: NADP sites within the states of Indiana, Illinois, Ohio, and Kentucky

Site ID	Site Name	County	State	Latitude	Longitude
IN20	Roush Lake	Huntington	IN	40.8401	-85.4639
IN22	Southwest Purdue Agriculture Center	Knox	IN	38.7408	-87.4855
IN34	Indiana Dunes National Lakeshore	Porter	IN	41.6318	-87.0881
IN41	Agronomy Center for Research and Extension	Tippecanoe	IN	40.4749	-86.9924
IL46	Alhambra	Madison	IL	38.8689	-89.6219
IL63	Dixon Springs Agricultural Center	Pope	IL	37.4356	-88.6719
OH09	Oxford	Butler	OH	39.5309	-84.7238
KY19	Cannons Lane	Jefferson	KY	38.2288	-85.6545

APPENDIX C. SUPPLEMENTARY DATA CHAPTER 4

C.1. Appendix table

Table C.1a: ^{14}N and ^{15}N species

No.	Species	Definition	Molecular Weight
3	NO	Nitric oxide	30
3a	^{15}NO		31
4	NO_2	Nitrogen dioxide	46
4a	$^{15}NO_2$		47
5	NO_3	Nitrogen trioxide	62
5a	$^{15}NO_3$		63
6	N_2O_5	Dinitrogen pentoxide	108
6a	$^{15}NNO_5$		109
6b	$^{15}N_2O_5$		110
7	HONO	Nitrous acid	47
7a	$HO^{15}NO$		48
8	HNO_3	Nitric acid	63
8a	$H^{15}NO_3$		64
9	HNO_4	Pernitric acid	79
9a	$H^{15}NO_4$		80
14	N_2	Nitrogen	28
14a	^{15}NN		29
14b	$^{15}N_2$		30
46	ONIT	Organic nitrate	119
46a	^{15}ONIT		120
47	PAN	Peroxyacyl nitrate and higher saturated PANs	121
47a	^{15}PAN		122
48	TPAN	Unsaturated PANs	147
48a	^{15}TPAN		148
75	OLNN	NO_3-alkene adduct reacting to form carbonitrates + HO2	136
75a	^{15}OLNN		137
76	OLND	NO_3-alkene adduct reacting via decomposition	136
76a	^{15}OLND		137

Table C.1b: Hydrocarbon species

No.	Species	Definition	Molecular Weight
37	HCHO	Formaldehyde	30
38	ALD	Acetaldehyde and higher aldehydes	44
40	GLY	Glyoxal	58
43	MACR	Methacrolein and other unsaturated monoaldehydes	70
41	MGLY	Methylglyxal and other α-carbonyl aldehydes	72
42	DCB	unsaturated dicarbonyls	87
36	CSL	cresol and other hydroxy substituted aromatics	108

Table C.2a: Photolysis reactions

Reaction No.	Reaction	Photolysis Frequency, s-1	Cross Section	Quantum Yield	α
R1	NO_2 --> O^3P + NO	7.50 x 10^{-3}	DeMore et al. [1994]	DeMore et al. [1994]	1
R1a	$^{15}NO_2$ --> O^3P + ^{15}NO	7.50 x 10^{-3}	DeMore et al. [1994]	DeMore et al. [1994]	1.0042
R2	O_3 --> O^1D + O_2	1.62 x 10^{-5}	DeMore et al. [1994]	DeMore et al. [1994]	1
R3	O_3 --> O^3P + O_2	4.17 x 10^{-4}	DeMore et al. [1994]	assumed to be unity	
R4	HONO --> HO + NO	1.63 x 10^{-3}	DeMore et al. [1994]	DeMore et al. [1994]	1
R4a	HO^{15}NO --> HO + ^{15}NO	1.63 x 10^{-3}	DeMore et al. [1994]	DeMore et al. [1994]	1
R5	HNO_3 --> HO + NO_2	4.50 x 10^{-7}	DeMore et al. [1994]	assumed to be unity	1
R5a	H$^{15}NO_3$ --> HO + $^{15}NO_2$	4.50 x 10^{-7}	DeMore et al. [1994]	assumed to be unity	1
R6	HNO_4 --> 0.65 HO_2 + 0.65 NO_2 + 0.35 HO + 0.35 NO_3	3.17 x 10^{-6}	DeMore et al. [1994]	assumed to be unity	1
R6a	H$^{15}NO_4$ --> 0.65 HO_2 + 0.65 $^{15}NO_2$ + 0.35 HO + 0.35 $^{15}NO_3$	3.17 x 10^{-6}	DeMore et al. [1994]	assumed to be unity	1
R7	NO_3--> NO + O_2	2.33 x 10^{-2}	Wayn et al. [1991]	Wayn et al. [1991]	1
R7a	$^{15}NO_3$--> ^{15}NO + O_2	2.33 x 10^{-2}	Wayn et al. [1991]	Wayn et al. [1991]	1
R8	NO_3 --> NO_2 + O^3P	1.87 x 10^{-1}	Wayn et al. [1991]	Wayn et al. [1991]	1
R8a	$^{15}NO_3$ --> $^{15}NO_2$ + O^3P	1.87 x 10^{-1}	Wayn et al. [1991]	Wayn et al. [1991]	1
R9	H_2O_2 --> HO + HO	6.00 x 10^{-6}	DeMore et al. [1994]	Wayn et al. [1991]	1

C.2a continued

R10	HCHO --> H_2 + CO	3.50 x 10^{-5}	Moortgat et al. [1980] Cantrell et al. [1990]	Atkinson et al. [1994] DeMore et al. [1994]	1
R11	HCHO --> 2HO_2 + CO	2.17 x 10^{-5}	Moortgat et al. [1980] Cantrell et al. [1990]	Atkinson et al. [1994] DeMore et al. [1994]	1
R12	ALD --> MO_2 + HO_2 + CO	3.67 x 10^{-6}	Martinez et al. [1992]	Atkinson et al. [1994]	1
R13	OP1 --> HCHO + HO_2 + HO	4.17 x 10^{-6}	DeMore et al. [1994]	DeMore et al. [1994]	1
R14	OP2 --> ALD + HO_2 + HO	4.17 x 10^{-6}	DeMore et al. [1994]	DeMore et al. [1994]	1
R15	PAA --> MO_2 + HO	1.57 x 10^{-6}	Giguere and Olmos [1956]	assumed to be unity	1
R16	KET --> ETHP + ACO_3	6.67 x 10^{-7}	Martinez et al. [1992]	Atkinson et al. [1994]	1
R17	GLY --> 0.13 HCHO + 1.87 CO + 0.87 H_2	5.83 x 10^{-5}	Atkinson et al. [1992]	Atkinson et al. [1992]	1
R18	GLY --> 0.45 HCHO + 1.55 CO + 0.80 HO_2 + 0.15 H_2	2.00 x 10^{-5}	Atkinson et al. [1992]	Atkinson et al. [1992]	1
R19	MGLY --> CO + HO2 + ACO_3	9.33 x 10^{-5}	Atkinson et al. [1994] Staffelbach et al. [1995]	Koch and Moortgat et al. [1996]	1
R20	DCB --> TCO_3 + HO_2	4.33 x 10^{-5}	Stockwell et al. [1990]	Stockwell et al. [1990]	1
R21	ONIT--> 0.20 ALD + 0.80 KET + HO_2 + NO_2	2.17 x 10^{-6}	Atkinson et al. [1994]	Atkinson et al. [1994]	1
R22	MACR --> CO + HCHO + HO_2 + ACO_3	1.33 x 10^{-6}	Gardner et al. [1987]	Gardner et al. [1987]	1
R23	HKET --> HCHO + HO_2 + ACO_3	6.67 x 10^{-7}	Martinez et al. [1992]	Atkinson et al. [1994]	1

Table C.2b: The RACM Mechanism

Reaction No.	Reaction	A, $cm^3\ s^{-1}$	E/R, K	k	α
R24	$O^3P + O_2$ --> O_3	Table C.2f		1.50×10^{-14}	1
R25	$O^3P + O_3$ --> $2\ O_2$	8.00×10^{-12}	2060	7.96×10^{-15}	1
R26	$O^1D + N_2$ --> $O^3P + N_2$	1.80×10^{-11}	-110	2.60×10^{-11}	1
R26a	$O^1D + {}^{15}NN$ --> $O^3P + {}^{15}NN$	1.80×10^{-11}	-110	2.60×10^{-11}	1
R27	$O^1D + O_2$ --> $O^3P + O_2$	3.20×10^{-11}	-70	4.05×10^{-11}	1
R28	$O^1D + H_2O$ --> $HO + HO$	2.20×10^{-10}		2.20×10^{-10}	1
R29	$O_3 + HO$ --> $HO_2 + O_2$	1.60×10^{-12}	940	6.83×10^{-14}	1
R30	$O_3 + HO_2$ --> $HO + O_2$	1.10×10^{-14}	500	2.05×10^{-15}	1
R31	$HO + HO_2$ --> $H_2O + O_2$	4.80×10^{-11}	-250	1.11×10^{-10}	1
R32	$H_2O_2 + HO$ --> $HO_2 + H_2O$	2.90×10^{-12}	160	1.70×10^{-12}	1
R33	$HO_2 + HO_2$ --> $H_2O_2 + O_2$	Table C.2f		2.92×10^{-12}	1
R34	$HO_2 + HO_2 + H_2O$ --> $H_2O_2 + O_2 + H_2O$	Table C.2f		6.58×10^{-30}	1
R35	$O^3P + NO$ --> NO_2	Table C.2d		1.66×10^{-12}	1
R35a	$O^3P + {}^{15}NO$ --> $^{15}NO_2$	Table C.2d		1.66×10^{-12}	1
R36	$O^3P + NO_2$ --> $NO + O_2$	6.50×10^{-12}	-120	9.72×10^{-12}	1
R36a	$O^3P + {}^{15}NO_2$ --> $^{15}NO + O_2$	6.50×10^{-12}	-120	9.72×10^{-12}	1
R37	$O^3P + NO_2$ --> NO_3	Table C.2d		1.58×10^{-12}	1
R37a	$O^3P + {}^{15}NO_2$ --> $^{15}NO_3$	Table C.2d		1.58×10^{-12}	1
R38	$HO + NO$ --> HONO	Table C.2d		4.87×10^{-12}	1
R38a	$HO + {}^{15}NO$ --> $HO^{15}NO$	Table C.2d		4.87×10^{-12}	1
R39	$HO + NO_2$ --> HNO_3	Table C.2d		1.15×10^{-11}	1
R39a	$HO + {}^{15}NO_2$ --> $H^{15}NO_3$	Table C.2d		1.15×10^{-11}	1.04
R40	$HO + NO_3$ --> $NO_2 + HO_2$	2.20×10^{-11}		2.20×10^{-11}	1
R40a	$HO + {}^{15}NO_3$ --> $^{15}NO_2 + HO_2$	2.20×10^{-11}		2.20×10^{-11}	1
R41	$HO_2 + NO$ --> $NO_2 + HO$	3.70×10^{-12}	-250	8.56×10^{-12}	1
R41a	$HO_2 + {}^{15}NO$ --> $^{15}NO_2 + HO$	3.70×10^{-12}	-250	8.56×10^{-12}	1

Table C.2c: continued

R42	$HO_2 + NO_2$ --> HNO_4	Table C.2d		1.39×10^{-12}	1
R42a	$HO_2 + {}^{15}NO_2$ --> $H{}^{15}NO_4$	Table C.2d		1.39×10^{-12}	1
R43	HNO4 --> $HO_2 + NO_2$	Table C.2e		8.62×10^{-2}	1
R43a	$H{}^{15}NO4$ --> $HO_2 + {}^{15}NO_2$	Table C.2e		8.62×10^{-2}	1
R44	$HO_2 + NO_3$--> 0.3 HNO_3 + 0.7 NO_2 + 0.7 HO + O_2	3.50×10^{-12}		3.50×10^{-12}	1
R44a	$HO_2 + {}^{15}NO_3$--> 0.3 $H{}^{15}NO_3$ + 0.7 $^{15}NO_2$ + 0.7 HO + O_2	3.50×10^{-12}		3.50×10^{-12}	1
R45	HO + HONO --> $NO_2 + H_2O$	1.80×10^{-11}	390	4.86×10^{-12}	1
R45a	HO + $HO{}^{15}NO$ --> $^{15}NO_2 + H_2O$	1.80×10^{-11}	390	4.86×10^{-12}	1
R46	HO + HNO_3 --> $NO_3 + H_2O$	Table C.2f		1.47×10^{-13}	1
R46a	HO + $H{}^{15}NO_3$ --> $^{15}NO_3 + H_2O$	Table C.2f		1.47×10^{-13}	1
R47	HO + HNO_4 --> NO_2+ $O_2 + H_2O$	1.30×10^{-12}	-380	4.65×10^{-12}	1
R47a	HO + $H{}^{15}NO_4$ --> $^{15}NO_2$+ O_2 + H_2O	1.30×10^{-12}	-380	4.65×10^{-12}	1
R48	$O_3 + NO$ --> $NO_2 + O_2$	2.00×10^{-12}	1400	1.82×10^{-14}	1
R48a	$O_3 + {}^{15}NO$ --> $^{15}NO_2 + O_2$	2.00×10^{-12}	1400	1.82×10^{-14}	0.9933
R49	$O_3 + NO_2$ --> $NO_3 + O_2$	1.20×10^{-13}	2450	3.23×10^{-17}	1
R49a	$O_3 + {}^{15}NO_2$ --> $^{15}NO_3 + O_2$	1.20×10^{-13}	2450	3.23×10^{-17}	1
R50	NO + NO + O_2 --> $NO_2 + NO_2$	3.30×10^{-39}	-530	1.95×10^{-38}	1
R50a	NO + ^{15}NO + O_2 --> $NO_2 + {}^{15}NO_2$	3.30×10^{-39}	-530	1.95×10^{-38}	1
R50b	^{15}NO + ^{15}NO + O_2 --> $^{15}NO_2$ + $^{15}NO_2$	3.30×10^{-39}	-530	1.95×10^{-38}	1
R51	$NO_3 + NO$ --> $NO_2 + NO_2$	1.50×10^{-11}	-170	2.65×10^{-11}	1
R51a	$^{15}NO_3 + NO$ --> $NO_2 + {}^{15}NO_2$	1.50×10^{-11}	-170	2.65×10^{-11}	1
R51b	$NO_3 + {}^{15}NO$ --> $NO_2 + {}^{15}NO_2$	1.50×10^{-11}	-170	2.65×10^{-11}	1
R51c	$^{15}NO_3 + {}^{15}NO$ --> $^{15}NO_2 + {}^{15}NO_2$	1.50×10^{-11}	-170	2.65×10^{-11}	1
R52	$NO_3 + NO_2$ --> $NO + NO_2 + O_2$	4.50×10^{-14}	1260	6.56×10^{-16}	1
R52a	$NO_3 + {}^{15}NO_2$ --> $^{15}NO + NO_2 + O_2$	4.50×10^{-14}	1260	6.56×10^{-16}	0.5

Table C.2d: continued

R52b	$NO_3 + {}^{15}NO_2$ --> $NO + {}^{15}NO_2 + O_2$	4.50×10^{-14}	1260	6.56×10^{-16}	0.5
R52c	${}^{15}NO_3 + NO_2$ --> ${}^{15}NO + NO_2 + O_2$	4.50×10^{-14}	1260	6.56×10^{-16}	0.5
R52d	${}^{15}NO_3 + NO_2$ --> $NO + {}^{15}NO_2 + O_2$	4.50×10^{-14}	1260	6.56×10^{-16}	0.5
R52e	${}^{15}NO_3 + {}^{15}NO_2$ --> ${}^{15}NO + {}^{15}NO_2 + O_2$	4.50×10^{-14}	1260	6.56×10^{-16}	1
R53	$NO_3 + NO_2$ --> N_2O_5	Table C.2d		1.27×10^{-12}	1
R53a	$NO_3 + {}^{15}NO_2$ --> ${}^{15}NNO_5$	Table C.2d		1.27×10^{-12}	1.0266
R53b	${}^{15}NO_3 + NO_2$ --> ${}^{15}NNO_5$	Table C.2d		1.27×10^{-12}	1.0309
R53c	${}^{15}NO_3 + {}^{15}NO_2$ --> ${}^{15}N_2O_5$	Table C.2d		1.27×10^{-12}	1.057
R54	N_2O_5 --> $NO_2 + NO_3$	Table C.2e		4.36×10^{-2}	1
R54a	${}^{15}NNO_5$ --> ${}^{15}NO_2 + NO_3$	Table C.2e		4.36×10^{-2}	0.5
R54b	${}^{15}NNO_5$ --> $NO_2 + {}^{15}NO_3$	Table C.2e		4.36×10^{-2}	0.5
R54c	${}^{15}N_2O_5$ --> ${}^{15}NO_2 + {}^{15}NO_3$	Table C.2e		4.36×10^{-2}	1
R55	$NO_3 + NO_3$ --> $NO_2 + NO_2 + O_2$	8.50×10^{-13}	2450	2.29×10^{-16}	1
R55a	$NO_3 + 15NO_3$ --> $NO_2 + {}^{15}NO_2 + O_2$	8.50×10^{-13}	2450	2.29×10^{-16}	1
R55b	${}^{15}NO_3 + {}^{15}NO_3$ --> ${}^{15}NO_2 + {}^{15}NO_2 + O_2$	8.50×10^{-13}	2450	2.29×10^{-16}	1
R56	$HO + H_2$ --> $H_2O + HO_2$	5.50×10^{-12}	2000	6.69×10^{-15}	1
R57	$HO + SO_2$ --> $SULF + HO_2$	Table C.2d		8.89×10^{-13}	1
R58	$CO + HO$ --> $HO_2 + CO_2$	Table C.2f		2.40×10^{-13}	1
R59	ISO + O^3P --> 0.86 OLT + 0.05 HCHO + 0.02 HO + 0.01 CO + 0.13 DCB + 0.28 HO2 + 0.15 XO_2	6.00×10^{-11}		6.00×10^{-11}	1
R60	MACR + O^3P -->ALD	1.59×10^{-11}	-13	1.66×10^{-11}	1
R61	CH4 + HO --> $MO_2 + H_2O$	Table C.2c		6.86×10^{-15}	1
R62	ETH + HO --> ETHP + H_2O	Table C.2c		2.57×10^{-13}	1

Table C.2e: continued

R63	HC3 + HO --> 0.583 HC3P + 0.381 HO_2 + 0.335 ALD + 0.036 ORA1 + 0.036 CO + 0.036 GLY + 0.036 HO + 0.010 HCHO + H_2O	5.26×10^{-12}	260	2.20×10^{-12}	1
R64	HC5 + HO --> 0.75 HC5P + 0.25 KET + 0.25 HO_2 + H_2O	8.02×10^{-12}	155	4.77×10^{-12}	1
R65	HC8 + HO --> 0.951 HC8P + 0.025 ALD + 0.024 HKET + 0.049 HO_2 + H_2O	1.64×10^{-11}	125	1.08×10^{-11}	1
R66	ETE + HO --> ETEP	1.96×10^{-12}	-438	8.52×10^{-12}	1
R67	OLT + HO --> OLTP	5.72×10^{-12}	-500	3.06×10^{-11}	1
R68	OLI + HO --> OLIP	1.33×10^{-11}	-500	7.12×10^{-11}	1
R69	DIEN + HO --> ISOP	1.48×10^{-11}	-448	6.65×10^{-11}	1
R70	ISO + HO --> ISOP	2.54×10^{-11}	-410	1.01×10^{-10}	1
R71	API + HO --> APIP	1.21×10^{-11}	-444	5.37×10^{-11}	1
R72	LIM + HO --> LIMP	1.70×10^{-10}		1.70×10^{-10}	1
R73	TOL + HO --> 0.90 ADDT + 0.10 XO_2 + 0.10 HO_2	1.81×10^{-12}	-355	5.96×10^{-12}	1
R74	XYL + HO --> 0.90 ADDX + 0.10 XO_2 + 0.10 HO_2	7.30×10^{-12}	-355	2.40×10^{-11}	1
R75	CSL + HO --> 0.85 ADDC + 0.10 PHO + 0.05 HO_2 + 0.05 XO_2	6.00×10^{-11}		6.00×10^{-11}	1
R76	HCHO + HO --> HO2 + CO + H_2O	1.00×10^{-11}		1.00×10^{-11}	1
R77	ALD + HO --> ACO_3+ H_2O	5.55×10^{-12}	-331	1.69×10^{-11}	1
R78	KET + HO --> KETP + H_2O	Table C.2c		6.87×10^{-13}	1
R79	HKET + HO --> HO_2 + MGLY + H_2O	3.00×10^{-12}		3.00×10^{-12}	1
R80	GLY + HO --> HO_2+ 2 CO + H_2O	1.14×10^{-11}		1.14×10^{-11}	1

Table C.2f: continued

R81	MGLY + HO --> ACO_3 + CO + H_2O	1.72×10^{-11}		1.72×10^{-11}	1
R82	MACR + HO --> 0.51 TCO_3 + 0.41 HKET + 0.08 MGLY + 0.41 CO + 0.08 HCHO + 0.49 HO_2 + 0.49 XO_2	1.86×10^{-11}	-175	3.35×10^{-11}	1
R83	DCB + HO --> 0.50 TCO_3 + 0.50 HO_2 + 0.50 XO_2 + 0.35 UDD + 0.15 GLY + 0.15 MGLY	2.80×10^{-11}	-175	5.04×10^{-11}	1
R84	UDD + HO --> 0.88 ALD + 0.12 KET + HO_2	2.70×10^{-10}		2.70×10^{-10}	1
R85	OP1 + HO --> 0.65 MO_2 + 0.35 HCHO + 0.35 HO	2.93×10^{-12}	-190	5.54×10^{-12}	1
R86	OP2 + HO --> 0.44 HC3P + 0.08 ALD + 0.41 KET + 0.49 HO + 0.07 XO_2	3.40×10^{-12}	-190	6.43×10^{-12}	1
R87	PAA + HO --> 0.35 HCHO + 0.65 ACO_3 + 0.35 HO_2 + 0.35 XO_2	2.93×10^{-12}	-190	5.54×10^{-12}	1
R88	PAN + HO --> HCHO + XO_2 + H_2O + NO_3	4.00×10^{-14}		4.00×10^{-14}	1
R88a	^{15}PAN + HO --> HCHO + XO_2 + H_2O + $^{15}NO_3$	4.00×10^{-14}		4.00×10^{-14}	1
R89	TPAN + HO --> 0.60 HKET + 0.40 HCHO + 0.40 HO_2 + XO_2 + 0.40 PAN + 0.60 NO_3	3.25×10^{-13}	-500	1.74×10^{-12}	1
R89a	^{15}TPAN + HO --> 0.60 HKET + 0.40 HCHO + 0.40 HO_2 + XO_2 + 0.40 ^{15}PAN + 0.60 $^{15}NO_3$	3.25×10^{-13}	-500	1.74×10^{-12}	1

Table C.2g: continued

R90	ONIT + HO --> HC3P + NO_2 + H_2O	5.31 x 10^{-12}	260	2.22 x 10^{-12}	1
R90a	^{15}ONIT + HO --> HC3P + $^{15}NO_2$ + H_2O	5.31 x 10^{-12}	260	2.22 x 10^{-12}	1
R91	HCHO + NO_3 --> HO_2 + HNO_3 + CO	3.40 x 10^{-13}	1900	5.79 x 10^{-16}	1
R91a	HCHO + $^{15}NO_3$ --> HO_2 + $H^{15}NO_3$ + CO	3.40 x 10^{-13}	1900	5.79 x 10^{-16}	0.9974
R92	ALD + NO_3 --> ACO_3 + HNO_3	1.40 x 10^{-12}	1900	2.38 x 10^{-15}	1
R92a	ALD + $^{15}NO_3$ --> ACO_3 + $H^{15}NO_3$	1.40 x 10^{-12}	1900	2.38 x 10^{-15}	0.9967
R93	GLY + NO_3 --> HNO_3 + HO_2 + 2 CO	2.90 x 10^{-12}	1900	4.94 x 10^{-15}	1
R93a	GLY + $^{15}NO_3$ --> $H^{15}NO_3$ + HO_2 + 2 CO	2.90 x 10^{-12}	1900	4.94 x 10^{-15}	0.9962
R94	MGLY + NO_3 --> HNO_3 + ACO_3 + CO	1.40 x 10^{-12}	1900	2.38 x 10^{-15}	1
R94a	MGLY + $^{15}NO_3$ --> $H^{15}NO_3$ + ACO_3 + CO	1.40 x 10^{-12}	1900	2.38 x 10^{-15}	0.9957
R95	MACR + NO_3 --> 0.20 TCO_3 + 0.20 HNO_3 + 0.80 OLNN + 0.80 CO	8.27 x 10^{-15}	150	5.00 x 10^{-15}	1
R95a	MACR + $^{15}NO_3$ --> 0.20 TCO_3 + 0.20 $H^{15}NO_3$ + 0.80 ^{15}OLNN + 0.80 CO	8.27 x 10^{-15}	150	5.00 x 10^{-15}	0.9958
R96	DCB + NO_3 --> 0.50 TCO_3 + 0.50 HO_2 + 0.50 XO_2 + 0.25 GLY + 0.25 ALD + 0.03 KET + 0.25 MGLY + 0.5 HNO_3 + 0.5 NO_2	2.87 x 10^{-13}	1000	1.00 x 10^{-14}	1

Table C.2h: continued

R96a	DCB + $^{15}NO_3$ --> 0.50 TCO_3 + 0.50 HO_2 + 0.50 XO_2 + 0.25 GLY + 0.25 ALD + 0.03 KET + 0.25 MGLY + 0.5 $H^{15}NO_3$ + 0.5 $^{15}NO_2$	2.87×10^{-13}	1000	1.00×10^{-14}	0.9954
R97	CSL + NO_3 --> HNO_3 + PHO	2.20×10^{-11}		2.20×10^{-11}	1
R97a	CSL + $^{15}NO_3$ --> $H^{15}NO_3$ + PHO	2.20×10^{-11}		2.20×10^{-11}	0.9949
R98	ETE + NO_3 --> 0.80 OLNN + 0.20 OLND	Table C.2c		2.05×10^{-16}	1
R98a	ETE + $^{15}NO_3$ --> 0.80 ^{15}OLNN + 0.20 ^{15}OLND	Table C.2c		2.05×10^{-16}	1
R99	OLT + NO_3 --> 0.43 OLNN + 0.57 OLND	1.79×10^{-13}	450	3.95×10^{-14}	1
R99a	OLT + $^{15}NO_3$ --> ^{15}0.43 OLNN + 0.57 ^{15}OLND	1.79×10^{-13}	450	3.95×10^{-14}	1
R100	OLI + NO_3 --> 0.11 OLNN + 0.89 OLND	8.64×10^{-13}	-450	3.91×10^{-12}	1
R100a	OLI + $^{15}NO_3$ --> 0.11 ^{15}OLNN + 0.89 ^{15}OLND	8.64×10^{-13}	-450	3.91×10^{-12}	1
R101	DIEN + NO_3 --> 0.90 OLNN + 0.10 OLND + 0.90 MACR	1.0×10^{-13}		1.0×10^{-13}	1
R101a	DIEN + $^{15}NO_3$ --> 0.90 ^{15}OLNN + 0.10 ^{15}OLND + 0.90 MACR	1.0×10^{-13}		1.0×10^{-13}	1
R102	ISO + NO_3 --> 0.90 OLNN + 0.10 OLND + 0.90 MACR	4.00×10^{-12}	446	8.96×10^{-13}	1
R102a	ISO + $^{15}NO_3$ --> 0.90 ^{15}OLNN + 0.10 ^{15}OLND + 0.90 MACR	4.00×10^{-12}	446	8.96×10^{-13}	1
R103	API + NO_3 --> 0.10 OLNN + 0.90 OLND	1.19×10^{-12}	-490	6.16×10^{-12}	1

Table C.2i: continued

R103a	API + $^{15}NO_3$ --> 0.10 ^{15}OLNN + 0.90 ^{15}OLND	1.19×10^{-12}	-490	6.16×10^{-12}	1
R104	LIM + NO_3 --> 0.13 OLNN + 0.87 OLND	1.22×10^{-11}		1.22×10^{-11}	1
R104a	LIM + $^{15}NO_3$ --> 0.13 ^{15}OLNN + 0.87 ^{15}OLND	1.22×10^{-11}		1.22×10^{-11}	1
R105	TPAN + NO_3 --> 0.60 ONIT + 0.60 NO_3 + 0.40 PAN + 0.40 HCHO + 0.40 NO_2 + XO_2	2.20×10^{-14}	500	4.11×10^{-15}	1
R105a	TPAN + $^{15}NO_3$ --> 0.30 ONIT + 0.30 ^{15}ONIT + 0.30 NO_3 + 0.30 $^{15}NO_3$ + 0.20 PAN + 0.20 ^{15}PAN + 0.40 HCHO + 0.20 NO_2 + 0.20 $^{15}NO_2$ + XO_2	2.20×10^{-14}	500	4.11×10^{-15}	1
R105b	^{15}TPAN + $^{15}NO_3$ --> 0.60 ^{15}ONIT + 0.60 $^{15}NO_3$ + 0.40 ^{15}PAN + 0.40 HCHO + 0.40 $^{15}NO_2$ + XO_2	2.20×10^{-14}	500	4.11×10^{-15}	1
R106	ETE + O_3 --> HCHO + 0.43 CO + 0.37 ORA1 + 0.26 HO_2+ 0.13 H_2 + 0.12 HO	9.14×10^{-15}	2580	1.59×10^{-18}	1
R107	OLT + O_3 --> 0.64 HCHO + 0.44 ALD + 0.37 CO + 0.14 ORA1 + 0.10 ORA2 + 0.25 HO_2 + 0.40 HO + 0.03 KET + 0.03 KETP + 0.06 CH_4 + 0.05 H_2 + 0.006 H_2O_2 + 0.03 ETH + 0.19 MO_2 + 0.10 ETHP	4.33×10^{-15}	1800	1.03×10^{-17}	1

Table C.2j: continued

R108	OLI + O_3 --> 0.02 HCHO + 0.99 ALD + 0.16 KET + 0.30 CO + 0.011 H_2O_2 + ORA2 + 0.07 CH_4 + 0.22 HO_2 + 0.63 HO + 0.23 MO_2 + 0.12 KETP + 0.06 ETH + 0.18 ETHP	4.40×10^{-15}	845	2.58×10^{-16}	1
R109	DIEN + O_3 --> 0.90 HCHO + 0.39 MACR + 0.36 CO + 0.15 ORA1 + 0.09 O^3P + 0.30 HO_2 + 0.35 OLT + 0.28 HO + 0.05 H_2 + 0.15 ACO_3 + 0.03 MO_2 + 0.02 KETP + 0.13 XO_2 + 0.001 H_2O_2	1.34×10^{-14}	2283	6.33×10^{-18}	1
R110	ISO + O_3 --> 0.90 HCHO + 0.39 MACR + 0.36 CO + 0.15 ORA1 + 0.09 O^3P + 0.30 HO_2 + 0.35 OLT + 0.28 HO + 0.05 H_2 + 0.15 ACO_3 + 0.03 MO_2 + 0.02 KETP + 0.13 XO_2 + 0.001 H_2O_2	7.86×10^{-15}	1913	1.28×10^{-17}	1
R111	API + O_3 --> 0.65 ALD + 0.53 KET + 0.14 CO + 0.20 ETHP + 0.42 KETP + 0.85 HO + 0.10 HO_2 + 0.02 H_2O_2	1.01×10^{-15}	736	8.66×10^{-17}	1
R112	LIM + O_3 --> 0.04 HCHO + 0.46 OLT + 0.14 CO + 0.16 ETHP + 0.42 KETP + 0.85 HO + 0.10 HO_2 + 0.02 H_2O_2 + 0.79 MACR + 0.01 ORA1 + 0.07 ORA2	2.00×10^{-16}		2.00×10^{-16}	1

Table C.2k: continued

R113	MACR + O_3 --> 0.40 HCHO + 0.60 MGLY + 0.13 ORA2 + 0.54 CO + 0.08 H_2 + 0.22 ORA1 + 0.29 HO_2 + 0.07 HO + 0.13 OP2 + 0.13 ACO_3	1.36×10^{-15}	2112	1.14×10^{-18}	1
R114	DCB + O_3 --> 0.21 HO + 0.29 HO_2 + 0.66 CO + 0.50 GLY + 0.28 ACO_3 + 0.16 ALD + 0.62 MGLY + 0.11 PAA + 0.11 ORA1 + 0.21 ORA2	2.00×10^{-18}		2.00×10^{-18}	1
R115	TPAN + O_3 --> 0.70 HCHO + 0.30 PAN + 0.70 NO_2 + 0.13 CO + 0.04 H_2 + 0.11 ORA1 + 0.08 HO_2 + 0.036 HO + 0.70 ACO_3	2.46×10^{-15}	1700	8.19×10^{-18}	1
R115a	^{15}TPAN + O_3 --> 0.70 HCHO + 0.30 ^{15}PAN + 0.70 $^{15}NO_2$ + 0.13 CO + 0.04 H_2 + 0.11 ORA1 + 0.08 HO_2 + 0.036 HO + 0.70 ACO_3	2.46×10^{-15}	1700	8.19×10^{-18}	1
R116	PHO + NO_2 --> 0.10 CSL + ONIT	2.00×10^{-11}		2.00×10^{-11}	1
R116a	PHO + $^{15}NO_2$ --> 0.10 CSL + ^{15}ONIT	2.00×10^{-11}		2.00×10^{-11}	1
R117	PHO + HO_2 --> CSL	1.00×10^{-11}		1.00×10^{-11}	1
R118	ADDT + NO_2 --> CSL + HONO	3.60×10^{-11}		3.60×10^{-11}	1
R118a	ADDT + $^{15}NO_2$ --> CSL + HO^{15}NO	3.60×10^{-11}		3.60×10^{-11}	1
R119	ADDT + O_2 --> 0.98 TOLP + 0.02 CSL + 0.02 HO_2	1.66×10^{-17}	-1044	5.52×10^{-16}	1
R120	ADDT + O_3 --> CSL + HO	5.00×10^{-11}		5.00×10^{-11}	1
R121	ADDX + NO_2 --> CSL + HONO	3.60×10^{-11}		3.60×10^{-11}	1

Table C.2l: continued

R121a	ADDX + $^{15}NO_2$ --> CSL + HO^{15}NO	3.60 x 10^{-11}		3.60 x 10^{-11}	1
R122	ADDX + O_2 --> 0.98 XYLP + 0.02 CSL + 0.02 HO_2	1.66 x 10^{-17}	-1044	5.52 x 10^{-16}	1
R123	ADDX + O_3 --> CSL + HO	1.00 x 10^{-11}		1.00 x 10^{-11}	1
R124	ADDC + NO_2 --> CSL + HONO	3.60 x 10^{-11}		3.60 x 10^{-11}	1
R124a	ADDC + $^{15}NO_2$ --> CSL + HO^{15}NO	3.60 x 10^{-11}		3.60 x 10^{-11}	1
R125	DDC + O_2 --> 0.98 CSLP + 0.02 CSL + 0.02 HO_2	1.66 x 10^{-17}	-1044	5.52 x 10^{-16}	1
R126	DDC + O3 --> CSL + HO_2	5.00 x 10^{-11}		5.00 x 10^{-11}	1
R127	ACO_3 + NO_2 --> PAN	Table C.2d		8.66 x 10^{-12}	1
R127a	ACO_3 + $^{15}NO_2$ --> ^{15}PAN	Table C.2d		8.66 x 10^{-12}	1
R128	PAN --> ACO_3 + NO_2	Table C.2e		4.63 x 10^{-4}	1
R128a	^{15}PAN --> ACO_3 + $^{15}NO_2$	Table C.2e		4.63 x 10^{-4}	1
R129	TCO_3 + NO_2 --> TPAN	Table C.2d		8.66 x 10^{-12}	1
R129a	TCO_3 + $^{15}NO_2$ --> ^{15}TPAN	Table C.2d		8.66 x 10^{-12}	1
R130	TPAN --> TCO_3 + NO_2	Table C.2e		4.63 x 10^{-4}	1
R130a	^{15}TPAN --> TCO_3 + $^{15}NO_2$	Table C.2e		4.63 x 10^{-4}	1
R131	MO_2 + NO --> HCHO + HO_2 + NO_2	4.2 x 10^{-12}	-180	7.68 x 10^{-12}	1
R131a	MO_2 + ^{15}NO --> HCHO + HO_2 + $^{15}NO_2$	4.2 x 10^{-12}	-180	7.68 x 10^{-12}	1
R132	ETHP + NO --> ALD + HO_2 + NO_2	8.7 x 10^{-12}		8.7 x 10^{-12}	1
R132a	ETHP + ^{15}NO --> ALD + HO_2 + $^{15}NO_2$	8.7 x 10^{-12}		8.7 x 10^{-12}	1

Table C.2m: continued

R133	HC3P + NO --> 0.047 HCHO + 0.233 ALD + 0.623 KET + 0.063 GLY + 0.742 HO_2 + 0.15 MO_2 + 0.048 ETHP + 0.048 XO_2 + 0.059 ONIT + 0.941 NO_2	4.0×10^{-12}		4.0×10^{-12}	1
R133a	HC3P + ^{15}NO --> 0.047 HCHO + 0.233 ALD + 0.623 KET + 0.063 GLY + 0.742 HO_2 + 0.15 MO_2 + 0.048 ETHP + 0.048 XO_2 + 0.059 $^{15}ONIT$ + 0.941 $^{15}NO_2$	4.0×10^{-12}		4.0×10^{-12}	1
R134	HC5P + NO --> 0.021 HCHO + 0.211 ALD + 0.722 KET + 0.599 HO_2 + 0.031 MO_2 + 0.245 ETHP + 0.334 XO_2 + 0.124 ONIT + 0.876 NO_2	4.0×10^{-12}		4.0×10^{-12}	1
R134a	HC5P + ^{15}NO --> 0.021 HCHO + 0.211 ALD + 0.722 KET + 0.599 HO_2 + 0.031 MO_2 + 0.245 ETHP + 0.334 XO_2 + 0.124 $^{15}ONIT$ + 0.876 $^{15}NO_2$	4.0×10^{-12}		4.0×10^{-12}	1
R135	HC8P + NO --> 0.15 ALD + 0.642 KET + 0.133 ETHP + 0.261 ONIT + 0.739 NO_2 + 0.606 HO_2 + 0.416 XO_2	4.0×10^{-12}		4.0×10^{-12}	1
R135a	HC8P + ^{15}NO --> 0.15 ALD + 0.642 KET + 0.133 ETHP + 0.261 $^{15}ONIT$ + 0.739 $^{15}NO_2$ + 0.606 HO_2 + 0.416 XO_2	4.0×10^{-12}		4.0×10^{-12}	1
R136	ETEP + NO --> 1.6 HCHO + HO_2 + NO_2 + 0.2 ALD	9.0×10^{-12}		9.0×10^{-12}	1

Table C.2n: continued

R136a	ETEP + ^{15}NO --> 1.6 HCHO + HO_2 + $^{15}NO_2$ + 0.2 ALD	9.0×10^{-12}		9.0×10^{-12}	1
R137	OLTP + NO --> 0.94 ALD + HCHO + HO_2 + NO_2 + 0.06 KET	4.0×10^{-12}		4.0×10^{-12}	1
R137a	OLTP + ^{15}NO --> 0.94 ALD + HCHO + HO_2 + $^{15}NO_2$ + 0.06 KET	4.0×10^{-12}		4.0×10^{-12}	1
R138	OLIP + NO --> HO2 + 1.71 ALD + 0.29 KET + NO_2	4.0×10^{-12}		4.0×10^{-12}	1
R138a	OLIP + ^{15}NO --> HO2 + 1.71 ALD + 0.29 KET + $^{15}NO_2$	4.0×10^{-12}		4.0×10^{-12}	1
R139	ISOP + NO --> 0.446 MACR + 0.354 OLT + 0.847 HO_2 + 0.606 HCHO + 0.153 ONIT + 0.847 NO_2	4.0×10^{-12}		4.0×10^{-12}	1
R139a	ISOP + ^{15}NO --> 0.446 MACR + 0.354 OLT + 0.847 HO_2 + 0.606 HCHO + 0.153 $^{15}ONIT$ + 0.847 $^{15}NO_2$	4.0×10^{-12}		4.0×10^{-12}	1
R140	APIP + NO --> 0.80 HO_2 + 0.80 ALD + 0.80 KET + 0.20 ONIT + 0.80 NO_2	4.0×10^{-12}		4.0×10^{-12}	1
R140a	APIP + ^{15}NO --> 0.80 HO_2 + 0.80 ALD + 0.80 KET + 0.20 $^{15}ONIT$ + 0.80 $^{15}NO_2$	4.0×10^{-12}		4.0×10^{-12}	1
R141	LIMP + NO --> 0.65 HO_2 + 0.40 MACR + 0.25 OLI + 0.25 HCHO + 0.35 ONIT + 0.65 NO_2	4.0×10^{-12}		4.0×10^{-12}	1

Table C.2o: continued

R141a	LIMP + ^{15}NO --> 0.65 HO_2 + 0.40 MACR + 0.25 OLI + 0.25 HCHO + 0.35 $^{15}ONIT$ + 0.65 $^{15}NO_2$	4.0×10^{-12}		4.0×10^{-12}	1
R142	TOLP + NO --> 0.95 NO_2 + 0.95 HO_2 + 0.65 MGLY + 1.20 GLY + 0.50 DCB + 0.05 ONIT	4.0×10^{-12}		4.0×10^{-12}	1
R142a	TOLP + ^{15}NO --> 0.95 $^{15}NO_2$ + 0.95 HO_2 + 0.65 MGLY + 1.20 GLY + 0.50 DCB + 0.05 $^{15}ONIT$	4.0×10^{-12}		4.0×10^{-12}	1
R143	XYLP + NO --> 0.95 NO_2 + 0.95 HO_2 + 0.60 MGLY + 0.35 GLY + 0.95 DCB + 0.05 ONIT	4.0×10^{-12}		4.0×10^{-12}	1
R143a	XYLP + ^{15}NO --> 0.95 $^{15}NO_2$ + 0.95 HO_2 + 0.60 MGLY + 0.35 GLY + 0.95 DCB + 0.05 $^{15}ONIT$	4.0×10^{-12}		4.0×10^{-12}	1
R144	CSLP + NO --> GLY + MGLY + HO_2 + NO_2	4.0×10^{-12}		4.0×10^{-12}	1
R144a	CSLP + ^{15}NO --> GLY + MGLY + HO_2 + $^{15}NO_2$	4.0×10^{-12}		4.0×10^{-12}	1
R145	ACO_3 + NO --> MO_2 + NO_2	2.0×10^{-11}		2.0×10^{-11}	1
R145a	ACO_3 + ^{15}NO --> MO_2 + $^{15}NO_2$	2.0×10^{-11}		2.0×10^{-11}	1
R146	TCO_3 + NO --> ACO_3 + HCHO + NO_2	2.0×10^{-11}		2.0×10^{-11}	1
R146a	TCO_3 + ^{15}NO --> ACO_3 + HCHO + $^{15}NO_2$	2.0×10^{-11}		2.0×10^{-11}	1
R147	KETP + NO --> 0.54 MGLY + 0.46 ALD + 0.23 ACO_3 + 0.77 HO_2 + 0.16XO_2 + NO_2	4.0×10^{-12}		4.0×10^{-12}	1

Table C.2p: continued

R147a	KETP + ^{15}NO --> 0.54 MGLY + 0.46 ALD + 0.23 ACO_3 + 0.77 HO_2 + 0.16XO_2 + $^{15}NO_2$	4.0 x 10^{-12}		4.0 x 10^{-12}	1
R148	OLNN + NO --> HO2 + ONIT + NO_2	4.0 x 10^{-12}		4.0 x 10^{-12}	1
R148a	^{15}OLNN + NO --> HO_2 + 0.5 ^{15}ONIT + 0.5 NO_2 + 0.5 ONIT + 0.5 $^{15}NO_2$	4.0 x 10^{-12}		4.0 x 10^{-12}	1
R148b	OLNN + ^{15}NO --> HO_2 + 0.5 ONIT + 0.5 $^{15}NO_2$ + 0.5 ^{15}ONIT + 0.5 NO_2	4.0 x 10^{-12}		4.0 x 10^{-12}	1
R148c	^{15}OLNN + ^{15}NO --> HO_2 + ^{15}ONIT + $^{15}NO_2$	4.0 x 10^{-12}		4.0 x 10^{-12}	1
R149	OLND + NO --> 0.287 HCHO + 1.24 ALD + 0.464 KET + 2 NO_2	4.0 x 10^{-12}		4.0 x 10^{-12}	1
R149a	OLND + ^{15}NO --> 0.287 HCHO + 1.24 ALD + 0.464 KET + NO_2 + $^{15}NO_2$	4.0 x 10^{-12}		4.0 x 10^{-12}	1
R149b	^{15}OLND + NO --> 0.287 HCHO + 1.24 ALD + 0.464 KET + NO_2 + $^{15}NO_2$	4.0 x 10^{-12}		4.0 x 10^{-12}	1
R149c	^{15}OLND + ^{15}NO --> 0.287 HCHO + 1.24 ALD + 0.464 KET + 2 $^{15}NO_2$	4.0 x 10^{-12}		4.0 x 10^{-12}	1
R150	MO_2 + HO_2 --> OP1	3.80 x 10^{-13}	-800	5.57 x 10^{-12}	1
R151	ETHP + HO_2 --> OP2	7.50 x 10^{-13}	-700	7.86 x 10^{-12}	1
R152	HC3P + HO_2 --> OP2	1.66 x 10^{-13}	-1300	1.30 x 10^{-11}	1
R153	HC5P + HO_2 --> OP2	1.66 x 10^{-13}	-1300	1.30 x 10^{-11}	1
R154	HC8P + HO_2 --> OP2	1.66 x 10^{-13}	-1300	1.30 x 10^{-11}	1

Table C.2q: continued

R155	ETEP + HO_2 --> OP2	1.90×10^{-13}	-1300	1.50×10^{-11}	1
R156	OLIP + HO_2 --> OP2	1.66×10^{-13}	-1300	1.30×10^{-11}	1
R157	OLTP + HO_2 --> OP2	1.66×10^{-13}	-1300	1.30×10^{-11}	1
R158	ISOP + HO_2 --> OP2	1.28×10^{-13}	-1300	1.00×10^{-11}	1
R159	APIP + HO_2 --> OP2	1.50×10^{-13}		1.50×10^{-11}	1
R160	LIMP + HO_2 --> OP2	1.50×10^{-13}		1.50×10^{-11}	1
R161	TOLP + HO_2 --> OP2	3.75×10^{-13}	-980	1.01×10^{-11}	1
R162	XYLP + HO_2 --> OP2	3.75×10^{-13}	-980	1.01×10^{-11}	1
R163	CSLP + HO_2 --> OP2	3.75×10^{-13}	-980	1.01×10^{-11}	1
R164	ACO_3 + HO_2 --> PAA	1.15×10^{-13}	-550	7.28×10^{-12}	1
R165	ACO_3 + HO_2 --> ORA2 + O_3	3.86×10^{-13}	-2640	2.72×10^{-12}	1
R166	TCO_3 + HO_2 --> OP2	1.15×10^{-13}	-550	7.28×10^{-12}	1
R167	TCO_3 + HO_2 --> ORA2 + O_3	3.86×10^{-13}	-2640	2.72×10^{-12}	1
R168	KETP + HO_2 --> OP2	1.15×10^{-13}	-1300	9.02×10^{-12}	1
R169	OLNN + HO_2 --> ONIT	1.66×10^{-13}	-1300	1.30×10^{-11}	1
R169a	^{15}OLNN + HO_2 --> ^{15}ONIT	1.66×10^{-13}	-1300	1.30×10^{-11}	1
R170	OLND + HO_2 --> ONIT	1.66×10^{-13}	-1300	1.30×10^{-11}	1
R170a	^{15}OLND + HO_2 --> ^{15}ONIT	1.66×10^{-13}	-1300	1.30×10^{-11}	1
R171	MO_2 + MO_2 --> 1.33 HCHO + 0.66 HO_2	9.10×10^{-14}	-416	3.68×10^{-13}	1
R172	ETHP + MO_2 --> 0.75 HCHO + HO_2 + 0.75 ALD	1.18×10^{-14}	-158	2.01×10^{-13}	1
R173	HC3P + MO_2 --> 0.81 HCHO + 0.992 HO_2 + 0.58 ALD + 0.018 KET + 0.007 MO_2 + 0.005 MGLY + 0.085 XO_2 + 0.119 GLY	9.46×10^{-14}	-431	4.02×10^{-13}	1

Table C.2r: continued

R174	HCSP + MO_2 --> 0.829 HCHO + 0.946 HO_2 + 0.523 ALD + 0.24 KET + 0.014 ETHP + 0.049 MO_2 + 0.245 XO_2	1.00×10^{-13}	-467	4.79×10^{-13}	1
R175	HC8P + MO_2 --> 0.753 HCHO + 0.993 HO_2 + 0.411 ALD + 0.419 KET + 0.322 XO_2 + 0.013 ETHP	4.34×10^{-14}	-633	3.63×10^{-13}	1
R176	ETEP + MO_2 --> 1.55 HCHO + HO_2 + 0.35 ALD	1.71×10^{-13}	-708	1.84×10^{-12}	1
R177	OLTP + MO_2 --> 1.25 HCHO + HO_2 + 0.669 ALD + 0.081 KET	1.46×10^{-13}	-708	1.57×10^{-12}	1
R178	OLIP + MO_2 --> 0.755 HCHO + HO_2 + 0.932 ALD + 0.313 KET	9.18×10^{-14}	-708	9.87×10^{-13}	1
R179	ISOP + MO_2 --> 0.550 MACR + 0.370 OLT + HO_2+ 0.08 OLI + 1.09 HCHO	1.36×10^{-13}	-708	1.46×10^{-12}	1
R180	APIP + MO_2 --> HCHO + ALD + KET + 2 HO_2	3.56×10^{-14}	-708	3.83×10^{-13}	1
R181	LIMP + MO_2 --> 1.4 HCHO + 0.60 MACR + 0.40 OLI + 2 HO_2	3.56×10^{-14}	-708	3.83×10^{-13}	1
R182	TOLP + MO_2 --> HCHO + HO_2 + 0.35 MGLY + 0.65 GLY + DCB	3.56×10^{-14}	-708	3.83×10^{-13}	1
R183	XYLP + MO_2 --> HCHO + HO_2 + 0.63 MGLY + 0.37 GLY + DCB	3.56×10^{-14}	-708	3.83×10^{-13}	1
R184	CSLP + MO_2 --> GLY + MGLY + HCHO + 2 HO_2	3.56×10^{-14}	-708	3.83×10^{-13}	1
R185	ACO_3 + MO_2 --> HCHO + HO_2 + MO_2	3.21×10^{-11}	440	7.33×10^{-12}	1
R186	ACO_3 + MO_2 --> HCHO + ORA2	2.68×10^{-16}	-2510	1.22×10^{-12}	1

Table C.2s: continued

R187	$TCO_3 + MO_2$ --> 2 HCHO + HO_2 + ACO_3	3.21×10^{-11}	440	7.33×10^{-12}	1
R188	TCO3 + MO_2 --> HCHO + ORA2	2.68×10^{-16}	-2510	1.22×10^{-12}	1
R189	KETP + MO_2 --> 0.75 HCHO + 0.88 HO_2 + 0.40 MGLY + 0.30 ALD + 0.30 HKET + 0.12 ACO_3 + 0.08 XO_2	6.91×10^{-13}	-508	3.80×10^{-12}	1
R190	OLNN + MO_2 --> 0.75 HCHO + HO_2 + ONIT	1.60×10^{-13}	-708	1.72×10^{-12}	1
R190a	^{15}OLNN + MO_2 --> 0.75 HCHO + HO_2 + ^{15}ONIT	1.60×10^{-13}	-708	1.72×10^{-12}	1
R191	OLND + MO_2 --> 0.96 HCHO + 0.5 HO_2 + 0.64 ALD + 0.149 KET + 0.5 NO_2 + 0.5 ONIT	9.68×10^{-14}	-708	1.04×10^{-12}	1
R191a	^{15}OLND + MO_2 --> 0.96 HCHO + 0.5 HO_2 + 0.64 ALD + 0.149 KET + 0.5 $^{15}NO_2$ + 0.5 ^{15}ONIT	9.68×10^{-14}	-708	1.04×10^{-12}	1
R192	ETHP + ACO_3 --> ALD + 0.5 HO_2 + 0.5 MO_2 + 0.5 ORA2	1.03×10^{-12}	-211	2.09×10^{-12}	1
R193	HC3P + ACO_3 --> 0.724 ALD + 0.127 KET + 0.488 HO_2 + 0.508 MO_2 + 0.006 ETHP + 0.071 XO_2 + 0.091 HCHO + 0.10 GLY + 0.499 ORA2 + 0.004 MGLY	6.90×10^{-14}	-460	3.23×10^{-12}	1
R194	HC5P + ACO_3 --> 0.677 ALD + 0.33 KET + 0.438 HO_2 + 0.554 MO_2 + 0.495 ORA2 + 0.018 ETHP + 0.237 XO_2 + 0.076 HCHO	5.59×10^{-13}	-522	3.22×10^{-12}	1

Table C.2t: continued

R195	HC8P + ACO_3 --> 0.497 ALD + 0.581 KET + 0.489 HO_2 + 0.507 MO_2 + 0.495 ORA2 + 0.015 ETHP + 0.318 XO_2	2.47×10^{-13}	-683	2.44×10^{-12}	1
R196	ETEP + ACO_3 --> 0.8 HCHO + 0.6 ALD + 0.5 HO_2 + 0.5 MO_2 + 0.5 ORA2	9.48×10^{-13}	-765	1.24×10^{-11}	1
R197	OLTP + ACO_3 --> 0.859 ALD + 0.501 HCHO + 0.501 HO_2 + 0.501 MO_2 + 0.499 ORA2 + 0.141 KET	8.11×10^{-13}	-765	1.06×10^{-11}	1
R198	OLIP + ACO_3 --> 0.941 ALD + 0.569 KET + 0.51 HO_2 + 0.51 MO_2 + 0.49 ORA2	5.09×10^{-13}	-765	6.63×10^{-12}	1
R199	ISOP + ACO_3 --> 0.771 MACR + 0.229 OLT + 0.506 HO_2 + 0.494 ORA2 + 0.340 HCHO + 0.506 MO_2	7.60×10^{-13}	-765	9.90×10^{-12}	1
R200	APIP + ACO_3 --> ALD + KET + HO_2 + MO_2	7.40×10^{-13}	-765	9.63×10^{-12}	1
R201	LIMP + ACO_3 --> 0.60 MACR + 0.40 OLI + 0.40 HCHO + HO_2 + MO_2	7.40×10^{-13}	-765	9.63×10^{-12}	1
R202	TOLP + ACO_3 --> MO_2 + HO_2 + 0.35 MGLY + 0.65 GLY + DCB	7.40×10^{-13}	-765	9.63×10^{-12}	1
R203	XYLP + ACO_3 --> MO_2 + HO_2 + 0.63 MGLY + 0.37 GLY + DCB	7.40×10^{-13}	-765	9.63×10^{-12}	1
R204	CSLP + ACO_3 --> GLY + MGLY + MO_2 + HO_2	7.40×10^{-13}	-765	9.63×10^{-12}	1
R205	ACO_3 + ACO_3 --> 2 MO_2	2.80×10^{-12}	-530	1.66×10^{-11}	1

Table C.2u: continued

R206	$TCO_3 + ACO_3 \rightarrow MO_2 + ACO_3 + HCHO$	2.80×10^{-12}	-530	1.66×10^{-11}	1
R207	$KETP + ACO_3 \rightarrow 0.54\ MGLY + 0.35\ ALD + 0.11\ KET + 0.12\ ACO_3 + 0.38\ HO_2 + 0.08\ XO_2 + 0.5\ MO_2 + 0.5\ ORA2$	7.51×10^{-13}	-765	5.00×10^{-12}	1
R208	$OLNN + ACO_3 \rightarrow ONIT + 0.5\ ORA2 + 0.5\ MO_2 + 0.50\ HO_2$	8.85×10^{-13}	-765	1.15×10^{-11}	1
R208a	$^{15}OLNN + ACO_3 \rightarrow {}^{15}ONIT + 0.5\ ORA2 + 0.5\ MO_2 + 0.50\ HO_2$	8.85×10^{-13}	-765	1.15×10^{-11}	1
R209	$OLND + ACO_3 \rightarrow 0.207\ HCHO + 0.65\ ALD + 0.167\ KET + 0.484\ ORA2 + 0.484\ ONIT + 0.516\ NO_2 + 0.516\ MO_2$	5.37×10^{-13}	-765	7.00×10^{-12}	1
R209a	$^{15}OLND + ACO_3 \rightarrow 0.207\ HCHO + 0.65\ ALD + 0.167\ KET + 0.484\ ORA2 + 0.484\ {}^{15}ONIT + 0.516\ {}^{15}NO_2 + 0.516\ MO_2$	5.37×10^{-13}	-765	7.00×10^{-12}	1
R210	$OLNN + OLNN \rightarrow 2\ 0NIT + HO_2$	7.0×10^{-14}	-1000	2.00×10^{-12}	1
R210a	$OLNN + {}^{15}OLNN \rightarrow ONIT + {}^{15}0NIT + HO_2$	7.0×10^{-14}	-1000	2.00×10^{-12}	1
R210b	$OLNN + {}^{15}OLNN \rightarrow 2\ {}^{15}0NIT + HO_2$	7.0×10^{-14}	-1000	2.00×10^{-12}	1
R211	$OLNN + OLND \rightarrow 0.202\ HCHO + 0.64\ ALD + 0.149\ KET + 0.50\ HO_2 + 1.50\ ONIT + 0.50\ NO_2$	4.25×10^{-14}	-1000	1.22×10^{-12}	1
R211a	$^{15}OLNN + OLND \rightarrow 0.202\ HCHO + 0.64\ ALD + 0.149\ KET + 0.50\ HO_2 + 0.75\ ONIT + 0.75\ {}^{15}ONIT + 0.25\ NO_2 + 0.25\ {}^{15}NO_2$	4.25×10^{-14}	-1000	1.22×10^{-12}	1

Table C.2v: continued

R211b	OLNN + ^{15}OLND --> 0.202 HCHO + 0.64 ALD + 0.149 KET + 0.50 HO_2 + 0.75 ONIT + 0.75 ^{15}ONIT + 0.25 NO_2 + 0.25 $^{15}NO_2$	4.25 x 10^{-14}	-1000	1.22 x 10^{-12}	1
R211c	^{15}OLNN + ^{15}OLND --> 0.202 HCHO + 0.64 ALD + 0.149 KET + 0.50 HO_2 + 1.50 ^{15}ONIT + 0.50 $^{15}NO_2$	4.25 x 10^{-14}	-1000	1.22 x 10^{-12}	1
R212	OLND + OLND --> 0.504 HCHO + 1.21 ALD + 0.285 KET + ONIT + NO_2	2.96 x 10^{-14}	-1000	8.50 x 10^{-13}	1
R212a	OLND + ^{15}OLND --> 0.504 HCHO + 1.21 ALD + 0.285 KET + ^{15}ONIT + NO_2	2.96 x 10^{-14}	-1000	8.50 x 10^{-13}	1
R212b	OLND + ^{15}OLND --> 0.504 HCHO + 1.21 ALD + 0.285 KET + ONIT + $^{15}NO_2$	2.96 x 10^{-14}	-1000	8.50 x 10^{-13}	1
R212c	^{15}OLND + ^{15}OLND --> 0.504 HCHO + 1.21 ALD + 0.285 KET + ^{15}ONIT + $^{15}NO_2$	2.96 x 10^{-14}	-1000	8.50 x 10^{-13}	1
R213	MO_2 + NO_3 --> HCHO + HO_2 + NO_2	1.20 x 10^{-12}		1.20 x 10^{-12}	1
R213a	MO_2 + $^{15}NO_3$ --> HCHO + HO_2 + $^{15}NO_2$	1.20 x 10^{-12}		1.20 x 10^{-12}	1
R214	ETHP + NO_3 --> ALD + HO_2 + NO_2	1.20 x 10^{-12}		1.20 x 10^{-12}	1
R214a	ETHP + $^{15}NO_3$ --> ALD + HO_2 + $^{15}NO_2$	1.20 x 10^{-12}		1.20 x 10^{-12}	1

Table C.2w: continued

R215	HC3P + NO_3 --> 0.048 HCHO + 0.243 ALD + 0.67 KET + 0.063 GLY + 0.792 HO_2 + 0.155 MO_2 + 0.053 ETHP + 0.051 XO_2 + NO_2	1.20×10^{-12}		1.20×10^{-12}	1
R215a	HC3P + $^{15}NO_3$ --> 0.048 HCHO + 0.243 ALD + 0.67 KET + 0.063 GLY + 0.792 HO_2 + 0.155 MO_2 + 0.053 ETHP + 0.051 XO_2 + $^{15}NO_2$	1.20×10^{-12}		1.20×10^{-12}	1
R216	HC5P + NO_3 --> 0.021 HCHO + 0.239 ALD + 0.828 KET + 0.699 HO_2 + 0.04 MO_2 + 0.262 ETHP + 0.391 XO_2 + NO_2	1.20×10^{-12}		1.20×10^{-12}	1
R216a	HC5P + $^{15}NO_3$ --> 0.021 HCHO + 0.239 ALD + 0.828 KET + 0.699 HO_2 + 0.04 MO_2 + 0.262 ETHP + 0.391 XO_2 + $^{15}NO_2$	1.20×10^{-12}		1.20×10^{-12}	1
R217	HC8P + NO_3 --> 0.187 ALD + 0.88 KET + 0.845 HO_2 + 0.155 ETHP + 0.587 XO_2 + NO_2	1.20×10^{-12}		1.20×10^{-12}	1
R217a	HC8P + $^{15}NO_3$ --> 0.187 ALD + 0.88 KET + 0.845 HO_2 + 0.155 ETHP + 0.587 XO_2 + $^{15}NO_2$	1.20×10^{-12}		1.20×10^{-12}	1
R218	ETEP + NO_3 --> 1.6 HCHO + 0.2 ALD + HO_2 + NO_2	1.20×10^{-12}		1.20×10^{-12}	1
R218a	ETEP + $^{15}NO_3$ --> 1.6 HCHO + 0.2 ALD + HO_2 + $^{15}NO_2$	1.20×10^{-12}		1.20×10^{-12}	1
R219	OLTP + NO_3 --> HCHO + 0.94 ALD + 0.06 KET + HO_2 + NO_2	1.20×10^{-12}		1.20×10^{-12}	1
R219a	OLTP + $^{15}NO_3$ --> HCHO + 0.94 ALD + 0.06 KET + HO_2 + $^{15}NO_2$	1.20×10^{-12}		1.20×10^{-12}	1

Table C.2x: continued

R220	OLIP + NO_3 --> 1.71 ALD + 0.29 KET + HO_2 + NO_2	1.20×10^{-12}		1.20×10^{-12}	1
R220a	OLIP + $^{15}NO_3$ --> 1.71 ALD + 0.29 KET + HO_2 + $^{15}NO_2$	1.20×10^{-12}		1.20×10^{-12}	1
R221	ISOP + NO_3 --> 0.60 MACR + 0.40 OLT + 0.686 HCHO + HO_2 + NO_2	1.20×10^{-12}		1.20×10^{-12}	1
R221a	ISOP + $^{15}NO_3$ --> 0.60 MACR + 0.40 OLT + 0.686 HCHO + HO_2 + $^{15}NO_2$	1.20×10^{-12}		1.20×10^{-12}	1
R222	APIP + NO_3 --> ALD + KET + HO_2 + NO_2	1.20×10^{-12}		1.20×10^{-12}	1
R222a	APIP + $^{15}NO_3$ --> ALD + KET + HO_2 + $^{15}NO_2$	1.20×10^{-12}		1.20×10^{-12}	1
R223	LIMP + NO_3 --> 0.60 MACR + 0.40 OLI + 0.40 HCHO + HO_2 + NO_2	1.20×10^{-12}		1.20×10^{-12}	1
R223a	LIMP + $^{15}NO_3$ --> 0.60 MACR + 0.40 OLI + 0.40 HCHO + HO_2 + $^{15}NO_2$	1.20×10^{-12}		1.20×10^{-12}	1
R224	TOLP + NO_3 --> 0.70 MGLY + 1.30GLY + 0.50 DCB + HO_2 + NO_2	1.20×10^{-12}		1.20×10^{-12}	1
R224a	TOLP + $^{15}NO_3$ --> 0.70 MGLY + 1.30GLY + 0.50 DCB + HO_2 + $^{15}NO_2$	1.20×10^{-12}		1.20×10^{-12}	1
R225	XYLP + NO_3 --> 1.26 MGLY + 0.74 GLY + DCB + HO_2 + NO_2	1.20×10^{-12}		1.20×10^{-12}	1

Table C.2y: continued

R225a	XYLP + $^{15}NO_3$ --> 1.26 MGLY + 0.74 GLY + DCB + HO_2 + $^{15}NO_2$	1.20×10^{-12}		1.20×10^{-12}	1
R226	CSLP + NO_3 --> GLY + MGLY + HO_2 + NO_2	1.20×10^{-12}		1.20×10^{-12}	1
R226a	CSLP + $^{15}NO_3$ --> GLY + MGLY + HO_2 + $^{15}NO_2$	1.20×10^{-12}		1.20×10^{-12}	1
R227	ACO3 + NO_3 --> MO_2 + NO_2	4.00×10^{-12}		4.00×10^{-12}	1
R227a	ACO3 + $^{15}NO_3$ --> MO_2 + $^{15}NO_2$	4.00×10^{-12}		4.00×10^{-12}	1
R228	TCO3 + NO_3 --> HCHO + ACO_3 + NO_2	4.00×10^{-12}		4.00×10^{-12}	1
R228a	TCO3 + $^{15}NO_3$ --> HCHO + ACO_3 + $^{15}NO_2$	4.00×10^{-12}		4.00×10^{-12}	1
R229	KETP + NO_3 --> 0.54 MGLY + 0.46 ALD + 0.77 HO_2 + 0.23 ACO_3 + 0.16 XO_2 + NO_2	1.20×10^{-12}		1.20×10^{-12}	1
R229a	KETP + $^{15}NO_3$ --> 0.54 MGLY + 0.46 ALD + 0.77 HO_2 + 0.23 ACO_3 + 0.16 XO_2 + $^{15}NO_2$	1.20×10^{-12}		1.20×10^{-12}	1
R230	OLNN + NO_3 --> ONIT + HO_2 + NO_2	1.20×10^{-12}		1.20×10^{-12}	1
R230a	OLNN + $^{15}NO_3$ --> ONIT + HO_2 + $^{15}NO_2$	1.20×10^{-12}		1.20×10^{-12}	1
R230b	^{15}OLNN + NO_3 --> ^{15}ONIT + HO_2 + NO_2	1.20×10^{-12}		1.20×10^{-12}	1
R230c	^{15}OLNN + $^{15}NO_3$ --> ^{15}ONIT + HO_2 + $^{15}NO_2$	1.20×10^{-12}		1.20×10^{-12}	1
R231	OLND + NO_3 --> 0.28 HCHO + 1.24 ALD + 0.469 KET + 2 NO_2	1.20×10^{-12}		1.20×10^{-12}	1

Table C.2z: continued

R231a	^{15}OLND + NO_3 --> 0.28 HCHO + 1.24 ALD + 0.469 KET + NO_2 + $^{15}NO_2$	1.20×10^{-12}		1.20×10^{-12}	1
R231b	OLND + $^{15}NO_3$ --> 0.28 HCHO + 1.24 ALD + 0.469 KET + NO_2 + $^{15}NO_2$	1.20×10^{-12}		1.20×10^{-12}	1
R231c	^{15}OLND + $^{15}NO_3$ --> 0.28 HCHO + 1.24 ALD + 0.469 KET + 2 $^{15}NO_2$	1.20×10^{-12}		1.20×10^{-12}	1
R232	XO_2 + HO_2 --> OP2	1.66×10^{-13}	-1300	1.30×10^{-11}	1
R233	XO_2 + MO_2 --> HCHO + HO_2	5.99×10^{-15}	-1510	9.50×10^{-13}	1
R234	XO_2 + ACO_3 --> MO_2	3.40×10^{-14}	-1516	6.38×10^{-12}	1
R235	XO_2 + XO_2 -->	7.13×10^{-17}	-2950	1.42×10^{-12}	1
R236	XO_2 + NO --> NO_2	4.00×10^{-12}		4.00×10^{-12}	1
R236a	XO_2 + ^{15}NO --> $^{15}NO_2$	4.00×10^{-12}		4.00×10^{-12}	1
R237	XO_2 + NO3 --> NO_2	1.20×10^{-12}		1.20×10^{-12}	1
R237a	XO_2 + ^{15}NO3 --> $^{15}NO_2$	1.20×10^{-12}		1.20×10^{-12}	1
R238	NO + $^{15}NO_2$ --> ^{15}NO + NO_2	3.60×10^{-14}		3.60×10^{-14}	1
R238a	^{15}NO + NO_2 --> NO + $^{15}NO_2$	3.60×10^{-14}	-18.467	3.83×10^{-14}	0.9771
R239	N_2O_5 --> HNO_3 + HNO_3	0.1		0.1	1
R239a	$^{15}NNO_5$ --> $^{15}HNO_3$ + HNO_3	0.1		0.1	0.9954
R239b	$^{15}N_2O_5$ --> $^{15}HNO_3$ + $^{15}HNO_3$	0.1		0.1	0.9909

Table C.2aa: Reaction rate constants of the form $k = T^2 C \exp(-D/T)$

Reaction No.	Reaction	C, K^{-2} cm^3 s^{-1}	D, K	α
R61	$CH_4 + HO \rightarrow MO_2 + H_2O$	7.44×10^{-18}	1361	1
R62	$ETH + HO \rightarrow ETHP + H_2O$	1.51×10^{-17}	492	1
R78	$KET + HO \rightarrow KETP + H_2O$	5.68×10^{-18}	-92	1
R98	$ETE + NO_3 \rightarrow 0.80\ OLNN + 0.20\ OLND$	4.88×10^{-18}	2282	1
R98a	$ETE + {}^{15}NO_3 \rightarrow 0.80\ {}^{15}OLNN + 0.20\ {}^{15}OLND$	4.88×10^{-18}	2282	0.9975

Table C.2bb: Troe reactions

Reaction No.	Reaction	K_0^{300}, cm^6 s^{-1}	n	K_∞^{300}, cm^6 s^{-1}	m	α
R35	$O^3P + NO \rightarrow NO_2$	9.00×10^{-32}	1.5	3.00×10^{-11}	0	1
R35a	$O^3P + {}^{15}NO \rightarrow {}^{15}NO_2$	9.00×10^{-32}	1.5	3.00×10^{-11}	0	1
R37	$O^3P + NO_2 \rightarrow NO_3$	9.00×10^{-32}	2	2.20×10^{-11}	0	1
R37a	$O^3P + {}^{15}NO_2 \rightarrow {}^{15}NO_3$	9.00×10^{-32}	2	2.20×10^{-11}	0	1
R38	$HO + NO \rightarrow HONO$	7.00×10^{-31}	2.6	1.50×10^{-11}	0.5	1
R38a	$HO + {}^{15}NO \rightarrow HO{}^{15}NO$	7.00×10^{-31}	2.6	1.50×10^{-11}	0.5	1
R39	$HO + NO_2 \rightarrow HNO_3$	2.60×10^{-30}	3.2	2.40×10^{-11}	1.3	1
R39a	$HO + {}^{15}NO_2 \rightarrow H{}^{15}NO_3$	2.60×10^{-30}	3.2	2.40×10^{-11}	1.3	1.04
R42	$HO_2 + NO_2 \rightarrow HNO_4$	2.80×10^{-31}	3.2	4.70×10^{-12}	1.4	1
R42a	$HO_2 + {}^{15}NO_2 \rightarrow H{}^{15}NO_4$	2.80×10^{-31}	3.2	4.70×10^{-12}	1.4	1
R53	$NO_3 + NO_2 \rightarrow N_2O_5$	2.20×10^{-30}	3.9	1.50×10^{-12}	0.7	1
R53a	$NO_3 + {}^{15}NO_2 \rightarrow {}^{15}NNO_5$	2.20×10^{-30}	3.9	1.50×10^{-12}	0.7	1.0266
R53b	$^{15}NO_3 + NO_2 \rightarrow {}^{15}NNO_5$	2.20×10^{-30}	3.9	1.50×10^{-12}	0.7	1.0309
R53c	$^{15}NO_3 + {}^{15}NO_2 \rightarrow {}^{15}N_2O_5$	2.20×10^{-30}	3.9	1.50×10^{-12}	0.7	1.057
R57	$HO + SO_2 \rightarrow SULF + HO_2$	3.0×10^{-31}	3.3	1.50×10^{-12}	0	1
R127	$ACO_3 + NO_2 \rightarrow PAN$	9.70×10^{-29}	5.6	9.30×10^{-12}	1.5	1
R127a	$ACO_3 + {}^{15}NO_2 \rightarrow {}^{15}PAN$	9.70×10^{-29}	5.6	9.30×10^{-12}	1.5	1
R129	$TCO_3 + NO_2 \rightarrow TPAN$	9.70×10^{-29}	5.6	9.30×10^{-12}	1.5	1
R129a	$TCO_3 + {}^{15}NO_2 \rightarrow {}^{15}TPAN$	9.70×10^{-29}	5.6	9.30×10^{-12}	1.5	1

Table C.2cc: Troe equilibrium reactions

Reaction No.	Reaction	A	B	K_0^{300}, $cm^6\ s^{-1}$	n	K_∞^{300}, $cm^6\ s^{-1}$	m	α
R43	$HNO4 \rightarrow HO_2 + NO_2$	$4.76 \times 10^{+26}$	10900	1.81×10^{-31}	3.2	4.70×10^{-12}	1.4	1
R43a	$H^{15}NO4 \rightarrow HO_2 + {}^{15}NO_2$	$4.76 \times 10^{+26}$	10900	1.81×10^{-31}	3.2	4.70×10^{-12}	1.4	1
R54	$N_2O_5 \rightarrow NO_2 + NO_3$	$3.70 \times 10^{+26}$	11000	2.20×10^{-30}	3.9	1.50×10^{-12}	0.7	1
R54a	${}^{15}NNO_5 \rightarrow {}^{15}NO_2 + NO_3$	$3.70 \times 10^{+26}$	11000	2.20×10^{-30}	3.9	1.50×10^{-12}	0.7	0.5
R54b	${}^{15}NNO_5 \rightarrow NO_2 + {}^{15}NO_3$	$3.70 \times 10^{+26}$	11000	2.20×10^{-30}	3.9	1.50×10^{-12}	0.7	0.5
R54c	${}^{15}N_2O_5 \rightarrow {}^{15}NO_2 + {}^{15}NO_3$	$3.70 \times 10^{+26}$	11000	2.20×10^{-30}	3.9	1.50×10^{-12}	0.7	1
R128	$PAN \rightarrow ACO_3 + NO_2$	$1.16 \times 10^{+28}$	13954	9.70×10^{-29}	5.6	9.30×10^{-12}	1.5	1
R128a	${}^{15}PAN \rightarrow ACO_3 + {}^{15}NO_2$	$1.16 \times 10^{+28}$	13954	9.70×10^{-29}	5.6	9.30×10^{-12}	1.5	1
R130	$TPAN \rightarrow TCO_3 + NO_2$	$1.16 \times 10^{+28}$	13954	9.70×10^{-29}	5.6	9.30×10^{-12}	1.5	1
R130a	${}^{15}TPAN \rightarrow TCO_3 + {}^{15}NO_2$	$1.16 \times 10^{+28}$	13954	9.70×10^{-29}	5.6	9.30×10^{-12}	1.5	1

Table C.2dd: Reactions with special rate expressions

Reaction No.	Reaction	Rate Constant Expression	α
R24	$O^3P + O_2 \rightarrow O_3$	$[M] \times 6.0 \times 10^{-34} \times (T/300\ K)^{-23}$	1
R33	$HO_2 + HO_2 \rightarrow H_2O_2 + O_2$	$2.3 \times 10^{-13} \times \exp(600/T) + 1.7 \times 10^{-33} \times [M] \times \exp(1000/T)$	1
R34	$HO_2 + HO_2 + H_2O \rightarrow H_2O_2 + O_2 + H_2O$	$3.22 \times 10^{-34} \times \exp(2800/T) + 2.38 \times 10^{-54} \times [M] \times \exp(3200/T)$	1
R46	$HO + HNO_3 \rightarrow NO_3 + H_2O$	$k = k_o + k_3/(1 + k_3/k_2)$ ko = 7.2 x 10-15 x exp(785/T) k2 = 4.1 x 10-16 x exp(1440/T) k3 = 1.9 x 10-33 x exp(725/T) x [M]	1
R46a	$HO + H^{15}NO_3 \rightarrow {}^{15}NO_3 + H_2O$		1
R58	$CO + HO \rightarrow HO_2 + CO_2$	$1.5 \times 10^{-13} \times (1 + 2.439 \times 10^{-20} \times [M])$	1

*[M] is the concentration of air in molecules cm^{-3}

Table C.3a: Initial concentrations and emission rates for test cases

Compound	Initial Concentrations, ppb	Emissions, ppt/min
H_2O	1E+07	-
O_3	10	-
NO	0.2	2.59
^{15}NO	0.00072	9.32E-03
NO_2	0.25	-
$^{15}NO_2$	0.0009	-
HNO_3	-	-
$H^{15}NO_3$	-	-
CO	1000	5.6
CH_4	3000	-
H_2	500	-
H_2O_2	2	-
SO_2	-	0.52
ETH	-	0.24
HC3	-	2.94
HC5	-	0.77
HC8	-	0.45
ETE	-	0.46
OLI	-	0.19
OLT	-	0.22
TOL	-	0.57
XYL	-	0.52
HCHO	1	0.14
ALD	-	0.04
KET	-	0.50
O_2	2.09E+08	-
N_2	7.74394109E+08	-
^{15}NN	5.59578240E+06	-
$^{15}N_2$	1.01088000E+04	-

Table C.3b: Meteorological conditions for test cases

Meteorological conditions	Values
Start Date/Time	Mar 1, 0300 LT
End Date/Time	Mar 6, 0000 LT
Latitude	33 °N
Longitude	0
Elevation, km	0
Temperature, K	298
Pressure, atm	1

Table C.3c: Initial concentrations and emission rates for the cases with low VOC emission rate

Compound	Initial Concentrations, ppb	Emissions, ppt/min
H_2O	1.00E+07	-
O_3	10	-
NO	5	2.59
^{15}NO	0.018	9.32E-03
NO_2	10	-
$^{15}NO_2$	0.036	-
HNO_3	-	-
$H^{15}NO_3$	-	-
CO	1000	5.6
CH_4	3000	-
H_2	500	-
H_2O_2	2	-
SO_2	-	0.52
ETH	-	0.24
HC3	-	2.94
HC5	-	0.77
HC8	-	0.45
ETE	-	0.46
OLI	-	0.19
OLT	-	0.22
TOL	-	0.57
XYL	-	0.52
HCHO	1	0.14
ALD	-	0.04
KET	-	0.50
O_2	2.09E+08	-
N_2	7.74394109E+08	-
^{15}NN	5.59578240E+06	-
$^{15}N_2$	1.01088000E+04	-

Table C.3d: Initial concentrations and emission rates for the cases with high NO_x concentration and high VOC emission rate

Compound	Initial Concentrations, ppb	Emissions, ppt/min
H_2O	1.00E+07	-
O_3	10	-
NO	50	2.59
^{15}NO	0.18	9.32E-03
NO_2	100	-
$^{15}NO_2$	0.36	-
HNO_3	-	-
$H^{15}NO_3$	-	-
CO	1000	5.6
CH_4	3000	-
H_2	500	-
H_2O_2	2	-
SO_2	-	0.52
ETH	-	1.20
HC3	-	14.7
HC5	-	3.85
HC8	-	2.26
ETE	-	2.28
OLI	-	0.94
OLT	-	1.09
TOL	-	2.86
XYL	-	2.59
HCHO	1	0.69
ALD	-	0.18
KET	-	2.51
O_2	2.09E+08	-
N_2	7.74394109E+08	-
^{15}NN	5.59578240E+06	-
$^{15}N_2$	1.01088000E+04	-

Table C.3e: Initial concentrations and emission rates for the cases with intermediate NO_x concentration and high VOC emission rate

Compound	Initial Concentrations, ppb	Emissions, ppt/min
H_2O	1.00E+07	-
O_3	10	-
NO	5	2.59
^{15}NO	0.018	9.32E-03
NO_2	10	-
$^{15}NO_2$	0.036	-
HNO_3	-	-
$H^{15}NO_3$	-	-
CO	1000	5.6
CH_4	3000	-
H_2	500	-
H_2O_2	2	-
SO_2	-	0.52
ETH	-	1.20
HC3	-	14.7
HC5	-	3.85
HC8	-	2.26
ETE	-	2.28
OLI	-	0.94
OLT	-	1.09
TOL	-	2.86
XYL	-	2.59
HCHO	1	0.69
ALD	-	0.18
KET	-	2.51
O_2	2.09E+08	-
N_2	7.74394109E+08	-
^{15}NN	5.59578240E+06	-
$^{15}N_2$	1.01088000E+04	-

Table C.3f: Initial concentrations and emission rates for the cases with low NO_x concentration and high VOC emission rate

Compound	Initial Concentrations, ppb	Emissions, ppt/min
H_2O	1.00E+07	-
O_3	10	-
NO	0.5	2.59
^{15}NO	0.0018	9.32E-03
NO_2	1	-
$^{15}NO_2$	0.0036	-
HNO_3	-	-
$H^{15}NO_3$	-	-
CO	1000	5.6
CH_4	3000	-
H_2	500	-
H_2O_2	2	-
SO_2	-	0.52
ETH	-	1.20
HC3	-	14.7
HC5	-	3.85
HC8	-	2.26
ETE	-	2.28
OLI	-	0.94
OLT	-	1.09
TOL	-	2.86
XYL	-	2.59
HCHO	1	0.69
ALD	-	0.18
KET	-	2.51
O_2	2.09E+08	-
N_2	7.74394109E+08	-
^{15}NN	5.59578240E+06	-
$^{15}N_2$	1.01088000E+04	-

Table C.4a: Initial concentrations for inter-comparison cases 1-18

	Rural								
Case	1	2	3	4	5	6	7	8	9
H_2O, %	1	1	1	1	1	1	1	1	1
NO, ppb	0.1	0.1	0.1	0.334	0.334	0.334	1	1	1
^{15}NO, ppb	3.600E-04	3.600E-04	3.600E-04	1.202E-03	1.202E-03	1.202E-03	3.600E-03	3.600E-03	3.600E-03
NO_2, ppb	0.4	0.4	0.4	1.336	1.336	1.336	4	4	4
$^{15}NO_2$, ppb	0.00144	0.00144	0.00144	0.00481	0.00481	0.00481	0.0144	0.0144	0.0144
HNO_3, ppb	0.1	0.1	0.1	0.1	0.1	0.1	0.1	0.1	0.1
$H^{15}NO_3$, ppb	0.00036	0.00036	0.00036	0.00036	0.00036	0.00036	0.00036	0.00036	0.00036
CH_4, ppb	1800	1800	1800	1800	1800	1800	1800	1800	1800
CO, ppb	200	200	200	200	200	200	200	200	200
SO_2, ppb	5	5	5	5	5	5	5	5	5
O_3, ppb	10	10	10	10	10	10	10	10	10
H_2, ppb	500	500	500	500	500	500	500	500	500
H_2O_2, ppb	2	2	2	2	2	2	2	2	2
ETH, ppb	0.79	2.607	7.9	0.79	2.607	7.9	0.79	2.607	7.9
HC3, ppb	0.6575	2.16975	6.575	0.6575	2.16975	6.575	0.6575	2.16975	6.575
HC5, ppb	0.295	0.9735	2.95	0.295	0.9735	2.95	0.295	0.9735	2.95
HC8, ppb	0.13	0.429	1.3	0.13	0.429	1.3	0.13	0.429	1.3
ETE, ppb	0.3	0.99	3	0.3	0.99	3	0.3	0.99	3
OLT, ppb	0.1	0.33	1	0.1	0.33	1	0.1	0.33	1
OLI, ppb	0	0	0	0	0	0	0	0	0
ISO, ppb	0.12	0.396	1.2	0.12	0.396	1.2	0.12	0.396	1.2
TOL, ppb	0.2667	0.88011	2.667	0.2667	0.88011	2.667	0.2667	0.88011	2.667

C.4a continued

XYL, ppb	0.0375	0.12375	0.375	0.0375	0.12375	0.375	0.0375	0.12375	0.375
CSL, ppb	0	0	0	0	0	0	0	0	0
HCHO, ppb	0.1	0.33	1	0.1	0.33	1	0.1	0.33	1
ALD, ppb	0.05	0.165	0.5	0.05	0.165	0.5	0.05	0.165	0.5
O_2, %	20.9	20.9	20.9	20.9	20.9	20.9	20.9	20.9	20.9
N_2, %	77.4394	77.4394	77.4394	77.4394	77.4394	77.4394	77.4394	77.4394	77.4394
^{15}NN, %	0.5596	0.5596	0.5596	0.5596	0.5596	0.5596	0.5596	0.5596	0.5596
$^{15}N_2$, %	0.0010	0.0010	0.0010	0.0010	0.0010	0.0010	0.0010	0.0010	0.0010
	Urban								
Case	10	11	12	13	14	15	16	17	18
H_2O, %	1	1	1	1	1	1	1	1	1
NO, ppb	8	8	8	26.4	26.4	26.4	80	80	80
^{15}NO, ppb	2.880E-02	2.880E-02	2.880E-02	9.504E-02	9.504E-02	9.504E-02	2.880E-01	2.880E-01	2.880E-01
NO_2, ppb	2	2	2	6.6	6.6	6.6	20	20	20
$^{15}NO_2$, ppb	0.0072	0.0072	0.0072	0.02376	0.02376	0.02376	0.072	0.072	0.072
HNO_3, ppb	0.1	0.1	0.1	0.1	0.1	0.1	0.1	0.1	0.1
$H^{15}NO_3$, ppb	0.00036	0.00036	0.00036	0.00036	0.00036	0.00036	0.00036	0.00036	0.00036
CH_4, ppb	3000	3000	3000	3000	3000	3000	3000	3000	3000
CO, ppb	1000	1000	1000	1000	1000	1000	1000	1000	1000
SO_2, ppb	30	30	30	30	30	30	30	30	30
O_3, ppb	10	10	10	10	10	10	10	10	10
H_2, ppb	500	500	500	500	500	500	500	500	500
H_2O_2, ppb	2	2	2	2	2	2	2	2	2
ETH, ppb	2.75	9.075	27.5	2.75	9.075	27.5	2.75	9.075	27.5

C.4a continued

HC3, ppb	4.842	15.9786	48.42	4.842	15.9786	48.42	4.842	15.9786	48.42
HC5, ppb	3.043	10.0419	30.43	3.043	10.0419	30.43	3.043	10.0419	30.43
HC8, ppb	2.223	7.3359	22.23	2.223	7.3359	22.23	2.223	7.3359	22.23
ETE, ppb	3.5	11.55	35	3.5	11.55	35	3.5	11.55	35
OLT, ppb	2.667	8.8011	26.67	2.667	8.8011	26.67	2.667	8.8011	26.67
OLI, ppb	1.25	4.125	12.5	1.25	4.125	12.5	1.25	4.125	12.5
ISO, ppb	0	0	0	0	0	0	0	0	0
TOL, ppb	1.81	5.973	18.1	1.81	5.973	18.1	1.81	5.973	18.1
XYL, ppb	0.625	2.0625	6.25	0.625	2.0625	6.25	0.625	2.0625	6.25
CSL, ppb	0.333	1.0989	3.33	0.333	1.0989	3.33	0.333	1.0989	3.33
HCHO, ppb	2.5	8.25	25	2.5	8.25	25	2.5	8.25	25
ALD, ppb	1.25	4.125	12.5	1.25	4.125	12.5	1.25	4.125	12.5
O_2, %	20.9	20.9	20.9	20.9	20.9	20.9	20.9	20.9	20.9
N_2, %	77.4394	77.4394	77.4394	77.4394	77.4394	77.4394	77.4394	77.4394	77.4394
^{15}NN, %	0.5596	0.5596	0.5596	0.5596	0.5596	0.5596	0.5596	0.5596	0.5596
$^{15}N_2$, %	0.0010	0.0010	0.0010	0.0010	0.0010	0.0010	0.0010	0.0010	0.0010

Table C.4b: Meteorological conditions for inter-comparison cases 1-18

Meteorological conditions	Values
Start Date/Time	June 21, 0600 LT
End Date/Time	June 23, 0600 LT
Latitude	40 °N
Longitude	0
Elevation, km	0
Temperature, K	298
Pressure, atm	1

Table C.5a: Initial concentrations and emission rates for inter-comparison cases 19-20

	Case 19		Case 20	
Compound	Initial Concentrations, ppb	Emissions, ppt/min	Initial Concentrations, ppb	Emissions, ppt/min
H_2O	1 x 10^7	-	1 x 10^7	-
O_3	50	-	30	-
NO	0.2	2.6	0.02	0.26
^{15}NO	7.20E-04	9.36E-03	7.20E-05	9.36E-04
NO_2	0.5	-	0.05	-
$^{15}NO_2$	0.0018	-	0.00018	-
HNO_3	0.1	-	0.01	-
$H^{15}NO_3$	0.00036	-	0.000036	-
CO	200	5.7	104	0.57
CH_4	1700	-	1700	-
H_2	500	-	500	-
H_2O_2	2	-	0.2	-
SO_2	-	0.52	-	0.052
ETH	-	0.24	-	0.024
HC3	-	2.6	-	0.26
HC5	-	0.76	-	0.076
HC8	-	0.45	-	0.045
ETE	-	0.46	-	0.046
OLI	-	0.19	-	0.019
OLT	-	0.22	-	0.022
TOL	-	0.57	-	0.057
XYL	-	0.52	-	0.052
HCHO	1	0.14	0.1	0.014
ALD	-	0.036	-	0.0036
KET	-	0.32	-	0.032
O_2	2.09E+08	-	2.09E+08	-
N_2	7.74394109E+08	-	7.74394109E+08	-
^{15}NN	5.59578240E+06	-	5.59578240E+06	-
$^{15}N_2$	1.01088000E+04	-	1.01088000E+04	-

Table C.5b: Meteorological conditions for inter-comparison cases 19-20

Meteorological conditions	Values
Start Date/Time	June 21, 0600 LT
End Date/Time	June 26, 0600 LT
Latitude	40 °N
Longitude	0
Elevation, km	0
Temperature, K	298
Pressure, atm	1

Table 0.1: Fractionation factors of Leighton cycle, NO_x isotope exchange, OH production of HNO_3, and KIE effects of NO3 reacting with hydrocarbons.

Reaction No.	Reaction	α
R1	NO_2 --> O^3P + NO	1
R1a	$^{15}NO_2$ --> O^3P + ^{15}NO	1.0042
R39	HO + NO_2 --> HNO_3	1
R39a	HO + $^{15}NO_2$ --> $H^{15}NO_3$	1.04
R48	O_3 + NO --> NO_2 + O_2	1
R48a	O_3 + ^{15}NO --> $^{15}NO_2$ + O_2	0.9933
R91	HCHO + NO_3 --> HO_2 + HNO_3 + CO	1
R91a	HCHO + $^{15}NO_3$ --> HO_2 + $H^{15}NO_3$ + CO	0.9974
R92	ALD + NO_3 --> ACO_3 + HNO_3	1
R92a	ALD + $^{15}NO_3$ --> ACO_3 + $H^{15}NO_3$	0.9967
R93	GLY + NO_3 --> HNO_3 + HO_2 + 2 CO	1
R93a	GLY + $^{15}NO_3$ --> $H^{15}NO_3$ + HO_2 + 2 CO	0.9962
R94	MGLY + NO_3 --> HNO_3 + ACO_3 + CO	1
R94a	MGLY + $^{15}NO_3$ --> $H^{15}NO_3$ + ACO_3 + CO	0.9957
R95	MACR + NO_3 --> 0.20 TCO_3 + 0.20 HNO_3 + 0.80 OLNN + 0.80 CO	1
R95a	MACR + $^{15}NO_3$ --> 0.20 TCO_3 + 0.20 $H^{15}NO_3$ + 0.80 ^{15}OLNN + 0.80 CO	0.9958
R96	DCB + NO_3 --> 0.50 TCO_3 + 0.50 HO_2 + 0.50 XO_2 + 0.25 GLY + 0.25 ALD + 0.03 KET + 0.25 MGLY + 0.5 HNO_3 + 0.5 NO_2	1
R96a	DCB + $^{15}NO_3$ --> 0.50 TCO_3 + 0.50 HO_2 + 0.50 XO_2 + 0.25 GLY + 0.25 ALD + 0.03 KET + 0.25 MGLY + 0.5 $H^{15}NO_3$ + 0.5 $^{15}NO_2$	0.9954
R97	CSL + NO_3 --> HNO_3 + PHO	1
R97a	CSL + $^{15}NO_3$ --> $H^{15}NO_3$ + PHO	0.9949
R238	NO + $^{15}NO_2$ --> ^{15}NO + NO_2	1
R238a	^{15}NO + NO_2 --> NO + $^{15}NO_2$	0.9771

Table 0.2: Fractionation factors of Leighton cycle, NO_x isotope exchange, OH production of HNO_3, and N_2O_5 heterogeneous reactions.

Reaction No.	Reaction	α
R1	NO_2 --> O^3P + NO	1
R1a	$^{15}NO_2$ --> O^3P + ^{15}NO	1.0042
R39	HO + NO_2 --> HNO_3	1
R39a	HO + $^{15}NO_2$ --> $H^{15}NO_3$	1.04
R48	O_3 + NO --> NO_2 + O_2	1
R48a	O_3 + ^{15}NO --> $^{15}NO_2$ + O_2	0.9933
R53	NO_3 + NO_2 --> N_2O_5	1
R53a	NO_3 + $^{15}NO_2$ --> $^{15}NNO_5$	1.0266
R53b	$^{15}NO_3$ + NO_2 --> $^{15}NNO_5$	1.0309
R53c	$^{15}NO_3$ + $^{15}NO_2$ --> $^{15}N_2O_5$	1.057
R54	N_2O_5 --> NO_2 + NO_3	1
R54a	$^{15}NNO_5$ --> $^{15}NO_2$ + NO_3	0.5
R54b	$^{15}NNO_5$ --> NO_2 + $^{15}NO_3$	0.5
R54c	$^{15}N_2O_5$ --> $^{15}NO_2$ + $^{15}NO_3$	1
R238	NO + $^{15}NO_2$ --> ^{15}NO + NO_2	1
R238a	^{15}NO + NO_2 --> NO + $^{15}NO_2$	0.9771
R239	N_2O_5 --> HNO_3 + HNO_3	1
R239a	$^{15}NNO_5$ --> $^{15}HNO_3$ + HNO_3	0.9954
R239b	$^{15}N_2O_5$ --> $^{15}HNO_3$ + $^{15}HNO_3$	0.9909

Table 0.3: Initial concentrations and emission rates for test cases under different environments

	Urban		Rural		Forest		Marine	
Compound	Initial Concentrations ppb	Emissions ppt/min	Initial Concentrations ppb	Emissions ppt/min	Initial Concentrations ppb	Emissions ppt/min	Initial Concentrations ppb	Emissions ppt/min
H_2O	1×10^7	-	1×10^7	-	1×10^7	-	1×10^7	-
O_3	300	-	50	-	10	-	10	-
NO	90	156	4.9	3.9	0.054	0.156	0.027	0.208
^{15}NO	0.324	0.5616	0.01764	0.01404	1.944E-04	0.0005616	9.720E-05	0.0007488
NO_2	90	-	2.1	-	0.006	-	0.003	-
$^{15}NO_2$	0.324	-	0.00756	-	2.160E-05	-	1.080E-05	-
HNO_3	20	-	6	-	0.29	-	0.145	-
$H^{15}NO_3$	0.072	-	0.0216	-	1.044E-03	-	5.22E-04	-
PAN	20	-	3	-	0.05	-	0.025	-
^{15}PAN	0.072	-	0.0108	-	1.800E-04	-	9.00E-05	-
CO	1000	5.7	200	5.7	207	5.7	-	5.7
CH_4	3000	-	1800	-	1657	-	-	-
H_2	500	-	500	-	500	-	500	-
H_2O_2	2	-	2	-	2	-	2	-
SO_2	30	0.52	5	0.52	-	0.52	-	0.52
ETH	30.730	4.8	2.557	0.36	0.98	0.216	1.304	0.144

Table C.8 continued

HC3	53.777	52	1.147	3.9	0.84	2.34	1.306	1.56
HC5	33.803	15.2	1.368	1.14	0.344	0.684	0.199	0.456
HC8	24.694	9	0.259	0.675	0.1	0.405	0.025	0.27
ETE	17.986	9.2	0.100	0.69	0.97	0.414	1.469	0.276
OLI	3.063	3.8	-	0.285	-	0.171	-	0.114
OLT	6.535	4.4	0.066	0.33	0.39	0.198	0.404	0.132
ISO	-	-	0.082	-	2.040	-	-	-
TOL	17.667	11.4	0.372	0.855	0.93	0.513	0.545	0.342
XYL	15.802	10.4	0.195	0.78	0.090	0.468	0.140	0.312
HCHO	22.610	2.8	1.748	0.21	-	0.126	-	0.084
ALD	25.694	0.72	0.368	0.054	-	0.0324	-	0.0216
KET	-	6.4	-	0.48	-	0.288	-	0.192
API	-	-	-	-	0.130	-	-	-
O_2	2.09E+08	-	2.09E+08	-	2.09E+08	-	2.09E+08	-
N_2	7.7439E+08	-	7.7439E+08	-	7.7439E+08	-	7.7439E+08	-
^{15}NN	5.5958E+06	-	5.5958E+06	-	5.5958E+06	-	5.5958E+06	-
$^{15}N_2$	1.0109E+04	-	1.0109E+04	-	1.0109E+04	-	1.0109E+04	-

C.2. Detail information for case studies inputs

The completed i_NRACM was tested with different cases with various initial concentrations and emission rates, which stands for the urban, rural, forest, and marine conditions. Stockwell (1997) provided 18 test cases without emission (9 for urban condition, 9 for rural condition), and 2 test cases with emission (1 for polluted atmosphere, 1 for clean atmosphere), while the concentration of chemicals in these test cases does not agree with atmospheric observations (Altshuller, 1989; Baugues, 1986; Greenberg & Zimmerman, 1984; Logan, 1989; National Research Council, 1992; Torres & Buchan, 1988; Zimmerman et al., 1988).

First, Stockwell used the exact same initial ozone concentration of 10 ppb in all of the 18 test cases without emission, which is severely underestimated for both urban (100-400 ppb) and rural (50-120 ppb) conditions (Cleveland et al., 1977; Gregory et al., 1988; Janach, 1989; Kirchhoff, 1988; LeFohn & Pinkerton, 1988; Logan, 1989). Even for the so-called polluted atmosphere case, the initial ozone concentration was set to 50 ppb, which is hard to recognize as "polluted". The constant ozone concentration among urban and rural in Stockwell's cases also causes the NO/NO_x ratio to be not reasonable. According to Toores and Buchan (1988), with higher ozone concentration during the day, NO/NO_x becomes lower. This agrees with R48 ($NO + O_3 \rightarrow NO_2 + O_2$), with higher ozone concentration, more NO is consumed, thus more NO_2 is produced. Thus, the NO/NO_x ratio in rural conditions will be higher than in urban conditions, which is opposite to Stockwell's cases. Second, Stockwell's cases considered NO_x to be the only compound of NO_y in all the test cases. In fact, as the distance between the sampling site and major anthropogenic sources increases, the conversion of NO_x to HNO_3 and PAN increases. As a result, NO_x account for 30-60% of NO_y at rural sites, and 15% at forest sites and marine sites (Carroll et al., 1992; Fahey et al., 1986; National Research Council, 1992; Parrish et al., 1986; Williams et al., 1987). Third, for Stockwell's 9 urban cases and 9 rural cases, the emission rates of all chemical compounds are set to zero. Without the emission of NO and VOC, the simulated NO_x and VOC deplete quickly, which decay the NO_x cycle and the conversion to NO_y, as well as ozone concentration (Fig. C.1). Fourth, the NO_x concentration in Stockwell's urban cases, is too low, with the maximum of 100 ppb at the initial state, but quickly deplete to be less than 10 ppb in 6 hours. Baugues (1986) measured NO_x concentration among 30 sites among major cities in the eastern and southern United States in 1984 and 1985. Baugues's measurement shows 17 out of 21 sites in 1984 and 15 out of 19 sites in 1985 with a maximum concentration of NO_x higher than 100 ppb, 10 out of 21 sites in 1984 and 7 out

of 19 sites in 1985 with a maximum concentration of NO_x higher than 200 ppb, which indicate the obvious higher NO_x concentration than Stockwell's cases. For the so-called polluted atmosphere, the initial concentration of NO_x is only 0.7 ppb, with an emission rate of 2.6 ppt/min, the maximum concentration only reaches 2.4 ppb around 6 am at day 2 to day 6, which again cannot stand for "polluted".

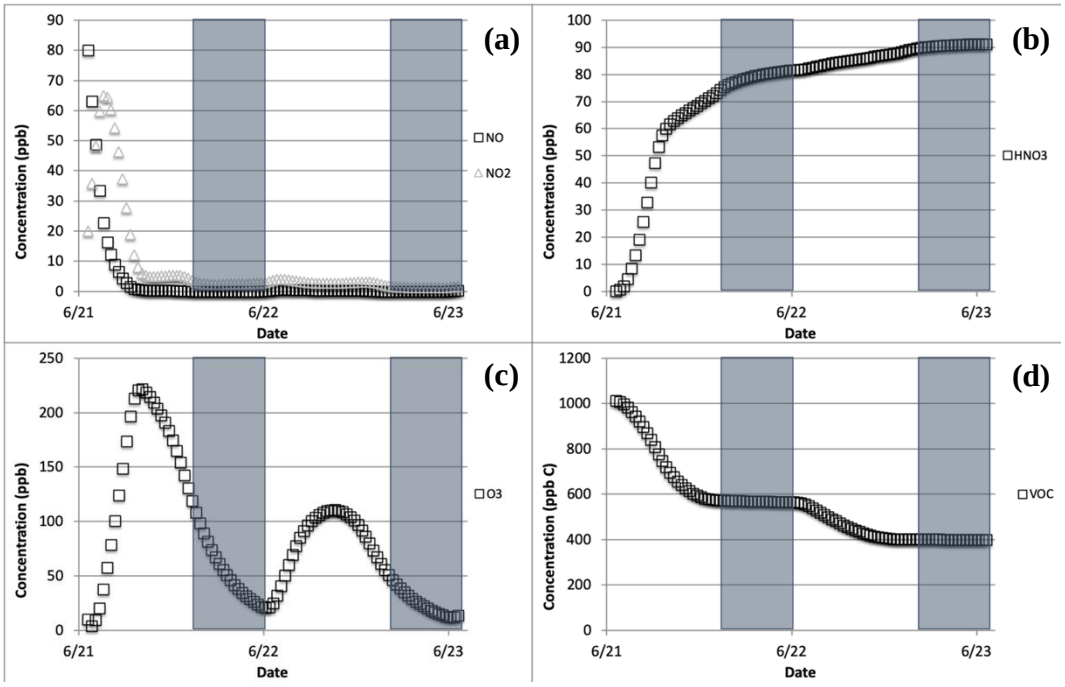

Figure 0.20: The concentrations of NO_x (top left, a), HNO_3 (top right, b), O_3 (bottom left, c), and total VOC (bottom right, d) for Stockwell's urban case with the initial concentration of NO_x at 100 ppb, VOC at 1000 ppb C, simulation starts from Jun 21.

Thus, instead of replicating Stockwell's cases, we set up four conditions that stand for urban, rural, forest, and marine, with the initial concentrations based on various measurements from previous studies. The emission rates of NO and total VOCs were tuned until the simulation results satisfied with these following features: a). The concentration of NO_x changes diurnally and stabilized through time; b). The concentration of O_3 changes diurnally and stabilized through time; c). HNO_3 is produced primarily during daytime; d). VOCs are produced primarily during nighttime (Fig. C.2-5). The molar fraction of each VOC species with respect to the total VOC emission rate was obtained from Stockwell's (1997) emission cases.

C.2.1 The initial concentrations and emission rates under the urban conditions

The simulations under the urban conditions were designed to simulate highly polluted urban environments such as current Asia megacities and early 1980's US cities. The initial concentration of NO_x (Table C.8) was set to 180 ppb, based on the 90th percentile of polluted US cities (Cincinnati, OH, Fort Worth, TX, Memphis, TN, Miami, FL, Cleveland, OH) during summers of 1984 and 1985 (Baugues, 1986), slightly lower than the maximum NO_x concentration (> 200 ppb) at Shenyang, China from Aug 20 to Sept 16, 2017 (Ma et al., 2018). For urban conditions, the NO/NO_x ratio was set to 0.5, and NO_x/NO_y ratio was set to 0.9, and we assumed the concentrations of HNO_3 and PAN are equal since they are minimal NO_y compounds in this case. The initial carbon (C) concentration of total VOC was set to 1000 ppb C, based on the weighted average of the measurements among 30 sites during the summers of 1984 and 1985 (Baugues, 1986). Baugues (1986) also provided the carbon fraction of toluene, xylene, HCHO, acetaldehyde, ethene, alkene other than ethene, and total alkane with respect to total VOC in ppb C. Thus, the initial concentration of toluene, xylene, HCHO, acetaldehyde, ethene was based on their carbon fraction provided by Baugues (1986). The initial concentration of each alkane and alkene species was based on the carbon fraction of their groups, provided by Stockwell et al. (1997). Thus, the initial concentration of total VOC was set to 252 ppb, which matches well with the recent year's measurement at Shenyang, a typical urban area of Northeast China (Ma et al., 2018). To stabilize the concentration of NO_x, the emission rates of NO and total VOCs were set to 9.36 ppb h^{-1} and 7.80 ppb h^{-1}, respectively. The initial concentration of O_3 at 300 ppb, which is closed to the average among five most polluted sites from the measurement among the Northeastern United States in the 1970s (Cleveland et al., 1977), and the maximum value (286 ppb) measured within three main megalopolises in China (Jinjinji, Yangtze River Delta, and Pearl River Delta) from 1997 to 2016 (Wang et al., 2017). During the simulations, the O_3 concentration stabilized, with summertime maximum hourly concentration around 200 ppb, which agrees well with previous studies (National Research Council, 1992).

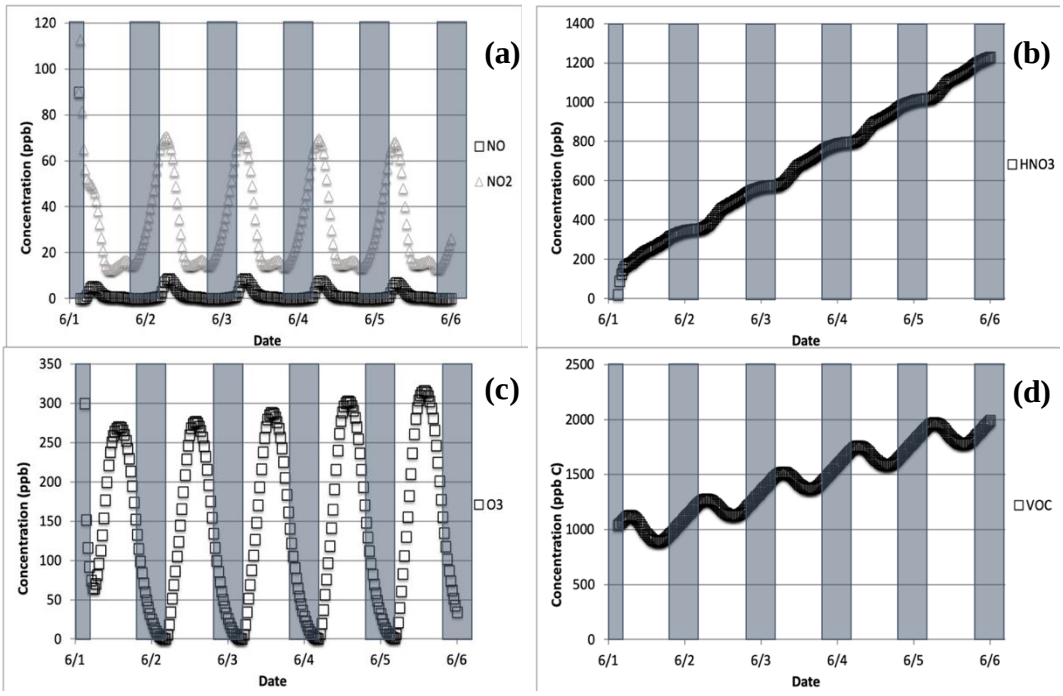

Figure 0.21: The concentrations of NO_x (top left, a), HNO_3 (top right, b), O_3 (bottom left, c), and total VOC (bottom right, d) for urban condition, with initial concentrations and emission rate listed in Table C.8, simulation starts from Jun 1.

C.2.2 The initial concentrations and emission rates under the rural conditions

The simulations under the rural conditions were designed to simulate moderately polluted environments upwind of such current Asia megacities and early 1980's US cities. The initial concentration of NO_x was set to 7 ppb (Table C.8), based on the average of 120 samples collected aloft upwind of six US cities (Dallas-Fort Worth, TX, Tulsa, OK, Birmingham, AL, Atlanta, GA, Philadelphia, PA, New York, NY) during summers of 1985 and 1986 (Altshuller, 1989). The 7 ppb NO_x also matches well with the value measured in Baltimore/Washington airshed in 2011 (He et al., 2013). For rural condition, NO_x/NO_y ratio was set to 0.44, based on the average ratio among previous studies (Carroll et al., 1992; Fahey et al., 1986; National Research Council, 1992; Parrish et al., 1986; Williams et al., 1987), NO/NO_x ratio was set to 0.7. According to Logan (1989), the ratio between NO_x and PAN has a median value of around 2.5. Thus, the initial concentrations of NO, NO_2, HNO_3, and PAN are 4.9 ppb, 2.1 ppb, 6 ppb, and 3 ppb, respectively (Table C.8). The initial concentrations of each VOC species were based on the weighted average of the measurements, upwind of the six US cities. The 8.3 ppb initial concentration of total OC matches well with the recent year measurement in the rural area of the Midwest, US (Sjostedt et al., 2011).

The initial concentration of O_3 was set to 50 ppb, based on the average summertime O_3 concentration among rural areas (Cooper et al., 2012, Janach, 1989; Logan, 1989). To stabilize the concentration of NO_x and O_3, the emission rates of NO and total VOCs were set to 0.24 ppb $h^{-1}$and 0.59 ppb h^{-1}, respectively.

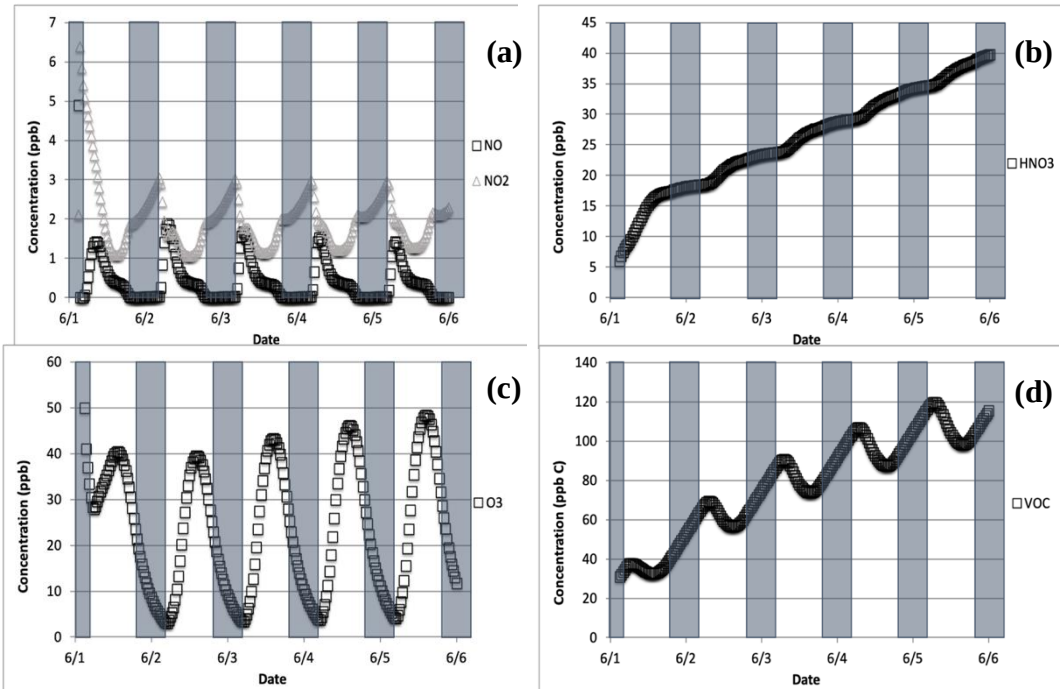

Figure 0.22: The concentrations of NO_x (top left, a), HNO_3 (top right, b), O_3 (bottom left, c), and total VOC (bottom right, d) for rural condition, with initial concentrations and emission rate listed in Table C.8, simulation starts from Jun 1.

C.2.3 The initial concentrations and emission rates under the forest conditions

The simulations under the forest conditions were designed to simulate low polluted environments (Table C.8), with high emissions of biogenic VOCs such as isoprene. The initial concentration of NO_x was set to 0.06 ppb, which is the minimum concentration at the central basin of Amazon tropical forest (Torres and Buchan, 1988). Typically, at the remote sites (forest and marine condition), the ratio of NO_x/NO_y is between 0.1 and 0.2, HNO_3/NO_x is less than 5, and PAN/NO_x is less than 1 (Carroll et al., 1992). To satisfy all three conditions, the initial concentration of HNO_3 and PAN were set to 0.29 ppb and 0.05 ppb, respectively. NO/NO_x ratio was set to 0.9. Thus, NO and NO_2 equal to 0.054 ppb and 0.006 ppb, respectively. The initial concentrations of each VOC species were based on the median concentration of 81 samples in

Amazon (Zimmerman et al., 1988). The 6.7 ppb initial concentration of total VOC matches well with the recent year's measurement in Amazon (Fuentes et al., 2016). The initial concentration of O_3 was set to 10 ppb, which is closed to the average hourly concentration during the summertime in Amazonia (Fuentes et al., 2016, Kirchhoff, 1988). To stabilize the concentration of NO_x and O_3, the emission rates of NO and total VOCs were set to 9.4 ppt h^{-1} and 0.35 ppb h^{-1}, respectively.

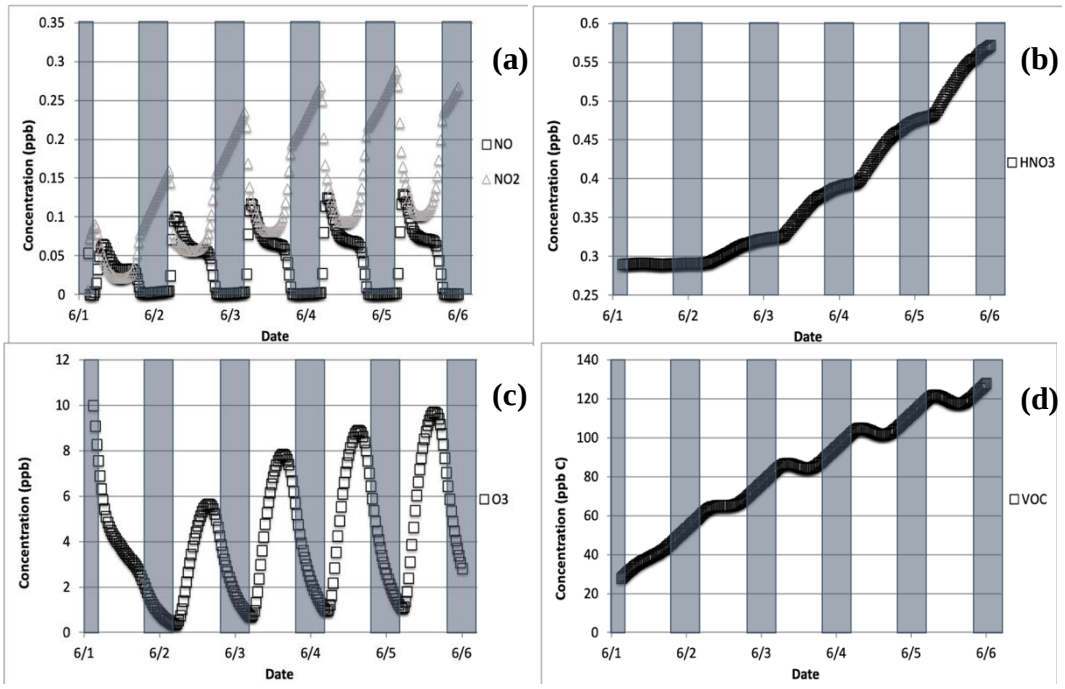

Figure 0.23: The concentrations of NO_x (top left, a), HNO_3 (top right, b), O_3 (bottom left, c), and total VOC (bottom right, d) for forest condition, with initial concentrations and emission rate listed in Table C.8, simulation starts from Jun 1.

C.2.4 The initial concentrations and emission rates under the marine conditions

The simulations under the marine conditions were designed to simulate remote, clean oceanic environments. The initial concentration of NO_x was set to 0.03 ppb (Table C.8), which is the medium value of 28,974 data points, measured simultaneously at Mauna Loa, Hawaii, from May 1 to June 4, 1988 (Carroll et al., 1992), as well as at Cape Norman, Canada, northern Atlantic coastal site, from February to April 1996 (Yang et al., 2004). Typically, at the remote sites (forest and marine condition), the ratio of NO_x/NO_y is between 0.1 and 0.2, HNO_3/NO_x is less than 5, and PAN/NO_x is less than 1 (Carroll et al., 1992). To satisfy all three conditions, the initial concentration of HNO_3 and PAN were set to 0.145 ppb and 0.025 ppb, respectively. NO/NO_x ratio

was set to 0.9. Thus, NO and NO_2 equal to 0.027 ppb and 0.003 ppb, respectively. The initial concentrations of each VOC species were based on the median values between the sample collected by two cruises over the tropical Pacific Ocean, during December 1982, and July 1982, respectively (Greenberg and Zimmerman, 1984). The 5.4 ppb initial concentration of total VOC matches well with the recent year measurement over the western North Pacific and eastern Indian Ocean (Saito et al., 2000). The initial concentration of O_3 was set to 10 ppb, which the average summertime concentration among maritime sites in both the north and south hemispheres (Janach, 1989). To stabilize the concentration of NO_x and O_3, the emission rates of NO and total VOCs were set to 12.48 ppt h^{-1} and 0.234 ppb h^{-1}, respectively

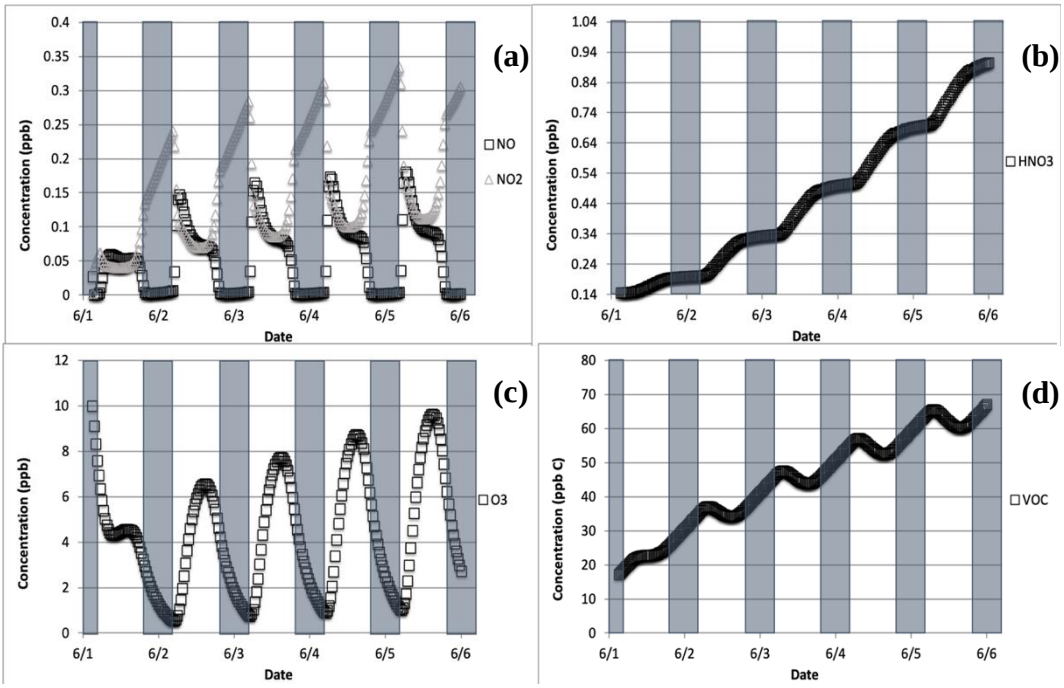

Figure 0.24: The concentrations of NO_x (top left, a), HNO_3 (top right, b), O_3 (bottom left, c), and total VOC (bottom right, d) for marine condition, with initial concentrations and emission rate listed in Table C.8, simulation starts from Jun 1.

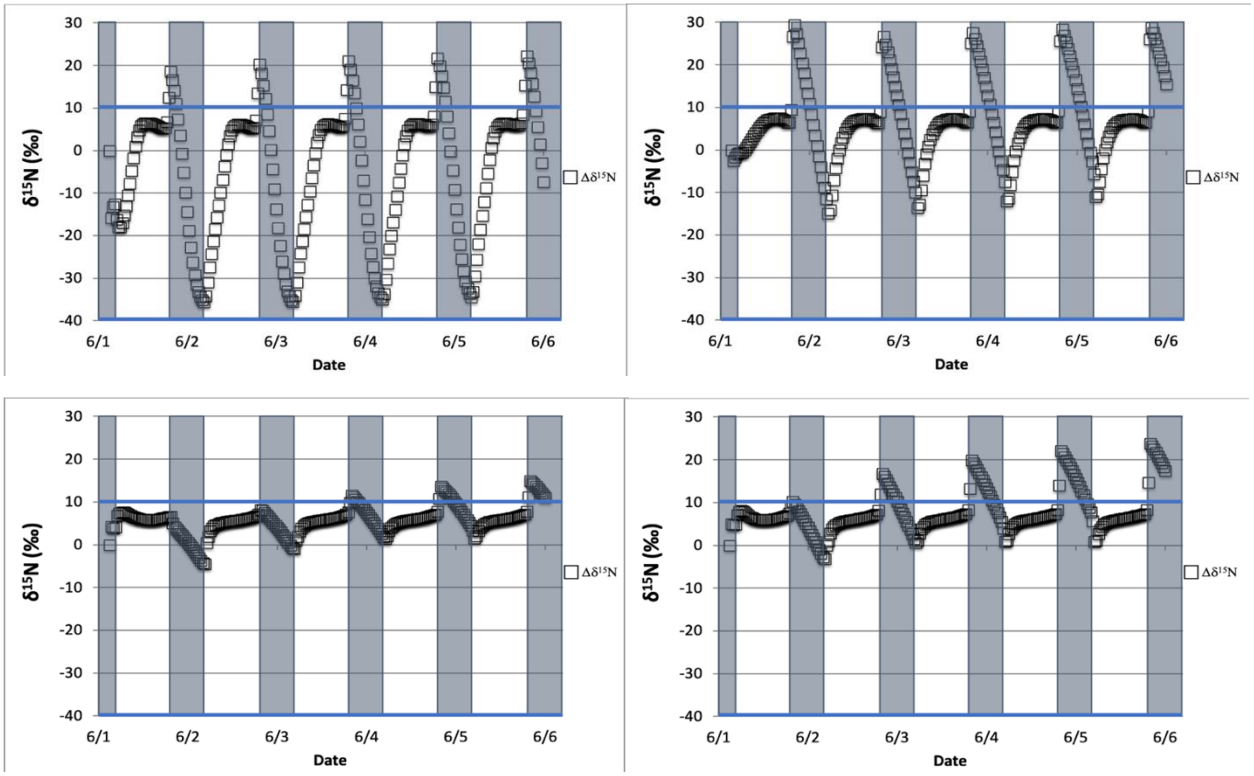

Figure 0.25: The difference between $\delta^{15}N(NO)$ and $\delta^{15}N(NO_2)$ for urban (top left, a), rural (top right, b), forest (bottom left, c), and marine (bottom right, d) conditions, with initial concentrations and emission rate listed in Table C.8, simulation starts from Jun 1.

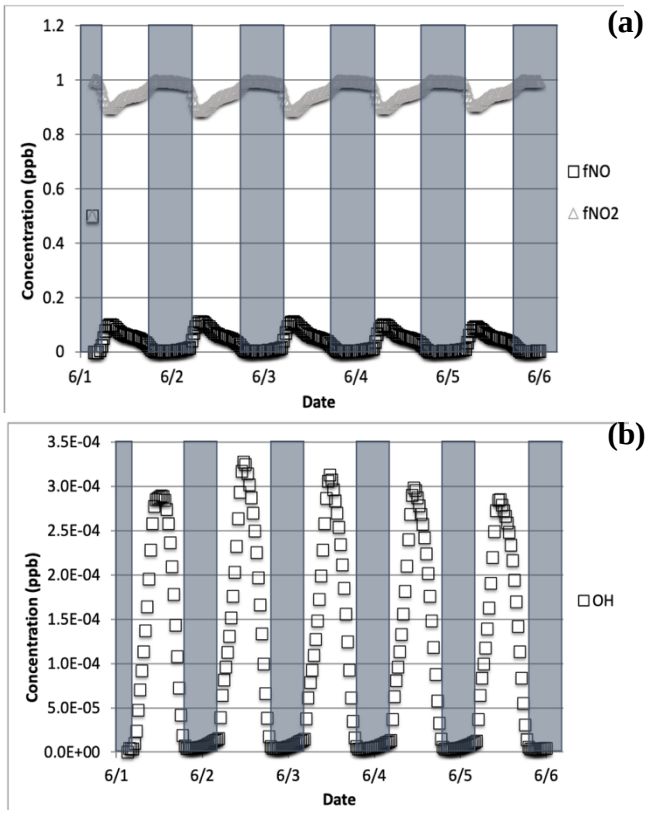

Figure 0.26: The fraction of NO and NO_2 relative to total NO_x (top, a), and the concentration of OH (bottom, b) for urban condition, with initial concentrations and emission rate listed in Table C.8, simulation starts from Jun 1.

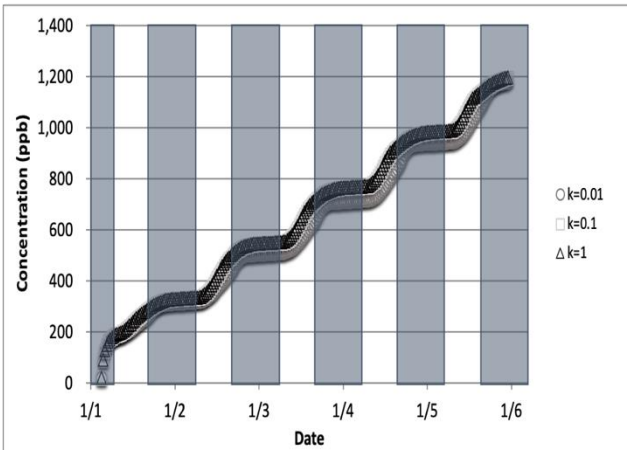

Figure 0.27: The difference in HNO_3 concentrations when the isotopic effect during N_2O_5 heterogeneous reactions is included and when it is excluded, for the simulation of $k_{N2O5} = 0.1$, relative to 0.01 (□) and 1.0 (o). The 5-day simulation starts on Jan 1, under the urban condition with initial concentrations and emission rate listed in Table C.8

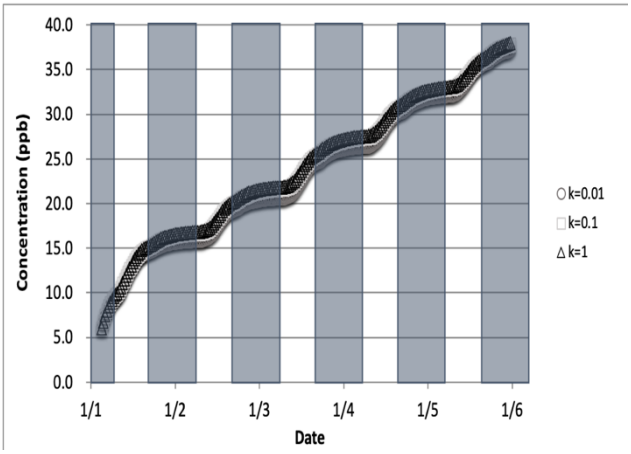

Figure 0.28: The difference in HNO_3 concentrations when the isotopic effect during N_2O_5 heterogeneous reactions is included and when it is excluded, for the simulation of $k_{N2O5} = 0.1$, relative to 0.01 (☐) and 1.0 (o). The 5-day simulation starts for Jan 1, under the rural condition with initial concentrations and emission rate listed in Table C.8

APPENDIX D. SUPPLEMENTARY DATA CHAPTER 5

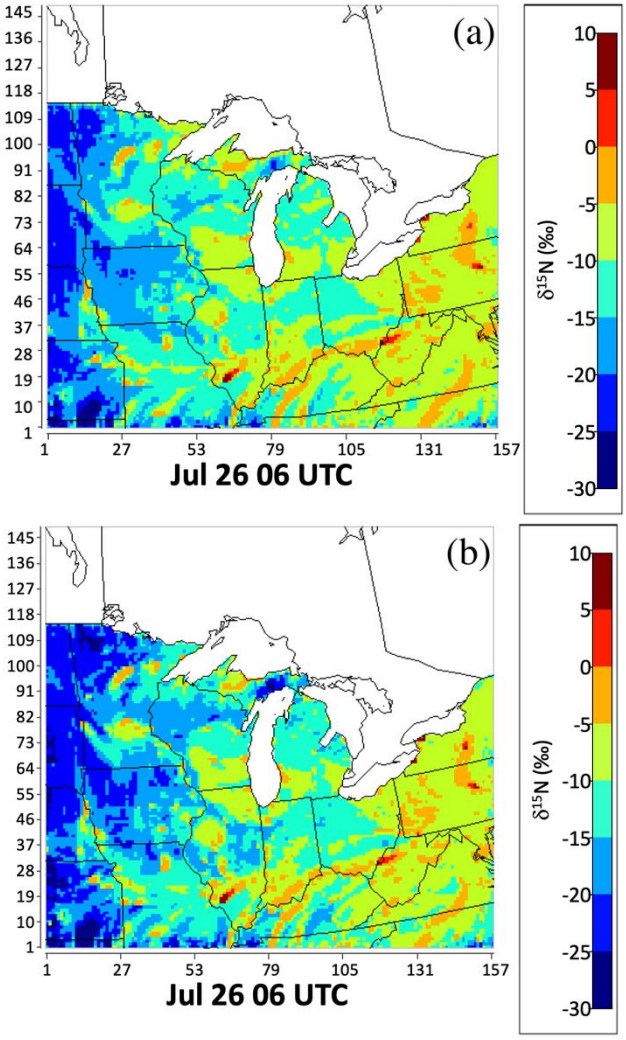

Figure 0.29: The $\delta^{15}N$ values of atmospheric NO_x based on NEI-2002 and 2016 meteorology (a: "no chemistry" scenario), based on NEI-2002, 2016 meteorology, and with the magnified dry and wet deposition rate (b: "fake chemistry" scenario), at 06 UTC on July 26, are presented by color in each grid. The warmer the color, the higher $\delta^{15}N$ values of atmospheric NO_x.

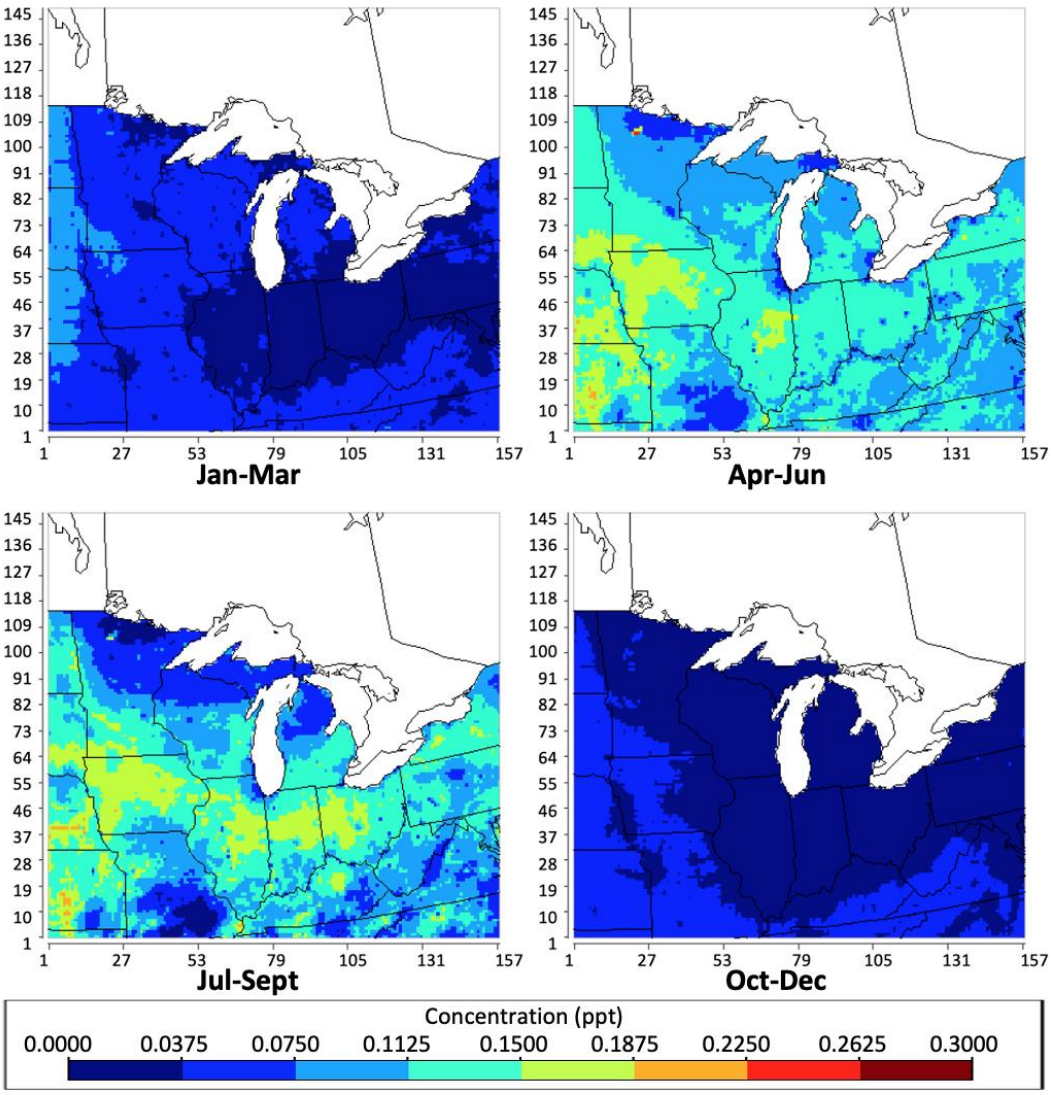

Figure 0.30: The geographical distribution of the concentration of atmospheric OH in each season (Winter: Jan-Mar; Spring: Apr-Jun; Summer: Jul-Sep; Fall: Oct-Dec) in ppt throughout the Midwest simulated by CMAQ, based on NEI-2002, 2016 meteorology, and CB.

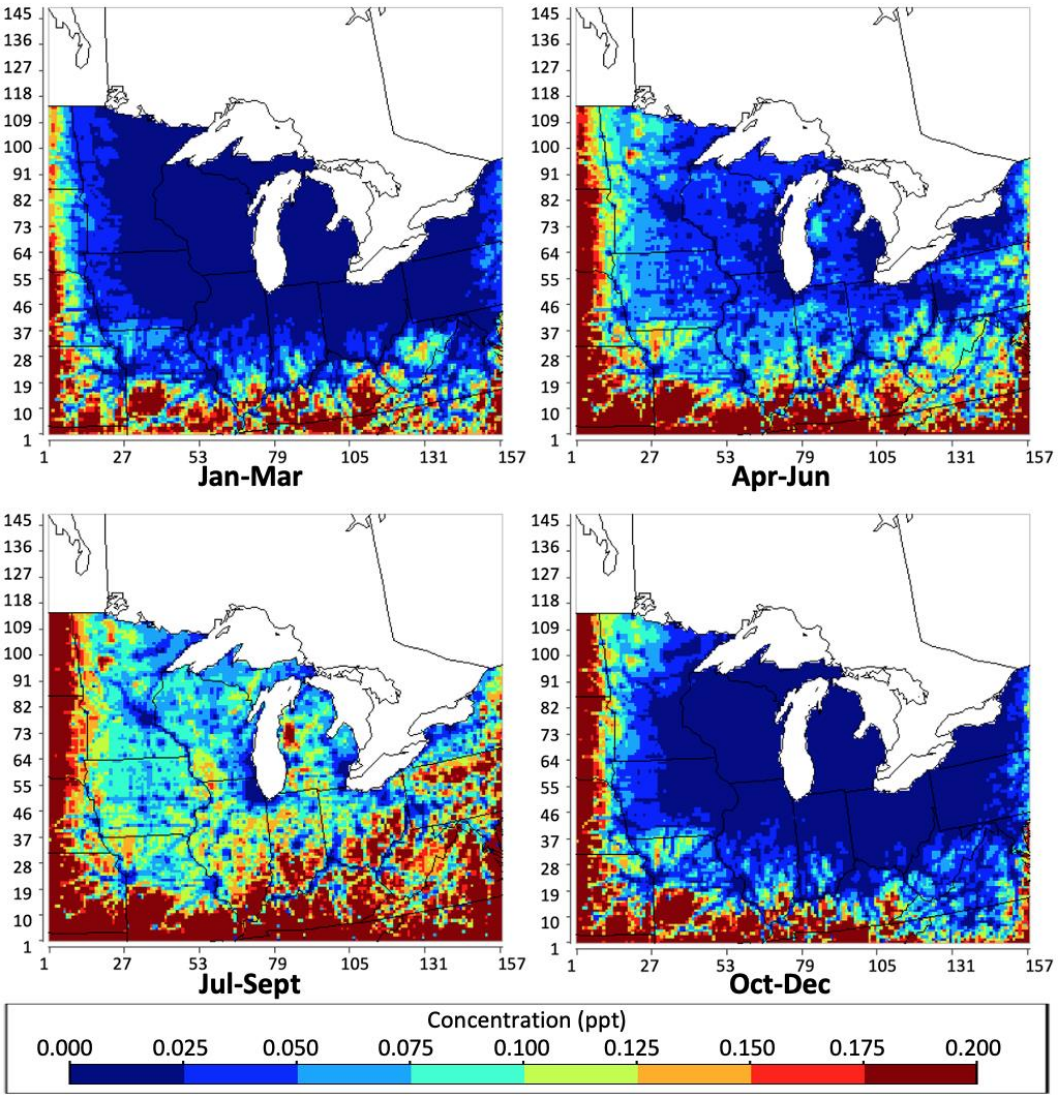

Figure 0.31: The geographical distribution of the concentration of atmospheric NO_3 in each season (Winter: Jan-Mar; Spring: Apr-Jun; Summer: Jul-Sep; Fall: Oct-Dec) in ppt throughout the Midwest simulated by CMAQ, based on NEI-2002, 2016 meteorology, and CB.

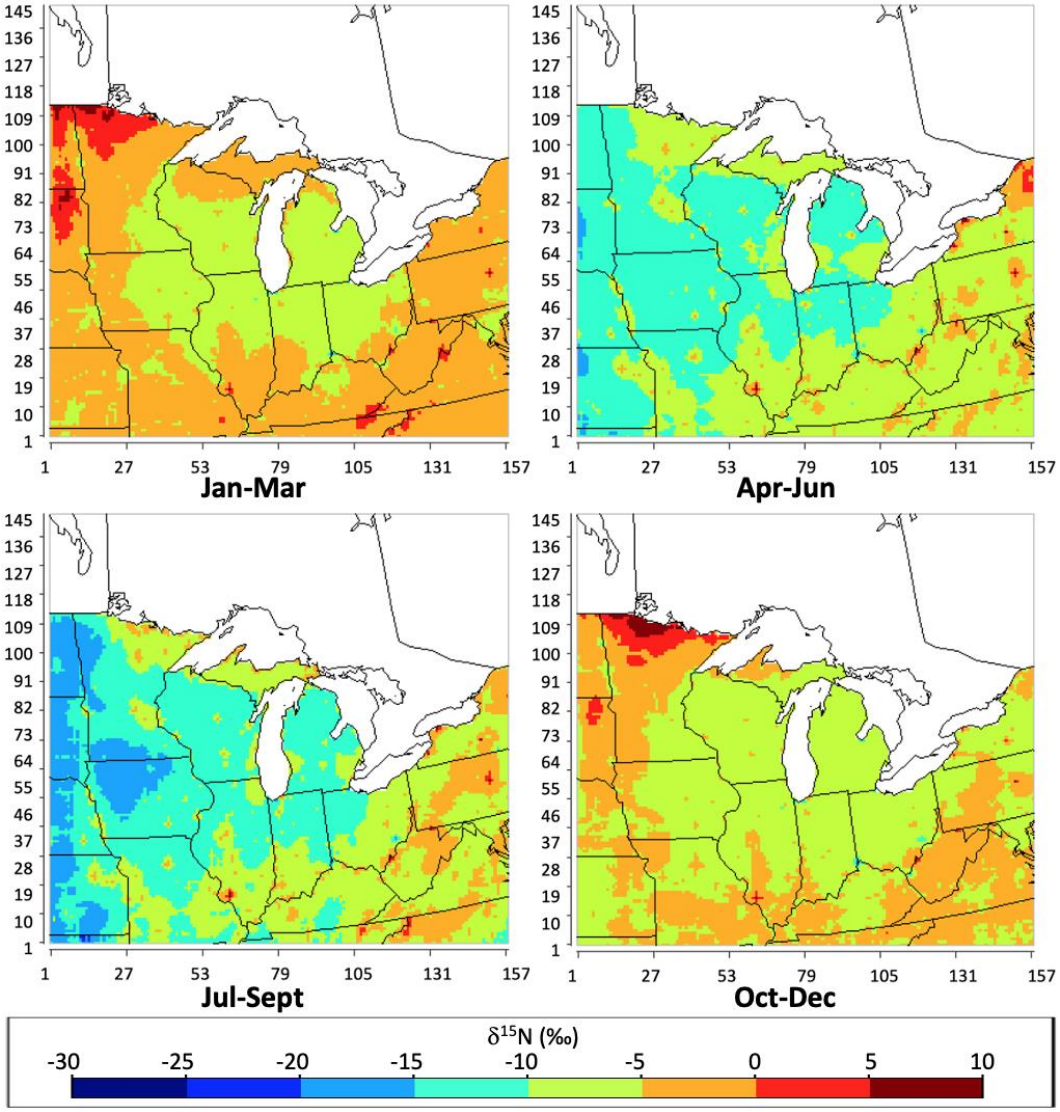

Figure 0.32: Figure S4: The difference between the $\delta^{15}N$ (‰) value of atmospheric NO_x under the "with chemistry" scenario and "no chemistry" scenario ($\Delta\delta^{15}N_{chem}$) during each season (Winter: Jan-Mar; Spring: Apr-Jun; Summer: Jul-Sep; Fall: Oct-Dec) in per mil (‰) throughout the Midwest simulated by CMAQ, based on NEI-2002, 2016 meteorology, and RACM.

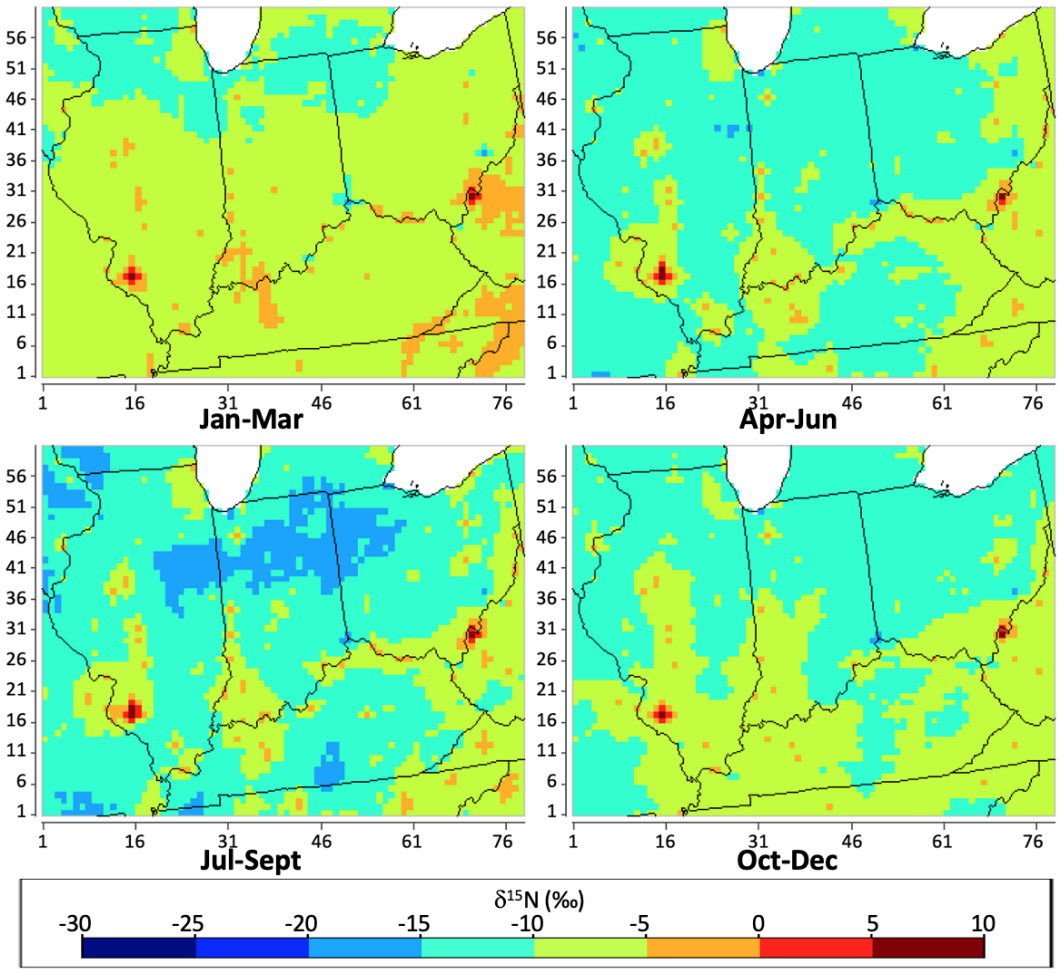

Figure 0.33: The geographical distribution of the $\delta^{15}N$ value the nested-domain simulation of atmospheric NO_x in each season (Winter: Jan-Mar; Spring: Apr-Jun; Summer: Jul-Sep; Fall: Oct-Dec) in per mil (‰) within IN, IL, OH, and KY, based on 2016 meteorology and CB.

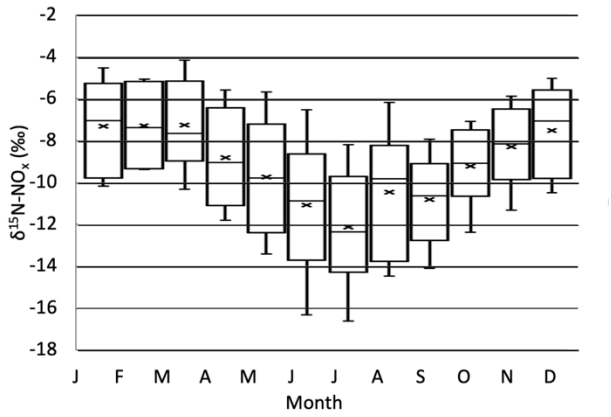

Figure 0.34: The CMAQ predicted $\delta^{15}N$ value of atmospheric NO_x at NADP sites within IN, IL, OH, and KY using 2002 meteorology and RACM.

Table 0.4: NADP sites within the states of Indiana, Illinois, Ohio, and Kentucky

Site ID	Site Name	County	State	Latitude	Longitude
IN20	Roush Lake	Huntington	IN	40.8401	-85.4639
IN22	Southwest Purdue Agriculture Center	Knox	IN	38.7408	-87.4855
IN34	Indiana Dunes National Lakeshore	Porter	IN	41.6318	-87.0881
IN41	Agronomy Center for Research and Extension	Tippecanoe	IN	40.4749	-86.9924
IL46	Alhambra	Madison	IL	38.8689	-89.6219
IL63	Dixon Springs Agricultural Center	Pope	IL	37.4356	-88.6719
OH09	Oxford	Butler	OH	39.5309	-84.7238
KY19	Cannons Lane	Jefferson	KY	38.2288	-85.6545

APPENDIX E. MANUAL FOR INCORPORATING ^{15}N INTO CMAQ SIMULATION

E.1 Incorporating ^{15}N into emission input dataset

As mentioned in Chapter 2, the emission input dataset for the CMAQ simulation was prepared by the EPA SMOKE model, which converts the county-level annual emission based on NEI into hourly emissions and partitions them into the gridded format. The input and output dataset of SMOKE are available from: https://drive.google.com/drive/folders/1caRJVHx_SzY0sSD6DL-TE7rgAoSDqrt-?usp=sharing. The Python programming language was used to incorporate ^{15}N into the emission input dataset.

The $\delta^{15}N$ values for different NO_x emission sources are different. Thus, ^{15}N was incorporated into the emission dataset simulated by SMOKE for each NEI sector sequentially. The demonstration below loads the netCDF file of the emissions from EGUs for each date, calculates the emission rates of $^{15}NO_x$, then generates the ^{15}N incorporated dataset into the new netCDF file.

```
import numpy as np
from netCDF4 import Dataset
import glob
import pandas as pd

def calc_tflag(tflag_old,numSteps,numElements):

    # create a new, empty array, shaped appropriately.
    # this variable will hold the new tflag data we are about to build.
    tflag_new = np.array([]).reshape(0,numElements,2)

    # loop through each time step
    for i in range(numSteps):
        # create a new array with the correct number of elements
        # reshape it to match tflag_new
        q = np.tile(tflag_old[i:(i+1),0],numElements).reshape(1,numElements,2)

        # append the q array to tflag_new
        tflag_new = np.concatenate((tflag_new,q),axis=0)
```

```
    return tflag_new
def update_netcdf(infile,outfile):

    with Dataset(infile) as src, Dataset(outfile, "w", format="NETCDF3_CLASSIC") as dst:
        # change the number of variables accordingly, from 58 to 60
        dimensions = {
            'VAR' : 60,
        }

        # copy old dimensions to new file
        for name, dimension in src.dimensions.items():
            if name in dimensions:
                dst.createDimension(name,dimensions[name])
            else:
                dst.createDimension(name, len(dimension) if not dimension.isunlimited() else None)



        # copy old variables to new file
        for name, variable in src.variables.items():

            x = dst.createVariable(name, variable.datatype, variable.dimensions)

            # copy variable attributes
            x.setncatts({k: variable.getncattr(k) for k in variable.ncattrs()})

            # copy variable data
            if name == 'TFLAG':
                # adjust the tflag variable
                x[:] = calc_tflag(variable, len(src.dimensions['TSTEP']), len(dst.dimensions['VAR']))[:]
            else :
                x[:] = variable[:]


        # copy global attributes
        for a in src.ncattrs():

            # get the value of the attribute from src
```

```
        # change the number of variables accordingly
        if a == 'NVARS':
            v = len(dst.dimensions['VAR'])
        # update the variable list accordingly
        elif a == 'VAR-LIST':
            v = getattr(src,a)
            v = v + 'ZO              ZO2             '
        else:
            v = getattr(src,a)

        # store the attribute and value in dst
        setattr(dst,a,v)


    # Add new variables below
    # Calculate delta
    D = np.full((1,1,299,459),0.0)
    # The delta values for coal fired and natural gas fired EGUs are different, assign the delta value based
on the coordinates of the EGUs
    df=pd.read_csv("matrix.csv")
    for idx,row in df.iterrows():
        c = int(row['COL'])
        r = int(row['ROW'])
        D[0][0][r][c] = row['del15N']
    delta = np.concatenate((D,D,D,D,D,D,D,D,D,D,D,D,D,D,D,D,D,D,D,D,D,D,D,D,D,D,D),axis=0)
    factor = (delta/1000 + 1)*0.0036

    # ZO is a factor times of NO
    no = dst.variables['NO']
    zo = dst.createVariable('ZO',no.datatype,no.dimensions)
    zo.setncattr('long_name','ZO              ')
    zo.setncattr('units','moles/s         ')
    zo.setncattr('var_desc','Model species NO                                                    ')
    zo[:] = factor*no[:]

    # ZO2 is a factor times of NO2
    no2 = dst.variables['NO2']
```

```
        zo2 = dst.createVariable('ZO2',no2.datatype,no2.dimensions)
        zo2.setncattr('long_name','ZO2            ')
        zo2.setncattr('units','moles/s        ')
        zo2.setncattr('var_desc','Model species NO2                                                    ')
        zo2[:] = factor*no2[:]

# save the 15N incorporated emission dataset into the new netCDF file
for infile in glob.glob('*_12US1_cmaq_cb6_2016ff_16j.ncf'):
    outfile = '_'.join(infile.split('_')[0:4]) + '.ncf'
    update_netcdf(infile,outfile)
```

The demonstration below handles the potential missing netCDF files of a certain date for the ^{15}N incorporated emission from each source, by using the data from the nearest previous date to fill out the missing data.

```
import glob
from shutil import copyfile
from datetime import datetime
from datetime import timedelta

# Replace “source” by the code for the source with missing file
f=(glob.glob("emis_mole_source*"))
f=sorted(f)
date=datetime(2016,1,1)

g=[]
for i in range(366):
    g.append('emis_mole_source_'+str(int(date.strftime('%Y%m%d')))+'.ncf')
    date+=timedelta(days=1)

# Use the data from the nearest previous date to fill out the missing data
for i in range(366):
    if g[i] in f:
        pass
    else:
        copyfile(f[i-1], g[i])
        f=(glob.glob("emis_mole_source*"))
        f=sorted(f)
```

```
    date+=timedelta(days=1)
```

After the ^{15}N incorporated emission of each date from each source are ready, the datasets were merged together to produce the CMAQ-ready emission input dataset with the incorporation of ^{15}N, based on the demonstration showing below.

The emission datasets throughout the year 2016 were used for this demonstration, thus, the 8785 hourly timesteps from 00 UTC on Jan 1, 2016 to 00 UTC on Jan 1, 2017 were generated by the following section:

```
from netCDF4 import Dataset
import numpy as np
import glob

sdate=2016001
stime=0
tstep=10000
tflag0=np.array([]).reshape(0,62,2)
for i in range(8785):
    q=np.tile([sdate+i//24%366+int(i//24//366*1000),stime+i%24*tstep],62).reshape(1,62,2)
    tflag0=np.concatenate((tflag0,q),axis=0)
```

The next step is to load the netCDF file of the ^{15}N incorporated emissions from each source, and sort them by date.

```
f1=(glob.glob("emis_mole_afdust*"))
f1=sorted(f1)
f2=(glob.glob("emis_mole_ag*"))
f2=sorted(f2)
f3=(glob.glob("emis_mole_beis*"))
f3=sorted(f3)
f4=(glob.glob("emis_mole_nonpt*"))
f4=sorted(f4)
f5=(glob.glob("emis_mole_nonroad*"))
f5=sorted(f5)
f6=(glob.glob("emis_mole_np_oilgas*"))
f6=sorted(f6)
f7=(glob.glob("emis_mole_onroad*"))
```

```
f7=sorted(f7)
f8=(glob.glob("emis_mole_othafdust*"))
f8=sorted(f8)
f9=(glob.glob("emis_mole_othar*"))
f9=sorted(f9)
f10=(glob.glob("emis_mole_pt_oilgas*"))
f10=sorted(f10)
f11=(glob.glob("emis_mole_ptnonipm*"))
f11=sorted(f11)
f12=(glob.glob("emis_mole_rail*"))
f12=sorted(f12)
f13=(glob.glob("emis_mole_rwc*"))
f13=sorted(f13)
f14=(glob.glob("emis_mole_othptdust*"))
f14=sorted(f14)
```

The netCDF of the ^{15}N incorporated emissions from each source were combined into one netCDF file for each day in a loop

```
for i in range(366):
    date_str=str(int(tflag0[i*24,0,0]))
    date_int=int(tflag0[i*24,0,0])
    dataset=Dataset('emis_mole_all_'+date_str+'.ncf',
                'w',format='NETCDF4_CLASSIC')
```

Inside each loop, create variables for the combined netCDF file for each date, which will be used as the CMAQ-ready emission input dataset. There are 62 chemicals in the emission input dataset for this research, only $^{15}NO_2$ (showing as zo2 in the code) were selected as an example in this demonstration.

```
    tstep=dataset.createDimension('TSTEP', None)
    date_time=dataset.createDimension('DATE-TIME', 2)
    lay=dataset.createDimension('LAY', 1)
    var=dataset.createDimension('VAR', 62)
    row=dataset.createDimension('ROW', 299)
    col=dataset.createDimension('COL', 459)
    tflag=dataset.createVariable('TFLAG', np.int32, ('TSTEP','VAR','DATE-TIME',))
    zo2=dataset.createVariable('ZO2', np.float64, ('TSTEP', 'LAY', 'ROW', 'COL',))
```

Inside each loop, identify the global attributes for the combined netCDF file for each date. Most of the global attributes are consistent with the global attributes of the emission dataset simulated by SMOKE. The start date (dataset.SDATE) of the dataset for each file and the number of chemicals (dataset.NVARS) were updated accordingly.

```
dataset.IOAPI_VERSION="$Id: @(#) ioapi library version 3.1 $                    "
dataset.FTYPE=1
dataset.CDATE=2020235
dataset.CTIME=200214
dataset.WDATE=2020235
dataset.WTIME=200214
dataset.SDATE=date_int
dataset.STIME=0
dataset.TSTEP=10000
dataset.NTHIK=1
dataset.NCOLS=459
dataset.NROWS=299
dataset.NLAYS=1
dataset.NVARS=62
dataset.GDTYP=2
dataset.P_ALP=33.
dataset.P_BET=45.
dataset.P_GAM=-97.
dataset.XCENT=-97.
dataset.YCENT=40.
dataset.XORIG=-2556000.
dataset.YORIG=-1728000.
dataset.XCELL=12000.
dataset.YCELL=12000.
dataset.VGTYP=-1
dataset.VGTOP=0
dataset.VGLVLS=0, 0
dataset.GDNAM="12US1_459X299   "
dataset.UPNAM="CREATESET       "
```

Inside each loop, identify the unit, long name, and description of each variable for the combined netCDF file for each date. $^{15}NO_2$ was used as the example in this demonstration.

```
tflag.units="<YYYYDDD,HHMMSS>"
zo2.units="moles/s        "
tflag.long_name="TFLAG          "
zo2.long_name="ZO2            "
tflag.var_desc="Timestep-valid flags:  (1) YYYYDDD or (2) HHMMSS                    "
zo2.var_desc="Model species ZO2                                                    "
```

Inside each loop, load the hourly timestep and the netCDF file of the ^{15}N incorporated emissions from each source, for the date being handled

```
tflag[:]=tflag0[i*24:i*24+25]
nc1=Dataset(f1[i],'r+')
nc2=Dataset(f2[i],'r+')
nc3=Dataset(f3[i],'r+')
nc4=Dataset(f4[i],'r+')
nc5=Dataset(f5[i],'r+')
nc6=Dataset(f6[i],'r+')
nc7=Dataset(f7[i],'r+')
nc8=Dataset(f8[i],'r+')
nc9=Dataset(f9[i],'r+')
nc10=Dataset(f10[i],'r+')
nc11=Dataset(f11[i],'r+')
nc12=Dataset(f12[i],'r+')
nc13=Dataset(f13[i],'r+')
nc14=Dataset(f14[i],'r+')
```

Inside each loop, sum up the emission rate from each source for each chemical. $^{15}NO_2$ was used as the example in this demonstration.

```
zo2[:]=nc4.variables['ZO2'][:]+nc5.variables['ZO2'][:]
    +nc6.variables['ZO2'][:]+nc7.variables['ZO2'][:]
    +nc9.variables['ZO2'][:]+nc10.variables['ZO2'][:]
    +nc11.variables['ZO2'][:]+nc12.variables['ZO2'][:]
    +nc13.variables['ZO2'][:]
```

Finally, the demonstration below selects the data within the domain of the research area, and store into the new netCDF file for each date.

```
import numpy as np
from netCDF4 import Dataset
import glob

def calc_tflag(tflag_old,numSteps,numElements):

    # create a new, empty array, shaped appropriately.
    # this variable will hold the new tflag data we are
    # about to build.
    tflag_new = np.array([]).reshape(0,numElements,2)

    # loop through each time step
    for i in range(numSteps):
        # create a new array with the correct number of elements
        # reshape it to match tflag_new
        q = np.tile(tflag_old[i:(i+1),0],numElements).reshape(1,numElements,2)

        # append the q array to tflag_new
        tflag_new = np.concatenate((tflag_new,q),axis=0)

    return tflag_new

def update_netcdf(infile,outfile):

    with Dataset(infile) as src, Dataset(outfile, "w", format="NETCDF3_CLASSIC") as dst:
        # adjust the dimension according to the domain of the research area
        dimensions = {
            'COL' : 157,
            'ROW' : 148
        }
        # copy old dimensions to new file
        for name, dimension in src.dimensions.items():
            if name in dimensions:
                dst.createDimension(name,dimensions[name])
            else:
```

```
        dst.createDimension(name, len(dimension) if not dimension.isunlimited() else None)

# copy old variables to new file
for name, variable in src.variables.items():
    x = dst.createVariable(name, variable.datatype, variable.dimensions)
    # copy variable attributes
    x.setncatts({k: variable.getncattr(k) for k in variable.ncattrs()})
    # copy variable data
    if name == 'TFLAG':
        # adjust the tflag variable
        x[:] = calc_tflag(variable, len(src.dimensions['TSTEP']), len(dst.dimensions['VAR']))[:]
    else :
        # select the data within the domain of the research area
        x[:]=variable[:,:,114:262,203:360]

# copy global attributes
for a in src.ncattrs():
    # get the value of the attribute from src
    # adjust the global attributes according to the domain of the research area
    if a == 'NCOLS':
        v = 157
    elif a == 'NROWS':
        v = 148
    elif a == 'P_GAM':
        v = -97.3
    elif a == 'XCENT':
        v = -97.3
    elif a == 'YCENT':
        v = 33.
    elif a == 'XORIG':
        v = -88500.
    elif a == 'YORIG':
        v = 409000.
    else:
        v = getattr(src,a)
    # store the attribute and value in dst
    setattr(dst,a,v)
```

```
# save the emission dataset covers the research area into the new netCDF file
for infile in glob.glob('emis_mole_all*.ncf'):
    outfile = '.'.join(infile.split('.')[0:1]) + '_us.nc'
    update_netcdf(infile,outfile)
```

E.2 Incorporating ^{15}N into initial condition and boundary condition

Similar to the emission input dataset, ^{15}N was also incorporated into the profile of initial condition (ICON) and boundary condition (BCON). The ICON and BCON profiles were simulated based on the CMAQ-default ASCII vertical profiles and the meteorological fields generated by MCIP output dataset. The demonstration below loads the background concentration of each chemical from ICON and BCON profiles, calculates the background concentrations of $^{15}NO_x$, then generates the ^{15}N incorporated ICON and BCON profiles into the new netCDF file. The background concentrations of $^{15}NO_x$ were set to 0.0036 of the concentrations of the background concentration of $^{14}NO_x$, which assumes $\delta^{15}N = 0$ at the initial time step and outside the domain of the simulation.

```
import numpy as np
from netCDF4 import Dataset
import glob

def calc_tflag(tflag_old,numSteps,numElements):

    # create a new, empty array, shaped appropriately.
    # this variable will hold the new tflag data we are
    # about to build.
    tflag_new = np.array([]).reshape(0,numElements,2)

    # loop through each time step
    for i in range(numSteps):
        # create a new array with the correct number of elements
        # reshape it to match tflag_new
        q = np.tile(tflag_old[i:(i+1),0],numElements).reshape(1,numElements,2)

        # append the q array to tflag_new
        tflag_new = np.concatenate((tflag_new,q),axis=0)
```

```
    return tflag_new


def update_netcdf(infile,outfile):

    with Dataset(infile) as src, Dataset(outfile, "w", format="NETCDF3_CLASSIC") as dst:

        # change the number of variables accordingly, from 76 to 86
        dimensions = {
            'VAR' : 86,
        }

        # copy old dimensions to new file
        for name, dimension in src.dimensions.items():
            if name in dimensions:
                dst.createDimension(name,dimensions[name])
            else:
                dst.createDimension(name, len(dimension) if not dimension.isunlimited() else None)



        # copy old variables to new file
        for name, variable in src.variables.items():

            x = dst.createVariable(name, variable.datatype, variable.dimensions)

            # copy variable attributes
            x.setncatts({k: variable.getncattr(k) for k in variable.ncattrs()})

            # copy variable data
            if name == 'TFLAG':
                # adjust the tflag variable
                x[:] = calc_tflag(variable, len(src.dimensions['TSTEP']), len(dst.dimensions['VAR']))[:]
            else :
                x[:] = variable[:]
```

```
    # copy global attributes
    for a in src.ncattrs():

        # get the value of the attribute from src
        # change the number of variables accordingly
        if a == 'NVARS':
            v = len(dst.dimensions['VAR'])
        elif a == 'VAR-LIST':
            v = getattr(src,a)
            v = v + 'ZO          ZO2          ZO3          Z2O5         ZNO5         HZO3         HOZO
PZA          PAZ          PAZX         '
        else:
            v = getattr(src,a)

        # store the attribute and value in dst
        setattr(dst,a,v)


    # Add new variables below

    # ZO is a factor times of NO
    no = dst.variables['NO']
    zo = dst.createVariable('ZO',no.datatype,no.dimensions)
    zo.setncattr('long_name','ZO          ')
    zo.setncattr('units','ppmV         ')
    zo.setncattr('var_desc','Model species ZO                                    ')
    zo[:] = 0.0036*no[:]

    # ZO2 is a factor times of NO2
    no2 = dst.variables['NO2']
    zo2 = dst.createVariable('ZO2',no2.datatype,no2.dimensions)
    zo2.setncattr('long_name','ZO2         ')
    zo2.setncattr('units','ppmV         ')
    zo2.setncattr('var_desc','Model species ZO2                                    ')
    zo2[:] = 0.0036*no2[:]

    # ZO3 is a factor times of NO3
```

```
no3 = dst.variables['NO3']
zo3 = dst.createVariable('ZO3',no3.datatype,no3.dimensions)
zo3.setncattr('long_name','ZO3           ')
zo3.setncattr('units','ppmV          ')
zo3.setncattr('var_desc','Model species ZO3                                    ')
zo3[:] = 0.0036*no3[:]

# Z2O5 is a factor times of N2O5
n2o5 = dst.variables['N2O5']
z2o5 = dst.createVariable('Z2O5',n2o5.datatype,n2o5.dimensions)
z2o5.setncattr('long_name','Z2O5          ')
z2o5.setncattr('units','ppmV          ')
z2o5.setncattr('var_desc','Model species Z2O5                                    ')
z2o5[:] = 0.0036*0.0036*n2o5[:]

# ZNO5 is a factor times of N2O5
zno5 = dst.createVariable('ZNO5',n2o5.datatype,n2o5.dimensions)
zno5.setncattr('long_name','ZNO5          ')
zno5.setncattr('units','ppmV          ')
zno5.setncattr('var_desc','Model species ZNO5                                    ')
zno5[:] = 2*0.0036*n2o5[:]

# HZO3 is a factor times of HNO3
hno3 = dst.variables['HNO3']
hzo3 = dst.createVariable('HZO3',hno3.datatype,hno3.dimensions)
hzo3.setncattr('long_name','HZO3          ')
hzo3.setncattr('units','ppmV          ')
hzo3.setncattr('var_desc','Model species HZO3                                    ')
hzo3[:] = 0.0036*hno3[:]

# HOZO is a factor times of HONO
hono = dst.variables['HONO']
hozo = dst.createVariable('HOZO',hono.datatype,hono.dimensions)
hozo.setncattr('long_name','HOZO          ')
hozo.setncattr('units','ppmV          ')
hozo.setncattr('var_desc','Model species HOZO                                    ')
hozo[:] = 0.0036*hono[:]
```

```
    # PZA is a factor times of PNA
    pna = dst.variables['PNA']
    pza = dst.createVariable('PZA',pna.datatype,pna.dimensions)
    pza.setncattr('long_name','PZA           ')
    pza.setncattr('units','ppmV          ')
    pza.setncattr('var_desc','Model species PZA                                    ')
    pza[:] = 0.0036*pna[:]

    # PAZ is a factor times of PAN
    pan = dst.variables['PAN']
    paz = dst.createVariable('PAZ',pan.datatype,pan.dimensions)
    paz.setncattr('long_name','PAZ           ')
    paz.setncattr('units','ppmV          ')
    paz.setncattr('var_desc','Model species PAZ                                    ')
    paz[:] = 0.0036*pan[:]

    # PAZX is a factor times of PANX
    panx = dst.variables['PANX']
    pazx = dst.createVariable('PAZX',panx.datatype,panx.dimensions)
    pazx.setncattr('long_name','PAZX          ')
    pazx.setncattr('units','ppmV          ')
    pazx.setncattr('var_desc','Model species PAZX                                     ')
    pazx[:] = 0.0036*panx[:]

# save the 15N incorporated ICON profile into the new netCDF file
# Replace “ICON” to “BCON” for generating 15N incorporated BCON profile
for infile in glob.glob('ICON_v52_2016_profile'):
   outfile = 'ICON_v52_2016_iso_all_profile'
   update_netcdf(infile,outfile)
```

E.3 Preparation of meteorology input dataset

As mentioned in Chapter 3, the meteorology input dataset was simulated by WRF, using the time-varying meteorological fields from NARR and NAM for this study, which are available from: https://www.ncdc.noaa.gov/data-access/model-data/model-datasets

The inputs for the real-data simulation were generated through the WRF Preprocessing System (WPS). WPS defines the appropriate coordinate system, spatial domain, and grid size of the simulation, with respect to those in emission dataset prepared by section E.1. WPS then loads the WRF-default static geographic data and meteorological fields from regional or global models. Finally, these datasets are extracted and interpolated, in order to ensure the consistency of coordinate system, spatial domain, and grid size between the emission dataset that prepared previously. The parameters for running WPS are shown in the demonstration below.

```
&share
 wrf_core = 'ARW',
 max_dom = 1,
 start_date = '2016-01-01_00:00:00',
 end_date   = '2017-01-01_00:00:00',
 interval_seconds = 21600,
 io_form_geogrid = 2,
/

&geogrid
 parent_id         =   1,
 parent_grid_ratio =   1,
 i_parent_start    =   1,
 j_parent_start    =   1,
 s_we              =   1,
 e_we              = 160,
 s_sn              =   1,
 e_sn              = 151,

geog_data_res = 'default',
 dx = 12000,
 dy = 12000,
 map_proj = 'lambert',
 ref_lat   =  44.256,
 ref_lon   = -86.541,
 truelat1  =  33.0,
 truelat2  =  45.0,
 stand_lon = -97.3,
 geog_data_path = '/opt/geog'
```

```
/

&ungrib
 out_format = 'WPS',
 prefix = 'FILE',
/

&metgrid
 fg_name = 'FILE'
 io_form_metgrid = 2,
/
```

Then, the meteorological fields with the appropriate coordinate system, spatial domain, and grid size will go through the real-data simulation of WRF, to generate the gridded meteorology files on an hourly basis. The parameters for running the real-data simulation of WRF are shown in the demonstration below. For each WRF output file, the cells near the boundary are inadequate for CMAQ simulation. Therefore, the domain for WPS and real-data WRF simulation is slightly larger than the domain of previously prepared emission dataset, which is 160 grids in the east-west direction and 151 grids in the north-south direction for this research.

```
&time_control
 run_days                  = 366,
 run_hours                 = 0,
 run_minutes               = 0,
 run_seconds               = 0,
 start_year                = 2016,
 start_month               = 01,
 start_day                 = 01,
 start_hour                = 00,
 start_minute              = 00,
 start_second              = 00,
 end_year                  = 2017,
 end_month                 = 01,
 end_day                   = 01,
 end_hour                  = 00,
 end_minute                = 00,
```

```
end_second                          = 00,
interval_seconds                    = 21600
input_from_file                     = .true.,
history_interval                    = 60,
frames_per_outfile                  = 1000,
restart                             = .false.,
restart_interval                    = 60,
io_form_history                     = 2
io_form_restart                     = 2
io_form_input                       = 2
io_form_boundary                    = 2
debug_level                         = 0
/

&domains
time_step                           = 60,
time_step_fract_num                 = 0,
time_step_fract_den                 = 1,
max_dom                             = 1,
s_we                                =  1,
e_we                                = 160,
s_sn                                =  1,
e_sn                                = 151,
e_vert                              =  34,
p_top_requested                     = 5000,
num_metgrid_levels                  = 30,
num_metgrid_soil_levels             = 4,
dx                                  = 12000,
dy                                  = 12000,
grid_id                             = 1,
parent_id                           = 1,
i_parent_start                      = 1,
j_parent_start                      = 1,
parent_grid_ratio                   = 1,
parent_time_step_ratio              = 1,
feedback                            = 1,
smooth_option                       = 0
```

```
/

&physics
mp_physics                          = 3,
ra_lw_physics                       = 1,
ra_sw_physics                       = 1,
radt                                = 30,
sf_sfclay_physics                   = 1,
sf_surface_physics                  = 2,
bl_pbl_physics                      = 1,
bldt                                = 0,
cu_physics                          = 1,
cudt                                = 5,
isfflx                              = 1,
ifsnow                              = 1,
icloud                              = 1,
surface_input_source                = 3,
num_soil_layers                     = 4,
num_land_cat                        = 21,
sf_urban_physics                    = 0,
/

&fdda
/

&dynamics
w_damping                           = 0,
diff_opt                            = 1,
km_opt                              = 4,
diff_6th_opt                        = 0,
diff_6th_factor                     = 0.12,
base_temp                           = 290.,
damp_opt                            = 0,
zdamp                               = 5000.,
dampcoef                            = 0.2,
khdif                               = 0,
kvdif                               = 0,
```

```
non_hydrostatic                 = .true.,
moist_adv_opt                   = 1,
scalar_adv_opt                  = 1,
/

&bdy_control
spec_bdy_width                   = 5,
spec_zone                       = 1,
relax_zone                      = 4,
specified                       = .true.,
nested                          = .false.,
/

&grib2
/

&namelist_quilt
nio_tasks_per_group = 0,
nio_groups = 1,
/
```

After the gridded meteorology files on an hourly basis being generated, the CMAQ module MCIP was run to extract the data of the necessary parameters for the same geographic domain as emission input dataset, convert the units and/or adjust the resolution of the data if necessary, then organize the parameters into seven netCDF files that embedded with I/O API. The demonstration below is the Fortran script for MCIP simulation.

```
#!/bin/csh -f

#------------------------------------------------------------------------
# Set identification for input and output files.
#
#   APPL       = Application Name (tag for MCIP output file names)
#   CoordName  = Coordinate system name for GRIDDESC
#   GridName   = Grid Name descriptor for GRIDDESC
#   InMetDir   = Directory that contains input meteorology files
#   InTerDir   = Directory that contains input MM5 "TERRAIN" file or
```

```
#              WRF Preprocessing System "GEOGRID" file.  (Used for
#              providing fractional land-use categories.  For MM5,
#              it will only work if IEXTRA was set to TRUE in
#              MM5's TERRAIN program.  Is TRUE for P-X simulations.
#              Not needed for WRF if "LANDUSEF" is part of history
#              file.)
#   InSatDir   = Directory that contains GOES satellite files.  (Used
#              with satellite processing from UAH; otherwise leave
#              blank.)
#   OutDir     = Directory to write MCIP output files
#   ProgDir    = Directory that contains the MCIP executable
#   WorkDir    = Working Directory for Fortran links and namelist
#------------------------------------------------------------------------

source /opt/cmaqv5.1/config.cmaq.csh

set APPL       = 2016
set CoordName  = LamCon_40N_97W # 16-character maximum
set GridName   = SE52BENCH     # 16-character maximum


set DataPath   = /opt/cmaqv5.1/CMAQv5.1/data
set InMetDir   = $DataPath/met/wrf
set InTerDir   = $DataPath/met/wrf
set InSatDir   = $DataPath/SE52BENCH
set OutDir     = $DataPath/met/mcip/$APPL
set ProgDir    = /opt/cmaqv5.1/CMAQv5.1/scripts/mcip/src
set WorkDir    = $OutDir

#------------------------------------------------------------------------
# Set name(s) of input meteorology file(s)
#
#   File name(s) must be set inside parentheses since "InMetFiles" is
#   a C-shell script array.  Multiple file names should be space-
#   delimited.  Additional lines can be used when separated by a
#   back-slash (\) continuation marker.  The file names can be as
#   they appear on your system; MCIP will link the files in by a
```

```
#   Fortran unit number and the explicit name via a namelist.  The
#   files must be listed in chronological order.  The maximum number
#   of input meteorology files must be less than or equal to the number
#   in MAX_MM in file_mod.F (default is 367).
#
#   Example:
#     set InMetFiles = ( $InMetDir/MMOUT_DOMAIN2.time1 \
#                        $InMetDir/MMOUT_DOMAIN2.time2 )
#
#------------------------------------------------------------------------

set InMetFiles = ( $InMetDir/wrfout_d01_2016-01-01_00:00:00 \
                   $InMetDir/wrfout_d01_2016-02-11_16:00:00 \
                   $InMetDir/wrfout_d01_2016-03-24_08:00:00 \
                   $InMetDir/wrfout_d01_2016-05-05_00:00:00 \
                   $InMetDir/wrfout_d01_2016-06-15_16:00:00 \
                   $InMetDir/wrfout_d01_2016-07-27_08:00:00 \
                   $InMetDir/wrfout_d01_2016-09-07_00:00:00 \
                   $InMetDir/wrfout_d01_2016-10-18_16:00:00 \
                   $InMetDir/wrfout_d01_2016-11-29_08:00:00 \
                    )
set IfTer      = "T"
set InTerFile  = $InTerDir/geo_em.d01.nc

set InSatFiles = ( )

#------------------------------------------------------------------------
# Set user control options.
#
#   LPV:     0 = Do not compute and output potential vorticity
#            1 = Compute and output potential vorticity
#
#   LWOUT:   0 = Do not output vertical velocity
#            1 = Output vertical velocity
#
#   LUVCOUT: 0 = Do not output u- and v-component winds on C-grid
#            1 = Output u- and v-component winds on C-grid
```

```
#
#   LSAT:    0 = No satellite input is available (default)
#            1 = GOES observed cloud info replaces model-derived input
#-------------------------------------------------------------------------

set LPV     = 0
set LWOUT   = 0
set LUVCOUT = 1
set LSAT    = 0

#-------------------------------------------------------------------------
# Set run start and end date.  (YYYY-MO-DD-HH:MI:SS.SSSS)
#   MCIP_START:  First date and time to be output [UTC]
#   MCIP_END:    Last date and time to be output  [UTC]
#   INTVL:       Frequency of output [minutes]
#-------------------------------------------------------------------------

set MCIP_START = 2016-01-01-00:00:00.0000  # [UTC]
set MCIP_END   = 2017-01-01-00:00:00.0000  # [UTC]

set INTVL      = 60 # [min]

#-------------------------------------------------------------------------
# Set CTM layers.  Should be in descending order starting at 1 and
# ending with 0.  There is currently a maximum of 100 layers allowed.
# To use all of the layers from the input meteorology without
# collapsing (or explicitly specifying), set CTMLAYS = -1.0.
#-------------------------------------------------------------------------

set CTMLAYS = "-1.0"

#-------------------------------------------------------------------------
# Determine whether or not static output (GRID) files will be created.
#-------------------------------------------------------------------------

set MKGRID = T
```

```
#-------------------------------------------------------------------
# Set number of meteorology "boundary" points to remove on each of four
# horizontal sides of MCIP domain.  This affects the output MCIP domain
# dimensions by reducing meteorology domain by 2*BTRIM + 2*NTHIK + 1,
# where NTHIK is the lateral boundary thickness (in BDY files), and the
# extra point reflects conversion from grid points (dot points) to grid
# cells (cross points).  Setting BTRIM = 0 will use maximum of input
# meteorology.  To remove MM5 lateral boundaries, set BTRIM = 5.
#
# *** If windowing a specific subset domain of input meteorology, set
#     BTRIM = -1, and BTRIM will be ignored in favor of specific window
#     information in X0, Y0, NCOLS, and NROWS.
#-------------------------------------------------------------------

set BTRIM = -1

#-------------------------------------------------------------------
# Define MCIP subset domain.  (Only used if BTRIM = -1.  Otherwise,
# the following variables will be set automatically from BTRIM and
# size of input meteorology fields.)
#   X0:    X-coordinate of lower-left corner of full MCIP "X" domain
#          (including MCIP lateral boundary) based on input MM5 domain.
#          X0 refers to the east-west dimension.  Minimum value is 1.
#   Y0:    Y-coordinate of lower-left corner of full MCIP "X" domain
#          (including MCIP lateral boundary) based on input MM5 domain.
#          Y0 refers to the north-south dimension.  Minimum value is 1.
#   NCOLS:  Number of columns in output MCIP domain (excluding MCIP
#          lateral boundaries).
#   NROWS:  Number of rows in output MCIP domain (excluding MCIP
#          lateral boundaries).
#-------------------------------------------------------------------

set X0    =  1
set Y0    =  1
set NCOLS = 157
set NROWS = 148
```

```
#-------------------------------------------------------------------
# Set coordinates for cell for diagnostic prints on output domain.
# If coordinate is set to 0, domain center cell will be used.
#-------------------------------------------------------------------

set LPRT_COL = 0
set LPRT_ROW = 0

#-------------------------------------------------------------------
# Optional:  Set WRF Lambert conformal reference latitude.
#            (Handy for matching WRF grids to existing MM5 grids.)
#            If not set, MCIP will use average of two true latitudes.
# To "unset" this variable, set the script variable to "-999.0".
# Alternatively, if the script variable is removed here, remove it
# from the setting of the namelist (toward the end of the script).
#-------------------------------------------------------------------

set WRF_LC_REF_LAT = 33.0

#===================================================================
#===================================================================
# Set up and run MCIP.
#   Should not need to change anything below here.
#===================================================================
#===================================================================

set PROG = mcip

date

#-------------------------------------------------------------------
# Make sure directories exist.
#-------------------------------------------------------------------

if ( ! -d $InMetDir ) then
  echo "No such input directory $InMetDir"
  exit 1
```

```
endif

if ( ! -d $OutDir ) then
  echo "No such output directory...will try to create one"
  mkdir -p $OutDir
  if ( $status != 0 ) then
    echo "Failed to make output directory, $OutDir"
    exit 1
  endif
endif

if ( ! -d $ProgDir ) then
  echo "No such program directory $ProgDir"
  exit 1
endif

if ( $LSAT == 1 ) then
  if ( ! -d $InSatDir ) then
    echo "No such satellite input directory $InSatDir"
    exit 1
  endif
endif

#-----------------------------------------------------------------
# Make sure the input files exist.
#-----------------------------------------------------------------

if ( $IfTer == "T" ) then
  if ( ! -f $InTerFile ) then
    echo "No such input file $InTerFile"
    exit 1
  endif
endif

foreach fil ( $InMetFiles )
  if ( ! -f $fil ) then
    echo "No such input file $fil"
```

```
    exit 1
  endif
end

if ( $LSAT == 1 ) then
  foreach fil ( $InSatFiles )
    if ( ! -f $fil ) then
      echo "No such input file $fil"
      exit 1
    endif
  end
endif

#-------------------------------------------------------------------
# Make sure the executable exists.
#-------------------------------------------------------------------

if ( ! -f $ProgDir/${PROG}.exe ) then
  echo "Could not find ${PROG}.exe"
  exit 1
endif

#-------------------------------------------------------------------
# Create a work directory for this job.
#-------------------------------------------------------------------

if ( ! -d $WorkDir ) then
  mkdir -p $WorkDir
  if ( $status != 0 ) then
    echo "Failed to make work directory, $WorkDir"
    exit 1
  endif
endif

cd $WorkDir

#-------------------------------------------------------------------
```

```
# Set up script variables for input files.
#-------------------------------------------------------------------

if ( $IfTer == "T" ) then
  if ( -f $InTerFile ) then
    set InTer = $InTerFile
  else
    set InTer = "no_file"
  endif
else
  set InTer = "no_file"
endif

set FILE_GD  = $OutDir/GRIDDESC
set FILE_HDR = $OutDir/mmheader.${APPL}

#-------------------------------------------------------------------
# Create namelist with user definitions.
#-------------------------------------------------------------------

set MACHTYPE = `uname`
if ( ( $MACHTYPE == "AIX" ) || ( $MACHTYPE == "Darwin" ) ) then
  set Marker = "/"
else
  set Marker = "&END"
endif

cat > $WorkDir/namelist.${PROG} << !

 &FILENAMES
  file_gd    = "$FILE_GD"
  file_hdr   = "$FILE_HDR"
  file_mm    = "$InMetFiles[1]",
!

if ( $#InMetFiles > 1 ) then
  @ nn = 2
```

```
  while ( $nn <= $#InMetFiles )
    cat >> $WorkDir/namelist.${PROG} << !
             "$InMetFiles[$nn]",
!
    @ nn ++
  end
endif

if ( $IfTer == "T" ) then
cat >> $WorkDir/namelist.${PROG} << !
  file_ter    = "$InTer"
!
endif

if ( $LSAT == 1 ) then
  cat >> $WorkDir/namelist.${PROG} << !
  file_sat    = "$InSatFiles[1]",
!
  if ( $#InSatFiles > 1 ) then
    @ nn = 2
    while ( $nn <= $#InSatFiles )
      cat >> $WorkDir/namelist.${PROG} << !
             "$InSatFiles[$nn]",
!
      @ nn ++
    end
  endif
endif

cat >> $WorkDir/namelist.${PROG} << !
  makegrid    = .${MKGRID}.
 $Marker

 &USERDEFS
  lpv        =  $LPV
  lwout      =  $LWOUT
  luvcout    =  $LUVCOUT
```

```
 lsat      = $LSAT
 mcip_start = "$MCIP_START"
 mcip_end   = "$MCIP_END"
 intvl     = $INTVL
 coordnam   = "$CoordName"
 grdnam     = "$GridName"
 ctmlays    = $CTMLAYS
 btrim      = $BTRIM
 lprt_col   = $LPRT_COL
 lprt_row   = $LPRT_ROW
 wrf_lc_ref_lat = $WRF_LC_REF_LAT
$Marker

 &WINDOWDEFS
 x0        = $X0
 y0        = $Y0
 ncolsin    = $NCOLS
 nrowsin    = $NROWS
$Marker

!

#-------------------------------------------------------------------------
# Set links to FORTRAN units.
#-------------------------------------------------------------------------

rm fort.*
if ( -f $FILE_GD ) rm -f $FILE_GD

ln -s $FILE_HDR                fort.2
ln -s $FILE_GD                 fort.4
ln -s $WorkDir/namelist.${PROG}  fort.8
if ( $IfTer == "T" ) then
  ln -s $InTerFile             fort.9
endif

set NUMFIL = 0
```

```
foreach fil ( $InMetFiles )
  @ NN = $NUMFIL + 10
  ln -s $fil fort.$NN
  @ NUMFIL ++
end

#-------------------------------------------------------------------------
# Set output file names and other miscellaneous environment variables.
#-------------------------------------------------------------------------

setenv IOAPI_CHECK_HEADERS  T
setenv EXECUTION_ID         $PROG

setenv GRID_BDY_2D          $OutDir/GRIDBDY2D_${APPL}.nc
setenv GRID_CRO_2D          $OutDir/GRIDCRO2D_${APPL}.nc
setenv GRID_CRO_3D          $OutDir/GRIDCRO3D_${APPL}.nc
setenv GRID_DOT_2D          $OutDir/GRIDDOT2D_${APPL}.nc
setenv MET_BDY_3D           $OutDir/METBDY3D_${APPL}.nc
setenv MET_CRO_2D           $OutDir/METCRO2D_${APPL}.nc
setenv MET_CRO_3D           $OutDir/METCRO3D_${APPL}.nc
setenv MET_DOT_3D           $OutDir/METDOT3D_${APPL}.nc

#-------------------------------------------------------------------------
# Execute MCIP.
#-------------------------------------------------------------------------

$ProgDir/${PROG}.exe

if ( $status == 0 ) then
  rm fort.*
  exit 0
else
  echo "Error running $PROG"
  exit 1
endif
```

E.4 Incorporating ^{15}N into chemical mechanisms

As mentioned in Chapter 5, ^{15}N was incorporated into chemical mechanisms CB and RACM to create new chemical mechanisms for CMAQ simulation. The CMAQ utility chemmech was used to create the Fortran 90 modules of data and function for the ^{15}N incorporated chemical mechanisms. For the ^{15}N incorporated chemical mechanisms, species namelist files and the chemical mechanism definition file were built upon the preexisting files of CMAQ-default CB and RACM.

The ^{15}N compounds were added into the species namelist files, with the proper species name, species molecular weight, scaling factor, as well as output file options. The demonstration below use NO_2 as an example to indicate how to add ^{15}N compounds into the species namelist files.

```
& &GC_nml
n_surr1 = 4,
n_surr2 = 2,
n_ctrl = 4,
TYPE_HEADER =
'SPC:MOLWT:EMIS_SUR:EMIS_FAC:DEPV_SUR:DEPV_FAC:ICBC_SUR:ICBC_FAC:SCAV_SUR:SCA
V_FAC:G2AE_SUR:G2AQ_SUR:TRNS:DDEP:WDEP:CONC',
TYPE_MATRIX =
'NO2:46:NO2:1:VD_NO2:1:::NO2:1:NO2::Yes:Yes:Yes:Yes',
'ZO2:47:ZO2:1:VD_NO2:1:::ZO2:1:ZO2::Yes:Yes:Yes:Yes',
```

In the chemical mechanism definition file, the reactions of ^{15}N compounds were replicated from the reactions of ^{14}N compounds, with the fractionation factors listed in Appendix C. The demonstration below shows how to add the reactions of ^{15}N compounds into the chemical mechanism definition file. The rate constants of ^{15}N compounds equal to the multiplication between their fractionation factors and the corresponding rate constants of ^{14}N compounds.

```
<R004>  NO2          =  O3P     + NO        # 1.0/<NO2_RACM2>;
<R364>  ZO2          =  O3P     + ZO        # 1.0/<ZO2_RACM2>;
<R036>  O3   + NO    = NO2                  # 1.4E-12 @ 1310.;
<R373>  O3   + ZO    = ZO2                  # 1.39062E-12 @ 1310.;
```

Unlike the kinetic rate constants and equilibrium rate constants, which were directly included in the Fortran 90 modules of data and function generated from the chemical mechanism definition file, the photodissociation rate constants were based on the separate cross-sections and

quantum yields (CSQY) dataset. The CMAQ utility inline_phot_preproc was used to generate the ^{15}N incorporated CSQY dataset. The demonstration below shows the portions of the file named NO2_RACM2, which is the CMAQ-default CSQY input for the photolysis of $^{14}NO_2$, as well as the same portion of the file named ZO2_RACM2, which is the CSQY input for the photolysis of $^{15}NO_2$, which was built upon NO2_RACM2 and the fractionation factor of $^{15}NO_2$ photolysis reaction.

```
NO2_RACM2
261.5  0.158E-19  1.000
265.0  0.205E-19  1.000
268.5  0.264E-19  1.000
272.2  0.324E-19  1.000
275.9  0.407E-19  1.000
279.8  0.521E-19  1.000
283.7  0.623E-19  1.000
287.8  0.759E-19  1.000
292.0  0.951E-19  1.000
296.3  0.115E-18  1.000

ZO2_RACM2
261.5  0.159E-19  1.000
265.0  0.206E-19  1.000
268.5  0.265E-19  1.000
272.2  0.325E-19  1.000
275.9  0.409E-19  1.000
279.8  0.523E-19  1.000
283.7  0.626E-19  1.000
287.8  0.762E-19  1.000
292.0  0.955E-19  1.000
296.3  0.115E-18  1.000
```

The Fortran 90 modules of data and function for the ^{15}N chemical mechanisms generated from chemmech, as well as the corresponding CSQY dataset generated from inline_phot_preproc were used as the input for another CMAQ utility create_ebi to enable the better accuracy and computational efficiency of CMAQ simulation through the Euler Backward Iterative (EBI) solver. Since this research only focus on gas-phase chemistry, the aerosol module was disable, by

commenting out the statement “CALL HETCHEM_RATES(TA, PRES, QV, CGRID)” and “CALL HETCHEM_UPDATE_AERO(CGRID)” inside the output file of create_ebi named hrdriver.F.

Finally, the output files of chemmech, inline_phot_preproc, and create_ebi were stored in the proper directory for the CMAQ simulation that incorporating ^{15}N. The output files of chemmech and inline_phot_preproc were organized into one directory (named “racm2_ae6_aq_iso_aero0” for this research) and stored under the directory “CCTM/src/MECHS/”. The output files of create_ebi were organized into one directory (named “ebi_racm2_ae6_aq_iso_aero0” for this research) and stored under the directory “CCTM/src/gas/”.

E.5 Preparation for the simulation over the nested domain

Since $\delta^{15}N$ was set to 0‰ for the boundary condition, the bias occurs near the border of the research area, under some particular circumstances (details in Chapter 3 and Chapter 5). Therefore, the nested domain simulation was conducted. The preparation of the emission input dataset, meteorology input dataset, and ICON profile for the nested domain simulation are similar to the preparation for the full domain simulation. The preparation of the BCON profile for the nested domain simulation are different. The BCON profiles for the simulation of day 1 were generated from the CMAQ-default ASCII vertical profiles and the meteorological fields based on MCIP output dataset. The BCON profiles for the simulation of day 2 and later time were extracted from the CCTM output of the full-domain simulation, using the demonstration below, which was built upon the CMAQ-default run_bcon.csh Fortran script, by inserting a loop to process the BCON profile of all the dates in one simulation.

```
#!/bin/csh -f
#> Choose compiler and set up CMAQ environment with correct
#> libraries using config.cmaq. Options: intel | gcc | pgi
 setenv compiler intel
 setenv compilerVrsn 15.0

#> Source the config_cmaq file to set the run environment
 pushd ../../../
 source ./config_cmaq.csh
 popd
```

```
#> Check that CMAQ_DATA is set:
 if ( ! -e $CMAQ_DATA ) then
   echo "   $CMAQ_DATA path does not exist"
   exit 1
 endif
 echo " "; echo " Input data path, CMAQ_DATA set to $CMAQ_DATA"; echo " "

#> Set General Parameters for Configuring the Simulation
 set VRSN     = v52                  #> Code Version
 set APPL     = 2016_mw              #> Application Name
 set INPT     = m3conc               #> Input data type: profile or m3conc?
 set MECH     = cb05e51_ae6_aq       #> Mechanism ID

#> Set the build directory (this is where the CMAQ executable is located by default).
 set BLD      = ${CMAQ_HOME}/PREP/bcon/scripts/BLD_BCON_${VRSN}_${INPT}_${compiler}
 set EXEC     = BCON_${VRSN}_$INPT.exe
 cat $BLD/BCON_${VRSN}_$INPT.cfg; echo " "; set echo

#> Horizontal grid definition
 setenv GRID_NAME SE52BENCH             #> check GRIDDESC file for GRID_NAME options
 setenv GRIDDESC $CMAQ_DATA/met/mcip/$APPL/GRIDDESC #> grid description file
 setenv IOAPI_ISPH 20                   #> GCTP spheroid, use 20 for WRF-based modeling

#> Vertical layer definition
 setenv LAYER_FILE $CMAQ_DATA/met/mcip/$APPL/METCRO3D_2016001.nc #>METCRO3D file from
MCIP

#> I/O Controls
 setenv IOAPI_LOG_WRITE F     #> turn on excess WRITE3 logging [ options: T | F ]
 setenv IOAPI_OFFSET_64 NO    #> support large timestep records (>2GB/timestep record) [ options:
YES | NO ]
 setenv EXECUTION_ID $EXEC    #> define the model execution id

# ======================================================================
#> BCON Configuration Options
#
# BCON can be run in one of two modes:
```

```
#     1) use default profile inputs (BC = profile)
#     2) use CMAQ CTM concentration files for nested runs (BC = m3conc)
# ==========================================================================

#> Set Start and End Days for looping
 setenv NEW_START TRUE           #> Set to FALSE for model restart
 set START_DATE = "2016-01-01"    #> beginning date (Jan 1, 2016)
 set END_DATE   = "2016-12-30"    #> ending date    (Dec 30, 2016)

set TODAYG = ${START_DATE}
set TODAYJ = `date -ud "${START_DATE}" +%Y%j` #> Convert YYYY-MM-DD to YYYYJJJ
set STOP_DAY = `date -ud "${END_DATE}" +%Y%j` #> Convert YYYY-MM-DD to YYYYJJJ

while ($TODAYJ <= $STOP_DAY )  #>Compare dates in terms of YYYYJJJ

  #> Retrieve Calendar day Information
  set YYYYMMDD = `date -ud "${TODAYG}" +%Y%m%d` #> Convert YYYY-MM-DD to YYYYMMDD
  set YYMMDD = `date -ud "${TODAYG}" +%y%m%d`   #> Convert YYYY-MM-DD to YYMMDD
  set YYYYJJJ = $TODAYJ



  set BC = m3conc      #> either profile or m3conc
  set DATE = ${YYYYJJJ}    #> only needed for nested runs

# ==========================================================================
#> Input/Output Directories
# ==========================================================================

  set OUTDIR   = $CMAQ_DATA/bcon/mw       #> output file directory

# ==========================================================================
#> Input Files
#
#  Profile Mode (BC = profile)
#     BC_PROFILE = static/default BC profiles
#  Nesting mode (BC = m3conc)
#     CTM_CONC_1 = the CTM concentration file for the coarse domain
```

```
#     MET_CRO_3D_CRS = the MET_CRO_3D met file for the coarse domain
#                 only set if the vertical grid type is
#                 changed between nests
#     MET_CRO_3D_FIN = the MET_CRO_3D met file for the inner, nested, domain
#                 only set if the vertical grid type is changed between
#                 nests
#
# NOTE: If SDATE (yyyyddd), STIME (hhmmss) and RUNLEN (hhmmss) are not set,
#       these variables will be set from the input CTM_CONC_1 file
# ======================================================================

  if ( $BC == profile ) then
    setenv BC_PROFILE      $BLD/bc_profile_CB05.dat
  endif

  if ( $BC == m3conc ) then
    setenv                                                                    CTM_CONC_1
$CMAQ_DATA/cctm/transport/output_CCTM_v521_intel_2016_tran_us/CCTM_CONC_v521_intel_2016
_${YYYYMMDD}.nc
    setenv MET_CRO_3D_CRS
    setenv MET_CRO_3D_FIN
  #   setenv SDATE          ${DATE}
  #   setenv STIME          000000
  #   setenv RUNLEN         240000
  endif

# ======================================================================
#> Output Files
# ======================================================================

  if ( $BC == profile ) then
    setenv BNDY_CONC_1    "$OUTDIR/BCON_${VRSN}_${APPL}_profile -v"
    endif
  if ( $BC == m3conc ) then
    set DATE = ${YYYYMMDD}
    setenv BNDY_CONC_1    "$OUTDIR/BCON_${VRSN}_${APPL}_${DATE} -v"
  endif
```

```
#>- - - - - - - - - - - - - - - - - - - - - - - - - - - - -

#> species defn
  setenv gc_matrix_nml ${BLD}/GC_$MECH.nml
  setenv ae_matrix_nml ${BLD}/AE_$MECH.nml
  setenv nr_matrix_nml ${BLD}/NR_$MECH.nml
  setenv tr_matrix_nml ${BLD}/Species_Table_TR_0.nml

  if ( ! -d "$OUTDIR" ) mkdir -p $OUTDIR

  ls -l $BLD/$EXEC; size $BLD/$EXEC
  unlimit
  limit

#> Executable call:
  time $BLD/$EXEC

  #> Increment both Gregorian and Julian Days
  set TODAYG = `date -ud "${TODAYG}+1days" +%Y-%m-%d` #> Add a day for tomorrow
  set TODAYJ = `date -ud "${TODAYG}" +%Y%j` #> Convert YYYY-MM-DD to YYYYJJJ

end  #Loop to the next Simulation Day

 exit()
```

VITA

Huan Fang

Purdue University

Department of Earth, Atmospheric, and Planetary Sciences

550 Stadium Mall Dr.

West Lafayette, IN, 47907

Email: fang63@purdue.edu

EDUCATION AND RESEARCH

Purdue University, West Lafayette, IN

Department of Earth, Atmospheric, and Planetary Sciences

Purdue Climate Change Research Center

Purdue Center for the Environment

- Graduate research with Dr. Greg Michalski, Aug. 2015 – Present
- Purdue Research Foundation (PRF) Research Grant Aug. 2019 – Aug. 2020

Purdue University, West Lafayette, IN

- B. S., Atmospheric Science, May 2015
- Undergraduate research with Dr. Greg Michalski, Jan. 2014 – Jul 2015
- Project: "Geographical Analysis of the sources of atmospheric NO_x in Tucson, AZ"

PUBLICATIONS

- Walters, W. W., **Fang, H.**, & Michalski, G. (2018). Summertime diurnal variations in the isotopic composition of atmospheric nitrogen dioxide at a small Midwestern United States city. *Atmospheric Environment*, *179*, 1-11.
- Walters, W. W., Tharp, B. D., **Fang, H.**, Kozak, B. J., & Michalski, G. (2015). Nitrogen isotope composition of thermally produced NO_x from various fossil-fuel combustion sources. *Environmental Science & Technology*, *49*(19), 11363-11371.

Manuscripts in press:

- **Fang, H.**, Michalski, G., Walters, W. W., & Mase, D. i_NRACM: Incorporating ^{15}N into the Regional Atmospheric Chemistry Mechanism (RACM) for assessing the role photochemistry plays in controlling the isotopic composition of NO_x, NO_y, and atmospheric nitrate. *Geoscientific Model Development.*

- **Fang, H.** & Michalski, G. Incorporating ^{15}N into the outputs of SMOKE version 4.6 as the emission input dataset for CMAQ version 5.2.1 for assessing the role emission sources plays in controlling the isotopic composition of NO_x, NO_y, and atmospheric nitrate. *Geoscientific Model Development.*
- **Fang, H.** & Michalski, G. Simulating $\delta^{15}N$ of atmospheric NO_x in CMAQ version 5.2.1, based on ^{15}N incorporated SMOKE version 4.6 and WRF version 4.0 for assessing the role atmospheric processes plays in controlling the isotopic composition of NO_x, NO_y, and atmospheric nitrate. *Geoscientific Model Development.*
- **Fang, H.** & Michalski, G. Simulating $\delta^{15}N$ of atmospheric NO_x in CMAQ version 5.2.1, based on ^{15}N incorporated SMOKE version 4.6, WRF version 4.0, as well as ^{15}N incorporated RACM version 2 and CB version 6, for assessing the role gas-phase tropospheric photochemistry plays in controlling the isotopic composition of NO_x, NO_y, and atmospheric nitrate. *Geoscientific Model Development.*
- Zhang, W., Zhang, Y., Li, J., **Fang, H.**, Fang, C., Lin, Y., Wilkins, B., Liu, X., Bao, M., Michalski, G. Diurnal story of $\Delta^{17}NO_3^-$: implication for atmospheric nitrate formation. *Environmental Science & Technology*
- Michalski, G., Welp, L., Valdivia, A. E. L., Valdivia, A. E. L., Larico, J. A. R., Peña, J. S., **Fang, H.**, Magara-Gomez, K. T., & Li, J. Sulfate aerosol sources in urban Peru identified by sulfur stable isotopes and water-soluble ions. *Atmospheric Environment.*

HONORS

Awards

- Category 2 (MS/PhD) Winner for the forecast of Minneapolis, MN during the 2019-20 season, WxChallenge, the North American collegiate weather forecasting competition, Dec 2019
- Category 2 (MS/PhD) Winner for the forecast of Anchorage, AK during the 2018-19 season, WxChallenge, the North American collegiate weather forecasting competition, Mar 2019
- Category 2 (MS/PhD) Winner for the forecast of Sioux Falls, SD during the 2017-18 season, WxChallenge, the North American collegiate weather forecasting competition, May 2018

Fellowships and Grants

- Purdue Research Foundation (PRF) Research Grant ($19,500), 2019
- Purdue Climate Change Research Center Travel Grant ($500), 2019
- Purdue University Department of Earth, Atmospheric, and Planetary Sciences Travel Grant ($400), 2019
- Purdue Climate Change Research Center Travel Grant ($350), 2018
- Purdue University Department of Earth, Atmospheric, and Planetary Sciences Travel Grant ($400), 2018
- Purdue University Office of Engagement Community Service/Service Learning Grant ($1500), 2018
- Purdue Climate Change Research Center Travel Grant ($400), 2017

- Purdue University Department of Earth, Atmospheric, and Planetary Sciences Travel Grant ($400), 2017

SOCIETIES AND ACTIVITIES

- Purdue University Meteorology Association, (2011-Present)
- Purdue Climate Change Research Center, (2017-Present)
- Purdue Center for the Environment, (2017-Present)
- American Geophysical Union, (2017-Present)
- American Meteorological Society, (2019-Present)

TEACHING

Purdue University, West Lafayette, IN

- Laboratory Instructor: EAPS 312, Capstone Environmental Science for Elementary Education, Fall 2018, Spring 2019
- Teaching Assistant: EAPS 104, Oceanography, Fall 2015, Spring 2016, Summer 2016, Fall 2016, Spring 2017, Summer 2017, Fall 2017, Spring 2018, Summer 2018
- Laboratory Instructor: EAPS 118, Introduction to Earth Science, Fall 2016
- Teaching Assistant: EAPS 100, Planet Earth, Fall 2015, Spring 2016

PRESENTATIONS

- American Geophysical Union Fall Meeting, Dec. 2020 (Poster)
- Purdue University, Department of Earth, Atmospheric, and Planetary Sciences StormSnack (weekly atmospheric science seminar), Feb. 2020 (Talk)
- Purdue University, Department of Earth, Atmospheric, and Planetary Sciences Expo, Feb. 2020 (Talk)
- Purdue University, Department of Earth, Atmospheric, and Planetary Sciences Expo, Feb. 2020 (Poster)
- American Meteorological Society Annual Meeting, Jan. 2020 (Talk)
- American Geophysical Union Fall Meeting, Dec. 2019 (Poster)
- Annual Community Modeling and Analysis System Conference, Oct. 2019 (Talk)
- Purdue University, Department of Earth, Atmospheric, and Planetary Sciences Expo, Feb. 2019 (Talk)
- Purdue University, Department of Earth, Atmospheric, and Planetary Sciences Expo, Feb. 2019 (Poster)
- American Geophysical Union Fall Meeting, Dec. 2018 (Poster)
- American Geophysical Union Fall Meeting, Dec. 2017 (Poster)
- American Geophysical Union Fall Meeting, Dec. 2016 (Poster)
- American Geophysical Union Fall Meeting, Dec. 2015 (Poster)
- Purdue Undergraduate Research Conference, Apr. 2015 (Poster)
- American Meteorological Society Annual Student Conference, Feb. 2014 (Poster)
- American Meteorological Society Annual Student Conference, Jan. 2013 (Poster)